DEVELOPMENT OF ZEIN-BASED BIONANOPARTICLES FOR HIGHLY EFFICIENT TARGETED GLIOBLASTOMA THERAPY AND INVESTIGATION OF CONFORMATIONAL DYNAMICS OF SARS-COV-2 VARIANTS RBDS AND THEIR INTERACTIONS WITH ACE2 BY MASS SPECTROMETRY

ZHANG DONG

PhD

The Hong Kong Polytechnic University

2023

The Hong Kong Polytechnic University

Department of Applied Biology and Chemical Technology

Development of Zein-based Bionanoparticles for Highly Efficient Targeted Glioblastoma Therapy and Investigation of Conformational Dynamics of SARS-CoV-2 Variants RBDs and their Interactions with ACE2 by Mass Spectrometry

Zhang Dong

A Thesis Submitted in Partial Fulfillment of

the Requirements of the Degree of Doctor of Philosophy

Aug 2022

Certificate of Originality

I hereby declare that this thesis is my own work and that, to the best of my knowledge and belief, it reproduces no material previously published or written, nor material that has been accepted for the award of any other degree or diploma, except where due acknowledgement has been made in the text.

_____

Zhang Dong

Abstract

Dactolisib (Dac) is an effective dual PI3K/mTOR inhibitor for cancer treatment. It was the first PI3K inhibitor to enter clinical trials, which, however, were terminated because of the toxicity of Dac to normal tissues. To apply Dac to cancer therapy while avoiding its toxicity, we developed a new brain-targeting drug delivery system self-assembled from zein, a cell membrane-penetrating amphiphilic protein found in corn. Specifically, the amphiphilicity of zein drives its self-assembly into nanoparticles (NPs) that encapsulate Dac with high efficiency. RVG29, a 29-mer brain-targeting peptide, is chemically conjugated to zein that constitutes the NPs to form Dac-encapsulated NPs (zein-RVG-Dac_NPs). Both zein and RVG29 facilitate the resultant NPs to cross the blood-brain tumor barrier (BBTB) and they are taken up by the glioblastoma (GBM) cells, with RVG29 being more efficient than zein in the BBB permeation. Administration of zein-RVG-Dac_NPs through tail veins significantly increased the accumulation of Dac in the orthotopic brain tumor of mice and effectively inhibited tumor growth. Neither toxicity nor adverse effects in the major organs were found due to the excellent biocompatibility of zein and the targeted delivery of Dac into brain tumor cells. These results showed that integrating a brain-targeting peptide (RVG29) to a cell-penetrating natural protein (zein) could form NPs that could effectively penetrate the blood-brain barriers (BBB) and BBTB and then enter brain tumor cells to release Dac, leading to highly effective targeted brain cancer therapy. The use of such NPs can be extended to the development of therapeutics for treating different brain diseases due to their unique combination of biocompatibility as well as brain-targeting, BBB-crossing and cell-penetrating properties.

COVID-19 has been posing serious health threat to and significant impact on the social life and economy globally since its first report in December 2019. The rapid evolution of SARS-CoV-2 to multiple variants with enhanced infectivity and transmissibility has made the combat against the pandemic more challenging. It is thus of great importance to understand how SARS-CoV-2 variants-associated mutations mediated the interaction between the SARS-CoV-2 spike protein, particularly its receptor binding domain (RBD), and the receptor in host cells, angiotensin-converting enzyme 2 (ACE2), which is closely related to the transmission of SARS-CoV-2. Until now, knowledge about this interaction is mainly based on the static structures obtained by Cryogenic electron microscopy (Cryo-EM) or X-ray crystallography, and no systematic study on this interaction has been conducted for various variants of SARS-CoV-2. In this study, RBDs of SARS-CoV-2 wild type (WT) and several major variants, including Alpha, Beta, Zeta, Kappa, Delta and Omicron, as well as their ACE2 complexes were investigated using hydrogen/deuterium exchange mass spectrometry (HDX-MS), a powerful technique for exploring in-solution conformational dynamics of proteins, in an effort to reveal the information that cannot be obtained by Cryo-EM or X-ray crystallography and understand how SARS-CoV-2 mutations affect the conformational dynamics of RBD and its interaction with ACE2.

HDX-MS of the unbound RBDs revealed the reduced flexibility of several regions in SARS-CoV-2 RBD variants, especially for those with the mutation N501Y in the key interaction loops, which helped to stabilize the loop (Y485-Y501, L1) at the closed conformation of RBD. In addition, the core of RBD became more rigid as SARS-CoV-2 variants developed. The Kappa variant (L452R/E484Q) presented the higher flexibility for

several vital binding interfaces, which emphasized the conformational effects of the mutation L452R. Compared with the Kappa variant, the Delta variant (L452R/T478K) showed a more rigid conformation in another interface loop (residues 444-452), suggesting that the dual mutations of E478K and L452R closely correlated with the increased binding affinity. Upon binding to ACE2, reduced deuterium uptake was observed at two binding interface regions covering residues 495-512 and 464-480. Increased HDX and thus higher flexibility of the sheet within the RBD core (residues 405-419) were observed for the Beta variant containing the mutation at N417K, which would break the existing salt bridge with D30 of ACE2. The most dramatically reduced HDX of L1 upon the binding was observed for the Alpha and Delta RBDs, which supported the higher transmission of the two variants. Moreover, the positively charged mutations Q493R and Q498R of Omicron created more favorable connections with the negatively charged E35 and D38 in ACE2, resulting in a more compact binding interface. The conformational dynamics of ACE2 and the changes upon binding to WT and variant RBDs were investigated as well. Among all the studied RBDs, the Alpha RBD (N501Y) was observed to induce the most dramatically decreased HDX uptake for the region covering residues F28-S43 of ACE2, which was associated with a newly formed π-π stacking between Y501 and Y41 of ACE2, resulting in the more compact interfaces of the RBD-ACE2 complex. Allosteric effects on the loops at the edge of ACE2, especially upon binding to the Beta, Delta or Omicron variants, which were the determinants for viral acceptance, were observed. The binding with the Beta variant induced higher flexibility of the edge loop covering S280-T294. Interestingly, the Delta RBD allosterically led to the more flexible regions at the edge of ACE2, while more compact regions were detected in the Omicron RBD-ACE2 complex. These findings might

provide evidence to explain the different performances and clinical symptoms for the patients infected with the Delta or Omicron variants. Overall, this study about the conformational dynamics of WT and variant RBDs and their binding to ACE2 provides valuable information for understanding the evolution of SARS-CoV-2 and improving the design of drugs and vaccines against SARS-CoV-2 variants.

Research Publications

Journal Papers

Dong Zhang, Yi Wang. Functional Protein-Based Bioinspired Nanomaterials: From Coupled Proteins, Synthetic Approaches, Nanostructures to Applications. International Journal of Molecular Sciences, 2019, 20(12): 3054.

Heting Hou^, **Dong Zhang**^, Jiewen Lin, Yingying Zhang, Chengyong Li, Zhe Wang, Jiaoyan Ren, Maojin Yao, Ka-hing Wong*, and Yi Wang*. Zein-Paclitaxel Prodrug Nanoparticles for Redox-Triggered Drug Delivery and Enhanced Therapeutic Efficiency. Journal of Agricultural and Food Chemistry, 2018, 66(44): 11812-11822.
(^Co-first author)

Heting Hou^, **Dong Zhang**^, Jie Zeng, Liping Zhou, Zhe Wang, Maojin Yao, Jiaoyan Ren, Nan Hu*, and Yi Wang*. Bilayer Nanocarrier with Protein-Acid Conjugation for Prolonged Release and Enhanced Anticancer Effects. Langmuir, 2019, 35(10), 3710-3716.
(Cover paper)
(^Co-first author)

Dong Zhang, Jianglong Kong, Xueying Huang, Jie Zeng, Qiaohui Du, Tao Yang, Hui Yue, Qing Bao, Yao Miao, Yajing Xu, Honglin Jiang, Fang Lei, Mingying Yang, Yi Wang*, and Chuanbin Mao*. Targeted Glioblastoma Therapy by Integrating Brain-Targeting Peptides and Corn-derived Cancer Cell-Penetrating Proteins into Nanoparticles to Cross Blood-Brain Tumor Barriers. Materials Today Nano, *23*, 100347.

Conference paper

Dong Zhang, Tszfung Wong, Puikin So, Zhongping Yao*. Conformational Dynamics of SARS-CoV-2 Variant RBDs and their Interactions with ACE2: Insights Revealed by Mass Spectrometry. HKSMS Symposium 2022, Hong Kong, 11 June 2022 (Outstanding Oral Presentation Awards)

Dong Zhang, Tszfung Wong, Puikin So, Zhongping Yao*. Conformational Dynamics of SARS-CoV-2 Variant RBDs and their Interactions with ACE2: Insights Revealed by Mass Spectrometry. ASMS Conference 2023, Houston, 4-8 June 2023 (Poster Presentation)

Acknowledgement

I would like to express my sincerest appreciation to my esteemed supervisor, Prof. Zhongping Yao, for his selfless help, patience, and advice in my complete PhD programme. His outstanding background in mass spectrometry provided the correct orientation for my research, besides, he gave me the maximum freedom to perform my study. In addition to the research life, he also showed kind concern for my daily life, especially during the pandemic of COVID-19. What impressed me more is his rigorous research attitude, this is a valuable guide for my future life. I also want to express my great gratitude to my co-supervisor, Dr. Yi Wang, for giving me a precious opportunity to firstly enter the research field. He always encouraged me and gave me many possibilities to try, no matter how difficult problems I met.

I express my special thanks to Dr. Pui Kin So, Dr. Melody Yee Man Wong, Dr. Sirius Pui Kam Tse and Dr. Chi Hang Chow, for the technical support and useful suggestions. Special thanks to my senior groupmate, Dr. Patrick Tsz Fung Wong, for his experimental guidance. I always obtained new insights after the discussion with him. Many thanks to all my groupmates, Dr. Suying Li, Dr. Jianying Wang, Dr. Dongqi Han, Miss Xuewei Lin, Mr. Eugene Zhen Yan Li, Miss Deejay Suen Yui Mak, Mr. Michael Ho Yin Ma, Mr. Jun Dai, Mr. Yin Zhou, Dr. Cheuk Chi Ng. With the help of other HDX users such as Dr. Patrick Tsz Fung Wong, Mr. Wai Po Kong, and Miss Yuanyuan Zheng, I also have made great progress in the instrumental use. I express my thanks to Dr. Du Qiaohui, for the guidance of many biological experiments and wholehearted support.

The technical and administrative support by the staffs in Department of Applied Biology and Chemical Technology, the instrumental platform supporting by The University Research Facility in Chemical and Environmental Analysis is appreciated.

Sincerest thanks to my parents and friends for their undivided support when I was in trouble. Although my parents couldn't be with me, they tried their best for providing me with everything I need. I would like to express my thanks to my friends, Mr. Xiao Yao and Miss Shichun Han. I truly cherished the time we spent together, which made me feel relaxed and happy.

Thank God for giving me this opportunity to do what I love.

Table of Content

List of Figures

Chapter 1

Chapter 2

Chapter 3

Chapter 4

Chapter 5

Chapter 6

List of Tables

Chapter 3

Chapter 5

Chapter 6

List of Abbreviations

Abbreviation	Full form
PET	positron emission tomography
BBB	blood brain barrier
CNS	central nervous system
BBTB	blood brain tumor barrier
NPs	nanoparticles
Trf	transferrin
Lf	lactoferrin
EGF	epidermal growth factor
HIP1	huntingtin interacting protein 1
AR	androgen receptor
LDL	low-density lipoprotein
LRP	low-density related lipoprotein
MM	matrix metalloproteinase
FR	folate receptor
FA	folate
IR	insulin receptor
nAChRs	nicotinic acetylcholine receptors
VIP	vasoactive intestinal peptide
RGD	cyclic arginine-glycine-aspartic
NGR	Asn-Gly-Arg
CB	cediranib

PTX	paclitaxel
RVG	rabies virus glycoprotein
SEM	scanning electron microscopy
TEM	transmission electron microscopy
DLS	dynamic light scattering
FTIR	fourier-transform infrared spectroscopy
NMR	nuclear magnetic resonance
MS	mass spectrometry
RBITC	rhodamine B isothiocyanate
ICG	indocyanine green
FDA	food and drug administration
BLI	bioluminescent imaging
MRI	magnetic resonance imaging
PET	percutaneous endoscopic gastrostomy
HA	hyaluronan
PLK1	polo-like kinase 1
hFn	heavy chain ferritin
lFn	light chain ferritin
HDL	high-density lipoprotein
RMT	receptor-mediated transcytosis
RME	receptor-mediated endocytosis
MWCO	molecular weight cut-off
PDI	polydispersity index

EE	encapsulation efficiency
LE	loading efficiency
UV-vis	ultraviolet-visible
MTS	2.3.8 3-(4,5-dimethylthiazol-2-yl)-5-(3-carboxymethoxyphenyl)-2-(4-sulfophenyl)-2H-tetrazolium
DPBS	dulbecco's Phosphate-Buffered Saline
MEM	minimum essential medium
SDS-PAGE	sodium dodecyl sulfate-polyacrylamide gel electrophoresis
PVDF	polyvinylidene fluoride
CLSM	confocal laser scanning microscopy
TEER	transepithelial electrical resistance
SD rat	sprague dawley rat
GBM	glioblastoma
IF	immunofluorescence
IHC	immunohistochemistry
TUNEL	terminal deoxynucleotidyl transferase dUTP nick end labeling
CD31	cluster of differentiation 31
H&E	hematoxylin and eosin
CSF	simulated cerebrospinal fluid
ALP	alkaline phosphatase
AST	aspartate transaminase
ALT	alanine transaminase
CREA	creatinine

SARS-CoV-2	severe acute respiratory syndrome coronavirus 2
COVID-19	coronavirus disease 2019
N	nucleocapsid
M	membrane
E	envelop
S	spike
ACE2	angiotensin-converting enzyme 2
Ang	angiotensin
PD	peptidase domain
CLD	C-terminal collectrin-like domain
RBD	receptor binding domain
VOI	Variants of Interest
mAbs	monoclonal antibodies
PCA	principal component analysis
MD	molecular dynamics
PCR	polymerase chain reaction
Cryo-EM	cryogenic electron microscopy
NTD	N-terminal domain
SPR	surface plasmon resonance
BLI	bio-layer interferometry
ELISA	enzyme-linked immunosorbent assay
HDX-MS	hydrogen/deuterium exchange mass spectrometry
MALDI	matrix assisted laser desorption/ionization

ESI	electrospray Ionization
LC	liquid chromatography
UPLC	ultra-performance liquid chromatography
TOF	time-of-flight
IM	ion mobility
CE	capillary electrophoresis
WT	wild type
PLGS	protein lynx global server
CI	confidence interval
PDB	protein data bank
RFU	relative fractional uptake
RBM	receptor binding motif

Part 1: Targeted Glioblastoma Therapy by Integrating Brain-Targeting Peptides and Amphiphilic Proteins into Nanoparticles to Cross Blood-Brain Barriers

Chapter 1. Introduction

1.1 Brain tumors

1.1.1 Epidemiology

These days, there is an increasing incidence of brain tumors, which make up of about 1% to 2% of all cancers. The major prescriptive malignant tumor is glioma, which may be related to different factors such as special class of radiation exposure and genetic potential. As a grade IV astrocytoma, glioblastoma is accountable for more than half of gliomas, which are more frequently detected among the elderly population. Compared to the less developed regions in Africa and Asia, developed countries in Americas and Europe show nearly twice the prevalence of malignant brain tumors. Brain cancer is more generally observed among male individuals.[1,2] For prognosis, the average survival period of patients who have undergone general therapeutic strategy (chemoradiotherapy) is 15 months, while that of combined treatment of radiotherapy and chemoradiotherapy is 2-5 years.[3]

1.1.2 Therapeutic strategies

1.1.2.1 Surgical resection

Since it is difficult to detect brain tumors are at the early stage, surgical resection is regarded as a basic and major choice for glioblastoma treatment for rapid improvement of symptoms. However, due to the limitation of complex structure and the location of neoplastic tissue within brains, complete removal of all the brain tumors without causing

any damage has become a considerable challenge. Recently, surgical resection could be accomplished by visual functional technological support of magnetic resonance imaging (MRI) and fluorescent tracking, and a slight prolonging of the tumor-free stage for 6 months results but the overall survival period remains unchanged. Therefore, in addition to several unresectable sufferers (20-30% patients), surgical strategies still present some major limitations for the treatment of brain cancer. [3,4,5, 6]

1.1.2.2 Radiation

Besides regular MRI, the progressive imaging strategies involving MR spectroscopy and positron emission tomography (PET) have improved therapeutic efficacy by precise visual tracking of tumor location. Radiation may lead to tissue injuries and curb the growth of brain tumors with the prompt effects, resulting in radiation necrosis of tumor tissues. However, although radiation therapy is carried out to specific areas, it may cause unwanted vessel damage and chronic injury. Radiation causes direct damage to endothelial cells and therefore contributes to the reduction of vessels, and finally causing the improper functioning of the blood brain barrier (BBB).[7] For children younger under five year old, the highly effective radiation treatment would create unacceptable adverse side effects, therefore not suitable for clinical therapy.[8]

1.1.2.3 Chemotherapy

Glioma presents resistance against major therapeutic strategies. Chemotherapy can prolong the overall survival among 10% of cancer patients. Rutkowski etc. conducted a

clinical survey with 43 patients (including young children below 3 years of age) who had been histologically diagnosed with medulloblastoma and had been treated with surgery. The patients who had undergone partial or complete surgical resection all accepted the same chemotherapy protocol without any undesired toxicity. The study suggested that chemotherapy was a more favorable strategy that would be solely or used in combination after surgery to reduce demand for radiotherapy among young children.[9] The tumor cells presenting chemo-resistant properties limited the utilization of chemotherapy. Besides, BBB plays its protective functions by blocking chemo-substances, which would cause failure of treatment. Although chemotherapy is a powerful remedy against brain cancer, the treatment effect of chemotherapy also depends on the various receptivity of cancer cells. For patients with significant resistance against several chemo-drugs, there is still an urgent need to establish novel systems for targeting specialized cancer types.[10]

1.1.3 Blood brain barrier (BBB)

1.1.3.1 Composition

The BBB mainly comprises blood vessels with two different cell types: endothelial cells for the interior protection and mural cells for inundating vessels. Endothelial dominates the delivery of substances between blood and the brain. It is worth mentioning that the arrangement of endothelial within the central nervous system (CNS) is distinctive from that of other organs. The surface barrier layer is composed of the tight attachment of endothelial cells, which plays a function in regulating the transcellular response.[11] Mural cells including the muscle cells are enclosed by pericytes and vessels, and pericytes contain

the highest covered density for endothelial vessels than any organs or tissues. Pericytes are associated with several vital bioactivities, such as monitoring angiogenesis, fluctuating the flow of blood, and adjusting the extracellular matrix, however, the characteristics of the single pericyte remain unclear.[12, 13]

The extraordinary structure of BBB has been much studied to reveal the transport mechanisms by identifying the appropriate molecular formation of BBB. Due to the tight attachment of endothelial cells, the highly organized structure then forms a barrier that contains unique size-dependent permeation properties and allows the transition of small molecules with sizes up to 4 nm, while creating limited permissibility for larger molecules.[14] The BBB may finitely permit the passing of many essential substances, and the specialized association among different cells supports a sufficient supply of the substances. Besides the defense against the entry of outside substances, the composition within the BBB is significantly different from that of plasma, which involves exceptional factors such as Cystatin-C with primary protective properties. In conclusion, BBB plays vital roles in maintaining the microenvironment inside the CNS and supports the ordered responses of neurons and avoids damage outside the BBB.[15] Therefore, BBB is the extensive protected layer that may display the refusal of drug delivery, therefore it diminishes the utilization of chemotherapy.[13]

To deliver substances permeating the BBB, several routes show significant differences in targeting the substances with varying degrees of surface polarity. The molecules with higher polar surfaces (higher than 80 $Å^2$) prefer being permitted through BBB, compared

to the lower polar ones, except plasma proteins. Due to the electronic microenvironment, the surfaces of molecules accompanied with charges are more accessible for the interactions with cell membranes, therefore promoting the entry of substances.[16] It is worth mentioning that the transportation of macromolecules including peptides and proteins mainly depends on vesicular mechanisms. The specific receptors on the surface of cells are recognized for binding to form a vesicle together with the bound macromolecules, followed by the internalized functions of endothelial cells.[17]

1.1.4 Blood brain tumor barrier (BBTB)

The low-level of glioma may not affect the expected functions of BBB.[18] However, the invading tumor cells results in the formation of intensified expression of vessels, thus forming BBTB of high-class glioma. The BBTB is mainly composed of an overexpression of capillaries derived from brain tumors. It is worth mentioning that the proliferation of high-class glioma cells may invade and expand outside the brains, simultaneously, while the inside the normal brains the ordinary protective properties of the BBB are retained. The co-operation between the BBTB and BBB has created a complementary barrier against the delivery of therapeutic substances.[19, 20]

BBB and BBTB are large and dynamic structures that are evolutionarily designed to protect the vulnerable brain from harmful substances, including about 98% of the drugs, in blood circulation. The BBB and BBTB are composed of cerebral blood endothelial cells, pericytes, astrocytes, and highly restrictive tight junctions, all of which work in unison to form a robust physical barrier at the interface between the blood and brain.[21, 22] The

transportation of NPs containing therapeutic substances between the intact BBB and BBTB into the brains remains a significant hurdle for general drug interventions.

1.2 Nanoparticles (NPs) for targeting delivery

To overcome the BBB/BBTB, various drug delivery technologies have been investigated. Physical and chemical means of BBB/BBTB manipulation are applied to break down the BBB/BBTB.[23-25] Molecular structures of the drugs are modified and designed, such as prodrugs. Nano-sized carriers are developed to protect the drugs and enrich the accumulation of the drugs at specific disease sites.[26] The surface modification of nanoparticles (NPs) using the brain-targeting agents are able to recognize the over-expressed receptors on the BBB and BBTB and allow the therapeutic agents to gain access to the brains via receptor-mediated transcytosis.[22, 27-29]

1.2.1 Physicochemical requirements for crossing BBB of NPs

There are various requirements in penetrating BBB, which are as follows. Firstly, with the high arrangement of endothelial cells of BBB, size limitation is one of the most vital considerations. The size of NPs below 200 nm is generally considered with the properties for being taken up via dominating pathway, while NPs with the size ranging from 200-500 nm are permitted of caveolae-mediated for passing the BBB.[30] Noticeably, clinical safety is another crucial prerequisite for utilizing NPs as the drug carrier, which requires higher drug loading efficacy, continuous drug release, and appropriate biodegradation through

metabolism. The controlled release of NPs makes it possible to release drugs with special targeting functions, resulting in sustained higher therapeutic efficacy within a period.[31]

1.2.2 The widespread receptors of the CNS

Based on the high level of the overexpressed receptors within the BBB or CNS, there is a superior platform via a receptor-mediated pathway to achieve targeting drug delivery and imaging diagnosis. The receptors under study with considerable expression and binding affinity together with the mechanical pathways for mediation are presented as follows. As a transporter, transferrin (Trf) receptor guides the conveying of iron, which plays functions in proliferation among normal functional cells. Due to the accelerated growth and replication of tumor cells, Trf is commonly detected on the cell surface, in which advanced Trf expression which contacts with iron from blood circulation is found.[32] Lactoferrin (Lf) receptor with microbicidal properties is another iron-associated protein of concern. It is related to the regulation within the immune system and differentiation of neurons. It has been regarded as a medium of targeting drug delivery for pharmeceutical treatment among CNS diseases.[33, 34] Besides, due to its more advanced expression and sensitivity, Lf receptor is selected as a modifier on the surface of NPs. The superior NPs present superior functions for the detection of glioma via in vivo experiments, indicating its utilization potential in glioma diagnosis at the early stage.[35]

A widespread receptor of epidermal growth factor (EGF) distributed on the epithelial is demonstrated with a higher expression level within glioma.[36, 37] Depending on the cell type, density, and microenvironment, EGF receptor (EGFR) participates in multiple signaling

pathways, and regulates tumor cells proliferation and metastasis.[38] Recently, a novel receptor of huntingtin interacting protein 1 (HIP1) associated with EGFR is reported for the direct interaction with EGFR and affects its degradation, which further impacts the growth of cancer cells.[39] There is another highly expressed androgen receptor (AR), AR-RNA, and AR-protein of glioma, especially among female patients, which is originally detected in breast cancer. Recently, several antagonists targeting AR are demonstrated for the apoptosis of glioma cell lines, which suggests their genetic effects and medical potential.[40] To study the low-density lipoprotein (LDL) receptor and its related protein (LRP), the binding properties and the expression level were determined by using seven brain cancer cell lines. Among them, three cell lines were evaluated with a rich expression of LDL, and SF-767 cells were observed with high binding affinity, which indicated the accumulation in LDL receptors.[41] Compared to the LRP1 knockdown cells, another study investigated the indirect facilitating properties of LRP1 to the migration of cancer cells by regulating the levels of matrix metalloproteinase 2 (MM2) and MM9.[42]

As a membrane protein, folate receptor (FR) performing advanced binding affinity with folate presents a high expression level among multiple types of cancer tissues. It provides a powerful basis for serving as markers of imaging detection and drug delivery. FRs mainly exhibit as clusters and locate on the exposed caveolae, participating in cellular internalization.[43, 44] Two isoforms of FRα and FRβ are also detected with their anti-cancer potential. FRα involves one pathway for folate (FA) transportation, followed by the uptake functions of cells. FRα has been demonstrated to suppress the growth of cancer cells in preclinical studies.[45, 46]

Insulin receptor (IR), which is characterized by insulin signaling functions, acts as medium and signaling transporters. The precise expression of IRs among various cancers is unclear, however, due to its regulated properties for downstream expression of surface receptors such as EGFR on cancer cells, it is still of great concern. Various IRs belonging to the IRs family accommodate multiple factors for slow down the development of cancers.[47]

Neuronal nicotinic acetylcholine receptors (nAChRs) of transmembrane proteins are widely positioned on the neuron cells both inside and outside of the CNS. nAChRs comprises two subunits of α and β with several subunits, which provide an entry for signaling transportation via an ion channel with voltage. It has been reported the proliferation function of nAChRs, especially for α7 nAChR, has been implicated in rectifying the effects of nicotine in lung cancer.[48]

1.2.3 Functional peptides for the permeation of the BBB

As mentioned before, the specific recognition and interaction of receptors on the BBB may establish a receptor-mediated transcytosis platform and provide entry for guiding the passing of NPs with sizes over 200 nm. As triggers, numerous peptides play functions in targeting various receptors and facilitating permeation of the BBB.

1.2.3.1 Vasoactive intestinal peptide (VIP)

As a neuron-peptide within the brain, VIP with 28 amino acids length and extraction from the intestine is evaluated to have higher binding efficiency for the interactions of receptors

within the targeting tissues and advanced sensitivity for detecting the location of tumors.[49] VIP has been approved with the permeated properties against the BBB through HPLC, of which the movement is unidirectional transmembrane diffusion.[50] VIP is also considered to facilitate survival and prevent the death of neuron cells.[51]

1.2.3.2 Angiopep-2 peptide

Angiopep-2 is another peptide that can organize transcytosis by detecting the expression of LRP-1 on the endothelial cells of the BBB. Several studies have indicated that the modified operations for the combined usage of angiopep-2 and anti-cancer drugs induce targeting delivery and assistance in chemotherapy.[52] Razelle et. indicated that angiopep-2 peptide displayed high safety and improved the recognizing of LRP-1, via human clinical experiments. The novel peptide-based drug with a long half-life presented extremely advanced curative effects on solid tumors. The investigation provided substantial support for exhibiting the practical implication of angiopep-2-based drugs.[53] Angiopep-2 conjugated with metal NPs displayed great potential in imaging therapy, too. The magnetic NPs showed significant suppression of the growth of glioma cells and minimal side effects on the healthy cells.[54]

1.2.3.3 Cyclic arginine-glycine-aspartic (RGD) peptides

Over the decades, RGD peptides, which are mainly used as radiotracers, have been identified with high binding efficacy with integrin αvβ3 antagonists from vessels surrounding the cancer cells with low expression among normal cells. The antagonists limit

the growth of newly generated vessels and therefore retard the development of tumors.[55, 56] Due to the distribution of antagonists, RGD peptides with high sensitivity would be suitable for the bioimaging treatment and radiotherapy.[57] A study that compared the targeting adequacy of permeating BBB among six common peptide-based NPs found that a dual decoration by RGD & angiopep-2 presented an admirable ratio for cellular uptake of BBB/BBTB and remarkable prolonged drug release. The findings were proved in vitro and in vivo imaging studies, which indicated the chemotherapy potential of RGD peptides.[58] Yutaka et. also demonstrated a higher accumulation of NPs containing the RGD ligand within the BBB. The NPs presented a long period of circulation, deep penetration of the BBB, and efficient arriving at glioma sites.[59]

1.2.3.4 Asn-Gly-Arg (NGR) peptides

An 8 amino acid length (CYGGRGNG) of NGR peptides have similar functions as that of RGD, which would recognize aminopeptidase N as its receptor and further improve the transition of NGR-conjugated NPs. Decades ago, researchers indicated the more advanced therapeutic potential of NGR-coupled anti-cancer drugs than pure drugs.[60] With NGR modification, NPs containing PTX with sizes around 50 nm were made and they could directly block the proliferation of cells in in vitro and glioma-bearing mice models.[61] Dual peptides conjugated NPs targeting various receptors were designed for the treatment of glioma, T7 and NGR peptides accompanied with a novel biomimetic carrier covering red blood cell membranes. The anticancer efficacy was observed in both in vitro and in vivo models with remarkable inhibitory for the development of glioma.[62]

1.2.3.5 HIV-1 TAT peptides

TAT peptides with 9 amino acids (RKKRRQRRR) showing outstanding transition properties for delivering NPs through the BBB and BBTB are first identified from HIV-1 Tat protein.[63] TAT may induce a positive charge of NPs/peptides/proteins, resulting in enhanced cellular uptake with higher transportation efficacy. To establish a system for monitoring the differentiation and evolving of cancer stem cells, a study indicated that the novel superparamagnetic NPs were modified by HIV-TAT via cell labeling strategy. The labelled cells retained the natural differentiation capability, which could be tracked through MR imaging.[64] TAT peptides on the surface of liposomes also were proven to be able to carry therapeutic substances of around 200 nm inside different types of cell cytoplasm without any side effects.[65] Gold NPs with superior water-soluble property and small sizes were designed by using TAT peptides. The biocompatible NPs were smaller than 30 nm and could be synthesized through direct steps. Their high accumulation in the nucleus of cells was detected, meaning they could be further utilized for cell imaging and targeting drug transportation.[66]

1.2.3.6 T7 peptides

As a peptide with small molecular weight, T7 (HAIYPRH) was shown to have a high binding affinity towards Trf. The overexpressed Trf was found on the surface of endothelial cells. The interaction between T7 and Trf was able to trigger the brain targeting delivery.[67, 68] The findings suggested the functions of T7 for genetic treatment of glioma via RNA interference. T7 was monitored with a 2.17-fold higher targeting capability in in

vitro and in vivo models. The NPs with high stability and biocompatibility were shown to participate in nanomedical-based glioma treatment.[69] These collaborated systems with T7 peptide ligands had a higher level of accumulation within brain tumors than the non-revised NPs. Besides, after administration of the NPs, the EGRF receptor was significantly decreased in the mice models, demonstrating less distribution and growth of tumor tissue.[70] Another study established a dual-functioned platform containing cediranib (CB) and paclitaxel (PTX) containing T7 peptides. It presented a remarkable higher level (7.89-fold) for penetration than the non-targeted ones. The BBB permeation ability of the T7-based system could be used for the synergetic drug with better anti-glioma effects.[71]

1.2.3.7 Rabies Virus Glycoprotein (RVG) peptides

Rabies virus glycoprotein (RVG) showed the capacity of specific binding to the nicotinic acetylcholine receptors (nAchR) located in the BBB, and the potential of RVG to facilitate the brain uptake has been widely investigated.[72] A peptide with 29 amino acids derived from RVG, RVG29, has been approved for the function of efficient crossing the BBB via nAchR-mediated transcytosis.[73] RVG was slightly reorganized by adding monomer residue such as Cys and Arg, resulting in an enabled binding of NPs and siRNA. The study displayed closable targeting towards neuron cells and made it possible for the direct transportation of DNA or siRNA in an imitated region without diffusion.[74]

1.2.3.8 GE11 peptides

More recently, a novel functionalized peptide GE11 (YHWYGYTPQNVI) with low price was supported by both in vitro and in vivo experiments for its precise binding ability targeting EGFR.[75] The probe-based NPs were coupling modified by Au and GE11, which was sensitive enough and could be visualized with forceful absorption for NIR spectral region, suggesting its functions in photothermal therapeutic strategy.[76]

1.3 Nanocarriers for anti-cancer drug delivery

1.3.1 Nanoparticles decoration and characterization

Various methodologies are developed for the preparation of NPs-based platforms, such as evaporation,[77] emulsion,[73, 78] self-assembly,[79] encapsulation,[80] and covalent bonds,[81] resulting in the surface modification and inside anti-cancer drug loading. Functional ligands conjugation commonly could be accomplished by simple covalent linking via crosslinker such as ester derivatives. Due to the vital roles of loading and conjugated efficiency, the physiochemical properties evaluation would be quantitively determined. The size of NPs acutely influences the targeting and permeation capability of NPs, therefore is of great concern. The size and morphography of NPs were widely evaluated by Scanning Electron Microscopy (SEM) and Transmission Electron microscopy (TEM) in a solid state, while the distribution and size could be measured by Dynamic Light Scattering (DLS), in solution. Evaluating the size of NPs in solution was deeply needed for determining their practical usage. The surface charging of NPs (zeta potential) was associated with the stability and pathway-mediated entry, which could be further obtained

via DLS. To ensure the reaction efficiency, Fourier-transform infrared spectroscopy (FTIR), Nuclear magnetic resonance (NMR), and Mass spectrometry (MS) could be used as the forceful means for certifying the chemical structural and molecular weight of the obtained NPs.[4]

1.3.2 Nanoparticles for facilitating drug delivery

There are several advantages of developing NP-based system against multiple cancers, as followings: 1) The loading level of anti-cancer agents can be designed by controlling the contents of linkers or NPs, which are useful to be utilized for achieving various therapeutic purposes. 2) The special targeting functions of NPs help to achieve the targeted delivery and a longer retention period. 3) NPs serve as a protected barrier for blocking the harmful effects of anti-cancer substances on normal tissues and reducing the side effects. 4) The environment of the digestive system could degrade the inner agents, of which, NPs provide protection for retaining the activity of the drugs. For brain cancer, several limitations such as size requirements and penetration properties decide that not all the NPs could perform appropriate responsibilities against BBB. So far, multiple biocompatible NPs obtained from either synthesis or extraction have attracted great attention for the early stage of brain cancer detection and chemotherapy.[4]

1.3.2.1 Polyethylene glycol (PEG)

At present, PEG polymer containing blood-persistent properties is one of the most attractive materials for clinical drug administration. Depending on the contents of PEG,

the molecular weight range of PEG is 2000-20000 g/moL and presents various surface densities.[82] PEG-based modifiers are also demonstrated with the higher accumulation level within tumor sites, when they are coupled with special targeting ligands or peptides such as FA and RGD.[83] A study prepared a PEG-PLGA-based carrier conjugating with RGD and encapsulating with paclitaxel (PTX), resulted in the enhanced binding towards glioma cells and remarkably increased accumulation in brains.[84] A previously mentioned penetrated peptides, Angiopep-2, was also selected for decorating PEG and expanding a brain-targeted drug delivery system. To study the entry mechanism of NPs towards BBB and the cellular uptake level of endothelial cells, rhodamine B isothiocyanate (RBITC) was utilized as a probe and quantitively evaluated the drug delivery efficiency. The findings presented that LRP receptor could display functions in mediating delivery and was observed with increased accumulation within different regions of brains, compared to that of PEG-NPs.[85]

1.3.2.2 Indocyanine green (ICG)

ICG-based NPs could detect glioma at the early stage and have been approved by Food and Drug Administration (FDA) as a NIR dye, for phototherapy. Dual functional biomimetic ICG-NPs surrounding glioma cell membranes were observed with accumulation in the glioma tissues after 12 hours of administration, moreover, 94.2% of the cells' growth and proliferation was blocked by the photothermal effects, via NIR laser irradiation.[77] Another study designed an ICG-Au nanoprobe carrying albumin for several imaging detections, such as Bioluminescent imaging (BLI), Magnetic resonance imaging (MRI), Percutaneous endoscopic gastrostomy (PET), and so on, via animal models. The results indicated that the NPs suppressed the growth of glioma, besides, FLI-based imaging

therapy presented advanced effects for orthotopic glioma resection, which was supported by the precise detected functions of the ICG-Au-based NPs.[86]

1.3.2.3 Hyaluronan (HA)

As a detector and carrier, HA is a natural glycosaminoglycan and plays a vital role in limiting the cancer development. CD44, a receptor overexpressed on glioma cells, could be recognized by HA. It was reported that the lipid-HA-based NPs containing Polo-Like Kinase 1 (PLK_1) and Cy3-siRNA were established, discovering that the NPs could strongly bind and accumulate within glioma cells. The findings described a dramatic longer survival rate of mice models treated with the NPs entrapping $siPLK_1$, which also suggested the localized accumulation and profitable implication of the therapeutic RNAi NPs.[87]

1.3.2.4 Ferritin

Ferritin is a naturally derived protein comprising 24 amino acids and presents as a shell structure via self-assembling.[88] It exists in two subtypes, respectively are heavy chain ferritin (hFn) and light chain ferritin (lFn). In contrast to (lFn), hFn was recently demonstrated with a similar localized manner towards TfR1 as Tr. To explore the permeation mechanism of hFn, due to its targeting properties, no extra functional ligands would be conjugated on the nanomedicine. After administration, in vivo results presented a considerable higher accumulation level of hFn, which was rapidly detected in the tumor sites of orthotopic mice, while hardly any accumulation could be observed among the normal brain tissues of orthotopic mice. Therefore, the NPs could show the maximum accumulation within brain tumor sites and high therapeutic value.[89]

1.3.2.5 High-density lipoprotein (HDL)

Due to the small size and high tolerance level in human bodies, DHL is able to overcome the barrier of BBB and diffuse among the tumor regions, therefore this biocompatible cargo is a potential nanocarrier for delivering therapeutic agents. A study conducted a DHL-based system co-delivered with CpG oligodeoxynucleotide, an immune responder, and DTX, a common chemotherapy agent. The NPs performed the dramatic effects on suppressing the growth of tumor cells. Whether the NPs were utilized together with IR treatment, 80% of animal tumor models performed the longer survival term, possibly contributed to the immunological memory leading by CpG. Since DHL-based NPs have been tested by human clinical phase I/II studies and were permitted for industrial scale-up,[90, 91] the novel nano discs were believed with practical implications.[92]

1.3.2.6 Zein

Plant-based proteins are inexpensive, abundant, biodegradable, and biocompatible. Many of them have been consumed as an integral part of the human diet. Compared to synthetic polymers and animal proteins, such as gelatin and albumin, the transfer of zein based drug carriers to the clinic can be more direct and rapid. Because of the good biodegradability, they undergo enzymatic or hydrolytic degradation in the biological environment into nontoxic byproducts. Over the past few decades, zein, the major protein of corn, has been investigated as drug and nutrient carriers in the forms of nano-/microcapsules, films, nanofibers, and hydrogels. Zein is insoluble in water but readily disperses in ethanol‑water

mixtures. Zein contains primarily hydrophobic and neutral amino acids but also polar amino acids. Thus, as an amphiphile, zein can self-assemble into various structures, including spheres, sponges, and films. Self-assembled particles made by amphiphiles, including zein, have the ability to transfer through cell membranes, and they also have better stability than normal particles because of their unique surface properties. In vivo, zein NPs are beneficial for prolonged blood residence of a 7.2-fold increase. Because of the good capability of chemical modification, zein and drugs can be conjugated through environmentally sensitive links to form prodrugs capable of triggering drug release.[81]

1.4 Summary

The usage of traditional drugs for brain cancer therapy involves several limitations, due to the protective mechanisms of BBB, there is the lower concentration of therapeutic substances in tumor tissues. Besides, without peculiar targeting functions, the drugs may cause damage to all cells comprising the normal ones and the cancer cells, resulting in severe side effects. Early development of nanocarriers achieved an extended retention period and increased accumulation of NPs through “passive targeting”, the complexes would permeate the tumor vasculature from the rapid formation of tumor generation.[93] Then, “targeting delivery” with higher efficiency accessed a new era in nano-therapeutics. The “active receptors” widely distributed on the tumor regions would be beneficial for cancer visualization and targeted therapy. Until now, many chemotherapeutic drugs conjugating with nano-agents underwent preclinical or clinical studies, which indicated the great success of nanotherapeutics in the treatment of brain tumors.

1.5 Objectives

Glioblastoma with severe survival threat has been considered almost impossible to be completely cured by resection or chemotherapy. Therefore, developing the nanotherapeutic system with longer circulation, higher tumor accumulation, and lower side effects, was of great interest and significance. The regular nanocarriers such as PEG and PLGA were comprehensively investigated, for tumor detection and treatment. Here we focused on exploring the delivery functions of natural-derived NPs, which were not implicated in CNS diseases.

The objectives of this study were to synthesize the RVG29-conjugated Dac-encapsulated zein-based NPs (zein-RVG-Dac_NP) for treating GBM (Figure 1.1). To the best of our knowledge, this is the first-time report on integrating a brain-targeting peptide (RVG29) and a cell-penetrating natural protein (zein) to deliver Dac for targeted GBM therapy. From the study, a natural protein (zein) is firstly selected as a drug carrier to treat CNS diseases in vivo, which provides an economical biomaterial system for application.

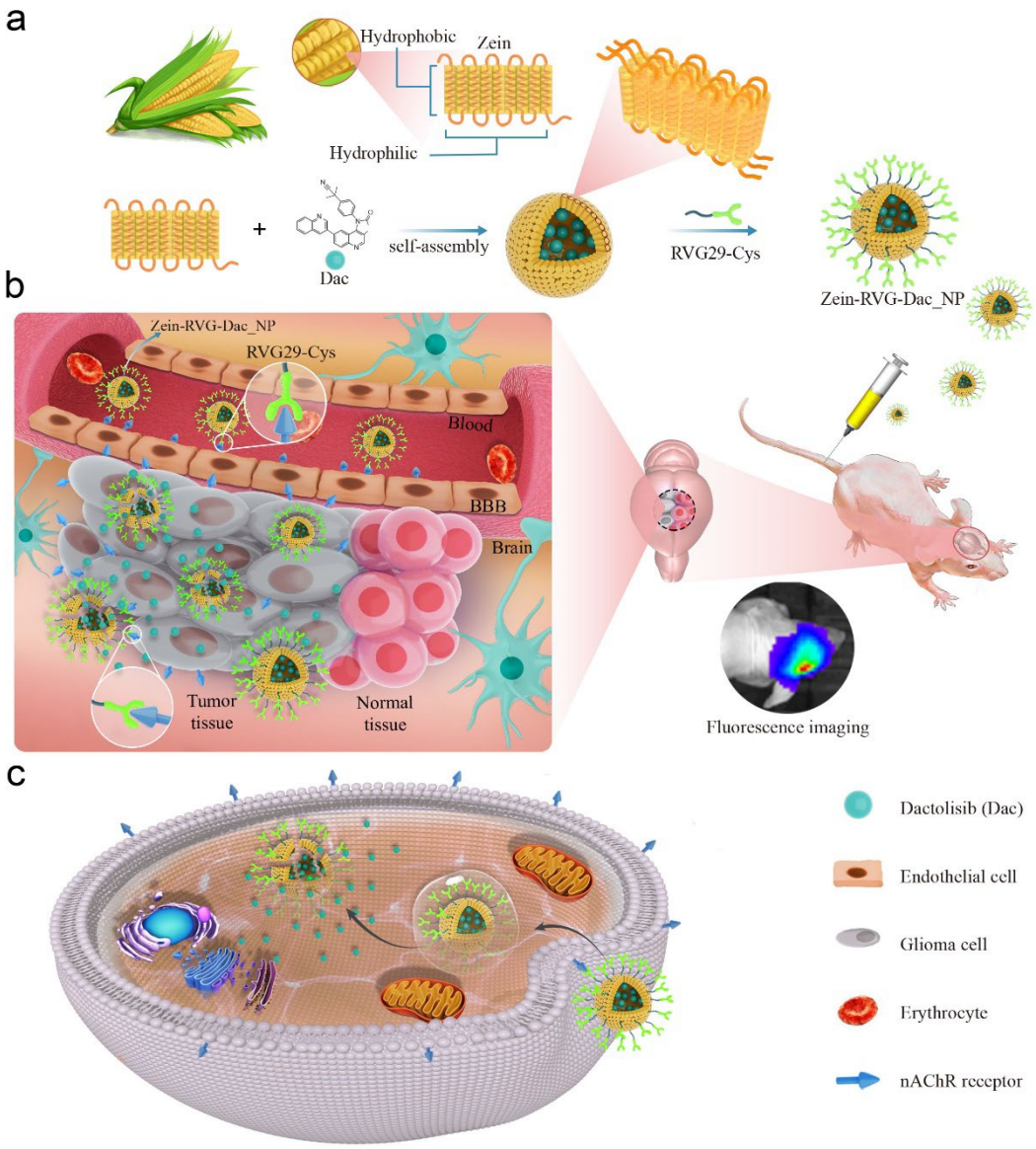

Figure 1.1 Scheme of the formation of zein-RVG-Dac_NPs and the proposed mechanism of action for the treatment of GBM.

a) Design of the zein-RVG-Dac_NPs. Zein is a major protein of corn and can self-assemble into NPs because of its amphiphilc molecular structure. The anti-GBM drug, Dac, was encapsulated by zein through self-assembly to form zein-Dac_NPs, which were surface-modified with the BBB and GBM-targeting peptide of RVG29 to form Zein-RVG-

Dac_NPs. b) Zein-RVG-Dac_NPs, administered by intravenous injection via tail vein, selectively target the overexpressed nAChR receptors on BBB and GBM via receptor-mediated transcytosis (RMT) to cross BBB and then trigger receptor-mediated endocytosis (RME) into GBM cells. c) Zein-RVG-Dac_NPs enter the GBM cells through endocytosis. Zein was degraded by the enzymes in the lysosome, and zein-RVG-Dac_NPs are disrupted to release the encapsulated Dac.

Chapter 2. Materials and Methods

2.1 Materials

Zein, dimethyl sulfoxide (anhydrous, DMSO, ≥99.9%), DMSO-d6, phenazine methosulfate (PMS), and paraformaldehyde (PFA) were obtained from Sigma-Aldrich (St. Louis, MO, USA). Peptide with 30 amino acids (RVG29-Cys, YTIWMPENPRPGTPCDIFTNSRGKRASNGC, 94.4%) was synthesized by GenScript (Zhejiang, China). Dactolisib (Dac) and coumarin-6 (C6) were obtained from Aladdin Industrial Corporation (Shanghai, China). Caspase-3 and cleaved caspased-3 antibodies were purchased from Cell Signaling Technology (Danvers, MA, USA). PI-9 and BAX antibodies were obtained from Lifespan Biosciences (Washington DC, USA). Phosphate buffered saline (PBS, pH 7.4) was purchased from VWR Life Science (Radnor, PA, USA). Hematoxylin was obtained from Solarbio Life Science (Beijing, China). Ethanol (ACS grade) was purchased from Anaqua (Hong Kong) Company Limited. Cy5-NHS ester was ordered from BroadPharm (San Diego, CA, USA).

2.2 Synthesis of Nanoparticles

2.2.1 Formation of the Nanoencapsulation of Dac

Dac was encapsulated via the self-assembly of zein to form zein-Dac_NPs. Firstly, zein was dissolved in an aqueous ethanol solution, then Dac was added with a mass ratio of 7:1. After the evaporation of the solvent using a nitrogen evaporator, zein-Dac_NPs were formed. The excess Dac was removed using a membrane dialysis bag (3 kD molecular weight cut-off (MWCO)), for 5 times. Then, the purified zein-Dac_NP was freeze-dried.

2.2.2 Conjugation of RVG29 and zein-Dac_NPs to Form zein-RVG-Dac_NPs

The reaction steps of the conjugation of the peptide RVG29 and the zein of the zein-Dac_NPs were shown as following. Zein-Dac_NPs were suspended in ethanol, and PBS was added to reach the pH of 7.5 and the final concentration of PBS in the mixture was around 45%. Sulfo-SMCC, a cross-linker, was added to the suspension in the molar mass ratio of sulfo-SMCC to zein at 10:1. The zein molecules on the surface of zein-Dac_NPs was reacted with sulfo-SMCC to obtain the maleimide-activated zein NPs (SMCC-zein-Dac_NPs). The amino group ('NH2-') of zein was reacted with sulfo-SMCC to obtain maleimide-activated zein. SMCC-zein-Dac_NPs were purified, and the excess sulfo-SMCC was removed using a membrane dialysis bag (3 kD MWCO). RVG29-Cys and SMCC-zein-Dac_NPs were mixed with a molar mass ratio of 1.1:1 in the PBS (pH 7.4). The thiol groups of RVG29-Cys were conjugated with the maleimide groups of SMCC-zein-Dac_NPs to obtain zein-RVG-Dac_NPs and the excess RVG29-Cys was removed using a membrane dialysis bag (5 kD MWCO). The conjugation efficiency of RVG29-Cys was calculated using the following equation:

$$\text{Conjugation Efficiency (\%)} = \frac{\text{Total RVG29-Free RVG29}}{\text{Total RVG29}} \times 100\%$$

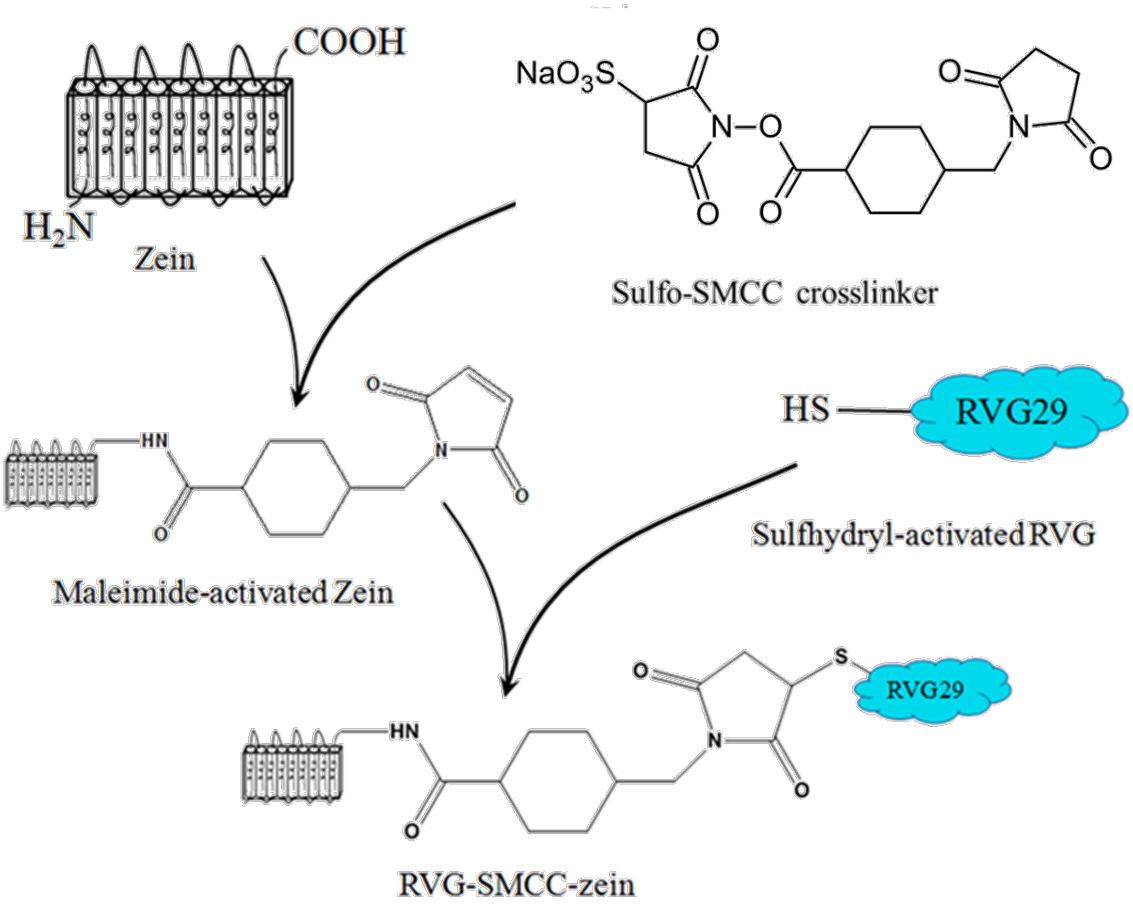

Figure 2.1 Synthetic routes for RVG-SMCC-zein obtention.

2.3 Characteristics of Nanoparticles

2.3.1 Dynamic Light Scattering (DLS)

Zein can self-assemble to make zein_NPs. The zeta potential, size, and polydispersity (PDI) of zein_NP, zein-Dac_NP, and zein-RVG-Dac_NP, respectively, were examined using DLS. The NP concentration of 1mg/mL was determined by adding 5 mg of dried NPs into 5 mL of water and stirred to form a stable dispersion and then was used for size and stability determination. For testing the electrophoretic mobility, PBS was added, and the final pH was set at 7.4 before the measurement of zeta potential.

2.3.2 Encapsulation Efficiency (EE) and Loading Efficiency (LE)

Zein-RVG-Dac_NPs were re-dispersed in the 80% aqueous ethanol solution. With the disruption of encapsulated NPs, the inner Dac was totally released, followed by the transferring to a membrane dialysis bag (3 kD MWCO). The UV absorbance at 269 nm of the samples was measured to obtain the Dac concentration using the ultraviolet-visible (UV-vis) spectrometer, which were performed for triplicate measurements. The EE and LE of Dac in zein-RVG-Dac_NP were obtained using the following formulas:

$$\text{Encapsulation Efficiency (\%)} = \frac{\text{Weight of the drug encapsulated}}{\text{Weight of the total drug added}} \times 100\%$$

$$\text{Loading Efficiency (\%)} = \frac{\text{Weight of the drug encapsulated}}{\text{Weight of the nanoencapsulation}} \times 100\%$$

2.3.3 Fourier Transform Infrared (FTIR) Spectroscopy

The characteristics and RVG conjugation effects on zein, and the encapsulation of Dac in the zein-RVG-Dac_NPs were analyzed using a FTIR spectrometer (Agilent Cary 670, Santa Clara, CA, USA). The prepared samples of zein, RVG29, zein-RVG, and zein-RVG-Dac_NP, respectively, were mixed and ground with potassium bromide and pressed into disks. The FTIR spectra in the range of 400-4000 cm^{-1} were recorded, and a resolution of 4 cm^{-1} was applied.

2.3.4 Nuclear Magnetic Resonance (NMR)

The conjugation of RVG29 and zein was analyzed using NMR. The samples of zein, RVG29, and zein-RVG, respectively, were dissolved in DMSO-d_6 before the NMR measurement. The ^1H NMR spectra, analyzing the appearance and position of the

hydrogen atoms in the molecules, were obtained using a Bruker Avance-III 400 MHz FT-NMR System (Karlsruhe, Germany).

2.3.5 In Vitro Stability of zein-RVG-Dac_NPs

1 mg/mL of zein-RVG-Dac_NP was re-suspended in milli Q water with 10% (v/v) fetal bovine serum (FBS) at the pH of 7.4. Two groups of the suspensions were keep stored at 4 °C and 37 °C, respectively. The profiles of the size change during the time period of 72 hr were determined via DLS following the previous process.

2.3.6 In Vitro Drug Release of zein-RVG-Dac_NPs

The in vitro Dac release from zein-RVG-Dac_NPs was investigated using the release media of the simulated cerebrospinal fluid (CSF, pH 7.3), PBS (pH 7.4) with or without 10% (v/v) serum, and PBS (pH 6.0) with 10% (v/v) serum, respectively. 2 mg/mL of NPs were re-suspended in the release media, followed by being transferred into a dialysis bag (3 kD MWCO). The dialysis bag was placed in 100 mL of PBS with vibration at 100 rpm. At the selected time points, 2 mL of the release medium was collected for analysis, and an additional 2 mL PBS was added into the original release medium.

2.3.7 Cell Culture

U87, Hela, bEnd.3, and C6 cell lines were obtained from American Type Culture Collection (Manassas, VA, USA). U87 MG-Red-Fluc cell line was a gift from Dr. Larry Ming-Cheung Chow. U87 cells were incubated in a mixture of DMEM, FBS, and penicillin-streptomycin.

2.3.8 3-(4,5-dimethylthiazol-2-yl)-5-(3-carboxymethoxyphenyl)-2-(4-sulfophenyl)-2H-tetrazolium (MTS) Assay

The in vitro cytotoxicity of zein-RVG-Dac_NPs, zein-RVG_NPs, and Dac was measured using an MTS assay. U87 cells were seeded in a 96-well plate with the cell density of 10^4 cells/well and separated into 4 groups (n = 6), including 3 sample groups and 1 control group. The sample groups were incubated with zein-RVG-Dac_NPs, pure Dac, and zein-Dac_NPs, respectively, in the Dac equivalent concentrations of 10, 25, and 50 nM for 24 hr. The activated MTS reagent was formed with the mixture of MTS and PMS, which were respectively dissolved in Dulbecco's Phosphate-Buffered Saline (DPBS) at the volume ratio of 20:1. Then, the forming MTS reagent was added to the incubated media, and the color intensity was recorded using a microplate spectrophotometer (Bio-Rad, Hercules, CA, USA).

2.3.9 The nAChR expression on the cell membranes of various cells

To explore the specific targeting mechanism, the cell-surface expression of nAChR on the cells of U87, C6, bEnd.3, and Hela was evaluated using ELISA. The antibody targeting at nAChR was prepared and placed in a micro-ELISA plate. The protein concentrations were measured, and the expression of nAChR was tested using the micro-ELISA plate under the same protein concentration. The fluorescent density at 450 nm was recorded to measure the nAChR concentration. The values of nAChR expression were calculated using the following formula:

$$\text{nAChR (\%)} = \frac{C_{nAChR}}{C_{protein}} \times 100\%$$

where nAChR was the concentration of nAChR and Cprotein was the concentration of the total protein.

2.3.10 Cellular Uptake

The cellular uptake of Dac, zein-RVG-Dac_NPs, and zein-Dac_NPs, was investigated using CLSM (Zeiss LSM 800, Oberkochen, Germany). NHS ester of Cy5 (Cy5) was selected as the dye to stain Dac to form Dac/Cy5. The cyanide group of Dac was reduced to amino group before the conjugation with Cy5. Zein-RVG-Dac_NPs and zein-Dac_NPs, respectively, were stained with the fluorescence dye, coumarin-6 (C6). 1.5×10^4 U87 cells were put in 1.5 mL growth media and cultured in 6-well plates at 37 °C for 48 hr. After the cell attachment, Dac/Cy5, zein-RVG-Dac_NPs, and zein-Dac_NPs, respectively, in the Dac equivalent concentration of 0.1 μg/mL were added to the cells. At 1 hr, three groups of the treated cells were obtained and fixed using glutaraldehyde (2.5% v/v). DAPI was selected to locate the nucleus in U87 cells before the observation using CLSM.

Flow cytometry was utilized for the analysis of cellular uptake. U87 cells were incubated in 1.5 mL of Minimum Essential Medium (MEM) for 24 hr. Cy5 was firstly dissolved in 100 μL DMSO to reach the concentration of 10 mg/mL. The pH of suspensions of zein-Dac_NPs and zein-RVG-Dac_NPs, respectively, was regulated to 8.3 using sodium bicarbonate. Cy5 was added to the suspensions of NPs to reach the final concentration of 2.5 mg/mL and reacted for 6 hr to realize the attachment of the dye on the NPs to form zein/Cy5-Dac_NPs and zein/Cy5-RVG-Dac_NPs. Excess Cy5 was removed using the dialysis bag (3 kD MWCO). Then, the cells were cultured with zein/Cy5-Dac_NPs,

zein/Cy5-RVG-Dac_NPs, and Dac/Cy5 for 1 hr. The cells were harvested with trypsin. Followed by the resuspension of the cells in PBS (500 μL), the quantitative cellular uptake was measured using a flow cytometry (Beckman, FCM, DxFLEX, USA).

2.3.11 Western Blot

U87 cells were treated with 10, 50, and 100 nM of zein-RVG-Dac_NPs, respectively, for 24 hr. The cells were under centrifuged to obtain the total proteins. The protein concentration was measured using the BCA Protein Assay Kit (Thermo Fisher Scientific, Waltham, MA, USA). The targeted biomarkers, P53, Bcl-2, caspase-3, and cleaved caspase-3, were separated from the total protein samples using sodium dodecyl sulfate-polyacrylamide gel Electrophoresis (SDS-PAGE). The protein markers were then transferred onto a polyvinylidene fluoride (PVDF) membrane. The pre-incubation process was conducted in the blocking solution, 5.0% BSA in TBST. It was followed by the incubation of PVDF membrane with the primary antibodies (1:1000) at 4 °C overnight. Then the membrane was incubated with the solution of secondary antibody of goat anti-rabbit IgG H&L (HRP) (1:2000) for 60 min at room temperature. Immunoreactive proteins were visualized using an imaging system.

2.3.12 Cell Proliferation Assay

U87 cells were seeded in 6-well plates at a density of 5×10^5 cells/well for 24 hr and treated by 0, 0.1, and 0.2 μM, respectively, of the zein-RVG-Dac_NPs for 6 hr. The cells were fixed, permeabilized, and blocked with 10% BSA. DAPI was used for the staining of the cell nucleus. Rabbit antihuman Caspase-3 antibody (1:400; Abcam, U.K.) was applied

for the immunofluorescence. After washed with PBS, the treatment with the secondary antibody of goat anti-rabbit IgG H&L (Alexa Fluor® 488) (1:1000) was followed. The cells were repeatedly washed before the observation using CLSM.

2.3.13 Apoptosis analysis by flow cytometry

U87 cells were cultured at a density of 5×10^4 cells /well and incubated for 24 hr. After that, the cells were treated with PBS, Dac, zein-RVG-Dac_NPs, and zein-Dac_NPs, respectively, for 2 hr in an incubator. After being washed, the cells were collected by trypsinization. Then, 1 mL of PBS was added, followed by centrifugation (1500 rpm) for 5 min. The supernatants were then removed, and the cells were resuspended in PBS. To identify the cells of interest, with the removal of debris and other events that are not of interest, 10,000 events were captured based on the gating strategy while the other events were eliminated from the analysis. Data of these 10,000 events were recorded and analyzed using flow cytometry.

2.3.14 In vitro Blood-Brain Barrier (BBB) Permeability Assay

The bEnd.3 cells (5.0×10^4 cells/well) were incubated in the 24-well transwell plates. After 7 days of cultivation, when the cells reached confluence, the cell monolayer mimicked the morphology and activity of the BBB. The TEER of the monolayer was a parameter indicating the tightness of the monolayer and was measured using a volt-ohmmeter. The cell monolayer with at least 180 $\Omega \cdot cm^2$ of TEER was considered to have reached confluence. Dac/Cy5, zein/Cy5-Dac_NPs, and zein/Cy5-RVG-Dac_NPs, respectively, were mixed in the apical chamber of the transwell. After 4 hr of incubation, the medium

in the apical chamber was removed and washed. The fluorescence of both the apical and basolateral chambers was recorded using the IVIS Spectrum Live Imaging System (PerkinElmer, USA).

2.3.15 Animal Studies

All the animal experiments strictly followed the guidelines of the Chinese Association for the Accreditation of Laboratory Animals Care. BALB/c nude mice were selected to establish the tumor-bearing models, and SD rats were chosen to evaluate the pharmacokinetics of the drugs. After transportation, the mice were given a week to acclimatize before the experiments. The nude mice were approximately 20 g in weight and were fed in cages with free food and water.

2.3.16 In vivo Fluorescence Imaging and Biodistribution

The biodistribution of zein-Dac_NPs, zein-RVG-Dac_NPs, and Dac was studied using the in vivo fluorescence imaging (Scientific Imaging System, ColdSpring Science Corporation, Beijing, China). 7.5×10^5 U87 MG-Red-Fluc cells were injected into the right brain of the 3-week-old BALB/c nude mice. After 10 days, the mice were randomly divided into four groups (n = 5). The zein molecules of zein-RVG-Dac_NPs and zein-Dac_NPs, respectively, were dyed using Cy5 to form zein/Cy5-RVG-Dac_NPs and zein/Cy5-Dac_NPs. Cy5 was applied to stain Dac to form Dac/Cy5. Samples of zein/Cy5-RVG-Dac_NPs, zein/Cy5-Dac_NPs, and Dac/Cy5, respectively, were intravenously administered to mice via tail vein. The intensity and distribution of the fluorescence was observed and recorded at 24 hr using the in vivo fluorescence imaging. The mice were

sacrificed 24 hr after the administration, and before that, the blood of mice was drained by perfusion. The major organs were obtained and observed using in vivo fluorescence imaging. The brain tumors were subsequently sliced and observed using CLSM.

2.3.17 Pharmacokinetics

To evaluate the circulation half-life, zein-RVG-Dac_NPs, zein-Dac_NPs, and Dac, respectively, in the Dac equivalent concentration of 20 mg/kg were administered to three randomly grouped SD rats intravenously via the tail vein. At selected time points of 0.1, 0.5, 1, 2, 4, 6, 8, 12, 16, and 24 hr, blood samples were obtained from the orbital cavity, followed by centrifugation. The Dac content in the plasma was quantitatively analyzed by using HPLC. Triplicate measurements were performed.

2.3.18 Anti-GBM Activity Using an Orthotopic GBM Model

7.5×10^5 U87 MG-Red-Fluc cells were injected into the right brain of the BALB/c nude mice. After 10 days, the mice were randomly divided into 4 groups (n = 12), and the date was assigned as Day 0. Three sample groups received the intravenous injections of Dac, zein-Dac_NPs, and zein-RVG-Dac_NPs, respectively, in a Dac equivalent concentration of 20 mg/kg every 5 days. The control group received saline. Then, six mice were randomly selected and sacrificed for each group on Day 20. The change of tumor size was observed using the in vivo fluorescence imaging system and the relative tumor volume was obtained using the following formula:

$$\text{Relative tumor volume} = \frac{\text{Tumor volume on Day 20}}{\text{Tumor volume on Day 0}}$$

The other mice were used for the assessment of the survival.

2.3.19 Immunofluorescence (IF) Histochemical and Immunohistochemistry (IHC) Analysis

The collected orthotopic brain tumors were fixed with 4.0 % PFA, embedded in paraffin, and sliced. For the immunofluorescence (IF) histochemical analysis, TUNEL staining was used to observe the apoptotic cells. CD31 staining was applied to show the distribution of the microvessels. Three replicates of each sample were studied using the TUNEL and CD31 staining, respectively, and analyzed using ImageJ to obtain the integral optical density.

For the immunohistochemistry (IHC) analysis, the 4 μm-thick tissue sections were incubated with the primary antibody of anti-P53 (1:200, Abcam, UK), anti-BAX, and anti-PI-9 (1:200, LSBio, USA). Then, the samples were cultured with HPR anti-mouse IgG for 30 min and restrained with hematoxylin (Solarbio, China) for 5 min. The immune expressions of P53, BAX, and PI-9 were determined using the CLSM (Leica microsystem, Wetzler, Germany).

2.3.20 Histopathological Analysis

To evaluate the safety of the NPs, traditional H&E staining was conducted to investigate the pathological changes of organs after the treatments. The tissues from the orthotopic GBM mice models were fixed in formaldehyde for 48 hr, and then dehydrated, permeabilized, and embedded in paraffin. The tissues were sliced into 3 μm-thick sections, deparaffinized, and washed with PBS. The sections were dyed using hematoxylin for 3 min, placed in a hydrochloric acid-ethanol mixture 5 min for differentiation, and stained

with eosin for 1 min. The pathological changes of the major organs were investigated using the binocular microscope (Zeiss Primo Star, Oberkochen, Germany).

Chapter 3. Results and discussion

3.1 Synthesis and Characterization of Zein Based NPs

The morphology and size distribution of zein-Dac_NP and zein-RVG-Dac_NP, respectively, were characterized using scanning electron microscopy (SEM) (Figures 3.1A and 3.1B). The well-dispersed spherical particles with uniform particle sizes were observed for both zein-Dac_NP and zein-RVG-Dac_NP. The size, surface charge, and polydispersity index (PDI) of the zein_NP, zein-RVG_NP, and zein-RVG-Dac_NP in the dispersions were analyzed using dynamic light scattering (DLS) (Table 3.1). The mean hydrodynamic sizes of zein_NP, zein-Dac_NP, and zein-RVG-Dac_NP, respectively, were 187.83 ± 0.14, 205.32 ± 0.37, and 219.74 ± 0.42 nm (Figures 3.1 C, D, and E). After the encapsulation of Dac, the size of zein-Dac_NP was slightly larger (17.49 nm) than that of zein_NP. After the conjugation of RVG29, the size of zein-RVG-Dac_NP was 14.42 nm larger than that of zein-Dac_NP. The PDI values of zein_NP, zein-RVG_NP, and zein-RVG-Dac_NP were 0.079 ± 0.003, 0.063 ± 0.015 and 0.057 ± 0.009, respectively. These values are all below 0.1, indicating the uniform distribution of the NPs. The zeta-potentials of zein_NP, zein-RVG_NP, and zein-RVG-Dac_NP were -16.17 ± 0.32, -18.86 ± 0.47, and -12.85 ± 0.29 mV, respectively.

The encapsulation efficiency (EE) and loading efficiency (LE) of the zein-RVG-Dac_NP were 77.9 ± 4.7% and 60.4 ± 3.2 mg/g, respectively. The high EE and LE indicated that Dac was successfully encapsulated, and the RVG29-conjugated zein protein (zein-RVG) serves as a good drug carrier. The conjugation efficiency of zein and RVG29 was 97.42 ±

0.18%, which indicated a successful synthesis. It was calculated that there were 1.43×10^5 of RVG29 on the surface of each zein-RVG-Dac_NP.

The conjugation between RVG29 and zein, and the encapsulation of Dac by zein-RVG were verified using Fourier transform infrared spectroscopy (FTIR). In Figure 3.2, the fingerprints of zein were found at 3295 and 2930 cm^{-1}, which were attributed to the vibration stretching of the −OH group and the amide A′, respectively. The fingerprints were also found at 1656 and 1540 cm^{-1}, which were contributed from the C=O stretching of the amide I and the C−N stretching of the amide II, respectively. Since both zein and RVG29 are composed of amino acids, RVG29 also had the fingerprints at 3295, 1656, and 1540 cm^{-1}, but with a much higher intensity because of the high concentrations of the related chemical bonds in RVG29. The same peaks with high intensities were also observed in the spectrum of zein-RVG, indicating the successful conjugation of RVG29 and zein. Zein is rich in glutamine while RVG29 does not contain glutamine,[94] in agreement with the finding that the peak at 1410 cm^{-1} corresponds to glutamine was found in the spectra of zein and zein-RVG but not in that of RVG29 (Figure 3.2). It was observed that the fingerprints of Dac mentioned above were also present in the spectrum of zein-RVG-Dac_NP but absent in the spectrum of zein-RVG. It was concluded that Dac was successfully encapsulated by zein-RVG to form zein-RVG-Dac_NP.

The proton nuclear magnetic resonance (^{1}H NMR) spectra of zein, RVG29, and zein-RVG, respectively, were obtained (Figure 3.3). The protons on zein were ascribed as following:

δ (ppm) ~ 9.16 (-NH), 8.0 (-NH_2), 7.97 (amide I, -C=ON-), 3.74 (*α*-CH, Leu), 1.75 (*β*-CH_2, Leu; *γ*-CH, Leu), 1.21 (-CH_2), 0.84 (*δ*-CH_2, Leu), and 0.8 (-CH_3).[95] The chemical shifts (δ, ppm) of the protons on RVG29 were ascribed as following: δ (ppm) ~ 9.33 (-NH), 8.64 (-NH_2), 7.82, 7.73 (CH-4 ring, Trp), 7.54 (CH-7 ring, Trp), 7.45(*m*-CH, Phe), 7.39 (*p*-CH, Phe), 7.34 (*o*-CH, Phe), 7.28 (CH-6 ring, Trp), 7.20 (CH-5 ring, Trp), 7.19 (*o*-CH, Tyr), 6.88 (*p*-CH, Tyr), 4.6, 4.25 (*β*-CH, Thr), 4.18 (*α*-CH, Pro), 4.10 (*α*-CH, Asp), 4.01 (*α*-CH, Asn), 3.94-4.06 (*α*-CH, Ser), 3.89 (*β*-CH, Ser), 3.78 (*α*-CH, Arg; *α*-CH, Ala), 3.77 (*α*-CH, Glu), 3.66 (*α*-CH, Ile), 3.61 (*α*-CH, Gly; *α*-CH, Lys), 3.6 (*α*-CH, Thr), 3.37-3.50 (*δ*-CH, Pro), 3.25(*δ*-CH, Arg), 3.06 (*ε*-CH, Lys), 3.03 (*β*-CH, Asp) and 2.96 (*β'*-CH, Asn), 2.86 (*β*-CH, Asn), 2.38-2.53 (*β*-CH, Pro), 2.12 (*β'*-CH, Glu), 2.06 (*β*-CH, Glu), 2.04-2.15 (*γ*-CH, Pro), 2.01, 1.98 (*β*-CH, Ile), 1.91 (*β*-CH, Arg), 1.76-1.85 (*β*-CH, Lys), 1.74 (*δ*-CH, Lys), 1.48 (*γ'*-CH, Thr; *β*-CH, Ala), 1.40-1.6 (*γ*-CH, Lys), 1.33 (*γ*-CH_3, Thr), 1.26 (*γ*-CH, Thr), 1.01(*γ*-CH_3, Ile), 0.94 (*δ*-CH, Ile).[96] The selected fingerprints of RVG29, with possible slight shifts, were also found in the spectra of zein-RVG, as δ (ppm) ~ 9.06 (-NH), 8.79 (-NH_2), 7.8 (amide I, -C=ON-), 7.7 (CH-4 ring, Trp), 7.3 (CH-6 ring, Trp), and 1.78 (*β*-CH_2, Leu; *γ*-CH, Leu), indicating the successful conjugation of RVG29 and zein. The spectra also showed that the characteristic peak of zein at 6.08 ppm corresponding to its MAL group disappeared in the spectrum of zein-RVG, suggesting that the MAL group of the sulfo-SMCC activated zein had reacted with the thiol group of the RVG29 to achieve the conjugation.[97]

Table 3. 1 The particle size, PDI, and zeta-potential of zein_NPs, zein-Dac_NPs and zein-RVG-Dac_NPs.

Formulation	Average size (nm)	PDI	Zeta-potential (mV)
zein_NP	187.83 ± 0.14	0.079 ± 0.003	-16.17 ± 0.32
zein-Dac_NP	205.32 ± 0.37	0.063 ± 0.015	-18.86 ± 0.47
zein-RVG-Dac_NP	219.74 ± 0.42	0.057 ± 0.009	-12.85 ± 0.29

Table 3.2 The LE, particle size, and PDI of zein-Dac_NPs made by different mass ratios of zein-to-Dac.

Mass ratios of zein-to-Dac	LE (%)	Average size (nm)	Zeta-potential (mV)
50	42.8 ± 1.1	217.83 ± 0.91	-16.98 ± 1.49
25	47.6 ± 2.4	215.41 ± 1.24	-15.64 ± 1.06
20	51.2 ± 3.1	216.82 ± 1.06	-13.41 ± 0.79
16.7	53.5 ± 2.8	208.44 ± 0.82	-15.58 ± 0.92
12.5	56.4 ± 2.2	205.72 ± 0.65	-17.07 ± 0.71
10	58.9 ± 2.6	209.41 ± 0.59	-16.57 ± 1.22
8.3	60.4 ± 3.2	205.33 ± 0.37	-18.86 ± 0.47
7.1	56.3 ± 1.7	205.61 ± 0.29	-19.33 ± 0.64

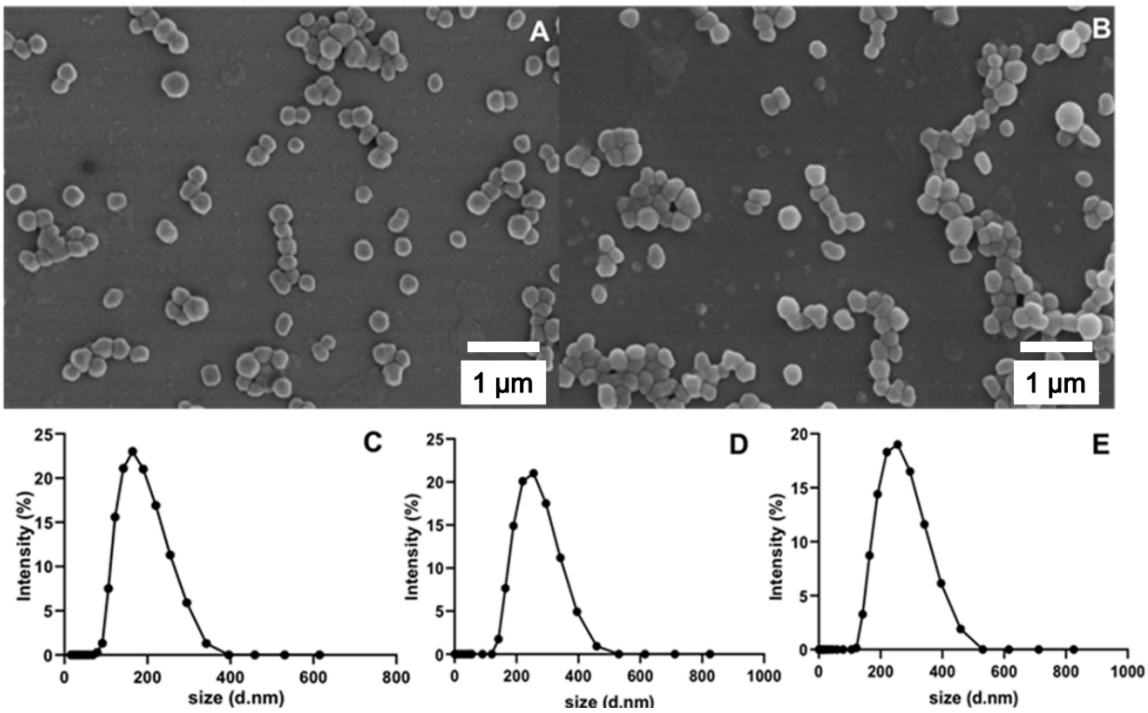

Figure 3.1 The structural characterizations and stability studies of zein-Dac_NPs and zein-RVG-Dac_NPs.

(A-B) SEM images of (A) zein-Dac_NPs and (B) zein-RVG-Dac_NPs. Scale bar=1 µm.

(C-E) The size profiles of (C) zein_NPs, (D) zein-RVG_NPs, and (E) zein-RVG-Dac_NPs.

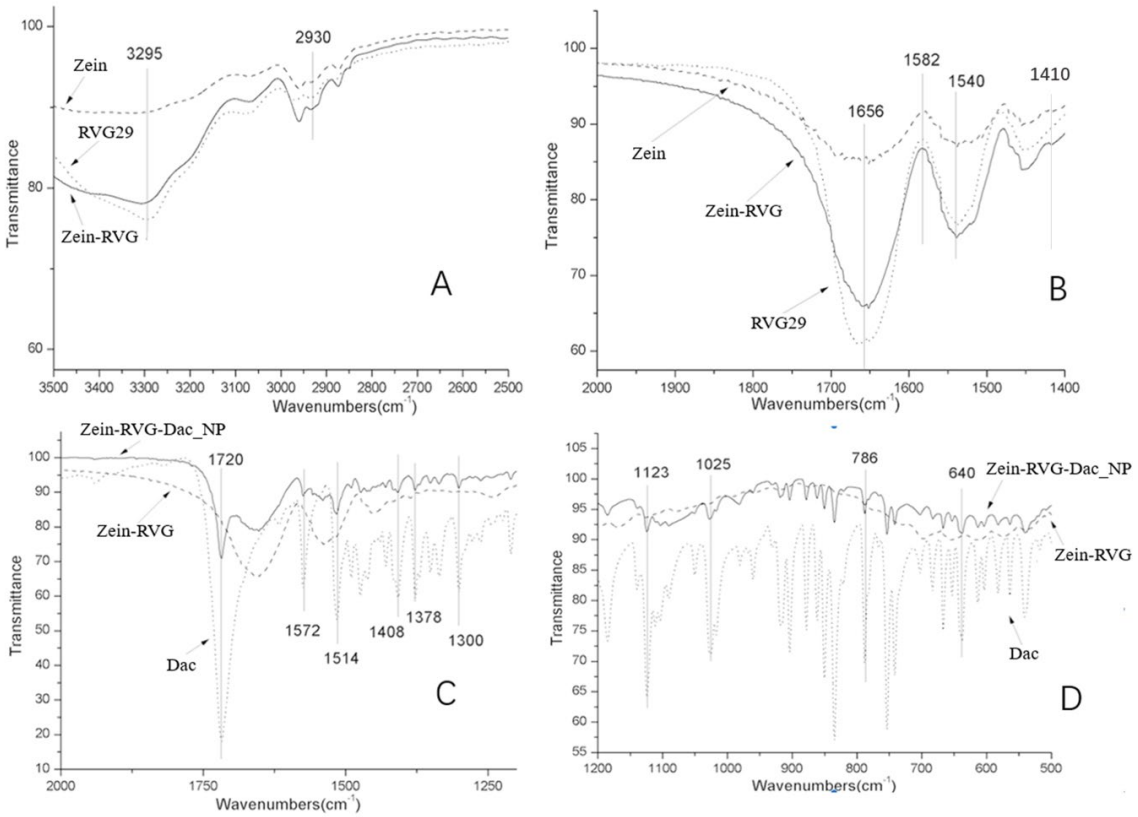

Figure 3.2 FTIR spectra of zein_NPs, RVG29, and zein-RVG_NPs in the wavenumber range of (A) 3500 to 2500 cm^{-1} and (B) 2000 to 1400 cm^{-1}. FTIR spectra of zein-RVG_NPs, pure Dac, and zein-RVG-Dac_NPs in the wavenumber range of (C) 2000 to 1200 cm^{-1} and (D) 1200 to 500 cm^{-1}.

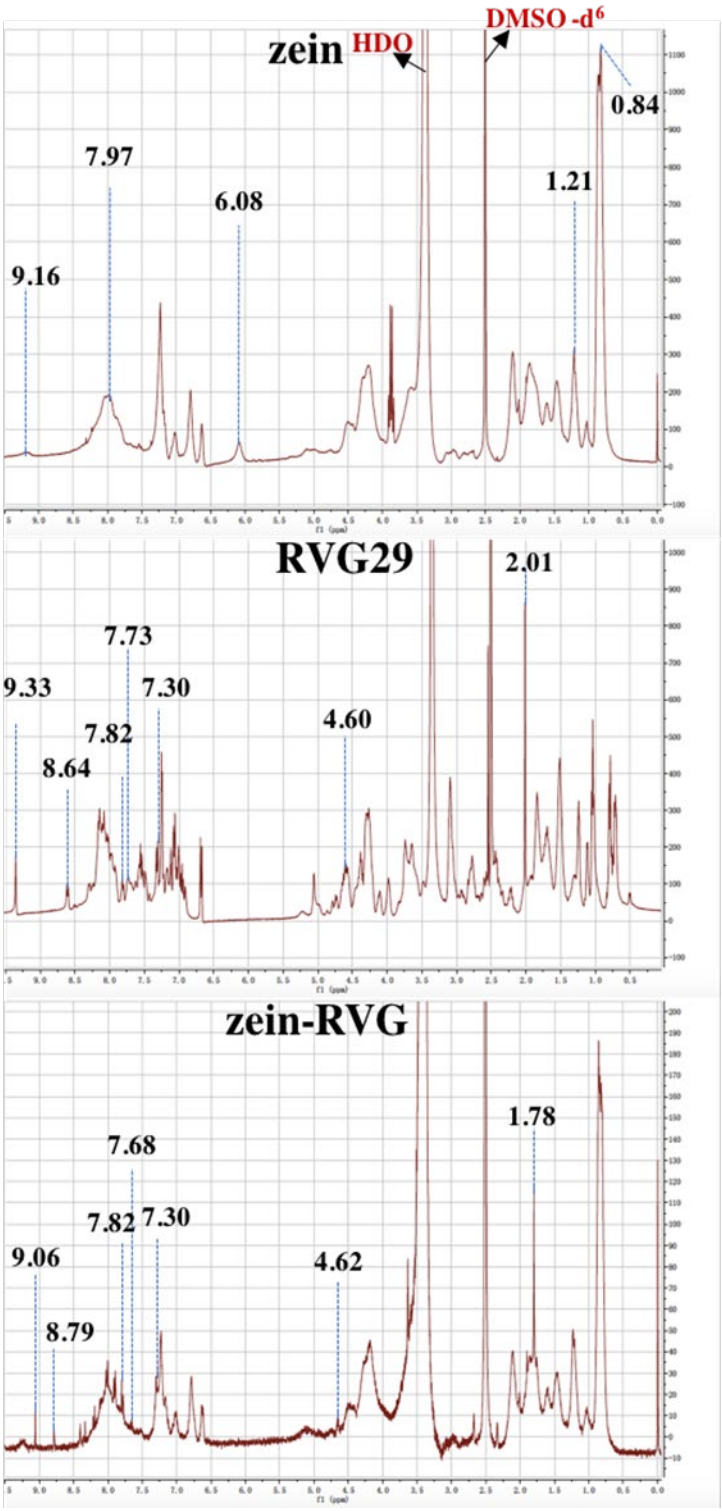

Figure 3.3 The ^{1}H NMR spectra of zein, RVG29, and zein-RVG.

3.2 In Vitro Drug Release and Stability

The *in vitro* release of Dac from zein-RVG-Dac_NP was investigated using the simulated cerebrospinal fluid (CSF, pH 7.3), PBS (pH 7.4), PBS (pH 7.4) with 10% (v/v) serum, and PBS (pH 6.0) with 10% (v/v) serum, respectively, at 37 °C (Figure 3.4A). The release amount was 37.4 ± 2.6% in CSF, 55.3 ± 3.7% in PBS (pH 7.4) with serum, 51.3 ± 5.1% in PBS (pH 7.4) with no serum, and 61.4 ± 2.9% in PBS (pH 6.0) with serum in 24 hr. The release rate was low in CSF compared to that in the other solutions. The total release of zein-RVG-Dac_NP at 100 hr was 57.2 ± 2.7%, 75.3 ± 1.8%, 72.7 ± 3.4%, and 83.5 ± 4.1% in CSF (pH 7.3), PBS (pH 7.4) with serum, PBS (pH 7.4) without serum, and PBS (pH 6.0) with serum, respectively.

The *in vitro* stability of zein-RVG-Dac_NP was further studied by first re-dispersing Zein-RVG-Dac_NPs in PBS solution (pH 7.4) with 10% (v/v) serum and then storing the solution at 4 °C and 37 °C, respectively. The particle size change in 72 hr was recorded and presented in Figure 3.4B. At 4 °C, the size of zein-RVG-Dac_NP was gradually increased from 219.7 to 229.1 nm, while at 37 °C it was elevated from 219.7 to 238.2 nm. The size change was negligible, suggesting that zein-RVG-Dac_NP had good stability in serum solution.

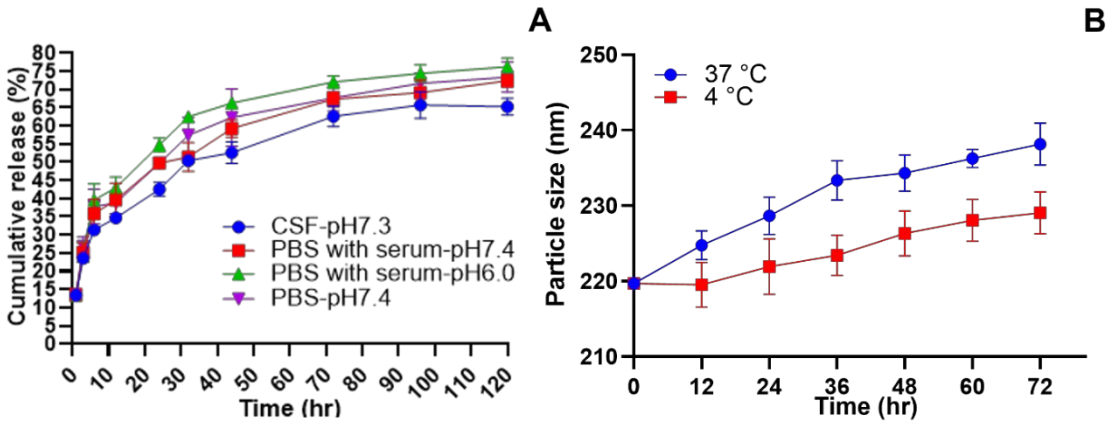

Figure 3.4 Cumulative release of Dac from zein-RVG-Dac_NPs.

(A) Cumulative release of Dac from zein-RVG-Dac_NPs in the simulated cerebrospinal fluid (CSF, pH 7.3), PBS (pH 7.4), PBS with 10 % (v/v) serum (pH 7.4), and PBS with 10 % (v/v) serum (pH 6.0), respectively, at 37 °C. (B) The profile of particle size change of zein-RVG-Dac_NPs in the serum solutions at 4 °C and 37 °C, respectively, for 72 hr.

3.3 In Vitro Tumor Targeting

The cellular uptake of zein-RVG-Dac_NP and zein-Dac_NP in U87 cells was investigated using confocal laser scanning microscopy (CLSM, Figure 3.5A). Cy5 was conjugated with the drug Dac to form Dac/Cy5 before the encapsulation of Dac/Cy5 to form zein-Dac/Cy5 and zein-RVG-Dac/Cy5. A fluorescent dye, coumarin-6 (C6), was conjugated with the zein molecules on the surface of the zein-RVG-Dac/Cy5 and zein-Dac/Cy5, respectively. U87 cells were treated with Dac/Cy5, and C6 labeled zein-Dac/Cy5 and zein-RVG-Dac/Cy5, respectively, for 1 hr. As shown in Figure 3A, 1hr after the administration of Dac/Cy5, zein-Dac/Cy5 and zein-RVG-Dac/Cy5, the green and red fluorescence, which were given by C6 and Dac/Cy5, respectively, were observed in the cytoplasm of the U87 cells. Both zein-Dac/Cy5 and zein-RVG-Dac/Cy5 rapidly entered the cells. The red

fluorescence was evenly distributed in the cell cytoplasm, and a clear boundary of the red fluorescence was observed (Figure 3.5A). These observations indicated that the zein-Dac/Cy5 and zein-RVG-Dac/Cy5 entered the cells. The fluorescence intensities in Figure 3.5A were measured and shown in Figure 3.5B. Zein facilitated the penetration of cell membrane,[50, 51, 52] while RVG29 promoted the cellular uptake through receptor-mediated endocytosis, as evidenced by the high expression of nAChR on the membrane of U87 cells (Figure 3.5C).

At 1 hr, zein-RVG-Dac/Cy5 showed significantly higher red fluorescence intensity ($p < 0.01$) than zein-Dac/Cy5, which indicated that the conjugation of RVG29 on the surface of the NPs facilitated the cellular uptake of the NPs to the U87 cells more than that of zein within 1 hr. The CLSM results concluded that both zein-Dac/Cy5 and zein-RVG-Dac/Cy5 successfully entered the U87 cells. Both zein and RVG29 promoted the cellular uptake of the NPs, which was potential for the delivery of the anti-cancer drugs that had low solubility and bioavailability.

This finding was further confirmed by the cellular uptake study using flow cytometry. The gating strategy was shown in Figures 3.5D and E, and the results were shown in Figures 3.5F, G, H, and I. Cy5 was applied to label Dac to form Dac/Cy5, while Cy5 was also used to label the zein molecule in zein-RVG-Dac and zein-Dac to form zein/Cy5-RVG-Dac and zein/Cy5-Dac. After U87 cells were treated with zein/Cy5-Dac, zein/Cy5-RVG-Dac, and Dac/Cy5 for 1 hr, zein/Cy5-RVG-Dac showed a 76.54% cellular uptake, while 40.30% of zein/Cy5-Dac entered the cells. It can be concluded that both zein and RVG29 facilitated

the cellular uptake of the NPs, while RVG29 showed a better effect than zein on the promotion of the cellular uptake. We believe that this is because the receptor-mediated endocytosis associated with RVG29 is more effective than the zein-assisted cell membrane penetration on cellular uptake of NPs.

To compare the ability of zein-RVG-Dac_NP, zein-Dac_NP, and Dac to promote apoptosis in the U87 cells, annexin V-FITC was applied to staining the cells. The apoptotic efficiency was recorded and analyzed using flow cytometry (Fig. 3M, N). This result suggested that the apoptotic efficiency induced by zein-RVG-Dac_NP was comparable to that of the zein-Dac_NP and pure Dac, respectively.

The *in vitro* cytotoxicity of zein-RVG-Dac_NP, zein-RVG_NP, and pure Dac was investigated. Various concentrations of zein-RVG-Dac_NP, zein-RVG_NP, and pure Dac, respectively, were added to the U87 cells, and the results are shown in Figure 3.5L. At the lowest concentration of 10 nM, only 49.4% of the cells survived after being treated with Dac, indicating that Dac was an effective inhibitor on the growth of the U87 cells. For all the concentrations including the Dac equivalent concentrations of 10, 25, and 50 nM, zein-RVG-Dac_NP showed no significant difference in the cell viability when compared to Dac, demonstrating that the zein-RVG-Dac_NPs and Dac had comparable cytotoxicity to the U87 cells. The U87 cells treated with various concentrations of the zein-RVG_NPs presented a nearly 100% survival rate, which indicated that the carrier itself had no cytotoxicity to the U87 cells.

To investigate the molecular mechanism of the zein-RVG-Dac_NP-induced apoptosis in U87 cells, the expression levels of the specific proteins, including tumor suppressor (P53), apoptosis markers (caspase-3 and cleaved caspase-3), and apoptosis regulator B-cell lymphoma 2 (Bcl-2), were determined by Western blotting. After treatment with various concentrations of zein-RVG-Dac_NP for 24 hr, the expression levels of Bcl-2, P53, caspase-3, and cleaved caspase-3, respectively, were measured and shown in Figure 3.5J. The expression of P53, which was a marker of the cell apoptosis, was increased with the increase of the concentration of the zein-RVG-Dac_NP. Caspase-3, a protein that was cleaved and thus activated upon the initiation of apoptosis, was an executioner of the programmed death of the cells. As shown in Figure 3.5J, the expression of the uncleaved caspase-3 was decreased dramatically while the activated forms of caspase-3, which was the cleaved caspase-3, were elevated with the increase of the concentration of the zein-RVG-Dac_NP. A higher level of the activated caspase 3 in tumor, an indicator of the activation of the caspase-3 pathway, was correlated with the increased rate of recurrence and deaths. Bcl-2 plays an essential role in blocking programmed cell death and promoting cell survival. As shown in Figure 3.5J, the treatment of zein-RVG-Dac_NP reduced the expression of Bcl-2. These results demonstrated that zein-RVG-Dac_NP induced significant cytotoxicity to the GBM cells through cell apoptosis.

The immunofluorescence analysis was conducted using the apoptotic marker caspase-3, associated with programmed cell death. The results are shown in Figure 3.5K. Hoechst, presenting blue fluorescence, was used to dye the cell nuclei, while caspase-3 showed green fluorescence. After the treatments of zein-RVG-Dac_NP in the concentrations of 0.1

and 0.2 μM, respectively, a significant reduction in the amount of the U87 cells was observed. According to the colocalization analysis, caspase-3 with the green fluorescence was distributed in the U87 cells, and the localization of the cell nuclei could be assisted by the blue fluorescence. A comparison among the treatments using 0, 0.1, and 0.2 μM of zein-RVG-Dac_NP showed that the amount of the caspase-3 positive cells was the highest in the control sample where no zein-RVG-Dac_NP was added. As the concentration of zein-RVG-Dac_NP increased, the amount of the caspase-3 positive cells reduced, indicating that the cell death was induced by zein-RVG-Dac_NP via caspase-mediated apoptosis. Compared to the control sample, the nuclei showed brighter fluorescence after the cells were treated with the zein-RVG-Dac_NP of 0.1 and 0.2 μM, indicating a high prevalence of nuclear chromatin and fragmentation.[98] The morphological changes of the U87 cells were also observed after the zein-RVG-Dac_NP treatment. The results concluded that zein-RVG-Dac_NP induced the caspase-3 mediated cell apoptosis of the U87 cells, which was consistent with the results of the western blot analysis (Figure 3.5J). To compare the ability of zein-RVG-Dac_NP, zein-Dac_NP, and Dac to promote apoptosis in the U87 cells, annexin V-FITC was applied to staining the cells. The apoptotic efficiency was recorded and analyzed using flow cytometry (Figures 3.5M and N). The gating strategy was shown in Figure 3.6. In Figure 3.5N, the amount of the apoptotic cells was 11.93 ± 1.42%, 8.17 ± 0.94%, and 8.94 ± 1.10% after the treatments with zein-RVG-Dac_NP, zein-Dac_NP, and Dac, respectively. This result suggested that the apoptotic efficiency induced by zein-RVG-Dac_NP was comparable to that of the zein-Dac_NP and pure Dac, respectively.

To further explore the RVG29-mediated transcytosis of NPs through BBB, a monolayer of the mouse brain capillary endothelial cells (bEnd.3) was applied as the *in vitro* BBB model. The monolayer of the compact cells was cultured on the insert of the transwell (Figure 3.5O). Dac/Cy5, zein/Cy5-Dac, and zein/Cy5-RVG-Dac, respectively, were added to the insert and incubated for 4 hr. As shown in Figure 3.5P, no significant changes in the transendothelial electrical resistance (TEER) of the BBB monolayer were detected after the incubation. It indicated that the treatments of Dac/Cy5, zein/Cy5-Dac, and zein/Cy5-RVG-Dac, respectively, had no effect on the integrity and did not cause the degradation of the cells constituting the BBB monolayer. Figures 3.5Q and R showed the fluorescence of both the insert well and the bottom chamber of the transwell. After the inset well was washed by PBS, the fluorescence of the insert well indicated the fluorescence of the NPs in the bEnd.3 cells after the cellular uptake. While the fluorescence of the bottom chamber indicated the fluorescence of the NPs in the bottom chamber, which had transferred through the bEnd.3 monolayer. Dac/Cy5 had no fluorescence in the bottom chamber, indicating that Dac/Cy5 cannot pass through the *in vitro* BBB. Zein/Cy5-Dac groups showed fluorescence in both the bEnd.3 cell monolayer and the bottom chamber. Zein, due to its cell penetration ability, could also facilitate the transfer of the NPs through the bEnd.3 cell monolayer. A noticeable stronger fluorescence intensity (~2-fold) was observed in the zein/Cy5-RVG-Dac group than that of the zein/Cy5-Dac groups in both the bEnd.3 monolayer and the bottom chamber. The results concluded that both zein and RVG29 in zein-RVG-Dac facilitated the penetration of zein-RVG-Dac through BBB with RVG29 being more effective than zein.

To study the internalization of the NPs in U87 cells, the markers of the early endosomes and late endosomes, Rab5 and Rab7, were applied (Figures 3.7A and B). It was reported that after endocytosis, most NPs would first be transported to early endosomes before they could be trafficked to other organelles.[99] The obvious overlap of the green and red fluorescence on the white dash line drawn in the cell area in the image of Figure 3.7A indicated that zein/Cy5-RVG-Dac colocalized with the early endosomes (Figure 3.7C). However, much less overlap of the green and red fluorescence on the white dash line drawn in the cell area in the images indicated that zein/Cy5-RVG-Dac generally did not colocalize with the late endosomes (Figure 3.7D). It suggested that zein/Cy5-RVG-Dac NPs were involved in the early endosomes during intracellular trafficking, while zein/Cy5-RVG-Dac NPs escaped from the late endosomes with high efficiency.

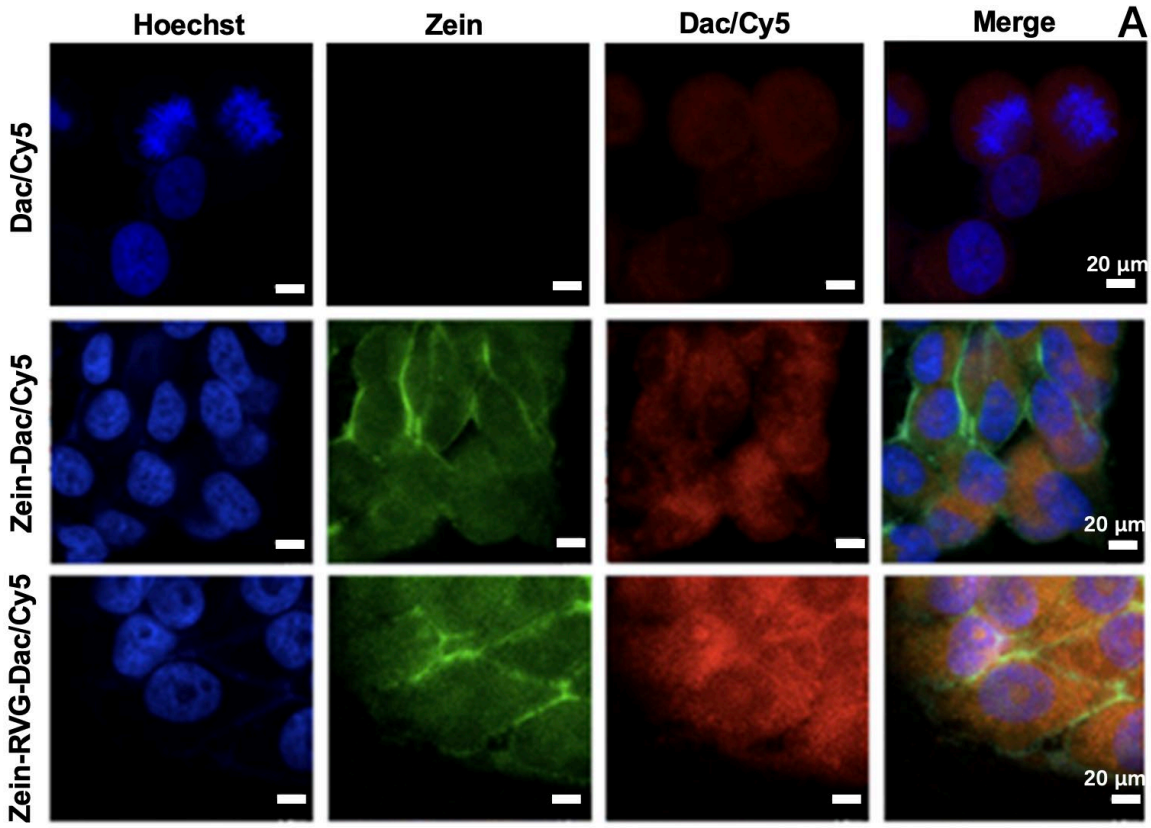

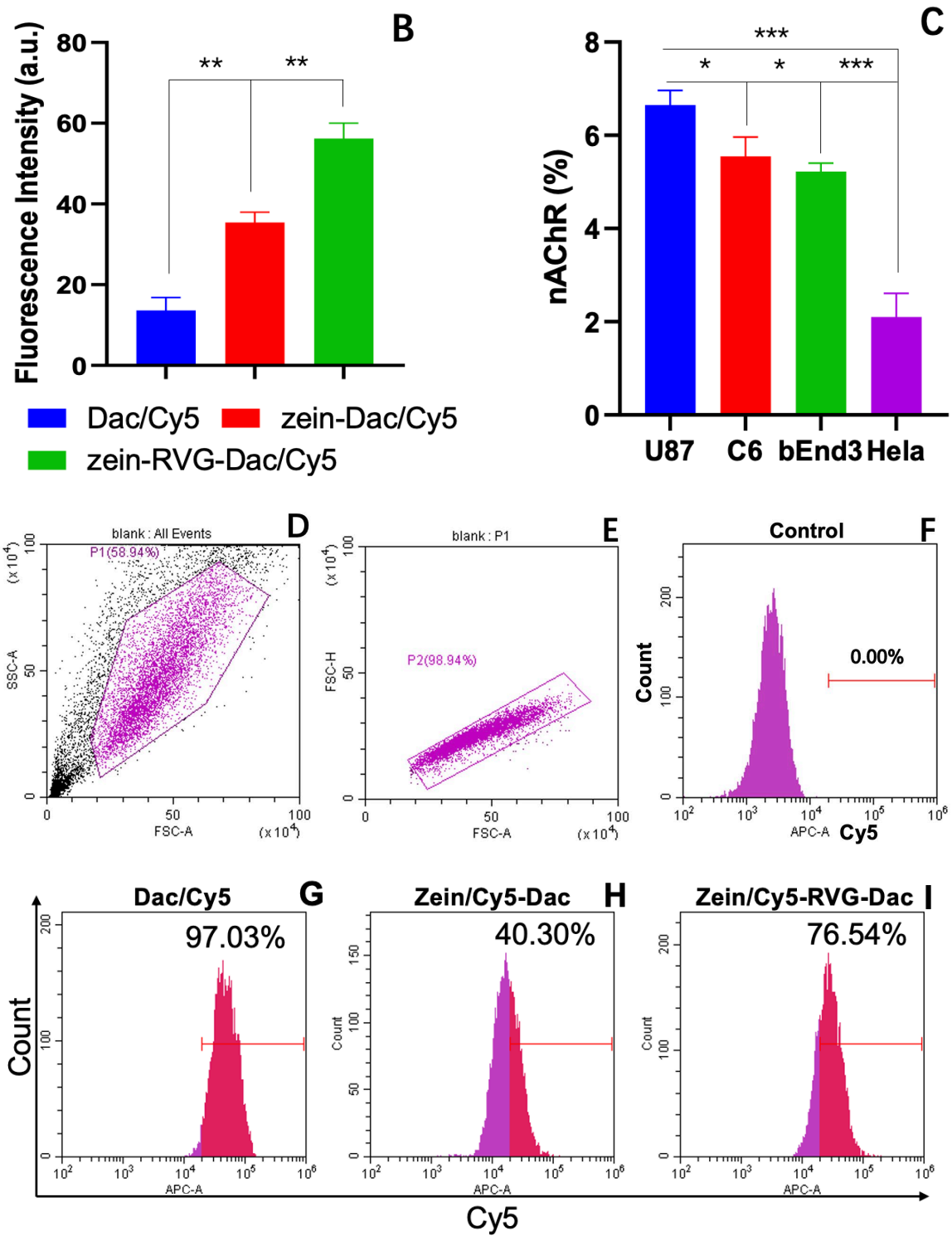
B
Fluorescence Intensity (a.u.)
80
60
40
20
0
**
**
Dac/Cy5
zein-Dac/Cy5
zein-RVG-Dac/Cy5
C
nAChR (%)
8
6
4
2
0
***
*
*
***
U87
C6
bEnd3
Hela
D
blank : All Events
P1(58.94%)
SSC-A
FSC-A
(x10⁴)
E
blank : P1
P2(98.94%)
FSC-H
FSC-A
F
Control
0.00%
Count
APC-A
Cy5
G
Dac/Cy5
97.03%
H
Zein/Cy5-Dac
40.30%
I
Zein/Cy5-RVG-Dac
76.54%
Count
APC-A
Cy5

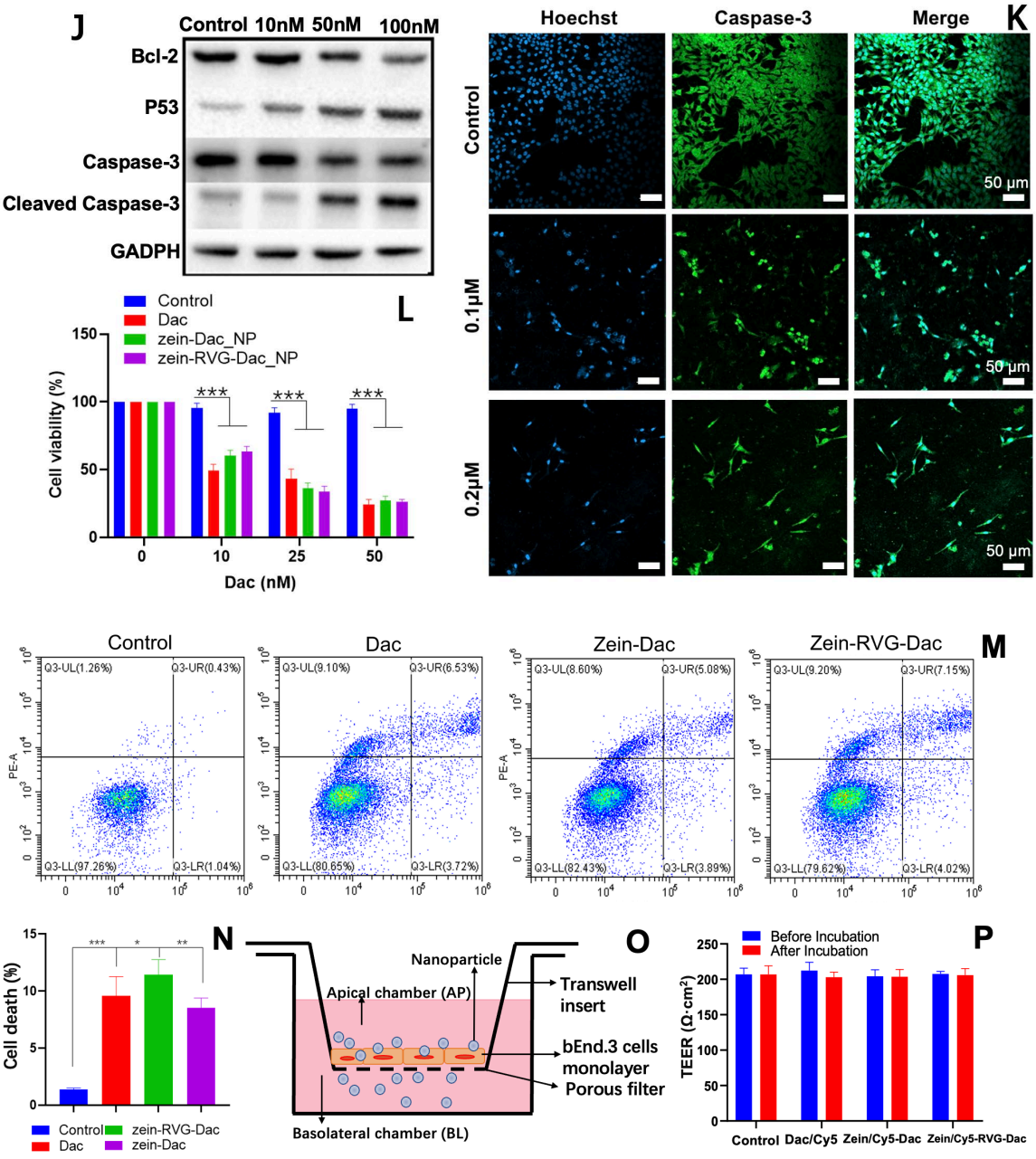
J
Control 10nM 50nM 100nM
Bcl-2
P53
Caspase-3
Cleaved Caspase-3
GADPH
L
Control
Dac
zein-Dac_NP
zein-RVG-Dac_NP
Cell viability (%)
Dac (nM)
K
Hoechst
Caspase-3
Merge
Control
0.1μM
0.2μM
50 μm
M
Control
Dac
Zein-Dac
Zein-RVG-Dac
Q3-UL(1.26%)
Q3-UR(0.43%)
Q3-LL(97.26%)
Q3-LR(1.04%)
Q3-UL(9.10%)
Q3-UR(6.53%)
Q3-LL(80.65%)
Q3-LR(3.72%)
Q3-UL(8.60%)
Q3-UR(5.08%)
Q3-LL(82.43%)
Q3-LR(3.89%)
Q3-UL(9.20%)
Q3-UR(7.15%)
Q3-LL(79.62%)
Q3-LR(4.02%)
PE-A
N
Cell death (%)
Control
Dac
zein-RVG-Dac
zein-Dac
O
Nanoparticle
Apical chamber (AP)
Transwell insert
bEnd.3 cells monolayer
Porous filter
Basolateral chamber (BL)
P
Before Incubation
After Incubation
TEER (Ω·cm²)
Control
Dac/Cy5
Zein/Cy5-Dac
Zein/Cy5-RVG-Dac

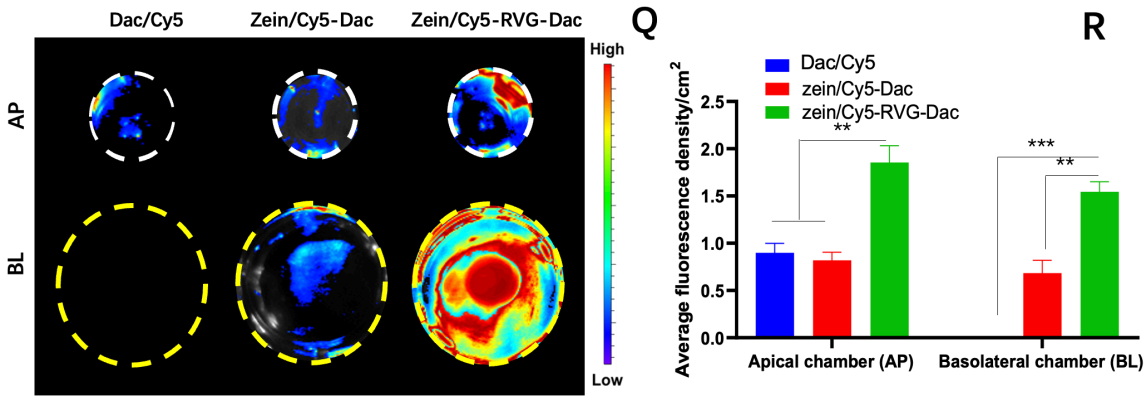

Figure 3.5 The cellular uptake, cytotoxicity, and in vitro BBTB penetration studies of zein-Dac_NPs and zein-RVG-Dac_NPs using the U87 cells.

(A) The CLSM images of U87 cells after treatment with Dac/Cy5, zein-Dac/Cy5 and zein-RVG-Dac/Cy5, respectively, for 1 hr. The blue fluorescence indicated the cell nucleus, while the red fluorescence indicated the Dac/Cy5, zein-Dac/Cy5, and zein-RVG-Dac/Cy5. (B) The red fluorescence intensity of Dac/Cy5, zein-Dac/Cy5, and zein-RVG-Dac/Cy5, respectively, at 1 hr in the CLSM images of Figure 3A was analyzed by ImageJ. Data are presented as mean ± SD (n = 5); $^{**}p < 0.01$. (C) The expression of nAChR in U87, C6, bEnd3, and Hela cells. Data are presented as mean ± SD (n = 5); $^{*}p < 0.05$; $^{***}p < 0.001$. Flow cytometry analysis for the cellular uptake. (D-E) Gating strategy of flow cytometry to determine the amount of the drugs and NPs in Figures 3F-I. (F-I) Flow cytometry analysis for the cellular uptake of (F) Control, (G) Dac/Cy5, (H) zein/Cy5-Dac, and (I) zein/Cy5-RVG-Dac in U87 cells for 1 hr. Data are presented as mean ± SD (n = 5). (J) The expression of Bcl-2, P53, caspase-3, and cleaved caspase-3, respectively, in the U87 cells after the treatments with 0, 10, 50, and 100 nM of zein-RVG-Dac_NPs, respectively, for 24 hr. The control sample was treated by PBS. (K) The CLSM images of the U87 cells treated with 0, 0.1, and 0.2 μM of zein-RVG-Dac_NPs, respectively, for 24 hr. Hoechst

(blue) was used to dye the nuclei of cells, while the caspase-3 showed green fluorescence. Scale bar = 50 μm. (L) MTS assay of U87 cells treated with zein-RVG_NPs, pure Dac, and zein-RVG-Dac_NPs, respectively, at 37 ◦C for 24 hr. Data are presented as mean ± SD (n = 5); ***$p < 0.001$. (M) Apoptosis assay using flow cytometry. Representative scatter plots of annexin V-FITC (x-axis) and propidium iodide (PI) (y-axis). (N) The percentage of apoptotic U87 cells treated with PBS, zein-RVG_NPs, pure Dac, and zein-RVG-Dac_NPs obtained from Figure 3M. Data are presented as mean ± SD (n = 5); **$p < 0.01$; *$p < 0.05$; ***$p < 0.001$. (O) *In vitro* BBB model. (P) The transendothelial electrical resistance (TEER) of the *in vitro* BBB cell monolayer recorded before and after the cultivation with Dac/Cy5, zein/Cy5-Dac, and zein/Cy5-RVG-Dac for 4 hr. (Q) CLSM images of the *in vitro* BBB cell monolayer after the cultivation with Dac/Cy5, zein/Cy5-Dac, and zein/Cy5-RVG-Dac for 4 hr. The yellow dash line indicated the boundary of the apical chamber or basolateral chamber. (R) The fluorescence intensity of Figure 3Q analyzed by ImageJ. Data are presented as mean ± SD (n = 6); **$p < 0.01$; ***$p < 0.001$.

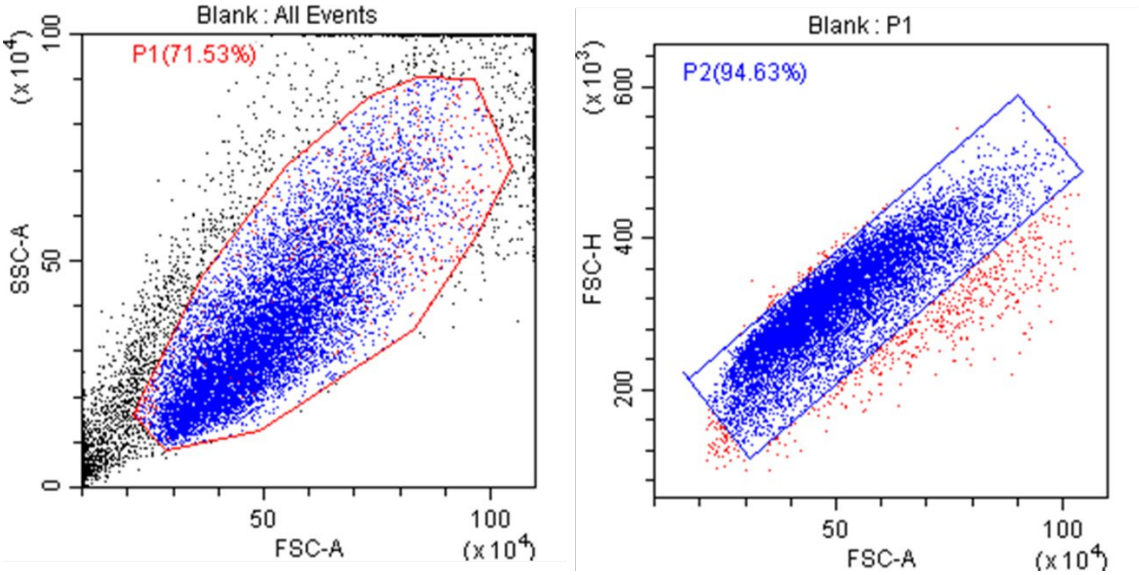

Figure 3.6 Gating strategy of the apoptosis analysis using flow cytometry.

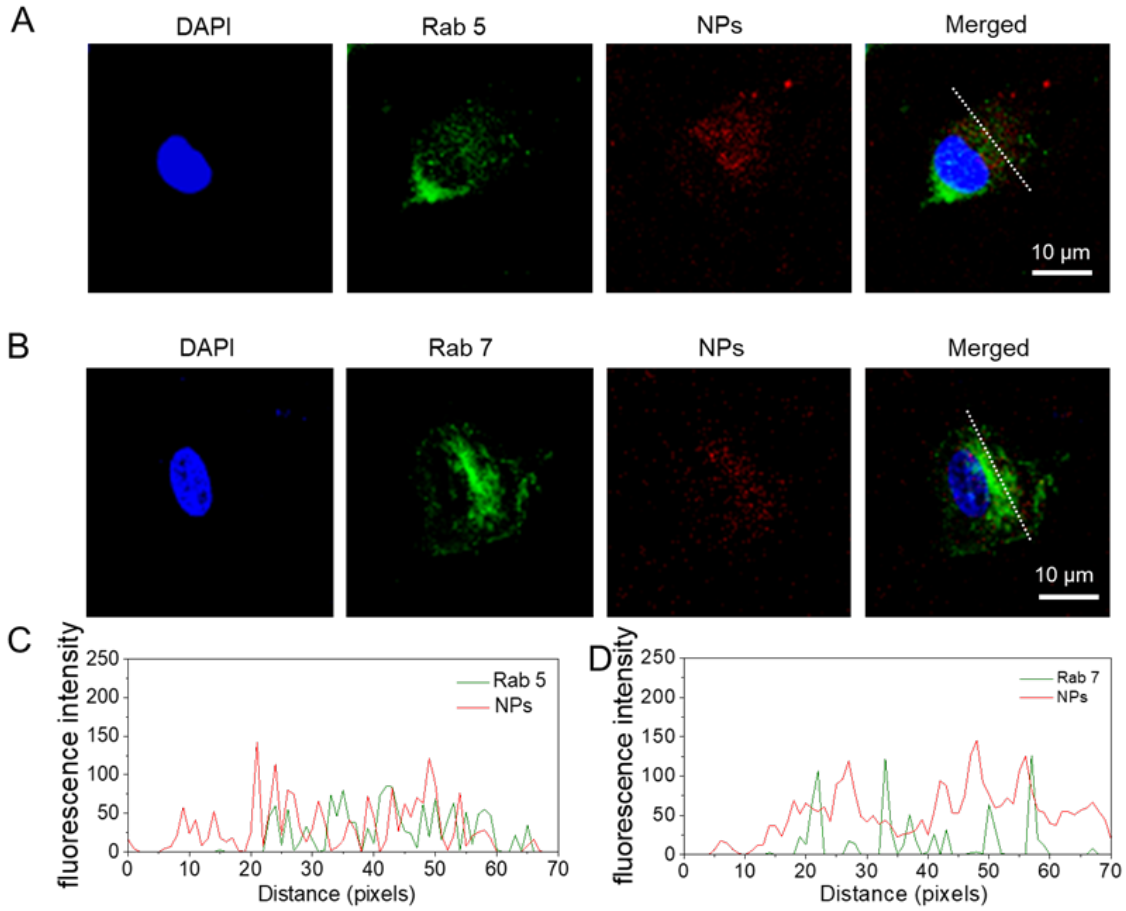

Figure 3.7 The internalization of zein/Cy5-RVG-Dac NPs in U87 cells.

CLSM images of zein/Cy5-RVG-Dac (red, NPs) and U87 cells stained with (A) Rab5, indicating early endosomes, and (B) Rab7, indicating late endosomes. scale bar = 10 μm. (C) One straight white dash line was drawn in the cell area of Figure (A) to study the colocalization of Rab5 and NPs. The fluorescence intensity of Rab5 (green) and NPs (red), respectively, on each point of the white dash line was shown. The distance (in pixels) of the X-axis indicated the distance of the point from one end (top left) of the white dash line. The overlap of the red and green fluorescence indicated the colocalization of Rab5 and NPs. (D) Similar as Figure (C), the fluorescence intensity of Rab7 (green) and NPs (red), respectively, on each point of the white dash line in Figure (B) was shown. The overlap of the red and green fluorescence indicated the colocalization of Rab7 and NPs.

3.4 In Vivo Studies of Biodistribution and Pharmacokinetics

The *in vivo* fluorescence imaging system was used to study the biodistribution and brain-targeting of the zein-RVG-Dac_NP on the GBM-bearing nude mice. Zein/Cy5-RVG-Dac, zein/Cy5-Dac, and Dac/Cy5, respectively, were administered to the mice by intravenous injection via tail vein. The biodistribution of the fluorescent NPs was investigated at 24 hr after the administrations, and the results were shown in Figure 3.8A. The treatment groups in the order of the fluorescence intensity in the brain area from high to low were zein/Cy5-RVG-Dac, zein/Cy5-Dac, and Dac/Cy5.

24 hr after the administrations, the mice were perfused and sacrificed. The major organs were obtained and observed using the fluorescence imaging system (Figure 3.8B). For the *ex vivo* imaging of the brains, the brain tissue of both the zein/Cy5-RVG-Dac and

zein/Cy5-Dac groups showed obvious fluorescence, while low or no fluorescence was observed in that of the Dac/Cy5 group. The fluorescent intensity of the major organs of the different treatment groups was measured and shown in Figure 3.8C. The mean fluorescent intensity of the brains was 45.83 ± 3.41, 35.36 ± 5.71, and 3.04 ± 0.82, respectively, after the administrations of zein/Cy5-RVG-Dac_NP, zein/Cy5-Dac_NP, Dac/Cy5. The mean fluorescence intensity of the brains treated with zein/Cy5-RVG-Dac was significantly higher than that of zein/Cy5-Dac, while the mean fluorescence intensity of the brains treated with Dac/Cy5 was negligible. The results of Figures 3.8A, B, and C indicated that both zein and RVG29 facilitated the *in vivo* BBB penetration of the NPs, still with RVG29 being more effective than zein. As shown in Figure 3.8B, among the organs of the heart, spleen, kidney, and liver, higher fluorescence was observed in the liver and kidney of the zein/Cy5-Dac and the Dac/Cy5 groups than that of the zein/Cy5-RVG-Dac group. It indicated that RVG29 conjugation reduced the accumulation of the zein-based NPs in the liver and kidney.

The amounts of the nAChR receptor, which facilitated the receptor-mediated transcytosis of RVG29, on the cell membranes of various cells were investigated. The expression of nAChR in U87, C6, bEnd.3, and Hela cells was measured using ELISA (Figure 3.5C). U87 cells showed the highest level of nAChR. The bEnd3 cells presented a 130% higher expression of the nAChR than that of Hela cells. High expression of nAChR provided abundant attachment sites for the receptor-mediated transcytosis of the NPs and facilitated both the penetration of BBTB and the targeting to GBM cells.

The Dac contents in the major organs at 2 and 24 hr after the administrations, which indicated the biodistribution of zein-based NPs, were quantitatively determined using HPLC and presented in Figures 3.8D and E. At 2 hr, zein-RVG-Dac_NP had significantly higher drug content in the brain than that of zein-Dac_NP and Dac, respectively. There was no significant difference between the drug contents of the zein-Dac_NP and Dac groups. At 24 hr, there was no significant difference in the drug contents of the zein-RVG-Dac_NP and zein-Dac_NP groups although they are significantly higher than that of Dac. Almost none of Dac was detected in the brain samples of the Dac group at 24 hr. It can be concluded that both zein and RVG29 facilitated the BBTB penetration and cellular uptake of GBM cells with the latter being more effective than the former.

To fully explore the brain targeting efficacy of zein-RVG-Dac_NP, 20 μm-thick slices of the brain tissues of the zein/Cy5-RVG-Dac, zein/Cy5-Dac, and Dac/Cy5 treatment groups were prepared and observed using the fluorescence microscope (Figure 3.8F). The colocalization analysis inside the tumor region showed that the NPs with the red fluorescence were distributed in the tumor region, indicating that the NPs could reach the GBM cells. The fluorescence intensity in the tumor regions given by the Cy5 was measured (Figure 3.8G). The zein/Cy5-RVG-Dac group exhibited significantly higher red fluorescence (2.4-fold) than the zein/Cy5-Dac group, indicating that more zein/Cy5-RVG-Dac entered the brain tumor than zein/Cy5-Dac. Almost no fluorescence was detected in the brains of the Dac/Cy5 group. These results further demonstrated that both zein and RVG29 promoted the BBTB penetration and the cellular uptake by the GBM cells, and RVG29 was more efficient than zein in such promotion.

The *in vivo* pharmacokinetics of the zein-based NPs were studied using the SD rats. The mice were administered with zein-Dac_NP, zein-RVG-Dac_NP, and pure Dac, respectively, in the Dac equivalent concentration of 20 mg/kg by intravenous injection via the tail vein. At the time points at 0.1, 0.5, 1, 2, 4, 6, 8, 12, 16, and 24 hr, blood samples were collected, and the concentrations of Dac were measured using HPLC (Figure 3.8H). After the injection, the amount of Dac in the blood of the Dac group decreased rapidly, with about 5% left in circulation at 4 hr. However, there were about 18.2% and 15.7% of Dac left at 4 hr in the zein-RVG-Dac_NP and zein-Dac_NP groups, respectively. The pure Dac was cleared out from the blood circulation at about 8 hr, while it took 12 hr for zein-Dac_NP and 16 hr for zein-RVG-Dac_NP, respectively, to be cleared from the circulation. It indicated that the protective effect of the zein shell of the zein-RVG-Dac_NP and zein-Dac_NP resulted in a prolonged controlled release of Dac. Also, the RVG29 conjugation on the zein shell further increased the retention time of the zein NPs.

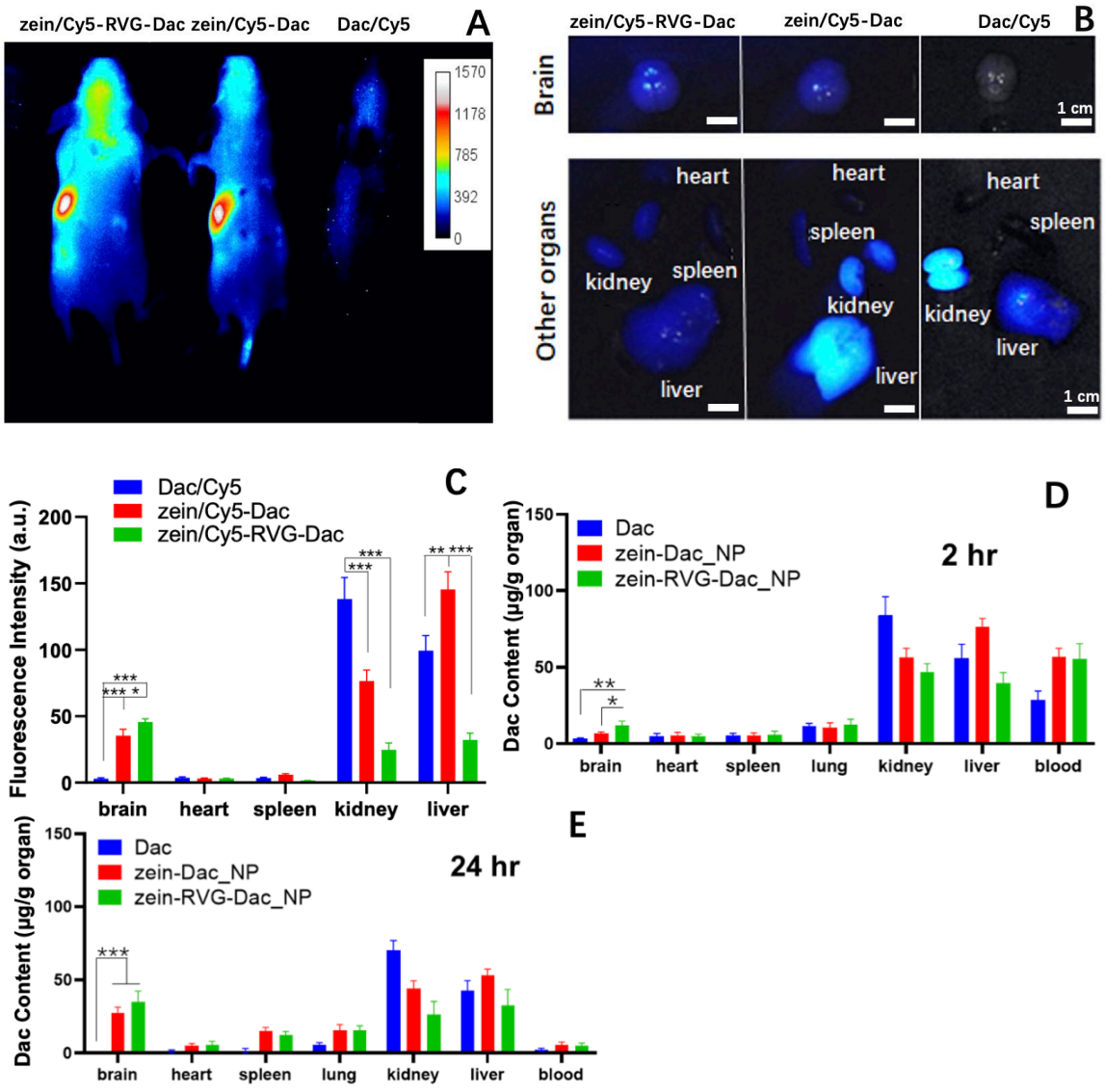
zein/Cy5-RVG-Dac zein/Cy5-Dac Dac/Cy5
A
1570
1178
785
392
0
zein/Cy5-RVG-Dac
zein/Cy5-Dac
Dac/Cy5
B
Brain
1 cm
Other organs
heart
spleen
kidney
liver
1 cm
C
Dac/Cy5
zein/Cy5-Dac
zein/Cy5-RVG-Dac
Fluorescence Intensity (a.u.)
brain
heart
spleen
kidney
liver
D
Dac
zein-Dac_NP
zein-RVG-Dac_NP
2 hr
Dac Content (μg/g organ)
brain
heart
spleen
lung
kidney
liver
blood
E
24 hr

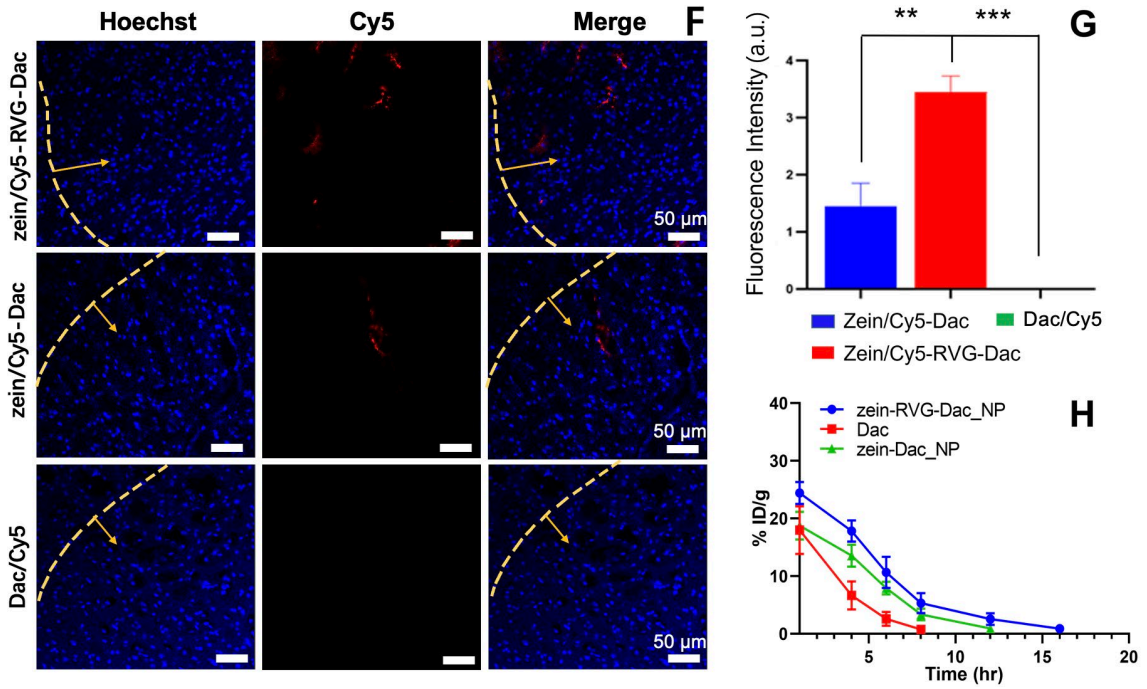

Figure 3.8 Biodistribution and pharmacokinetics studies of the zein-RVG-Dac_NPs and zein-Dac_NPs using the orthotopic GBM mice model.

(A) *In vivo* fluorescence images of mice treated with zein/Cy5-RVG-Dac, zein/Cy5-Dac, and Dac/Cy5 respectively, for 24 hr. (B) *Ex vivo* fluorescence images of the major organs. Scale bar = 1 cm. (C) The fluorescence intensity of Figure 4B was calculated using ImageJ. Data are presented as mean ± SD (n = 5); $^{**}p < 0.01$; $^{*}p < 0.05$; $^{***}p < 0.001$. Dac accumulation in the major organs and blood of the orthotopic GBM mice model for 2 hr (D) and 24 hr (E) was quantified by HPLC. Data are presented as mean ± SD (n = 5); $^{**}p < 0.01$; $^{*}p < 0.05$; $^{***}p < 0.001$. (F) CSLM images of the slices of the brain tumor tissues. Hoechst (blue) was used to dye the nuclei of the GBM cells. The yellow arrow and dash line indicated the tumor region. Scale bar = 50 μm. (G) The fluorescence intensity of Figure 4F was analyzed by ImageJ. Data are presented

as mean ± SD (n = 5); *$p < 0.05$; ***$p < 0.001$. (H) *In vivo* pharmacokinetics of pure Dac, zein-Dac_NPs, and zein-RVG-Dac_NPs.

3.5 In Vivo Anti-tumor Efficacy Study Using an Orthotopic GBM Model

To evaluate the anti-GBM activity, zein-RVG-Dac_NP, zein-Dac_NP, and pure Dac, respectively, were administrated to the orthotopic GBM mice model. The mice in the control group were administrated with saline. The change of tumor size was recorded using the fluorescence imaging system (Figure 3.9A). The relative tumor volume was calculated and shown in Figure 3.9B. On Day 20, after 5 times of drug administration, the relative tumor volume of the control group and pure Dac group reached 505.19 ± 74.90% and 389.52 ± 159.37%, respectively. There was no significant difference between the two groups. This is probably because ABCG2 at the BBTB impaired the brain penetration of Dac, resulting in the hampered intracranial target engagement and thus restricting the therapeutic efficacy.[100] Zein-RVG-Dac_NP had the best anti-GBM activity among the groups, and the relative tumor volume was 14.97% on Day 20. It was observed that the tumor volume of zein-RVG-Dac_NP group increased from Day 0 to Day 5 and decreased from Day 5 to Day 20. This is because from Day 0 to Day 5, the tumor was still fast growing and zein-RVG-Dac_NP slowed down the growth rate of the tumor. However, the size of the tumor still increased in the zein-RVG-Dac_NP group from Day 0 to Day 5. From Day 5 to Day 20, zein-RVG-Dac_NP continued to suppress the growth of the tumor and the tumor size became smaller. The zein-Dac_NP group had a relative tumor volume of 164.53% on Day 20. The GBM tumor size was also studied using the H&E staining of the brain tissues (Figure 3.10). On Day 20, the tumor size of the zein-RVG-Dac_NP group

was the smallest among all of the groups. Since both RVG29 and zein could favor the BBTB penetration and the cellular uptake of the GBM, they effectively increased the accumulation of NPs at the tumor sites and significantly improved the therapeutic effect. The body weight change and the survival time of the mice of different treatment groups were also recorded (Figures 3.9C and D). The median survival time of the mice model treated with saline, Dac, zein-Dac_NP, and zein-RVG-Dac_NP was 24, 26, 30, and 36 days, respectively. The survival period of the zein-RVG-Dac_NP treatment group was significantly prolonged compared with that of the zein-Dac_NP group ($p < 0.05$), Dac group ($p < 0.01$), and saline group ($p < 0.01$).

The brain tumor tissues were stained with Terminal deoxynucleotidyl transferase dUTP nick end labeling (TUNEL), an apoptosis marker for the quantification of apoptosis, and CD31, a hematopoietic function marker for the observation of angiogenesis. The images were shown in Figures 3.9E and F, and the fluorescence intensities were calculated and shown in Figures 3.9G and H. As shown in Figures 3.9E and G, the amount of the TUNEL-positive cells, with green fluorescence, in the order from high to low was the zein-RVG-Dac_NP, zein-Dac_NP, Dac, and control groups. Compared to the other groups, zein-RVG-Dac_NP induced significantly higher inhibition (19.1 ± 4.8%) on the tumor growth. For the images stained with CD31, lower expression of CD31 indicated the fewer microvessels and the increased number of the apoptotic tumor endothelial cells. As shown in Figures 3.9F and H, the higher amount of red fluorescence, which indicated the higher expression of CD31, was observed in the control and pure Dac groups. The zein-Dac_NP group showed a notable reduced amount of red fluorescence, and the zein-RVG-Dac_NP

group displayed the lowest CD31 expression. These results clearly showed that zein-RVG-Dac_NP increased the ablation of the blood vessels in the GBM, which could cause the apoptosis of the GBM cells.

IHC staining was widely used in the observation of abnormal cells, such as cancer cells. In this study, specific molecular makers, including the tumor protein P53, the Bcl-2-associated X protein (BAX), and the proteinase inhibitor 9 (PI-9), were used to characterize the proliferation and apoptosis of the tumor cells. The images were shown in Figure 3.9I, and the amount of the expression of P53, BAX, and PI-9 was calculated and shown in Figures 3.9J, K, and L, respectively.

P53 plays a vital role in the pathway of the cellular response of the apoptotic cell death and was widely used as a marker of cell apoptosis in cancer studies. In Figures 3.9I and J, the zein-RVG-Dac_NP group showed an increased expression of P53 compared to the zein-Dac_NP, Dac, and control groups, indicating that the zein-RVG-Dac_NP group induced more cell apoptosis in the brain tumors than the other groups. BAX, another marker of apoptosis, also presented increased expression in the zein-RVG-Dac_NP group than the other groups (Figure 3.9K). PI-9, an apoptosis inhibitor, presented the highest level of expression in the control group, and showed the lowest expression in the zein-RVG-Dac_NP group (Figure 3.9L). The results consistently concluded that zein-RVG-Dac_NP showed better induction of apoptosis of tumor cells than zein-Dac_NP and Dac, which was in agreement with the results of the *in vitro* western blot study (Figure 3.5J).

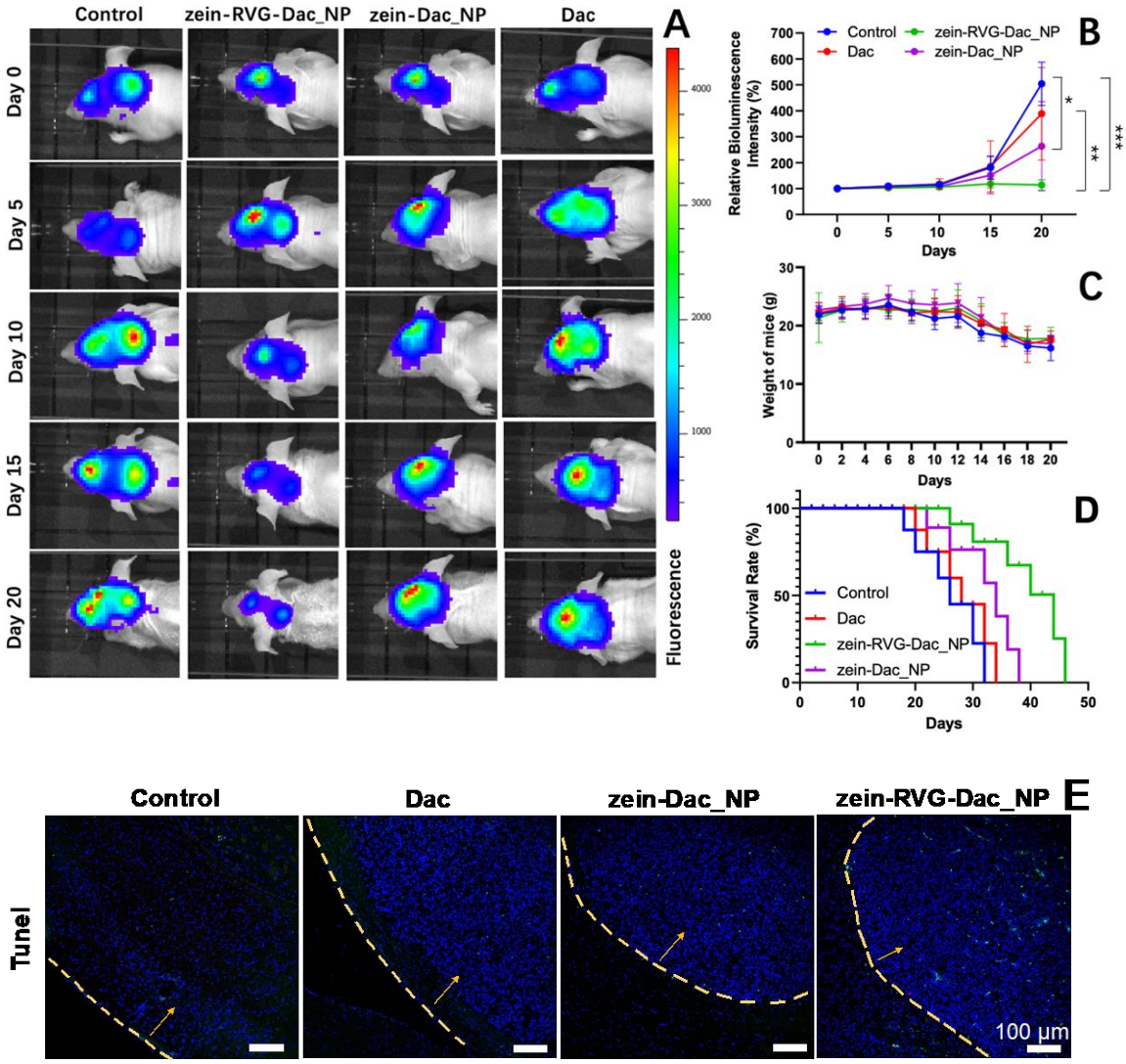
Control
zein-RVG-Dac_NP
zein-Dac_NP
Dac
A
Day 0
Day 5
Day 10
Day 15
Day 20
Fluorescence
B
Relative Bioluminescence Intensity (%)
Days
C
Weight of mice (g)
Days
D
Survival Rate (%)
Control
Dac
zein-RVG-Dac_NP
zein-Dac_NP
Days
E
Tunel
100 μm

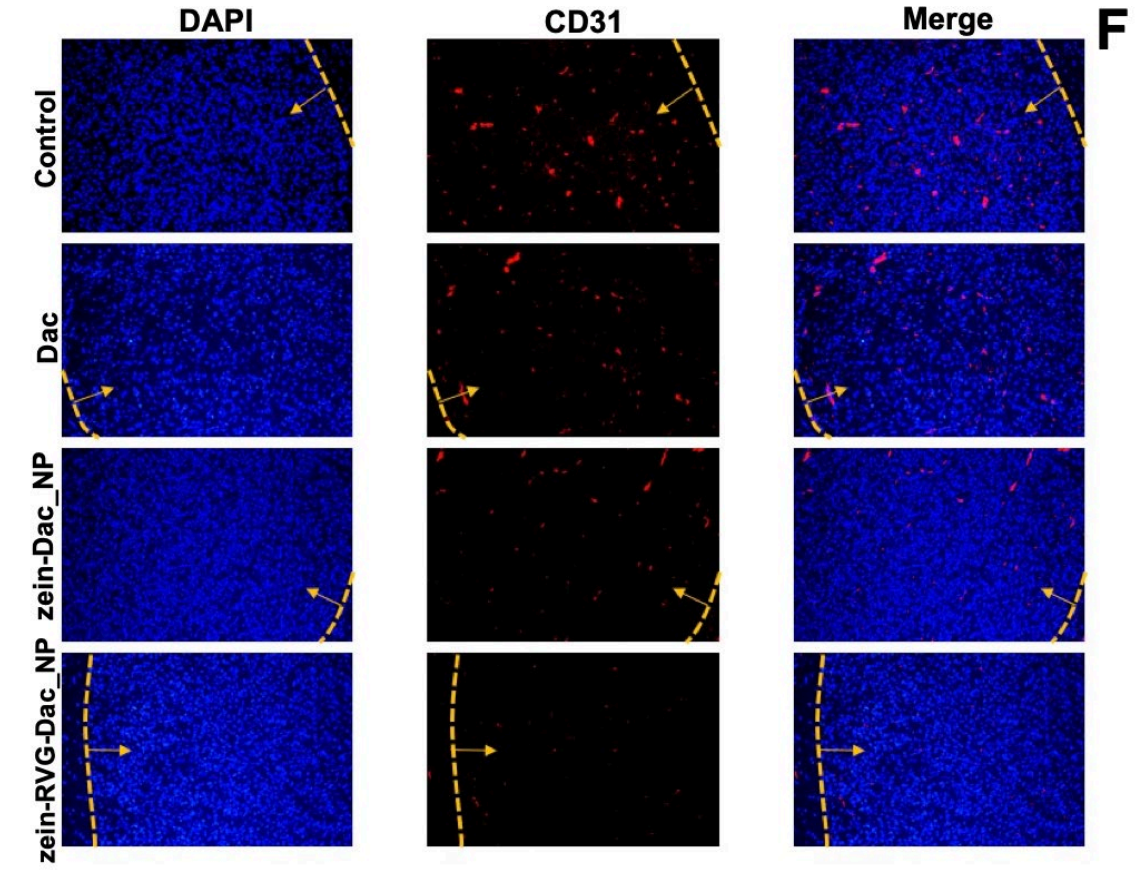
DAPI
CD31
Merge
F
Control
Dac
zein-Dac_NP
zein-RVG-Dac_NP

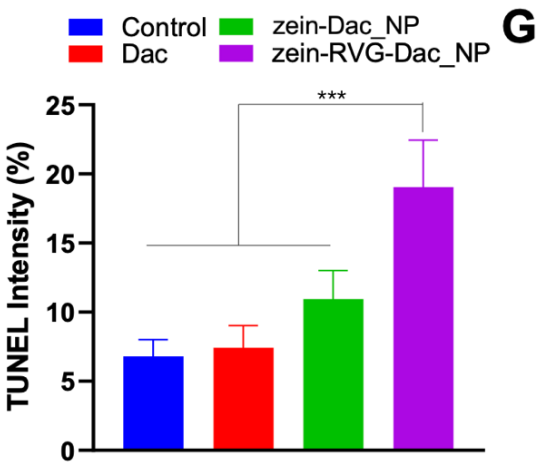
Control
Dac
zein-Dac_NP
zein-RVG-Dac_NP
G
***
TUNEL Intensity (%)
25
20
15
10
5
0

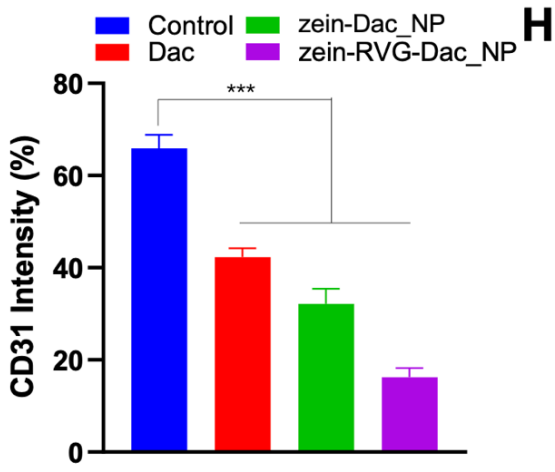
Control
Dac
zein-Dac_NP
zein-RVG-Dac_NP
H
***
CD31 Intensity (%)
80
60
40
20
0

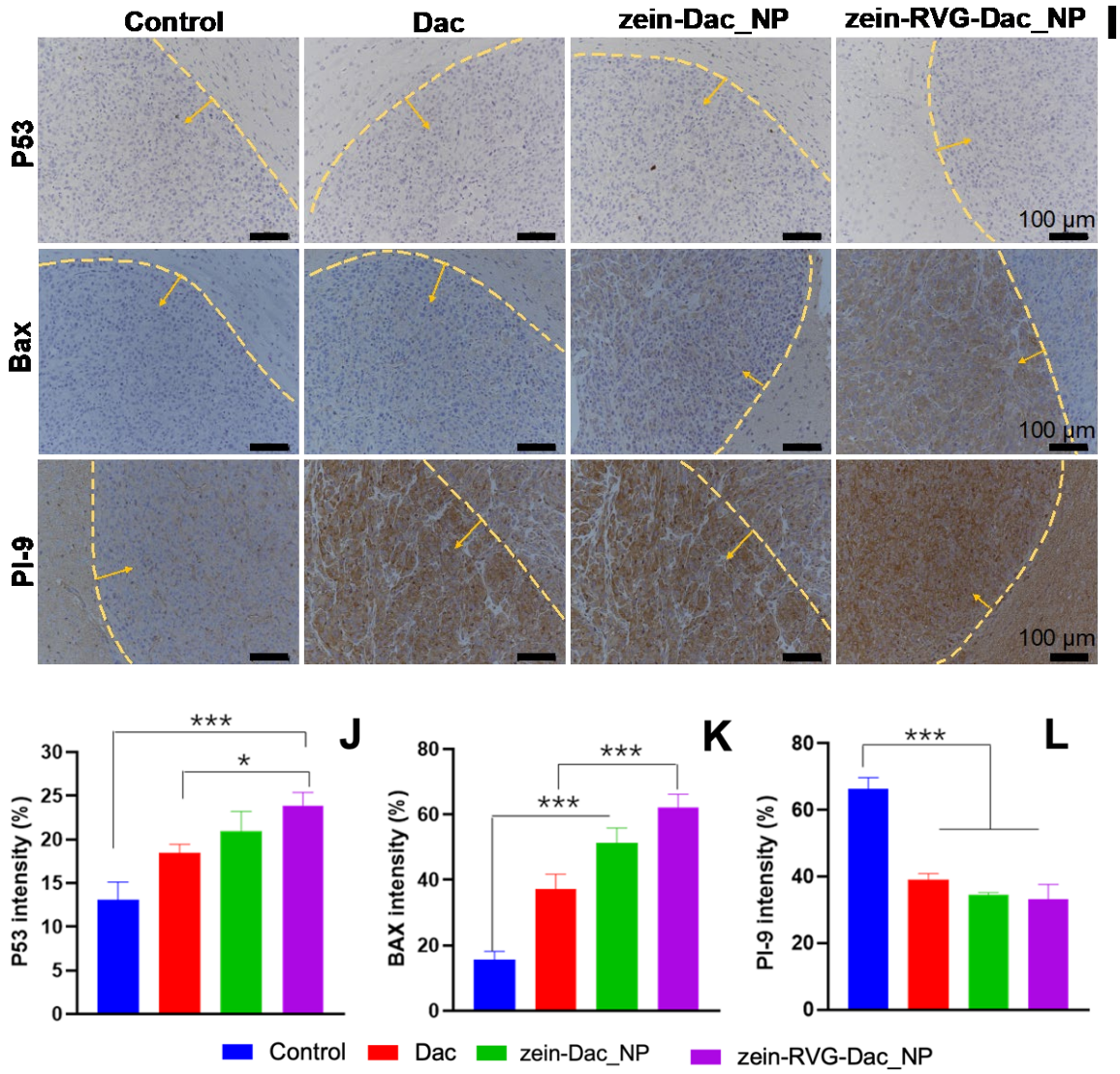

Figure 3.9 In vivo anti-tumor activity study of the zein-RVG-Dac_NPs, zein-Dac_NPs, and pure Dac using the orthotopic GBM mice model.

(A) In vivo imaging of the brain tumors, (B) the relative tumor volume (n = 12) as reflected by the ratio of bioluminescence on a specific day to day zero, (C) the profiles of the change of the body weight (n = 12), and (D) the cumulative survival (n = 6) of the U87 MG-Red-Fluc GBM-bearing mice after the administrations of zein-Dac_NPs, zein-RVG-Dac_NPs, and pure Dac, respectively. Data are presented as mean ± SD; **p < 0.01; *p < 0.05; ***p < 0.001. (E) TUNEL staining (green) and Hoechst staining (blue), and (F) CD31 staining

(red) and DAPI staining (blue) of the brain tumor tissues were analyzed using CLSM. The yellow arrow and dash line indicated the tumor region. Scale bar = 100 μm. Mean fluorescence intensities of the (G) TUNEL and (H) CD31 staining were calculated. (I) IHC analysis of the brain tumor tissues using the molecular makers, P53, BAX, and PI-9. The yellow arrow and dash line indicated the tumor region. Scale bar = 100 μm. Mean fluorescence intensities of the (J) P53, (K) BAX, and (L) PI-9 in the images were calculated. Data are presented as mean ± SD; *p < 0.05; **p < 0.01; ***p < 0.001.

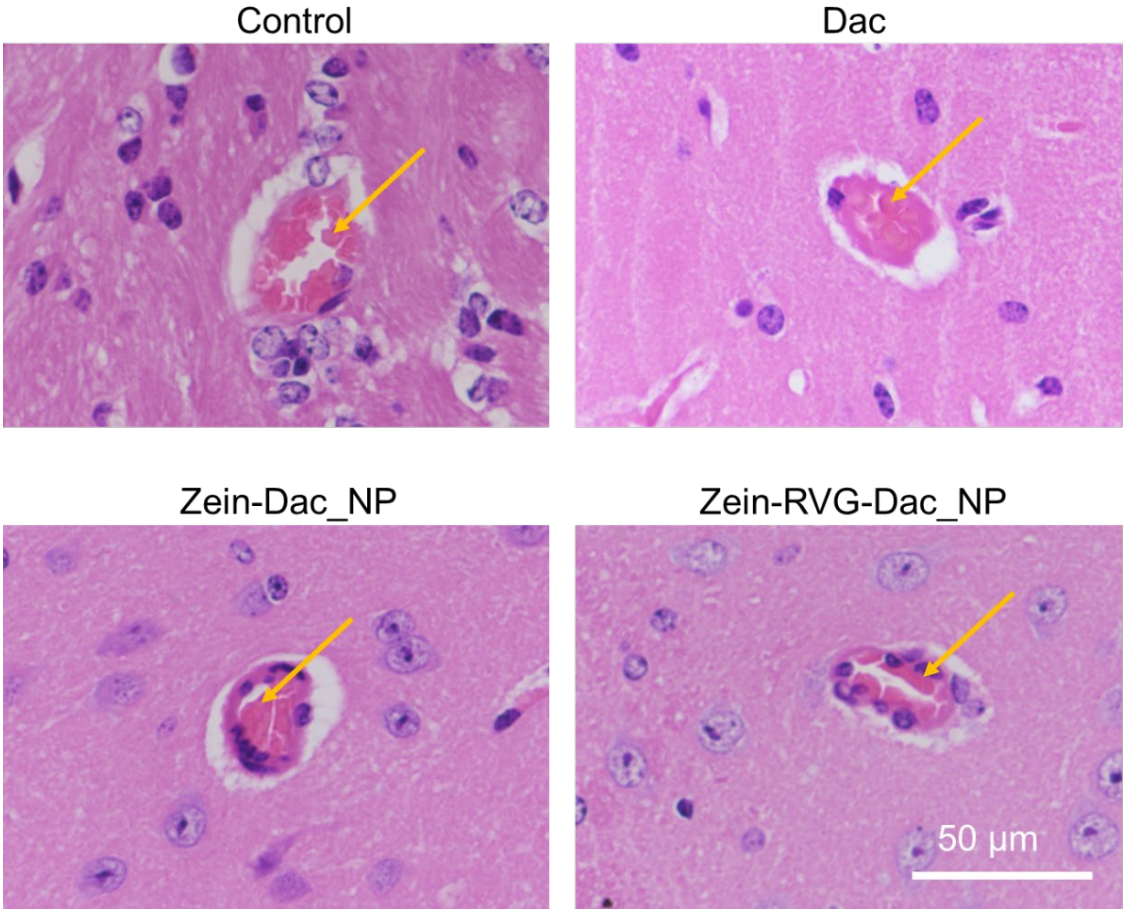

Figure 3.10 H&E staining of mouse brain sections.

Yellow arrows indicate the red blood cells in the blood vessels.

3.6 Histopathological analysis

To further assess the potential toxicity of zein-RVG-Dac_NP, the histopathological analysis was conducted on the major organs, including the heart, liver, spleen, lung, and kidney, collected from the orthotopic GBM model after the treatments (Figure 3.11). The organ tissues were sliced before the hematoxylin and eosin (H&E) staining. As shown in Figure 3.11, obvious necrosis (labelled by A) and aggregates of inflammatory cells (labelled by B) were observed in the kidney of the pure Dac group, indicating that pure Dac caused notable kidney damages. In contrast, no pathological inflammation was observed in the other groups. These results approved that zein-RVG-Dac_NP had no safety problems and no side effects on the major organs as a brain-targeting drug carrier.

The brain sections were stained with H&E to observe the effect of different treatments on the integrity of the cerebral blood vessels of the mice (Figure 3.12). Yellow arrows point the erythrocytes in the blood vessels. The results showed that the blood vessels of the mice in each group were intact, and the blood vessel walls were clear. The morphology of the blood vessels in the Dac, zein-Dac_NP, and zein-RVG-Dac_NP groups was consistent with that of the control group. There was no erythrocyte extravasation observed in the images, indicating that the integrity of the cerebral blood vessels was kept after the treatments.[101] It concluded that the long-term administrations of NPs would not affect the integrity of cerebral blood vessels.

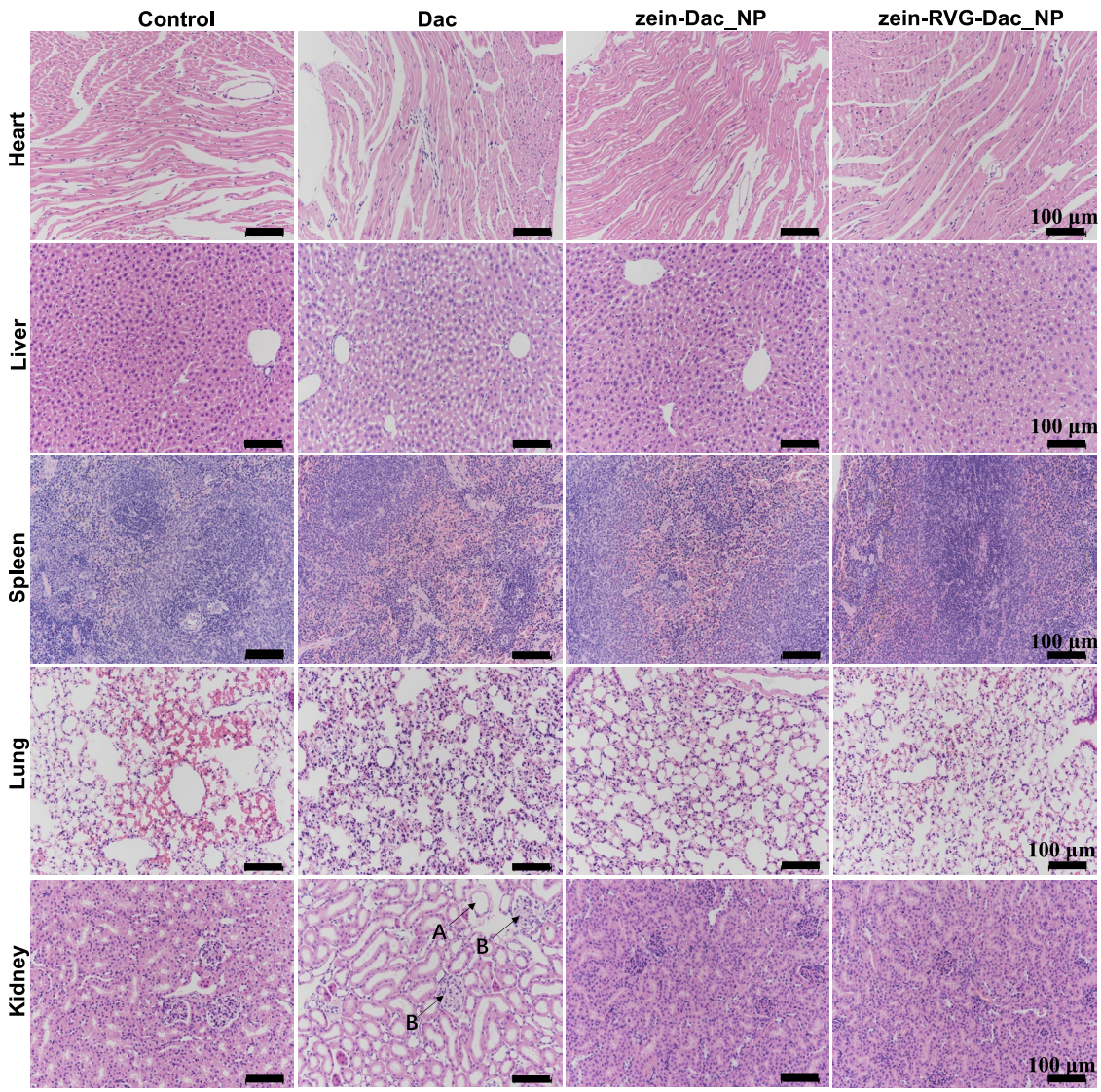

Figure 3.11 Histopathological analysis using the orthotopic tumor mice model. The major organs, including heart, liver, spleen, lung, and kidney, collected from the mice after the treatments with saline, Dac, zein-Dac_NPs and zein-RVG-Dac_NPs, respectively, were evaluated by the H&E staining. Scale bar = 100 μm. Label A indicated the necrosis. Label B showed the aggregates of inflammatory cells.

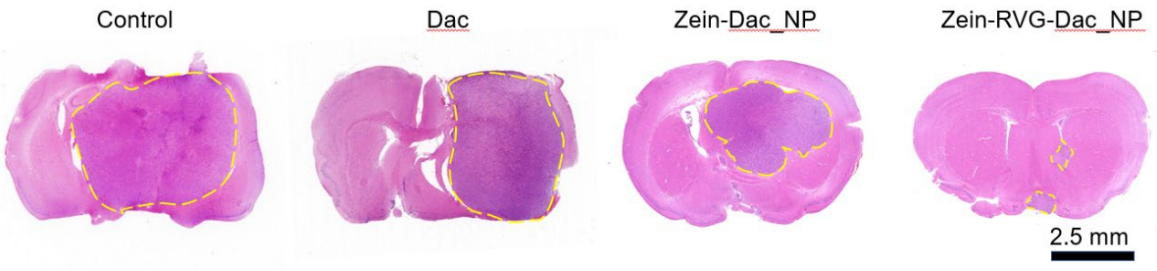

Figure 3.12 H&E staining of mouse brain sections with the tumors after various treatments.

The tumor regions were marked using yellow dash lines.

3.7 Assessment of the serum biomarkers

Alkaline phosphatase (ALP), Aspartate transaminase (AST), and Alanine transaminase (ALT) were biomarkers of liver function. The increased levels of ALT, AST, and ALP were usually caused by the damage or disease of the liver. The level of creatinine (CREA) in serum was used as an indicator of kidney function, and an elevated CREA level indicated the impaired function or disease of the kidney. The results in Figure 3.13 showed that there was no significant difference in the amounts of ALT and ALP among the four groups. However, the Dac group showed higher serum CREA and AST levels than the other groups, indicating that Dac induced damage of the hepatic cells. The results confirmed that the administration of pure Dac could induce acute renal and hepatic toxicities. In contrast, the zein based NPs as the brain-targeting drug carriers could circumvent the damage to the renal and hepatic tissues and reduced the intrinsic toxicity of the Dac.

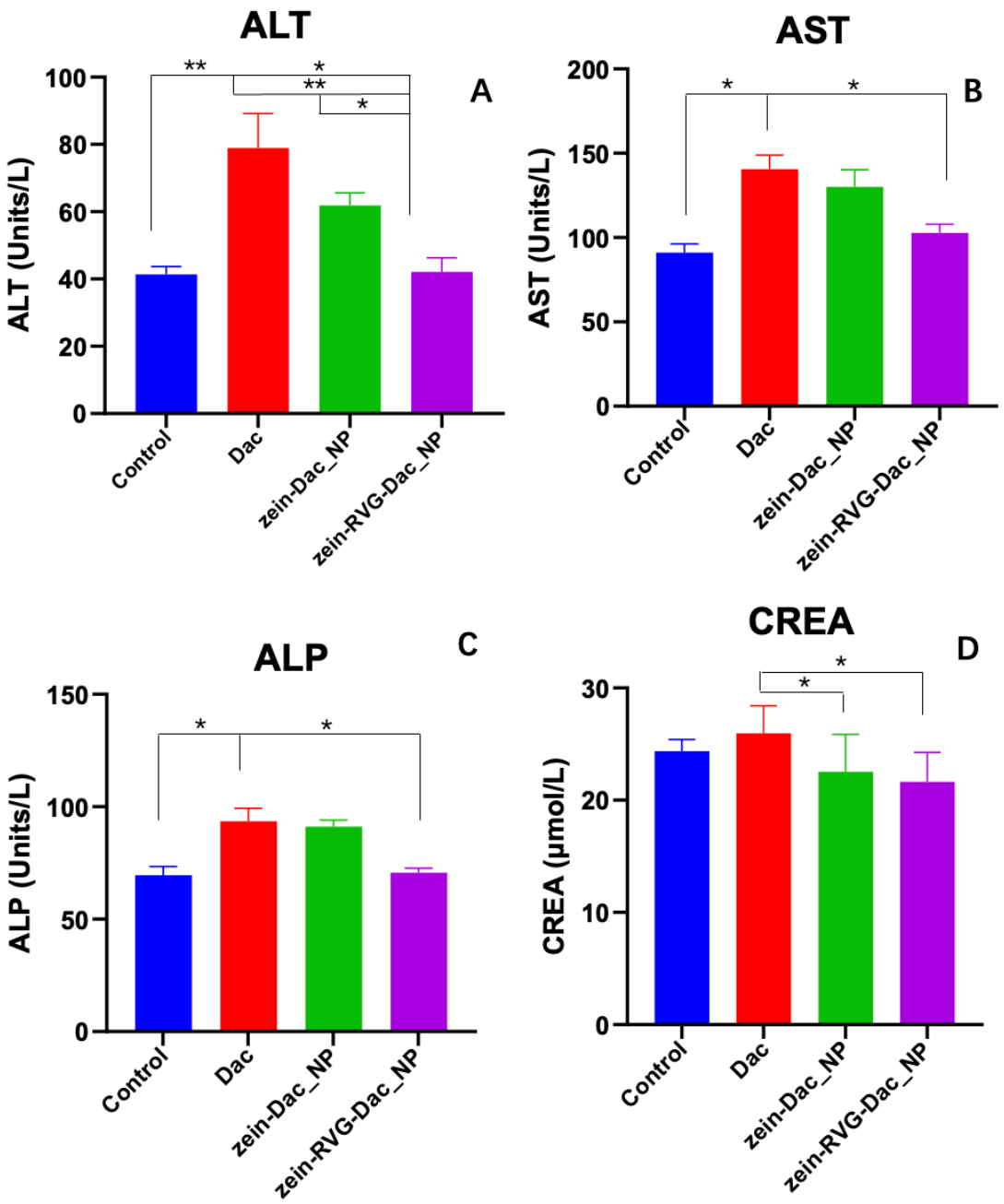

Figure 3.13 The blood biochemistry study was conducted using the orthotopic GBM mice model.

The levels of serum biomarkers in mice were measured after a 20-day treatment. Data are presented as mean ± SD (n = 3); *p < 0.05; **p < 0.01.

3.8 Summary

In this study, a novel brain-targeting drug delivery system, zein-RVG-Dac_NP, was formed by the conjugation of RVG29 on the surface of the self-assembled zein NPs with the encapsulation of Dac. The results of FTIR and NMR confirmed the successful conjugation of zein and RVG29 as well as the encapsulation of Dac in the zein-RVG-Dac_NPs. The in vitro cytotoxicity study revealed that zein-RVG-Dac_NPs had similar cytotoxicity to the U87 cells as pure Dac in the Dac equivalent concentration range of 10-50 nM. Both zein and RVG29 enhanced the cellular uptake of the NPs to U87 cells with the latter being more efficient than the former. In the in vivo studies of biodistribution and brain targeting, both zein and RVG29 facilitated the BBTB penetration and GBM targeting although RVG29 was more efficient than zein in this effect. As a result, a significantly higher amount (2.4-fold) of the zein-RVG-Dac_NPs penetrated through the BBTB than that of the zein-Dac_NPs, enabling zein-RVG-Dac_NPs to present a better therapeutic effect than pure Dac on the orthotopic GBM mice models. In addition, no histopathological changes and side effects were detected in the major organs of the mice after the administration of the zein-RVG-Dac_NP. In summary, the RVG29-conjugated zein NPs are highly potential for drug delivery to the brain to treat brain-related diseases.

Part 2: Conformational Dynamics of SARS-CoV-2 Variant RBDs and their Interactions with ACE2: Insights Revealed by Mass Spectrometry

Chapter 4. Introduction

4.1 COVID-19 and SARS-CoV-2

Since its outbreak in Wuhan, China in December 2019, Coronavirus Disease 2019 (COVID-19) has affected more than 200 countries, and as of 18 October 2021, it has caused more than 240 million confirmed infections and more than 4.8 million deaths,[102] rendering substantial social and economic disruption worldwide. Severe Acute Respiratory Syndrome Coronavirus 2 (SARS-CoV-2),[103] the causative agent of COVID-19, was found to show 79% genomic similarity to SARS-CoV, but the high transmission rate under weakly symptomatic or even asymptomatic condition of this novel coronavirus sparks the global pandemic. The structure of SARS-CoV-2 is similar to those of other members in the family Coronavirinae, and contains a 29.9 kb long single strand RNA that encodes four structural proteins, i.e., nucleocapsid (N), membrane (M), envelop (E) and spike (S) proteins, and a batch of 16 non-structural proteins that are responsible for virus replication (Figure 1).[103, 104] The viral RNA wrapped by N protein forms the capsid, which is buried inside the viral envelop constructed by M and E proteins. The characteristic corona appearance of SARS-CoV-2 is attributed to the crown-like S protein linked to the outermost surface of the envelop.

4.2 Interaction of S protein with ACE2

4.2.1 Angiotensin-converting enzyme 2 (ACE2)

As a type I membrane protein, ACE2 is widely expressed in many organs such as the lung, pancreas, heart, kidney, and liver. Its main function is the regulation of the level of

angiotensin (Ang), which is a potential modifier for vasoconstriction and blood pressure.[105] However, ACE2 mediates cell entry and therefore supports the entry of SARS-CoV-2 into the target host cells.[106] ACE2 forms a dimer and contains an N-terminal peptidase domain (PD) and a C-terminal collectrin-like domain (CLD). The PD domain of ACE2 is regarded as a trigger for endocytosis and translocation of both virus and ACE2. The domain involves two lobes, between which, the peptide substrate binding sites are formed.[107, 108]

ACE2 serves as a regulator for the blood pressure and cardiac functions. Besides, due to a high expression level of ACE2 on the surface of endothelial cells, which are mainly located along the lining of the lung and small intestine, access for SARS-CoV-2 is allowed and might exhibit the manifestations of SARS infections.[109] As a human receptor, the molecular mechanisms of ACE2 were firstly indicated by in vivo models expressing SARS-CoV, explaining what often led to lung failure.[110] By evaluating the pathologies of lungs infected by COVID-19, the activated ACE2 was confirmed to exhibit mitigated tissue damage engendering from SARS-CoV-2.[111] More recently, genetic differences of the expressions of ACE2 have been observed, among Asian males. These genetic differences of ACE2 might affect its functions, which could explain the different infectivity among the population.[112]

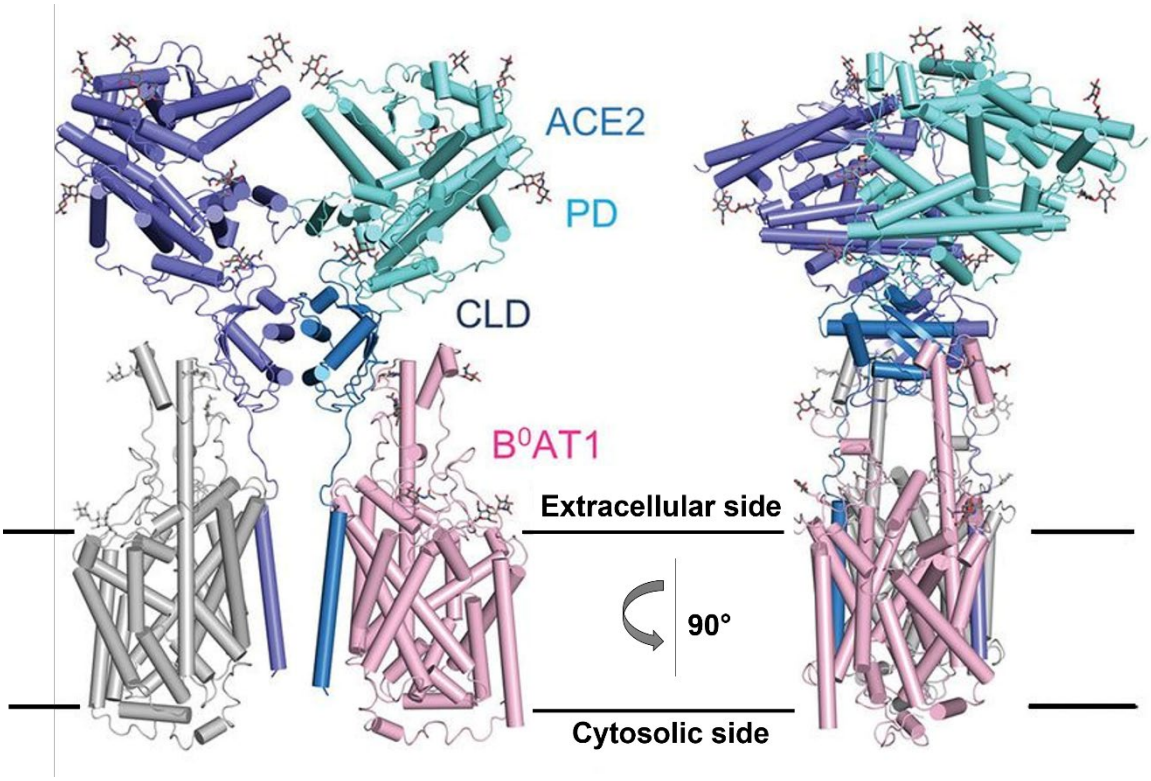

Figure 4.1 Structure of the full-length ACE2-B0AT1 complex.[105]

4.2.2 Spike protein

The spike (S) protein is high-density glycosylated and covers the surface of SARS-CoV-2.[113] It exhibits major roles in viral entry, and as a most accessible target, it is responsible for the development of virus attachment inhibitors, neutralizing antibodies, and vaccines.[114] S protein consists of two subunits: the receptor recognition subunit S1 (residues 14-685), and the transmembrane fusion subunit S2 (residues 686-1273).[115] S1 and S2 subunits are connected by the furin cleavage site. S1 subunit belongs to the C-terminal domain and contains the receptor binding domain (RBD, residues 333-527), which is able to specifically recognize and bind to the host receptor, ACE2.[106] On the other

hand, the S2 subunit plays crucial functions in mediating the fusion between virus and host cells and subsequently providing a cell entry for the S1 subunit.[116]

As a highly movable trimer protein, the transmission of S protein from the prefusion state to the postfusion state is initiated by the targeting cells' attachment. To understand the potential functions of S protein, Cryo-EM is selected to perform the structural details of full-length S trimer, at the two states. In both prefusion and postfusion states, the furin cleavage site of concerns is located in a disordered loop and exposed to the surface of the S trimer. In addition, mild condition alterations using detergents can trigger states transmission, suggesting a low kinetic barrier for S1/S2 boundary.[117]

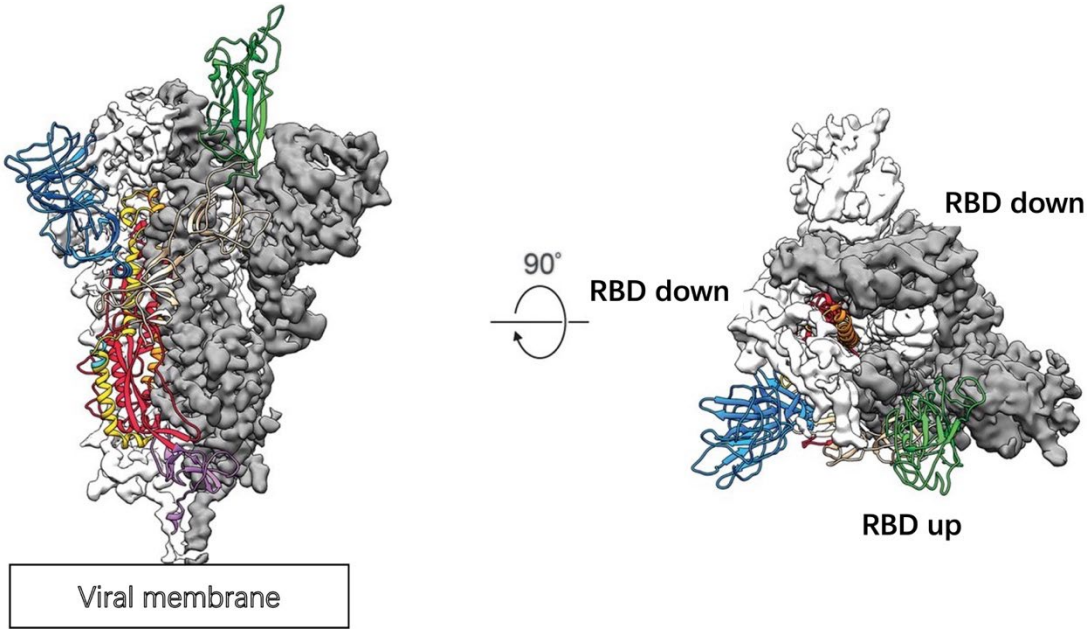

Figure 4.2 Crystal structure of S protein at prefusion state.[115]

4.2.3 S protein binding to ACE2

Before entry to the host cells, the S protein occurs as a trimetric in the metastable prefusion conformation. RBD can have two conformations at the prefusion state, “up” and “down”, the flexible RBD is able to bind the receptor when it is in the “up” conformation.[115] Once the S1 subunit completes binding to the host cell receptor, the membrane fusion between the viral membrane and host membrane is triggered, resulting in the rearrangement of the S protein conformation from prefusion state to postfusion state. The changes of conformational state provide energy to overcome the kinetic barriers of the membrane fusion process caused by repulsive hydration forces.[118] In this process, the S2 subunit serves as a trigger and driver. In addition, a cellular serine protease, TMPRSS2, cleaves the boundary between S1 and S2 subdomain and facilitates the efficient cell entry of S protein.[119] Furthermore, TMPRSS2 is the first to be clinically identified as a blocker for preventing SARS-CoV-2 infection.[119]

4.3 SARS-CoV-2 variants

S trimer plays vital functions of viral entry. It has been utilized as a main target for antibodies, which means the mutations on S trimer, especially on RBD, may take effects on the efficiency of therapeutic strategies and vaccines.[120] Therefore, the continuous emergence of new SARS-CoV-2 variants has complicated the situation and become a challenging issue of the pandemic. Several prevalent variants, including Alpha, Beta, Gamma, and Delta variants, are categorized as the Variant of Concern (VOC) by the World Health Organization (WHO), which have enhanced transmissibility and infectivity, and currently used diagnostic methods, therapeutics and vaccines have reduced effectiveness

against these variants.[121] Multiple variants such as Zeta and Kappa have been identified as the Variants of Interest (VOIs). More recently, a novel variant named Omicron has been identified with multiple mutations on S trimer, especially in the RBD region, through sequence alignment. Omicron has been approved with the strongest loss of antibodies' potential, therefore is of great attention.[122]

4.3.1 Alpha

4.3.1.1 Infectious properties and immune performance

The B.1.1.7 variant, also known as Alpha, was firstly reported in the United Kingdom in early December 2020,[123] which rapidly spread among European countries and then became predominant in America. It involved a mutation in RBD, at position Y501, which presented ~ 10-fold higher binding affinity to ACE2 than that of N501.[124] Besides, increased transmission (43%-90%) and higher mortality (~30%-50%)[125] rates were estimated using various mathematical models.

For neutralization, similar efficiency of Pfizer Cominarty against the variant was observed compared to the wild type strain among the individuals who obtained two doses of vaccines.[126] Bamlanivimab (LY-CoV555) played the functions of blocking the interactions between WT SARS-CoV-2 and ACE2, and the binding region was extremely close to the site N501. Therefore, to detect the immune potential, the binding affinities of Bamlanivimab towards WT and the Alpha variant were measured. Interestingly, WT and Alpha were observed to have very similar binding capabilities, which indicated the similar immune response of Alpha compared to WT.[124]

4.3.1.2 Structural alteration

The local structural changes induced by the mutation at N501Y were revealed by MD study, and resulted in a weaker connection of E498 (a residue close to N501Y) with N38 and Y41 of ACE2.[127] The mutation also led to conformational alterations, the Cryo-EM structure introduced a new π–π stacking formation between Y501 and Y41 of ACE2, provided a more stable structure of SARS-CoV-2-ACE2-complex.[128, 129] The conformational changes strongly supported the increased binding affinity between the Alpha variant and ACE2.

4.3.2 Beta

4.3.2.1 Infectious properties and immune performance

The B.1.351 variant was named Beta and initially discovered in South Africa on December 18, 2020, slightly later than the B.1.1.7 variant.[123] The genomic and epidemiological data indicated that the emergence of this variant caused a rapid increase in the number of infections.[130] Several studies demonstrated the possible immune escape of this variant, which contained three mutations in RBD, respectively K417N, E484K, and N501Y.

The neutralizing activities of convalescent plasma from the early infected individuals showed a remarkable reduction against the Beta variant, and it presented resistant properties against the major monoclonal antibodies (mAbs) targeting RBD.[131] Another study indicated that E484K and K417N contributed to the immune escape, allowing B.1.351 to completely escape from three classes of the applicated antibodies.[132]

4.3.2.2 Structural alteration

Recently, MD simulations showed the most significant structural changes in the Beta variant, which involved the formation of several new hydrogen bonds. The RBD loop segment containing K484 exhibited higher flexibility, resulted in a more stable RBD-ACE2 complex.[133] Similar MD simulations were conducted and showed the formation of a new salt bridge and other interactions, possibly due to the increase of positive charge in E484K mutation.[134] Additionally, MD simulations and Principal Component Analysis (PCA) confirmed the highest degree of structural changes were observed through the triple combination mutations of K417N, E484K, and N501Y, compared to the single/dual mutations.[135] Another in silico study demonstrated that Beta RBD interactional region was quite flexible, while the complex of RBD-ACE2 was more stable with strong binding, which could be explained by the increased number and strength of hydrogen bonds. In conclusion, the Beta variant displayed a more suitable conformation for molecular interactions with ACE2, which might be correlated with its higher infectivity and transmission, compared to that of WT strain.[136]

4.3.3 Zeta

4.3.3.1 Infectious properties and immune performance

The variants of P.1 and P.2 (Zeta) both initially spread among Brazil, P.1 lineage contained three mutations in RBD, but Zeta only involved a single mutation at position E484K. For E484K mutation, due to the possible evasion from monoclonal and neutralizing antibodies, it has attracted the great attention of researchers. For binding affinity, the experimental results presented a minor difference of 1.6 fold reduction (11 nM) compared to that of wild

type RBD (7 nM).[137] A study indicated that the slightly increased binding affinity E484K might correlate to higher transmissibility .[138]

The Zeta variant is generally regarded as a variant that could dramatically reduce the efficiency of vaccines and antibodies.[139] The study demonstrated that the neutralization sensitivities of the Zeta variant against two widely used mRNA vaccines, BNT162b2 and mRNA-1273, were significantly decreased by 2.9-5.8 fold.[120] Similar negative impact has been observed for the utilization of several class I antibodies, which led to decreased or completely nullified neutralizing functions.[140] Besides, less sensitivity to neutralization of E484K was visualized for convalescent human sera.[141]

4.3.3.2 Structural alteration

To explore the internal connection between S (E484K)-ACE2 binding affinity and viral spread, MD simulations were conducted. Since a change from Glu to Lys means a change from a negatively charged side chain to a positive one, the mutation permitted a new transient contact ion-pair interface with E75 of ACE2.[135] The conformational changes showed the slight conformational changes of the Beta variant, upon binding to ACE2.

4.3.4 Kappa

4.3.4.1 Infectious properties and immune performance

The sudden emergence of the variant in India was rapidly spread with a higher prevalence and stronger transmission. The lineage B.1.617.1 (Kappa) contained double mutations in RBD, respectively were E484Q and L452R. In which, E484Q shows similar immune

escape ability as E484K.[142] In vitro experiments demonstrated an increment in infectivity of L452R mutation, slightly lower than that of N501Y mutation, in pseudovirus infection. A 4-fold decrease in neutralization antibodies of convalescent plasma was reported in the study.[143] Another study also indicated the mutation L452R leads to significant increase in the binding affinity where the K_D value was 1.20 ± 0.06 nM. In addition, similar in vitro results confirmed a higher infectivity in pseudovirus infection and stronger viral replication capacity.[144] It was reported that the mutation of L452R close to the RBD "receptor binding ridge" was much easier to leading the immune escape against mAbs LY-CoV555 and its related cocktail product, LY-CoV016. For bamlanivimab, FDA confirmed that the L452R could reduce bamlanivimab neutralization for over 1000-fold.[145]

4.3.4.2 Structural alteration

The computational simulations help to understand the interactions between the Kappa RBD and ACE2 and indicated a stronger binding affinity and three newly formed hydrogen bonds of L452R and E484Q.[146] The position 452 was in a hydrophobic patch of RBD, L452R mutation promoted the interaction between S trimer and ACE2, and then enhanced the infectivity. Another MD simulations showed that E484Q disrupted the initial salt bridge between E484 and K31 of ACE2 and increased the stability of S trimer at the same time.[147] These newly formed connections supported the more rigid conformation for the Kappa-ACE2 complex.

4.3.5 Delta

The emergence of the Delta variant (lineage B.1.617.2) closely followed the Kappa variant, at the end of 2020, and then spread across India. The Delta variant shared a common mutation at L452R with Kappa, with an additional mutation at T478K of RBD. The prevalence of the Delta variant rapidly overcame the previous predominant variants of Kappa and Alpha.[148]

4.3.5.1 Infectious properties and immune performance

At the first emergence of the Delta variant, a study summarizing five studies gave an estimated mean reproductive statistic of 5.08, and therefore predicted a possible continuous epidemic.[149] It was reported that the Delta variant displayed higher replication and exceptional viral mediated entry capabilities, which may explain the prominence of Delta. Besides, as seen in infected patients, the Delta variant was observed with lower vaccine efficiency and remarkably reduced antibody responses.[150] The Delta variant was also proved to have higher infectivity for the early stage of infectious patients. Surprisingly, the PCR-testing of the infected patients demonstrated a 1000-fold stronger positive result compared to the previous variants, indicating a considerably increased viral replication with this variant.[151] There was a study that also investigated the transmission of the Delta variant and suggested an improved capability of membrane fusion for the S trimer compared to the other variants, facilitating interactions with human receptors even at a low ACE2 level.[152] Another study revealed a 1.5-fold higher transmission and 20% reduction of immune potential, together with 27% reinfections of the Delta variant, resulted in the rapid spread of this variant.[153]

Infections of the Delta variant were identified in the population who has been fully vaccinated, raising the concern for the immune escape potential of the variant. In the vaccinated population, the individuals diagnosed with positive PCR results for SARS-CoV-2 had significantly higher antibody levels than the ones with negative results. The findings suggested an enhanced antibody response in the vaccinated population who has been infected by the Delta variant, indicating a large-scale improvement of population immunity via extensive vaccination and developed infections.[154] A clinical study was conducted for evaluating the vaccine breakthrough cases of Delta, where six Delta infected patients with full vaccination supported the possibility of immune escape.[155]

4.3.5.2 Structural alteration

The Cryo-EM structures of the Delta S trimer containing RBDs at various states were visualized without major structural alterations. To study the structural response of the Delta variant, the S trimer of the Delta variant was superposed onto the conformation of D614G, followed by the alignment of the S2 subunit. The results identified the differences in N-terminal domain (NTD) involving five mutations, which rearranged to give a loop (fragments 173-187) and substantially affected the antigenic surface of the S2 subunit. This structural rearrangement mainly changed the antigenic surface close to NTD, which supported the possible loss of functions and neutralizations of antibodies targeting NTD.[152] The interactions between the Delta RBD and ACE2 were explored by MD simulations, which exhibited a β-loop-β alteration (fragments 472-490) within the RBD. Compared to other strains such as WT, Alpha, and Beta, the loop of Delta with T478K mutation exhibited lower flexibility, which might be mainly owing to the changes of a disulfide

bond that resulted in different conformations towards various directions with increased stability.[156] Another study indicated that the Delta variant involved the more flexible loop containing a mutation at T478K and therefore enhanced the interactions with ACE2, by identifying the Cryo-EM structure of the Delta S trimer.[157]

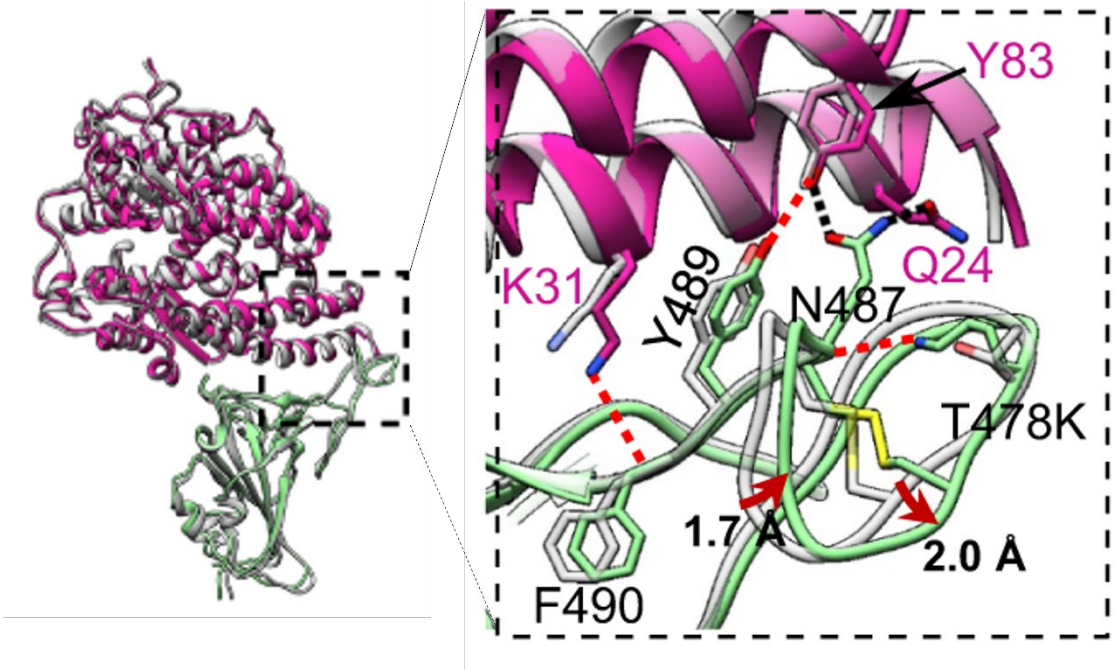

Figure 4.3 The structure alignment between Delta RBD-ACE-complex and WT RBD-ACE2-complex (PDB ID:6M0J).

Newly formed hydrogen bonds were shown as the red dotted lines.[157]

4.3.6 Omicron

23 months after the first detection of SARS-CoV-2 a new variant emerged. This variant of concern was named Omicron and rapidly spread among the world, overcoming the previous predominant variant Delta.[158] So far, the Omicron variant with several

sublineages was the most heavily mutated variant (including 15 mutations within RBD for BA.2) showing large-scale conformational changes,[159] and therefore led to a new consideration of natural immune escape.[160]

4.3.6.1 Infectious properties and immune performance

In silico study was used for evaluating the binding affinity of the Omicron variant towards ACE2 compared to that of WT and the Delta strains. Compared to the Delta variant, the Omicron variant comprised more hydrophobic amino acids (Phe and Leu) in the core of RBD, which help to create a more stable structure.[161] Another study also demonstrated that the environmental endurance of Omicron might also improve due to the increased stability, leading to increased infectivity,[162] even though the Surface plasmon resonance (SPR) assay displayed a similar binding affinity for Omicron S protein towards ACE2 as that of Beta, Delta, and D614 strains. In vitro experiments were conducted for testing the infectivity of the Omicron variant, which exhibited enhanced infectivity of about 10-fold for S-mediated viral entry compared to the Beta and Gamma variants.[163] Another study indicated different findings, which observed a lower entry efficiency together with reduced cleavage capability for Omicron. These findings may explain the reduced accumulation of virus in the lung in in vitro and ex vivo models, resulting in less severe symptoms of the Omicron variant.[164]

Nowadays, the heavily mutated Omicron variant has been confirmed to have immune escape potential. A study reported a significant reduction of the antibodies level in the convalescent sera for the patients infected with previous strains. These findings strongly

supported the reduced immune properties against the Omicron variant for the full-vaccinated people and previous infectious ones.[163] Several studies repeatedly demonstrated the comprehensive reduction of immune responses against the Omicron variant. In the study, two types of T cells ($CD8^+$ and $CD4^+$) obtained from the individuals who received BNT162b2 and Ad26.COV2.S vaccines were selected for testing the immune strength. The results were consistent with previous conclusions, but it also suggested $CD8^+$ T cells have cellular immunity roles for the protection against severe SARS-CoV-2 diseases, which further explained the importance of increasing the vaccination rate among the population.[165]

4.3.6.2 Structural alteration

Recently, the structural details of the Omicron S trimer in free state and Omicron RBD-ACE2 complex were displayed. The X-ray crystallography and Cryo-EM structure indicated that the mutations of the Omicron variant led to the significant interaction differences upon ACE2 interaction, mainly caused by the charge reversal. A study investigated the structure of S trimer, which indicated a compact arrangement of three S2 subunits, resulting in a highly stable structure. At the prefusion state, enhanced internal contacts of S1-S1 and S2-S2 subunits were observed, possibly due to the localized shift of internal subunit interfaces, explanative of the improved tolerance and lower plasticity of the Omicron variant.[162] Upon binding to ACE2, the Omicron RBD displayed a preliminary scale of positive district possibly contributed by the mutations of T478K, Q493R, and Q498R. Q493R and Q498R could attract a negative region containing E35 and D38 of hACE2 and enhance the hydrogen bonds, therefore improving the binding affinity.[166]

Another cryo-EM study also revealed the structural information of Omicron RBD-ACE2 complex, which indicated a newly formed interaction between N477 and S19/Q24 of ACE2 not seen with the WT RBD. Besides the external connections with ACE2, the mutations of S371L, S373P, and S375F within a loop located in the core of the Omicron RBD reduced the main-chain connection.[166, 167] The conformational studies revealed the most significant conformational changes of binding interfaces between the Omicron variant and ACE2.

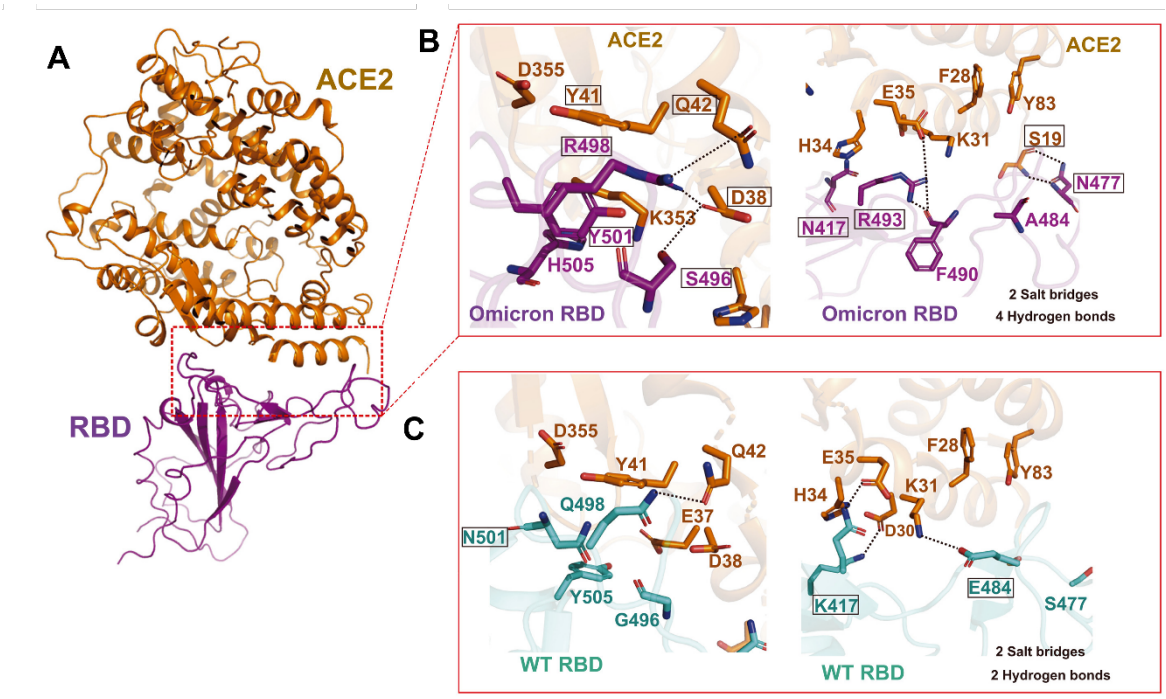

Figure 4.4 (A) Crystal structure of Omicron RBD-ACE2-complex. (B) Magnified view presenting the interactions between Omicron RBD and ACE2. (C) Magnified view presenting the interactions between WT RBD and ACE2.[168]

4.4 Methodologies for revealing the proteins interactions

4.4.1 X-ray crystallography

X-ray crystallography has become a powerful strategy to provide structural interaction details of proteins and macromolecules. Under x-ray beam exposure, diffraction patterns of the highly concentrated crystallized samples are measured to calculate the electron density of the structure. The structure model can then be deduced via optimization of the three dimension (3D) map.[169]

The X-ray crystallography structure experiment for revealing the details of interfaces between SARS-CoV-2 RBD and ACE2 was first performed in Mar 2020. Following the process of SARS-CoV-ACE2 complex crystallization, a study determined the structure of SARS-CoV-2-ACE2 complex to 2.68 Å. Compared to SARS-CoV, SARS-CoV-2 created a larger attachable interface with ACE2, mainly contributed from the loops interactions with ACE2 ridge with a disulfide bond, resulting in a notable conformational alteration. With a main chain hydrogen bond addition between N487 and A475, the loop became closer to its receptor.[170]

In recent months, several structural studies showed the information for viral interactions with its receptor, which further revealed the conformational alterations of SARS-CoV-2 at atomic level. However, the difficult sample preparation process still limited the usage of X-ray crystallography.

4.4.2 Electron cryo-microscopy (Cryo-EM)

The development of Cryo-EM also facilitated structural determination by providing more structural details. The major benefit of Cryo-EM over X-ray crystallography is the structure could be visualized via thin film compared to crystallizing proteins. The rapid development of cryo-EM technology may provide a strong structural basis for evaluating protein interactions and antibodies responses.[171]

Multiple comparative experiments have been conducted for indicating the potential targets for special antibodies designation and highlighting the special viral features of SARS-CoV-2, such as the overall structure similarities among SARS-CoV, MERS-CoV, and SARS-CoV-2. From Cryo-EM structures, an inherently flexible RBD has been identified all three viruses, supporting viral entry. A study emphasized the vital regions of SARS-CoV-2 RBD including T470-T478 loop and point residue Y505, which displayed remarkable characteristics for binding to ACE2.[172-174] In addition, the crucial functions of S2 subunit accompanied with glycans were explored. Critically, researchers found that due to the ability of glycans to prevent the accessible surface of state transition, they might protect the S2 subunit from the recognition of antibodies. The glycans also played functions in facilitating membrane fusion steps.[175] Besides the crystal structure of S protein at prefusion and postfusion state, the overall Cryo-EM structure also revealed an intermedium state. These findings helped to understand mRNA replication circles of CoV.[176]

Cryo-EM can also be utilized for detecting the immune potential of mAbs, especially the neutralizing sensitivity for the continuous evolution of variants. The Beta and Gamma variants containing point mutation at E484 were generally regarded as having notable immune escape properties. However, the Cryo-EM structures exhibited different immune responses between the Beta and Gamma variants, mainly caused by the NTD mutations, in which the Gamma variant displayed higher immune sensitivities.[177] More recently, structures of several antibodies interfaces with the Omicron variant were displayed via Cryo-EM. Due to multiple mutations within the RBD of the Omicron variant, the mAbs directly targeting RBD demonstrated significant escape ability.[178]

Taken together, Cryo-EM structures can display the effects of extended mutations on viral conformations and mAbs activities. However, Cryo-EM with the size limitation of proteins could only show the static structure of SARS-CoV-2 and its binding complexes, the in-solution conformation was still unrevealed.

4.4.3 Kinetics and thermodynamics

Studying binding kinetics of viral glycoproteins may provide insights for understanding the infectivity and spread of viruses. Several strategies have been applied for evaluating the binding affinity between SARS-CoV-2 S/RBD and ACE2. The binding process between proteins is a rate limiting step. Smoluchowski equation[179] firstly proposed the reactive collision rate between two systematic spherical particles in solution. Surface plasmon resonance (SPR), Bio-layer interferometry (BLI), and Enzyme-linked

immunosorbent assay (ELISA) are the most general methodologies permitting precise binding kinetics.

As SARS-CoV-2 continuously evolved, the behaviors of emerging strains have been investigated. Specifically, a study quantified the impact of existing single/combined mutations within RBD among Alpha, Beta, and Gamma, and general mutated ACE2, on binding kinetics. To simulate the physiological conditions, the experiments in this study were conducted at 37°C. The kinetic and equilibrium constants were correlated with pH and temperature. The results indicated that, most mutations performed higher binding affinity with ACE2 except for the point mutation at K417N. Furthermore, S477N (within the Omicron variant) and N501Y in several VOCs not only contributed to higher binding but also to improved transmission.[180] Another study selecting BLI built a 1:1 molar ratio binding model at pH 7.4, and the results also demonstrated reduced binding kinetics for the mutation K417N, while the other mutations such as E484K displayed a minimal effect on the binding properties.[181] To investigate the binding affinity to ACE2 of more recent variants, data for WT, Delta and Omicron variants were compared. According to ELISA results, Delta displayed the highest affinity, while much weaker binding was observed for Omicron.[182] Another study mentioned the point mutation S477N within Omicron induced a 37-fold increment for binding affinity to ACE2. Combined with the other mutations such as Q498R and N501Y that causes tighter binding, the targeting capability of the Omicron variant towards ACE2 is retained.[167]

In summary, with the natural evolution of variants, the point mutations located inside RBD could increase or decrease the viral fitness for survival. For the combined mutations, the variants maintained binding potential with ACE2, which was beneficial for viral spread. Revealing the binding kinetics would be helpful for providing an explanation for the rebalance of viral attachment with ACE2.

4.4.4 Molecular dynamics (MD) simulation

The computer simulations are useful for displaying protein interactions at the atomic level, especially emphasizing the effect of single amino acid on protein structure. MD simulation can reveal the direct and indirect interfaces between proteins such as charge influences, which are invisible from the crystal structures. The single residue within "hot spots" can be altered and then predict its possible causes for the change in binding affinity, which would be an advanced means for predicting the development of mutations.

As a mutation firstly presented a rapid spread in the population, the complex model of the Alpha RBD-ACE2 was built and used for determining its molecular mechanism. The complex arrangement for environmental transformation was accomplished during 185-ns MD simulation. WT RBD binding complex indicated the interfaces containing fragment A475-N487 and external hydrogen bonds at the residue N501. While Alpha RBD increased a π stacking interaction with ACE2, which was consistent with the x-ray structure.[183] Another study described an extremely flexible loop, which comprised three naturally emerged mutations T478I, S477N, and V483A, at unbound state. This loop was undetected from several Cryo-EM structures, suggesting higher bioactivity and conformational

dynamics. Therefore, building the whole structural models with the loop demonstrated the significant impacts on current and ongoing mutations.[184]

To detect the binding profiles towards ACE2, a recent study compared the interactions of WT, the Delta, and Omicron RBD with ACE2. MD simulation described slight changes caused mostly by point mutations inside RBD, while mainly displaying the effects on their binding with mAbs. The mutation at L452R indirectly enhanced a hydrogen bond at Q493, and further stabilized the side chain of RBD. As a heavily mutated variant, Omicron was observed with two additional salt bridges with ACE2, which also emphasized the special binding functions of Q493R.[185] Besides evaluating the properties of the existing variants, MD study was utilized for prediction of possible functions of mutations, which might be helpful for epidemic prevention.[186]

4.5 Hydrogen/deuterium exchange mass spectrometry (HDX-MS)

4.5.1 Development of HDX

HDX is a well-developed strategy with significant benefits for detecting the conformational dynamics and protein interactions. This methodology focused on isotopic labeling could be traced to the study of Linderstrøm-Lang in the 1950s.[187] With the recognition of protein secondary structure as α-helix and β-sheet, HDX was initially used for testing the kinetics of proteins[188] and their inner hydrogen interactions.[189] In the early days of HDX development, it was combined with nuclear magnetic resonance (NMR), as a detecto.[190] Since the late 1980s, as methodologies for obtention ionization, Matrix Assisted Laser Desorption/Ionization (MALDI) and Electrospray Ionization (ESI) were

selected and cooperated with LC separations and pH adjustment for quenching.[191, 192] Due to the leading contribution, these two methodologies making outstanding macromolecular detection possible were awarded for Nobel Prize in 2002. The LC-MS-based strategy has the most significant advances superior to NMR for achieving HDX measurement, gradually became a useful mean for structural biological studies. HDX is able to break the limitations of cryo-EM size constraints, although unable to perform atomic resolution. It can also provide conformational dynamic details, which is a dramatic improvement compared to the classic X-ray crystallography strategy, especially for the utilization in protein studies.

4.5.2 HDX conception

The exchange of amide backbone within protein is directly correlated with the structural dynamics, which can be further studied for revealing the effects on biological functions of proteins.[193] All the sites containing the labile hydrogens are possible for exchange to occur, however, HDX mainly focuses on recording the exchange of -NH located in the peptide backbone due to the uniform distribution and hydrogen bonds formation. Besides, the quenching process with pH variation can be rapidly accomplished at different time points of exchange for the amide backbones.[194]

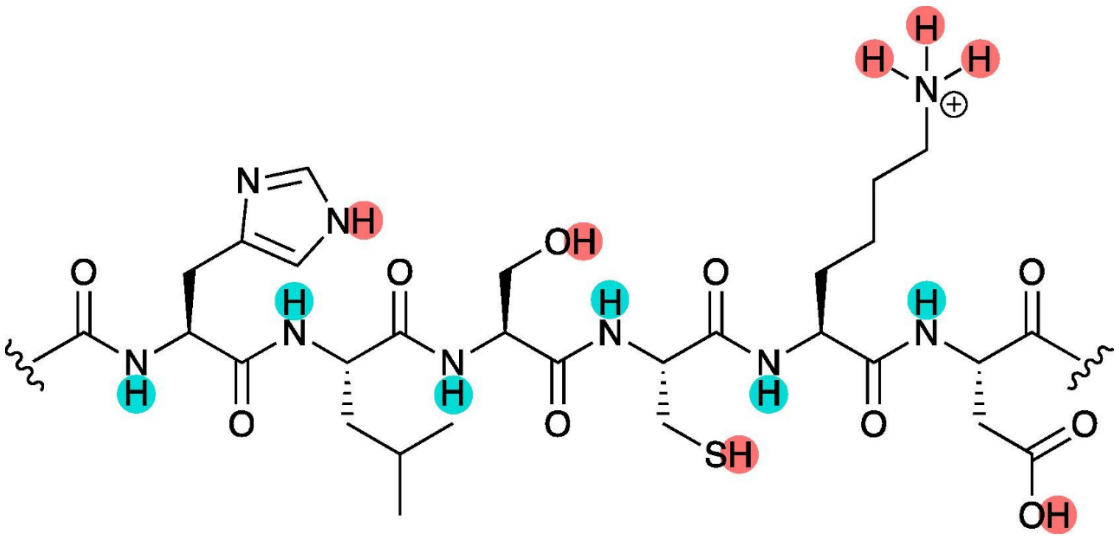

Figure 4.5 Presenting the hydrogen types. Hydrogens at amide backbones were labeled in cyan and side chain hydrogens as grapefruit color.[195]

Multiple parameters determine the exchange rate of HDX, such as pH, temperature, and the polarity of samples. The definition of pH_{min} is the lowest deuterium exchange with similar acid- and base-catalyzed rate, at the range of 2.5-3. Both the pH increment and decrement contributed to a higher exchange rate. Another vital factor affecting exchange is temperature, which is positively related to the exchange rate. Compared to 0 °C, about 14-fold increment in exchange is observed, at 25 °C.

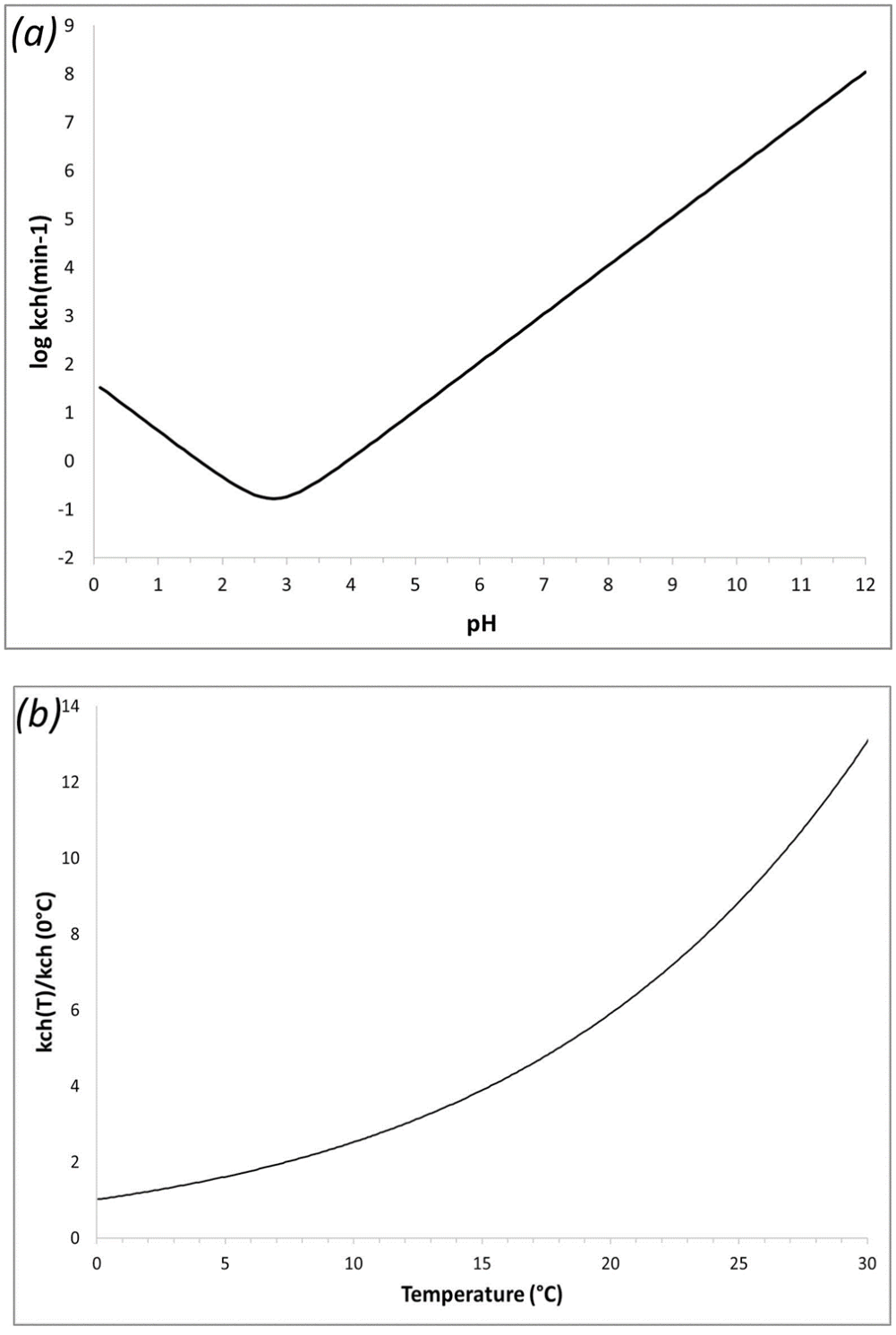

Figure 4.6 Factors affecting the exchange rate of (a) pH and (b) temperature.[195]

Linderstrøm-Lang had developed the HDX model with proposal of two steps for achieving exchange. Two states of amides were indicated, as -NH (close) state of solvent inaccessibility and exchange attainable at -NH (open) state, respectively. However, the proteins with high bioactivity can lead to the structural unfolding and therefore resulting in the state transformation between -NH (close) and -NH (open) state. The HDX kinetics were displayed as following:

$$NH_{\text{closed}} \underset{K_{cl}}{\overset{K_{op}}{\rightleftharpoons}} NH_{\text{open}} \xrightarrow{K_{ch}} ND_{open} \underset{K_{op}}{\overset{K_{cl}}{\rightleftharpoons}} ND_{\text{closed}}$$

K_{op} and K_{cl} are responsible for the rate constants at opened and closed states, while K_{ch} is the intrinsic exchanging rate. The exchange equation was proposed as following:

$$k_{\text{HDX}} = \frac{k_{\text{op}} \times k_{\text{ch}}}{k_{\text{op}} + k_{\text{cl}} + k_{\text{ch}}} = K_{\text{op}} k_{\text{ch}}$$

The observed exchange rate is mainly determined by the rate of proteins back to the closed state. With the kinetic limitations, there are two kinetics, EX1 and EX2. EX1 displays two recognizable mass sections for peak distribution, while EX2 displays a steady increment in mass. EX2 is preferable and more commonly used for observing the exchanges under natural conditions, but in contrast EX1 involves in less frequent envelopes.[196] The two distinct steps in HDX are widely accepted for investigating the conformational dynamics of proteins.

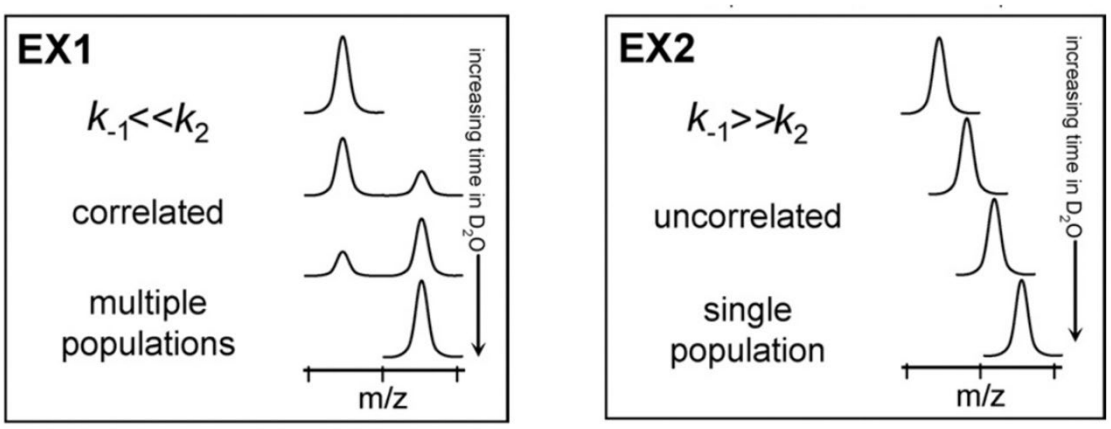

Figure 4.7 The performances of two different kinetic limits, EX1 and EX2.[197]

4.5.3 HDX workflow

4.5.3.1 HDX-MS

Various workflows would be applied depending on the different protein types and monitoring detectors but ultimately HDX-MS employs the same sample preparation process. After protein expression and purification, the highly pure protein samples undergo labeling. Deuterium labeling is conducted by diluting protein samples in 10-fold deuterium buffer, resulting in isotopic exchange of hydrogens located on the proteins. Subsequently, adjusting the final pH to 2.5 is accomplished by adding a quenching buffer which mainly consists of acid, while denatured ingredients can be added. The quenched samples can be injected into MS for studying the local HDX (online digestion) or can be digested by various enzymes before MS detection. These two methods are referred to as global (protein detection) and local HDX (peptide detection) respectively (Figure 4.8). Ultra-performance liquid chromatography (UPLC) separation can be added before MS detection, with the desalting process via trap column and then performing separation via C_4 or C_{18} column.

As MS detectors, time-of-flight (TOF) and orbitrap are the most general instruments for analyzing.

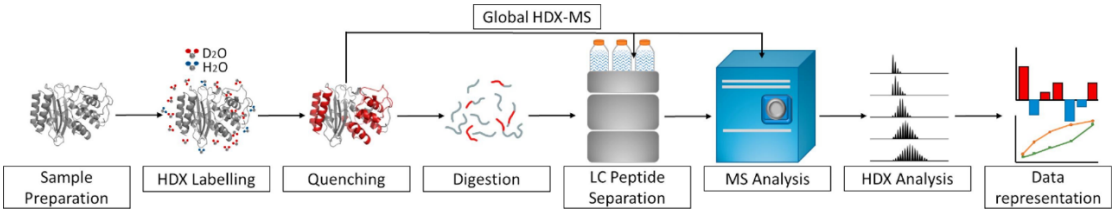

Figure 4. 8 The workflow of global/local HDX-MS.[195]

4.5.3.2 Mass spectrometry

To achieve high-resolution detection, ESI (including nano-ESI) and MALDI are ionization techniques mainly used for achieving soft ionization. Besides, ion mobility (IM) enables full recognition of the isotopically labeled peptides using size separation, and therefore is often combined and utilized with MS detector. First developed by Waters, it could dramatically improve the separation efficiency while allowing real-time observation, which is especially useful for structural studies .[198, 199] Another methodology providing less back exchanges for peptides separation was capillary electrophoresis (CE), which isolate peptides by charges and size. Recently, a study demonstrated a more rapid approach with high digestion efficiency of bovine hemoglobin using CE-ESI compared to UPLC platform. Therefore, CE based separation might achieve a higher deuterated level and more reliable results with the decreased back exchange due to the faster process.[200]

4.5.3.3 Deuterium labeling

There are two labeling approaches named on exchange and off exchange. On-exchange is a straightforward and more widely accepted strategy for labeling within the chosen timeframe. In contrast, off-exchange is a less frequently selected method, which records the reduced mass for the fully deuterated proteins or peptides in the H_2O buffer.[201, 202]

It was worth to mention that, depending on the different purposes of studies, pulse labelling could be utilized in HDX. It is used for recording the folding transition and inter-medium state of proteins, while continuous labelling reveals the conformational dynamics of the same proteins at various states.[203] Continuous labelling follows classic workflow with different labelling periods and quenching at pH 2.5/0 °C.[201] However, pulse labelling exhibits at the fixed period starting from deuterium labelling, therefore, each time scale with unique conformation is attributed for exploring the folding mechanisms of proteins.[204]

4.5.3.4 Bottom-up and top-down

The fragmentation process of local HDX for the labelled proteins can be classified into bottom-up proteolytic digestion and top-down gas-phase formation. Bottom-up with online/offline proteolytic digestion is a well-developed and widely used method compared to the top-down method. In this step, pepsin is the predominant choice due to its acid-stable properties and extraordinary performance at 0 °C.[205] In addition, protease XIII designed as dual functional proteases together with pepsin is observed to have well sequence coverage, resulting in a better digested performance for online digestion.[206] Online digestion

following LC separation and MS recording can be accomplished via a lower sample dosage but carryover can be a problem of concern.[207]

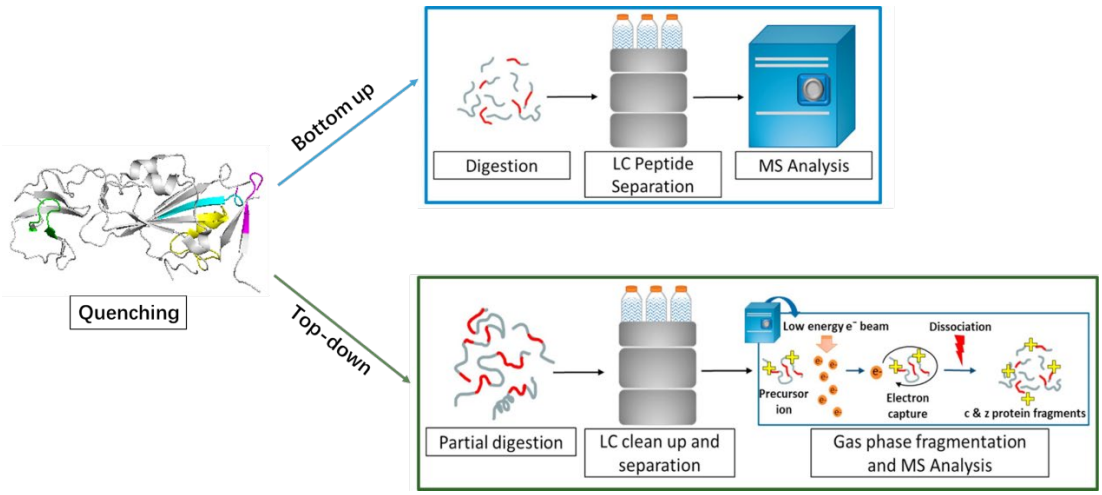

Figure 4.9 The workflow of bottom-up and top-down methods.[195]

4.5.3.5 Data analysis

With the development of computational technologies, data analysis as a vital section for HDX study is currently trending towards automated systems. Nonetheless, the manual data analysis process remains critical for verification the misrecognition by software processing.[208, 209] At the beginning of data analysis, the digested peptide list should be identified, depending on the software verification, such as ExPASy and FindPept. These software could provide a peptide list with MS/MS sequencing as supporting materials, for further targeting peptides analysis.[210, 211] With the peptides list, the deuterium uptake level for each obtained peptide could then be recorded and calculated by many software (e.g. DynamX, HDX Workbench, HDExaminer, etc.) With the relative deuterium uptake for

peptides at different states, it could be conducted for data interpretation, and therefore deduced several novel findings.[212]

4.5.3.6 Limitations and opportunities

HDX-MS is a powerful technique that is able to reveal important information on the in-solution conformational dynamics of proteins. This technique shows several advantages over conventional techniques for studying protein structures, e.g., X-ray crystallography and NMR, including less limitation in protein size, higher tolerance to sample purities, requiring only a minimal amount of samples and eliminating the labor-intensive quality protein crystal preparation.[213] Obviously, software development has revolutionized and changed the utilization of HDX-MS, resulting in a more reliable and rapid methodology for data processing and further creating advancements for the acquisition of more conformational information.

There remain several shortcomings of concern: 1) LC separation may lead to retention for minutes of several peptides and then cause back exchange.[214] 2) Due to the acid tolerance limitations, few proteases can perform regular digested functions. The proteases display weak digested capacity for proteins with several disulfide bonds, which is still a great challenge for HDX.[215] 3) The analysis of hydrophobic membrane proteins is another considerable challenge.[216]

4.6 Objectives

Currently, the whole world is still suffering from COVID-19, with the impact wave of the pandemic coming one after another. The numbers of infected and dead people continue to surge, causing great economic loss to the world and dramatic changes to our living styles. Even though vaccination has been commonly applied, there are still many uncertainties, and it has been proposed that SARS-CoV-2, the causative agent of COVID-19, may co-exist with humans for the long term. More seriously, the evolution of SARS-CoV-2 has led to the emergence of various variants, and some of the variants were found to have the properties such as higher transmission and infectivity, as well as immune escape from the vaccines. To combat the pandemic and develop the drugs and vaccines, it is necessary to have a good understanding of the molecular mechanism of evolutionary properties of the SARS-CoV-2 variants, which is still lacking now.

In this project, we focused on the key elements and steps of SARS-CoV-2 infection, i.e., SARS-CoV-2 RBD and its interaction with the host receptor ACE2, and used hydrogen/deuterium exchange mass spectrometry (HDX-MS) to provide unique information about the effects of SARS-CoV-2 variants on conformational dynamics of RBSs and their interaction with ACE2. The outcomes of this project will allow us to obtain insights into the molecular mechanism of SARS-CoV-2 variant infection, understand the relation of the conformational dynamics changes with the evolutionary properties (e.g., transmission and infectivity) of SARS-CoV-2 variants, and provide valuable information for the design of drugs and vaccines against SARS-CoV-2 variants.

Chapter 5. Materials and Methods

5.1 Protein preparation and characterization

RBD and its variants were expressed according to the literature.[105, 217] The same length (residues 319-591, GenBank: P0DTC2) of wild type (WT), the Alpha, Beta, Zeta, Kappa, and Delta RBD were expressed with HEK293 cells, and Omicron (residues 319-541, GenBank: P0DTC2) was expressed by HEK293 cells. The mutations within various RBDs were described in Table 6.1. The recombinant proteins contained his & avi tag and Omicron with his tags at the C-terminus. The expression system of human ACE2 (fragments Gln18-Ser740, GenBank: Q9BYF1) was expressed by using CHO cell line. All the proteins were obtained from Genscript (Singapore).

5.2 Protein characterization

After expression, all proteins were purified with sodium dodecyl-sulfate polyacrylamide gel electrophoresis (SDS-PAGE) certification, and then transferred into phosphate-buffered saline for maintaining similar pH at 7.4 as human body condition. The concentration of samples was determined by using Bradford Protein Assay, in which BSA played a function as standard. The purification was assessed by SDS-PAGE, supporting for over 95% purity.[218] WT RBD and its variants at 1 μg/mL were certified with a high binding activity with ACE2, which was tested by enzyme-linked immunosorbent assay (ELISA).[219] All the proteins were obtained from Genscript (Singapore).

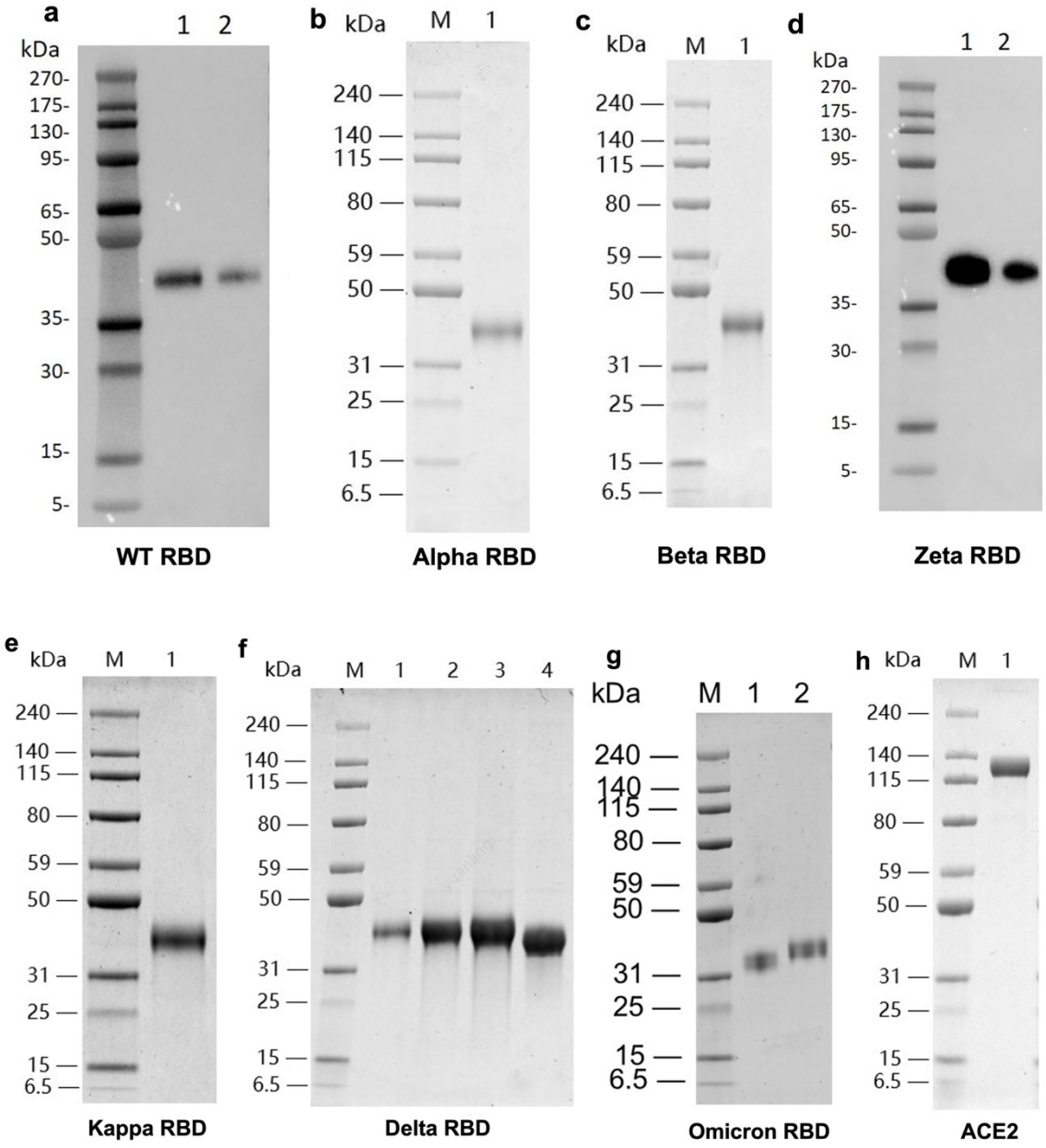

Figure 5.1 The purification of RBDs.

The purification was certified as > 95% of (a) the WT RBD; (b) the Alpha RBD; (c) the Beta RBD; (d) the Zeta RBD; (e) the Kappa RBD; (f) the Delta RBD; (g) the Omicron RBD; and (h) ACE2, via SDS-PAGE.

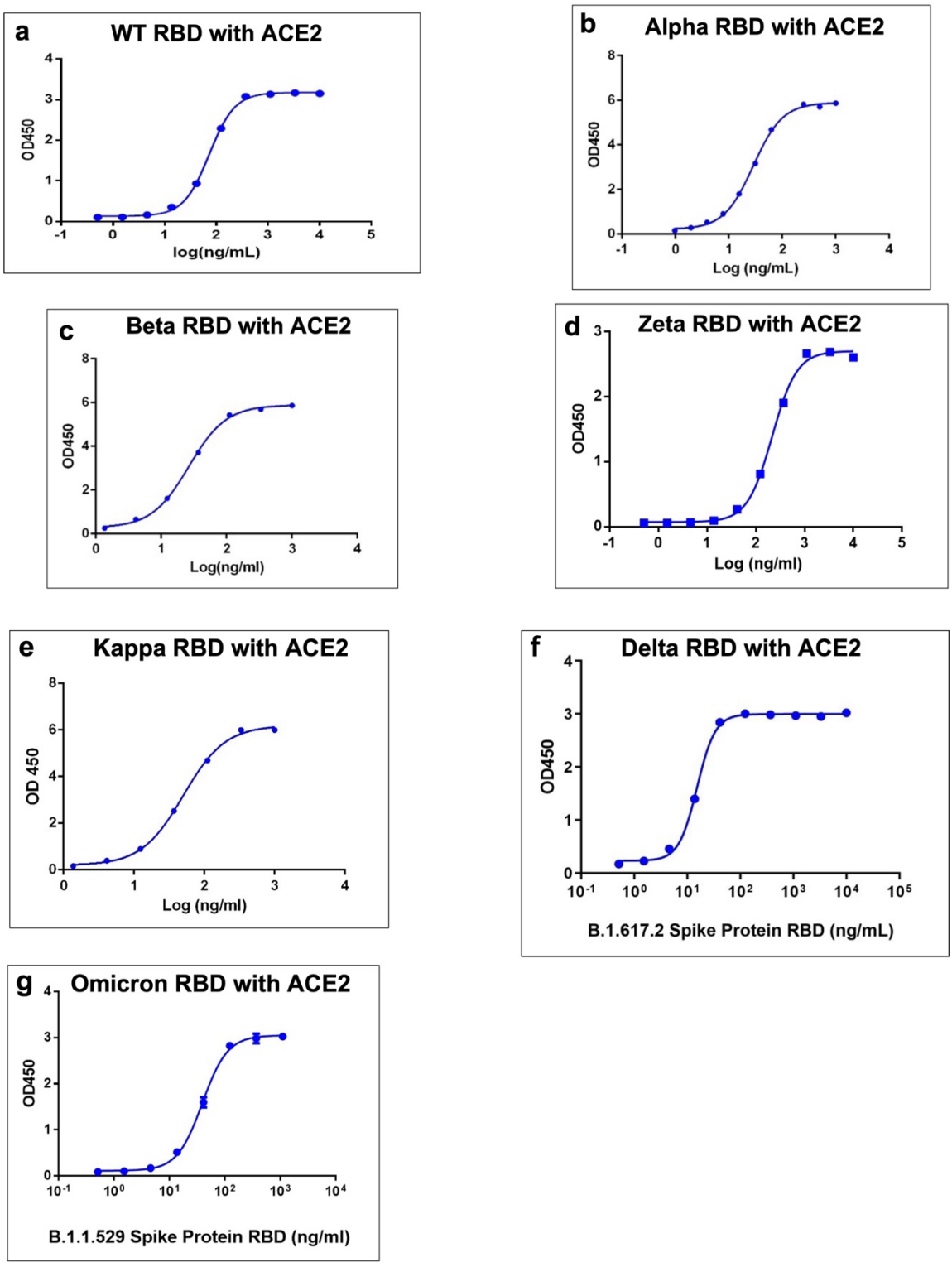

Figure 5.2 Binding potential analysis of RBDs.

Binding potential analysis of (a) WT RBD; (b) the Alpha RBD; (c) the Beta RBD; (d) the Zeta RBD; (e) the Kappa RBD; (f) the Delta RBD; and (g) the Omicron RBD, with ACE2.

5.3 HDX-MS

5.3.1 HDX

The acquisition of RBDs-ACE2-complex was conducted, seven RBDs with various concentrations respectively were diluted to 15 μM, followed by gentle mixing with ACE2 at molar ratio of 1:1, for each RBD. On the basis of k_D value (0.566-31.4 nM) and the samples' concentration, the RBD-ACE2-complexes were calculated with more than 90% binding efficacy. RBDs and ACE2 were cultured in PBS (pH 7.4) at room temperature for 30 min with 500 rpm. Deuterium exchange was performed at room temperature, 45 μL of labelling (PBS buffer in D_2O, pD 7.4) was added into 5 μL of proteins. The protein samples of ACE2, RBDs, and RBD-ACE2-complex, respectively, were diluted by using deuterated PBS buffer for 1, 10, and 60 min. Control samples were prepared by dilution with normal PBS buffer. After exchange for selecting periods, reactions were quenched by 10 μL of prechilled 1.5 M GnHCl and 3.2% formic acid, resulting in the pH value around 2.5 and temperature at 0 °C. The obtained solution was then incubated 1 min for better protein denaturing, followed by LC-MS analysis.

5.3.2 LC-Mass Spectrometry

The quenched solution (50 μL, 30 pmol) was injected into a Waters nanoACQUITY UPLC combined to a Synapt G2-Si QTOF mass spectrometer system, manipulating the positive

ion and resolution mode with mass range of 50-2000 Da, at 0 ℃. The syringed samples were undergone online pepsin digestion (Waters BEH pepsin column, 300Å, 5 μm, 2.1 mm x 30 mm). The desalted processing (Waters BEH C18 trap column, 130 Å, 5 μm, 300 μm × 50 mm) was applied for better MS signal, flowing with 0.1% formic acid for 3 min at 100 μL/min. Then, the digested peptides were eluted via reverse phase Waters UPLC BEH C18 column (130Å, 1.7 μm, 2.1 mm × 100 mm), flowing with ACN gradient of 5-40% with 0.1% formic acid as solvent B, at 60 μL/min for 12 min. Pepsin washing (1.5 M guanidine hydrochloride, 4% acetonitrile, 0.8% formic acid, pH 2.5) was used for three times after individual sample digestion and lockspray at 10 μL/min was selected as references for avoiding mass interferences. In this study, three replicates of each sample were under investigated.[217]

5.3.3 Data collection and analysis

To generate the peptide maps, the recorded proteins in MS^E mode without deuteration were selected for analysis, by using Waters ProteinLynx Global Server (PLGS, v3.0.2). Based on the protein sequence database, PLGS was used for peptides identification, performing with no specific protease. After that, the peptide lists from PLGS were analyzed by Waters DynamX 3.0, of which were filtered by following parameters.

1) the minimum PLGS score: 6.5

2) the minimum intensity: 4000

3) the minimum products per amino acids: 0.2

4) the selected eluting time: 3-7 min

The filtered peptides with over two out of three presenting in undeuterated samples were individually studied and reported, without back exchange correction. We detected all the peptides covering glycosylation sites including two of RBSs and eight of ACE2.

The fractional deuterium uptake showed the average deuterons level of exchanged peptides within the maximum exchangeable amides of the peptide. The relative uptake figures for proteins in unbound state and HDX plots were both recorded by Microsoft Excel via the analyzed data exporting from DynamX. To further monitor the structural dynamics, HDX with a 95% confidence interval (CI) was calculated and served as a significant change among HDX plots. The details for experiments were concluded in Tables 5.1-5.3 and shown as following.

5.3.4 Modelling for HDX-MS

Based on the previous processed HDX data, the relative fractional uptake of proteins was mapped onto different crystal models of proteins through PyMol 2.0.7 (Schrodinger, LLC). The Cryo-EM structures of full-length S trimers at closed position, Protein Data Bank (PDB) 6ZGE of WT, PDB 7R13 of Alpha, PDB 7VX1 of Beta, PDB 7DF3 of Zeta, PDB 7SBP of Kappa, PDB 7SBK of Delta, and PDB 7QO7 of Omicron were selected for modeling the individual conformation of RBDs in free state. The structures of RBD-ACE2-complexes, PDB 6M0J of WT, PDB 7EKF of Alpha, PDB 7EKG of Beta, PDB 6M0J of Zeta, PDB 7VX5 of Kappa, PDB 7W9I of Delta, and PDB 7WBL of Omicron were exhibited by using the crystal structures for RBD-ACE2-complexes.

Table 5.1 HDX summary for RBD wild type and its variants in free state

Data set	WT	Alpha	Beta	Zeta	Kappa	Delta	Omicron
HDX conditions	Phosphate buffer in 90% D_2O, pH 7.4, room temperature						
HDX time (min)	1 min, 10 min, and 60 min						
Number of peptides	116	127	130	124	130	155	99
Sequence coverage	100%	98.7%	100%	100%	98.5%	100%	90.1%
Average peptide length	15.2	14.8	14.7	15.6	15.4	18.6	21.3
Redundancy	6.53	7.39	7.26	6.98	7.44	10.45	10.54
Replicates	3						

Table 5.2 HDX summary for RBD wild type and its variants upon binding to ACE2.

Data set	WT	Alpha	Beta	Zeta	Kappa	Delta	Omicron
HDX conditions	Phosphate buffer in 90% D_2O, pH 7.4, room temperature						
HDX time (min)	1 min, 10 min, and 60 min						
Number of peptides	81	71	81	86	105	82	62
Sequence coverage	97.1%	92.3%	96.7%	97.4%	98.2%	96%	87%
Average peptide length	16.4	16.1	16.5	16.2	16.8	15.0	20.3
Redundancy	5	4.54	5.07	5.22	6.57	6.34	6.5
Replicates	3						
Significant differences in HDX (ΔHDX > X D)	0.23	0.29	0.27	0.27	0.24	0.22	0.25

`

Table 5.3 HDX summary for ACE2 upon binding to different types of RBD.

Data set	ACE2	WT	Alpha	Beta	Zeta	Kappa	Delta
HDX conditions	Phosphate buffer in 90% D_2O, pH 7.4, room temperature						
HDX time (min)	1 min, 10 min, and 60 min						
Number of peptides	299	162	166	163	154	153	128
Sequence coverage	99.2%	87.4%	87.4%	89.3%	81.3%	82%	82.3%
Average peptide length	12.5	13.8	13.9	13.8	13.7	13.4	15.6
Redundancy	5.23	3.54	3.65	3.47	3.59	3.46	2.98
Replicates	3						
Significant differences in HDX (ΔHDX > X D)	NA	0.23	0.21	0.19	0.2	0.18	0.15

Chapter 6. Results and discussion

6.1 Introduction

The emergence of SARS-CoV-2 variants is causing grave difficulties for the whole world. Developing new vaccines and drugs, particularly targeting variants, crucially depends on a good understanding of the structural details of the emerged variants. In this project, we will apply HDX-MS to investigate conformational dynamics of SARS-CoV-2 RBD and its variants, as well as their interactions with ACE2. Since RBD played a vital function in binding to the human receptor, many researchers focused on exploring the interaction of RBD or S1 and ACE2. Recently, a study reported the conformational dynamic of S trimer at in-solution prefusion and postfusion state by using HDX-MS. They investigated unbound long-range allosteric propagation of wild type S trimer, and interestingly, after ACE2 interaction, S2 subunit exhibited the significant conformational changes.[220] As a driver of membrane fusion, the conformational changes of S2 subunit may accelerate cell fusion and facilitate vital attachment. In this project, we aim to develop an HDX-MS based methodology to detect the differences in allosteric propagation for ACE2, with binding to the emerged variants.

Due to the infectious advantages and natural selection, the widespread variants in the population may affect the effectiveness of existed vaccines. The determination of possible interactions between RBD and its mutants with ACE2 could show the hotspots for the binding of vaccines and antibodies targeting RBD. It performed the changes of flexible

fragments in RBD and provided strong support to predict the possible escape of mutations from current therapy.

Recently, several crystal structures of WT RBD and newly emerged variants, such as Delta and Omicron, have been revealed via Cryo-EM and X-ray crystallography.[157, 178, 221] Our understanding of viral entry mechanisms was mainly prescribed from static details, there were few studies displaying conformational alterations. Therefore, our study would be crucial for guiding the insights of viral interfaces and additional potential "hotspots" for vaccine development.

```
319 RVQPTESIVR  FPNITNLCPF  GEVFNATRFA  SVYAWNRKRI  SNCVADYSVL  YNSASFSTFK
379 CYGVSPTKLN  DLCFTNVYAD  SFVIRGDEVR  QIAPGQTGKI  ADYNYKLPDD  FTGCVIAWNS
439 NNLDSKVGGN  YNYLYRLFRK  SNLKPFERDI  STEIYQAGST  PCNGVEGFNC  YFPLQSYGFQ
499 PTNGVGYQPY  RVVVLSFELL  HAPATVCGPK  KSTNLVKNKC  VNFNFNGLTG  TGVLTESNKK
559 FLPFQQFGRD  IADTTDAVRD  PQTLEILDIT  PCS
```

Figure 6.1 Sequence identification of wild type RBD (residues 319-391).

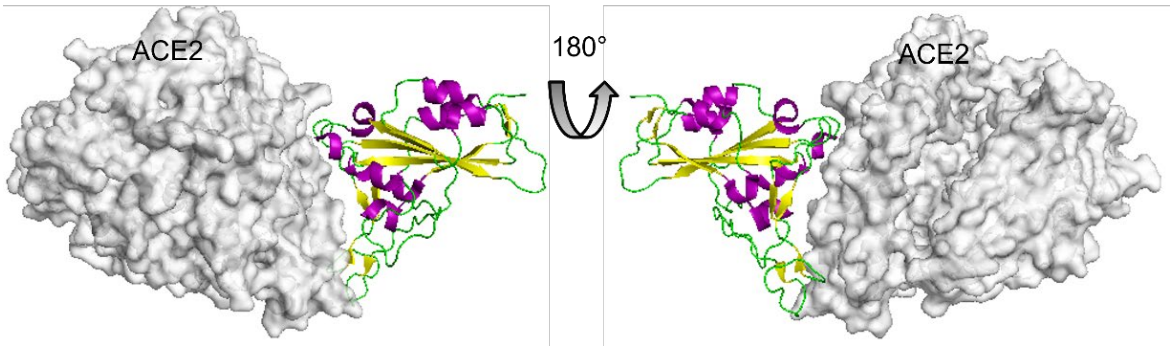

Figure 6.2 X-ray structure of RBD-ACE2-complex.

Loops in RBD are presented in green, purple for helix and yellow for sheet. (PDB ID: 6M0J)

Table 6.1 Residue mutations of several widely spread variants.

Name of variant	Lineage	First identified country	Mutations in RBD	Binding affinity with ACE2 (Dissociation constant, Kd)
Alpha	B.1.1.7	UK	**N501Y**	3.3 nM[181]
Beta	B.1.351	South Africa	**K417N**, **E484K**, and **N501Y**	6.5 nM[181]
Zeta	P.2	Brazil	**E484K**	11.3 nM[181]
Kappa	B.1.617.1	India	**L452R** and **E484Q**	25.0 nM[222]
Delta	B.1.617.2	India	**L452R** and **T478K**	25.1 nM[166]
Omicron	B.1.1.529	South Africa	G339D, S371L, S373P, S375F, **K417N**, N440K, G446S, S477N, **T478K**, **E484A**, Q493R, G496S, Q498R, **N501Y**, and Y505H	31.4 nM[166]

In the chapter, the effects of the major SARS-CoV-2 variants on the conformational dynamics of the RBD and its interaction with ACE2 would be revealed. Therefore, we

deeply investigated the relations between the conformational dynamics changes and the evolutionary properties.

6.2 The local flexibility of WT RBD and its variants (early emerged strains)

To explore the structural features of various variants of SARS-CoV-2, the same length of RBDs were purchased from Genscript (U.S.A.), which were certified with over 95% purity and confirmed by SDS-PAGE (Figure 5.1). In the study, to deeply reveal the internal association between conformational dynamics and viral spread of SARS-CoV-2, HDX-MS was selected for comparing the structural dynamics of wild type RBD and its mutants. With online pepsin digestion, deuterium exchanged peptides were obtained and analyzed by using LC-MS. The coverage maps of RBDs in free state were shown in Figure 6.3 and the profile presenting the differences in deuterium uptake of WT RBD and its mutants for 1 min deuterium exposure was shown as Figure 6.4. The same length of RBDs (residues 319-591) were undergone online pepsin digestion, generating over 100 peptides with high signal to noise ratios. Although RBDs contained two glycosylation sites at N331 and N343, the overall sequence coverage has arrived 95% with good redundancy.

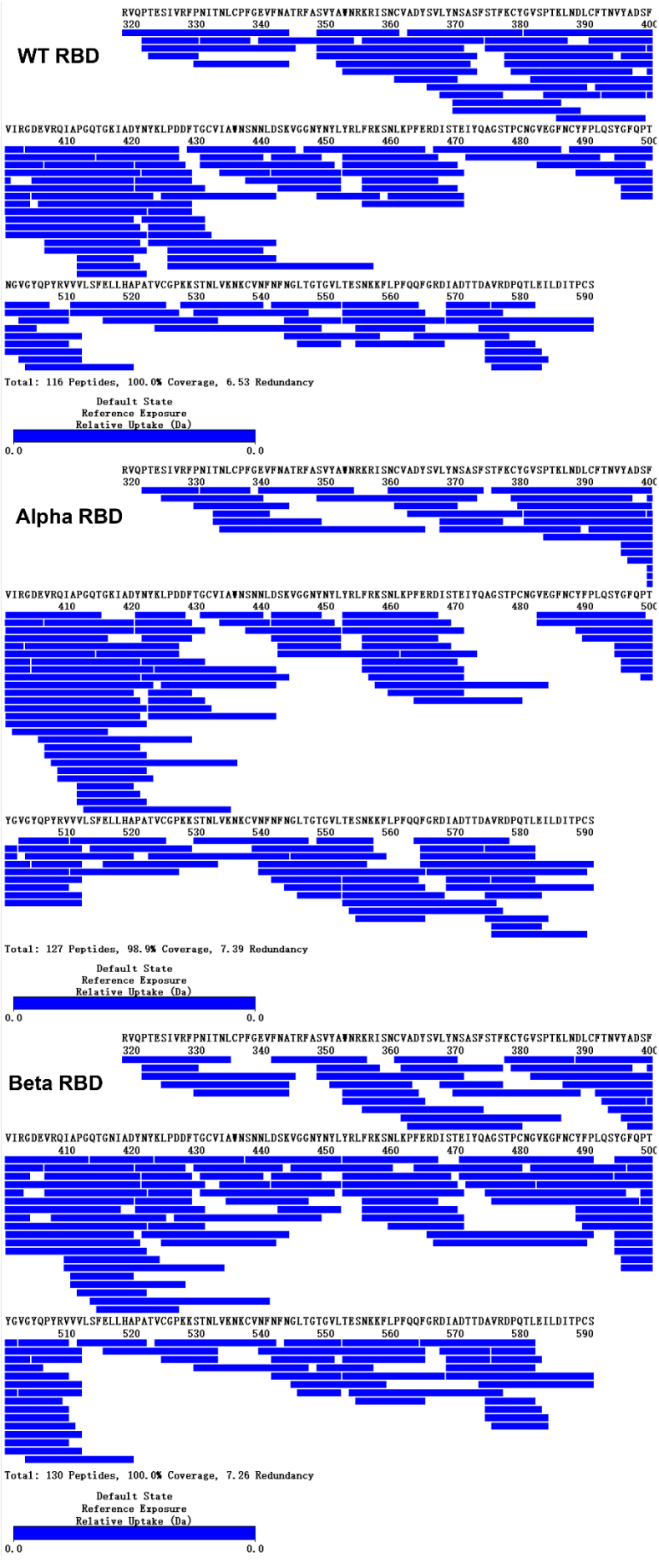
WT RBD
RVQPTESIVRFPNITNLCPFGEVFNATRFASVYAWNRKRISNCVADYSVLYNSASFSTFKCYGVSPTKLNDLCFTNVYADSF
320 330 340 350 360 370 380 390 400
VIRGDEVRQIAPGQTGKIADYNYKLPDDFTGCVIAWNSNNLDSKVGGNYNYLYRLFRKSNLKPFERDISTEIYQAGSTPCNGVEGFNCYFPLQSYGFQPT
410 420 430 440 450 460 470 480 490 500
NGVGYQPYRVVVLSFELLHAPATVCGPKKSTNLVKNKCVNFNFNGLTGTGVLTESNKKFLPFQQFGRDIADTTDAVRDPQTLEILDITPCS
510 520 530 540 550 560 570 580 590
Total: 116 Peptides, 100.0% Coverage, 6.53 Redundancy
Default State
Reference Exposure
Relative Uptake (Da)
0.0
0.0
Alpha RBD
RVQPTESIVRFPNITNLCPFGEVFNATRFASVYAWNRKRISNCVADYSVLYNSASFSTFKCYGVSPTKLNDLCFTNVYADSF
320 330 340 350 360 370 380 390 400
VIRGDEVRQIAPGQTGKIADYNYKLPDDFTGCVIAWNSNNLDSKVGGNYNYLYRLFRKSNLKPFERDISTEIYQAGSTPCNGVEGFNCYFPLQSYGFQPT
410 420 430 440 450 460 470 480 490 500
YGVGYQPYRVVVLSFELLHAPATVCGPKKSTNLVKNKCVNFNFNGLTGTGVLTESNKKFLPFQQFGRDIADTTDAVRDPQTLEILDITPCS
510 520 530 540 550 560 570 580 590
Total: 127 Peptides, 98.9% Coverage, 7.39 Redundancy
Default State
Reference Exposure
Relative Uptake (Da)
0.0
0.0
Beta RBD
RVQPTESIVRFPNITNLCPFGEVFNATRFASVYAWNRKRISNCVADYSVLYNSASFSTFKCYGVSPTKLNDLCFTNVYADSF
320 330 340 350 360 370 380 390 400
VIRGDEVRQIAPGQTGNIADYNYKLPDDFTGCVIAWNSNNLDSKVGGNYNYLYRLFRKSNLKPFERDISTEIYQAGSTPCNGVKGFNCYFPLQSYGFQPT
410 420 430 440 450 460 470 480 490 500
YGVGYQPYRVVVLSFELLHAPATVCGPKKSTNLVKNKCVNFNFNGLTGTGVLTESNKKFLPFQQFGRDIADTTDAVRDPQTLEILDITPCS
510 520 530 540 550 560 570 580 590
Total: 130 Peptides, 100.0% Coverage, 7.26 Redundancy
Default State
Reference Exposure
Relative Uptake (Da)
0.0
0.0


Zeta RBD
RVQPTESIVRFPNITNLCPFGEVFNATRFASVYAWNRKRISNCVADYSVLYNSASFSTFKCYGVSPTKLNDLCFTNVYADSF
320 330 340 350 360 370 380 390 400
VIRGDEVRQIAPGQTGKIADYNYKLPDDFTGCVIAWNSNNLDSKVGGNYNYLYRLFRKSNLKPFERDISTEIYQAGSTPCNGVKGFNCYFPLQSYGFQPT
410 420 430 440 450 460 470 480 490 500
NGVGYQPYRVVVLSFELLHAPATVCGPKKSTNLVKNKCVNFNFNGLTGTGVLTESNKKFLPFQQFGRDIADTTDAVRDPQTLEILDITPCS
510 520 530 540 550 560 570 580 590
Total: 124 Peptides, 100.0% Coverage, 6.98 Redundancy
Default State
Reference Exposure
Relative Uptake (Da)
0.0
0.0

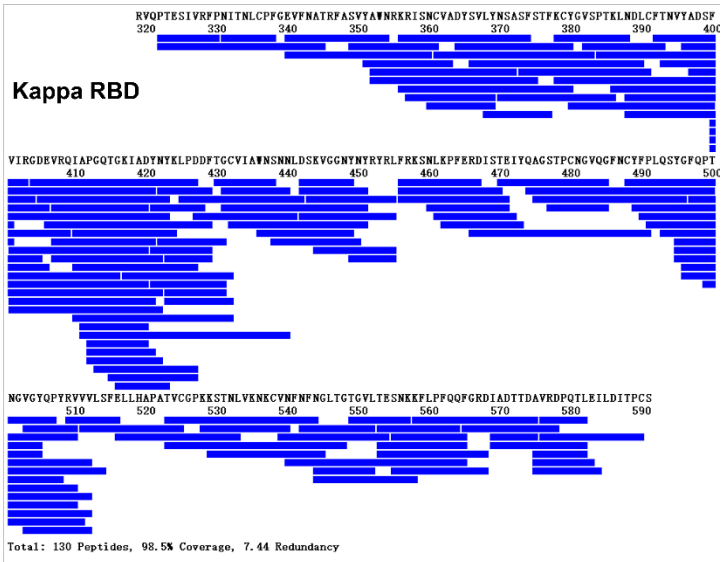
Kappa RBD
RVQPTESIVRFPNITNLCPFGEVFNATRFASVYAWNRKRISNCVADYSVLYNSASFSTFKCYGVSPTKLNDLCFTNVYADSF
320 330 340 350 360 370 380 390 400
VIRGDEVRQIAPGQTGKIADYNYKLPDDFTGCVIAWNSNNLDSKVGGNYNYRYRLFRKSNLKPFERDISTEIYQAGSTPCNGVQGFNCYFPLQSYGFQPT
410 420 430 440 450 460 470 480 490 500
NGVGYQPYRVVVLSFELLHAPATVCGPKKSTNLVKNKCVNFNFNGLTGTGVLTESNKKFLPFQQFGRDIADTTDAVRDPQTLEILDITPCS
510 520 530 540 550 560 570 580 590
Total: 130 Peptides, 98.5% Coverage, 7.44 Redundancy
Default State
Reference Exposure
Relative Uptake (Da)
0.0
0.0


Delta RBD
RVQPTESIVRFPNITNLCPFGEVFNATRFASVYAWNRKRISNCVADYSVLYNSASFSTFKCYGVSPTKLNDLCFTNVYADSF
320 330 340 350 360 370 380 390 400
VIRGDEVRQIAPGQTGKIADYNYKLPDDFTGCVIAWNSNNLDSKVGGNYNYRYRLFRKSNLKPFERDISTEIYQAGSKPCNGVKGFNCYFPLQSYGFQPT
410 420 430 440 450 460 470 480 490 500
NGVGYQPYRVVVLSFELLHAPATVCGPKKSTNLVKNKCVNFNFNGLTGTGVLTESNKKFLPFQQFGRDIADTTDAVRDPQTLEILDITPCS
510 520 530 540 550 560 570 580 590
Total: 155 Peptides, 99.6% Coverage, 10.79 Redundancy
Default State
Reference Exposure
Relative Uptake (Da)
0.0
0.0

Figure 6.3 Coverage map for identified peptides of WT, the Alpha, Beta, Zeta, Kappa, Delta, and Omicron RBD.

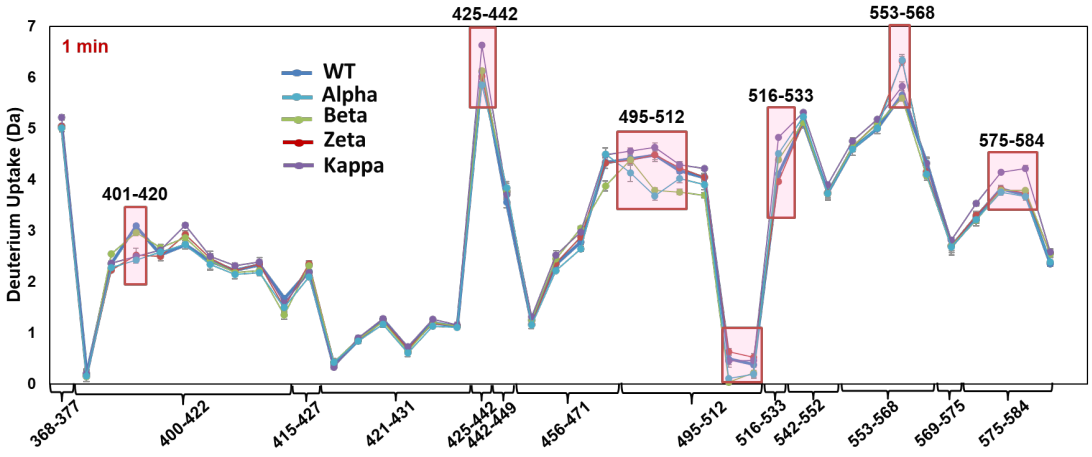

Figure 6.4 Deuterium uptake of unbound RBD and its mutants at 1 min.

Two partially occupied glycosylated residues locating in the core of RBD (Figure 6.5) were still observed within various peptides among RBD and its variants. The previous

study suggested that the independent presence of N343 played a vital role in triggering states changing of RBD, from “closing” to “opening”.[223] In this project, the relative fractional uptake (RFU) of N343 among various RBDs presented a similar level as 12.8% -16.7% at 1 min and 21.1%-26.9% at 60 min, without apparent differences in exchange rates. The abundance level of glycans was mainly affected by the cell types for RBDs expression, which was retained with less diversity via the same cell source.[224] Thus, in the study, we will not focus on extending the special characteristics of glycans for facilitating viral entry.

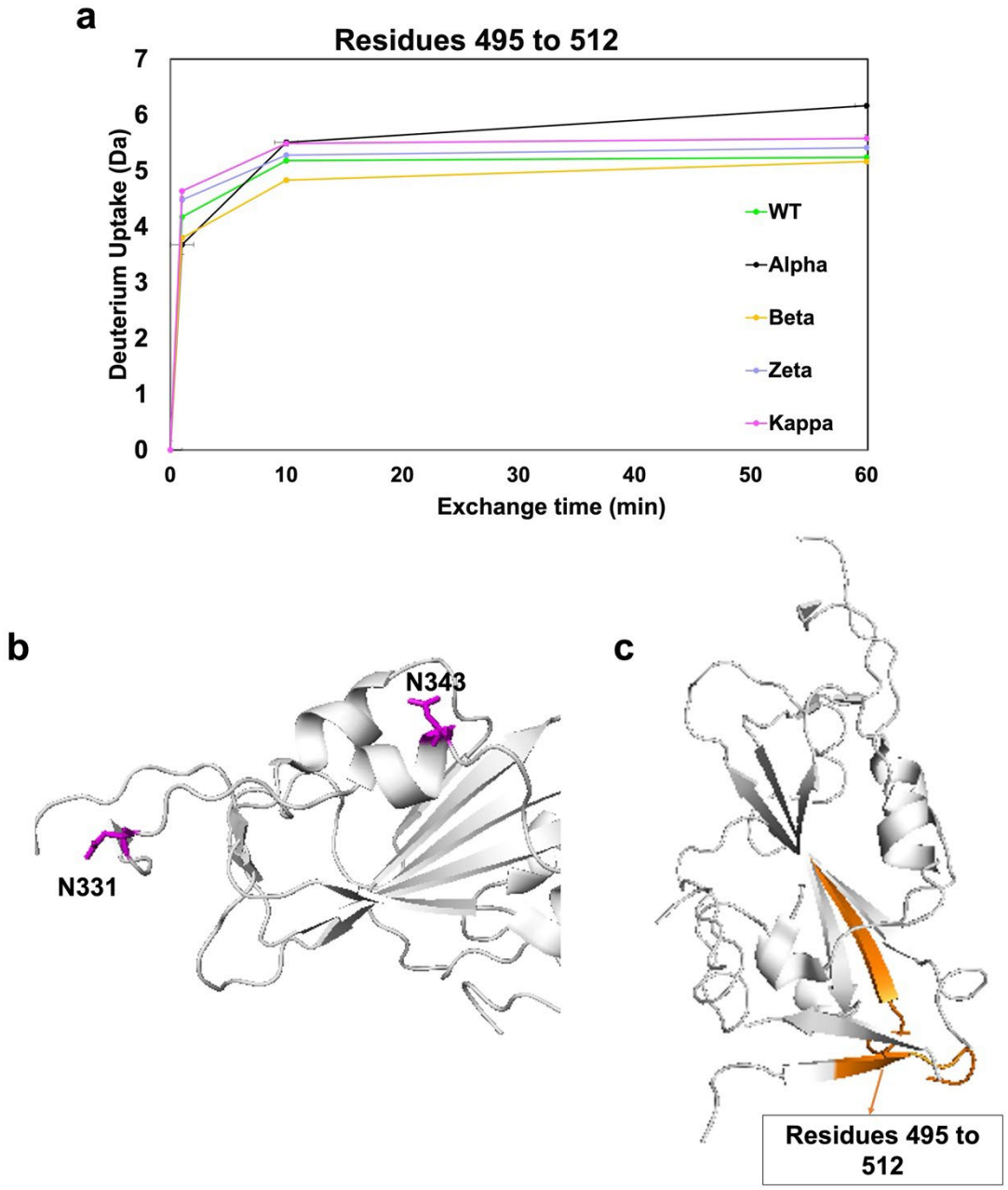

Figure 6.5 Deuterium exchange of the key region.

(a) Deuterium exchange of key region containing residues 495-512. (b) Two glycosylated residues inside RBD. (PDB ID: 6VXX) (c) The location of residues 495-512. (PDBID: 6VXX)

The structural flexibility and viral infectivity of RBDs could be investigated in accordance with the relative deuterium uptake. As shown in Figure 6.4, the Kappa variant including the mutations at L452 and E484 presented higher deuterium uptake in four regions, respectively were residues 425-442, 495-512, 516-533, and 575-584. The mutation E484 was detected among the Beta, Kappa, and Zeta variants, of which, the Beta and Zeta (E484Q) variants exhibited similar deuterium uptake levels in the four regions, compared to wild type RBD. Therefore, the higher conformational dynamics of the Kappa variant might assume to be caused by the dual mutations of E484Q and L452R. In addition, the previous study indicated that L452R contributed to a more flexible structure of the Kappa variant.[225] The existence of L452 in the Delta variant also could explain the higher replication and viral fitness of the variant, as previously mentioned.[150] The region (residues 495-512) containing three tyrosine residues of RBD was reported to play a vital function for receptor binding, which has the potential to form hydrogen bonds with the polar hydroxyl group of ACE2 among all the variants. Interestingly, the Alpha and Beta variants with the mutation at N501 position, induced lower deuterium uptake levels in the region, which may help to stabilize the loop (Tyr495-Asn501) at the closed conformation of RBD.

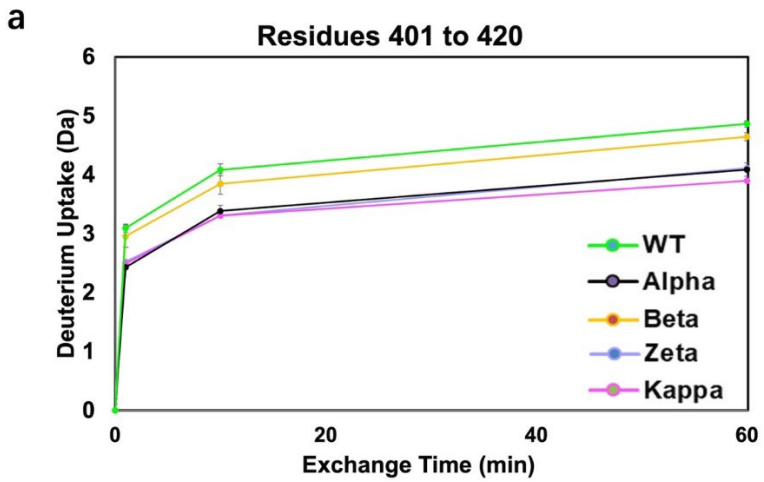

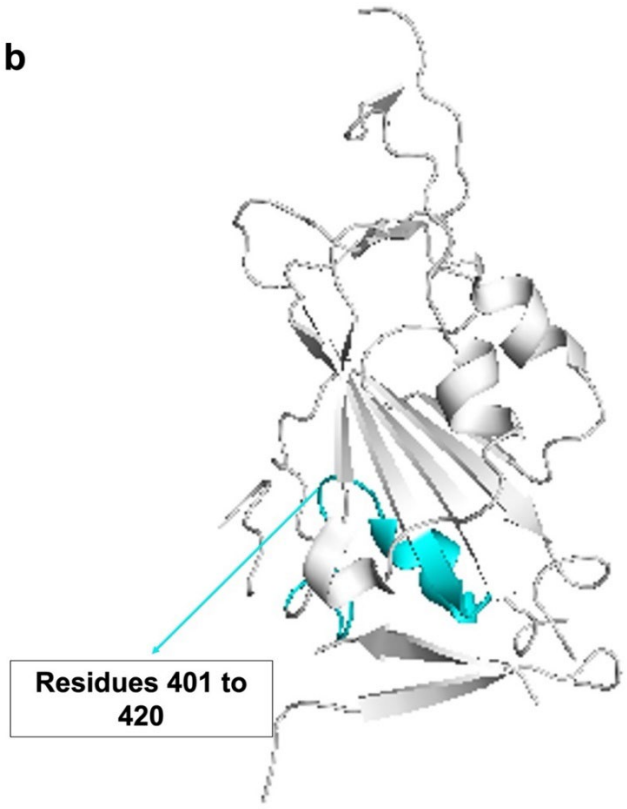

Figure 6.6 Deuterium exchange of key region containing residues 401-420.

(a) Deuterium exchange of the key region containing residues 401-420. (b) The location of residues from 401 to 410. (PDBID: 6VXX)

It was worth to mention that the region covering V401-Y420 comprised a loop between two helices. In which, WT and the Beta variant performed a faster deuterium exchange than other variants (Figure 6.6). For RBDs in free state at closed conformation, hydrogen bonds were observed between K417 of RBD and N370 in the neighboring S trimer, resulting in a more stable structure. The deuterium uptake level between WT and the Beta variant (containing N417K) was considerably similar, suggested an unnoticeable structural change of the region covering N417 at RBD closed state.[226] The mutation at K417N occurred in a stable helix locating at the back of RBD would allow significant

conformational changes and create a favorable formation of RBD upon binding to ACE2, and nonvisible impacts for RBD in free state.[227]

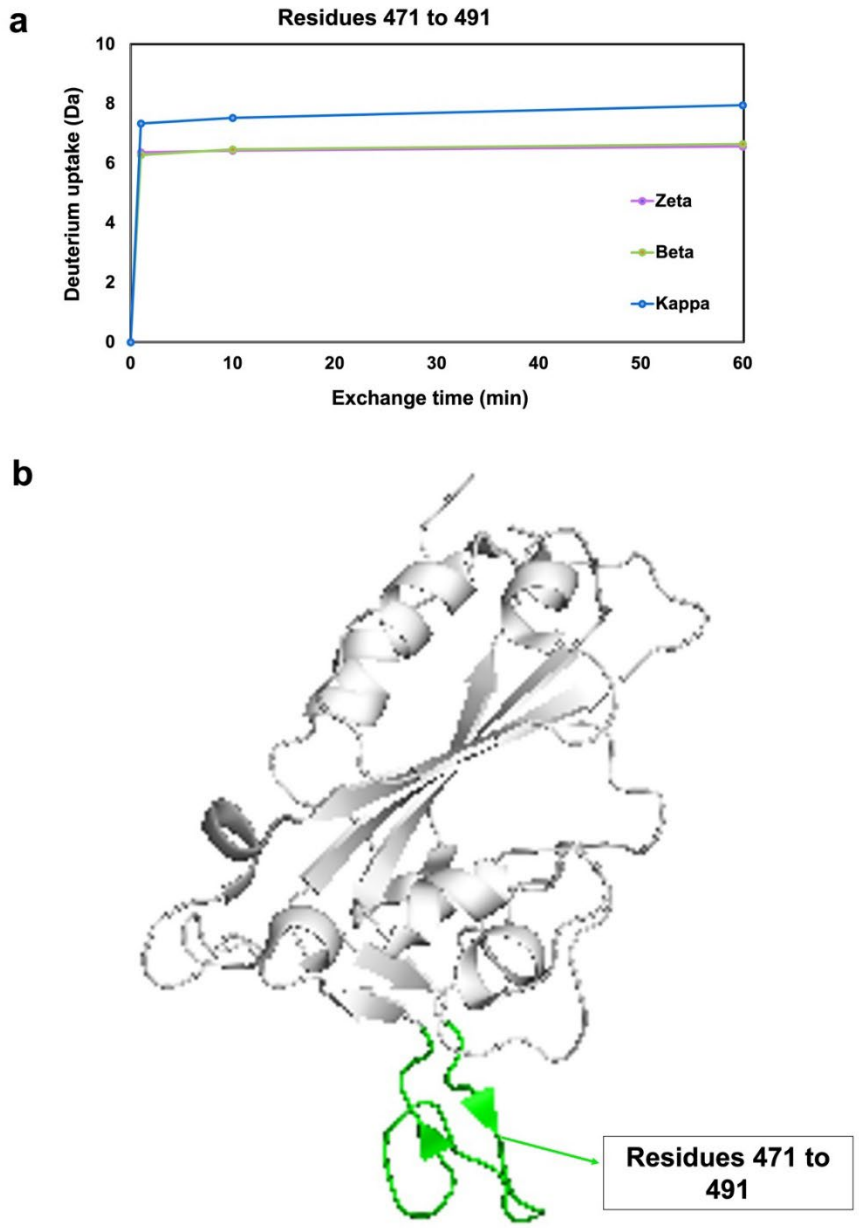

Figure 6.7 Local HDX uptake plots (residues 471-491) of the Zeta, Beta, and Kappa RBD.

(a) Local HDX uptake plots (residues 471-491) of the Zeta, Beta, and Kappa RBD. (b) The location of residues 471-491. (PDBID: 6M0J)

Figure 6.7 presented a local deuterium uptake plot for the Zeta, Beta, and Kappa RBD covering the residues 471-491. All the three variants contained the mutation at E484, which is located in a highly flexible loop.[186] Besides, the residues of C480-C488 are the region connects another key loop inside receptor binding motif (RBM), which is indicated as the binding domain for receptor and antibodies.[228] The Beta and Zeta variants contained a mutation at position E484K, while Kappa was mutated to glutamine (Q) at residue 484. Among the three strains, the Kappa RBD showed a significant enhancement in deuterium uptake, while the Beta and Zeta variants performed a relatively lower and similar exchange uptake level. These results suggested when combined with L452R mutation, the Kappa variant was closely related to the changing structure of the vital region, which presented a more flexible structure.

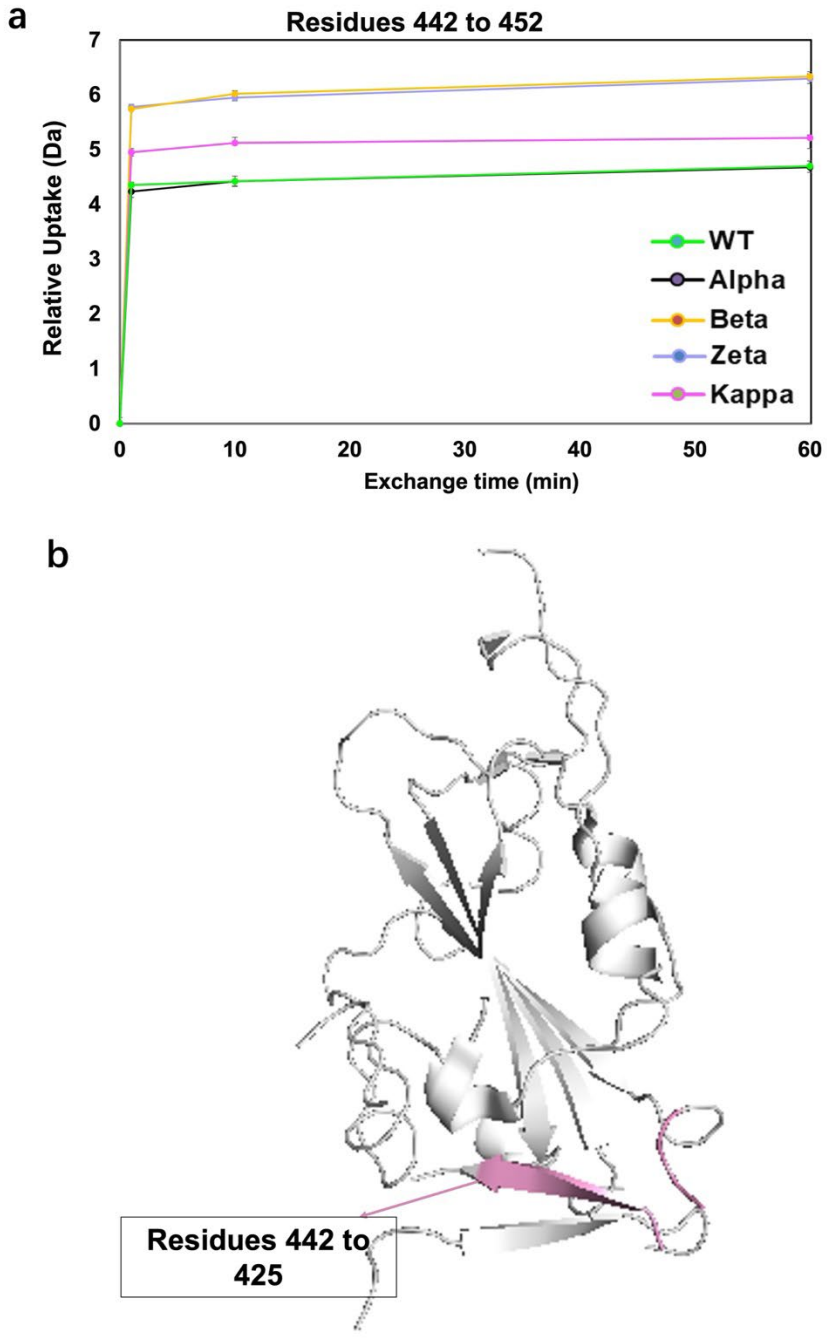

Figure 6.8 Deuterium exchange of key region containing residues 442-453.

(a) Deuterium exchange of the key region containing residues 442-453. (b) The location of residues 401-410. (PDBID: 6VXX)

To reveal more precise conformational behavior of RBDs, changes of deuterium uptake were labeled onto the structure of isolated RBD (PDB ID: 6VXX) and shown as Figure 6.8b. The local deuterium uptake plots of Figure 6.8a presented the individual differences in deuterium exchange among the variants. The Beta and Zeta RBDs presented the highest deuterium exchange level, suggested a high mobile potential of the region covering residues 442-452. The results indicated that the Kappa variant with a mutation at residue L452R performed higher deuterium uptake levels compared to WT and Alpha. The mutation L452R is also within RBM but not directly contacts the interactions of ACE2. The results focused on revealing individual features of the special peptides covering fragments 442-452, which further showed a positive correlation between charge reversal (emergence in the Beta and Zeta variants) and structural flexibility. A computational study selecting several modeling methodologies such as MD and Principal Component Analysis (PCA) also supported our results, that L452R might destabilize RBD structure at free state.[229]

In this study, we firstly described the individual conformational dynamics among the various variants based on their crystal structures. We pointed out the flexibility diversity of possible binding domains among the variants and the conformational changes caused by the single or combined mutations. Despite such results consistent with the viral residues for binding, as previously mentioned, besides the reported immune potential, we paid more attention to the possible conformational alterations caused by E484 mutation. Another mutation at L452R of concern may lead to a significant contribution to the extensibility of

RBD. These mutations are indicative of a favorable conformation for binding and higher receptor fitness.

6.3 Localized conformational characteristics of the Kappa and Delta variants

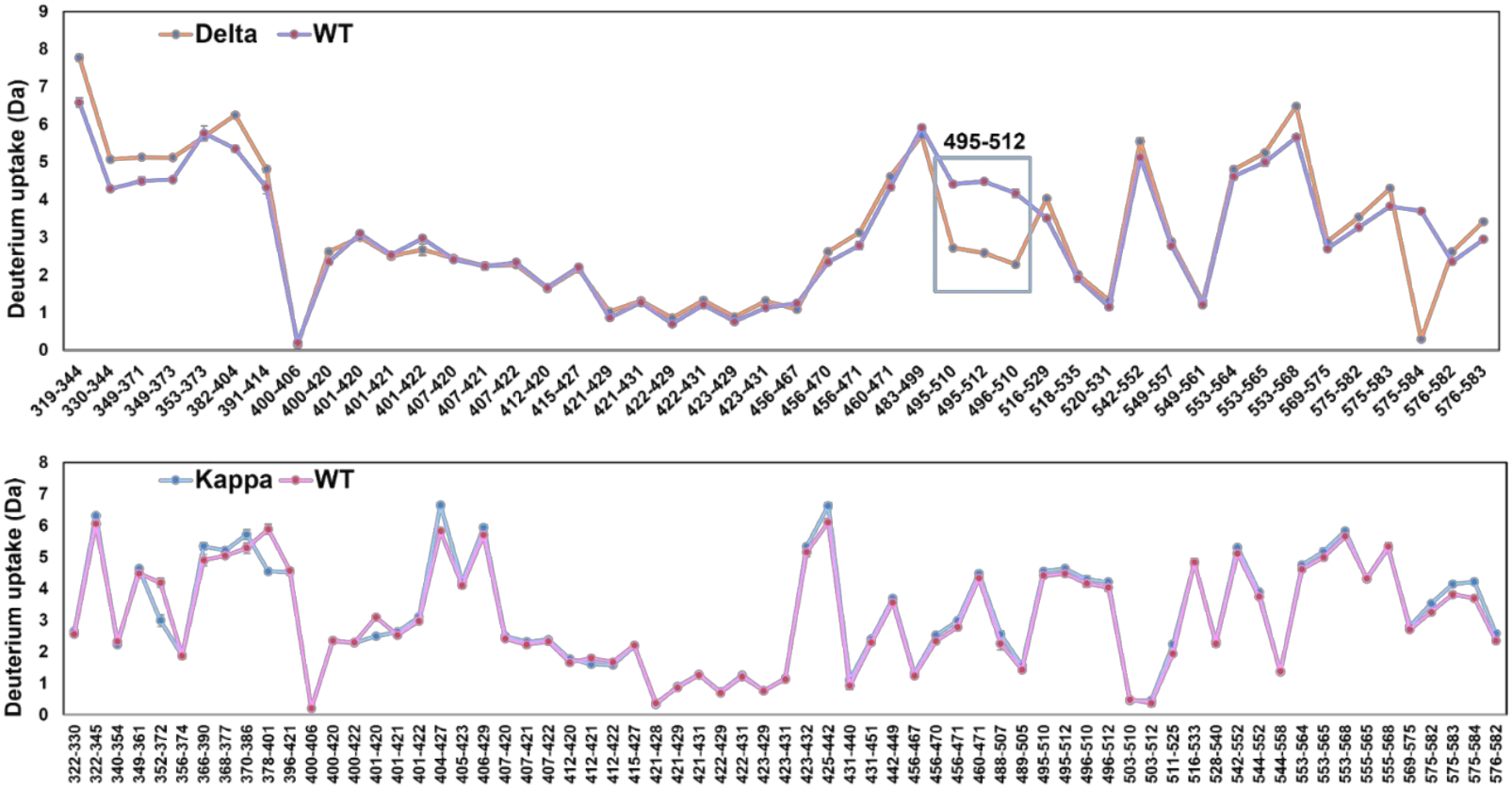

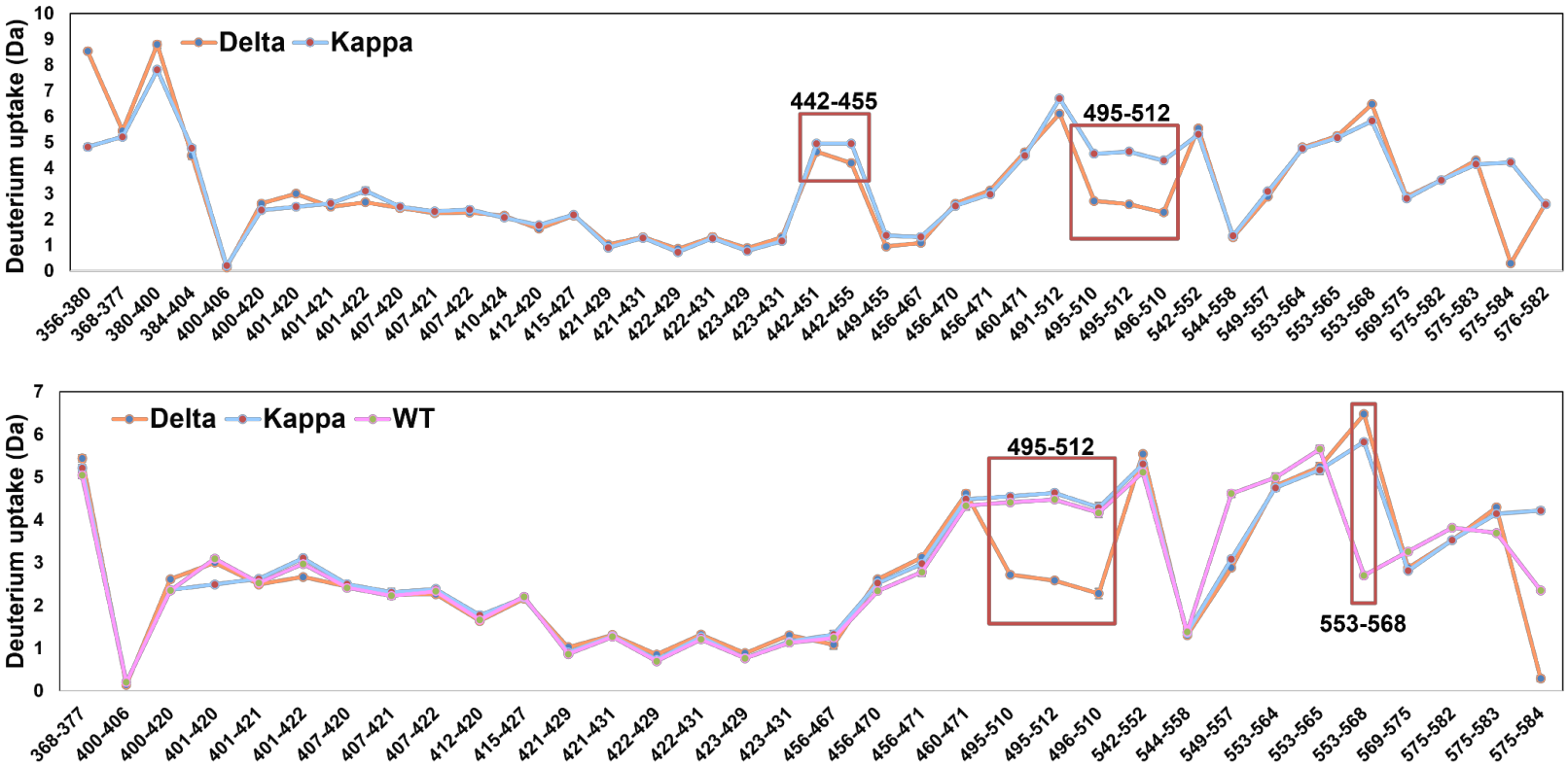

Figure 6.9 Deuterium uptake comparisons for WT, the Kappa, and Delta RBD at unbound state, for 1 min.

To detect the structural effects of the variants, Kappa and Delta, our investigation comprehensively revealed the differences for RBDs at unbound state, by using HDX-MS. Deuterium uptake level of Kappa (mutations at residues L452R and E484Q) and Delta (mutations at residues L452R and T478K) has been individually compared to that of WT. Besides, the commonly recorded peptides between the Delta and Kappa variants, and among the three strains, were obtained for further understanding the correlation of the mutations and the viral conformations.

Generally, the Kappa variant displayed a similar deuterium uptake level as WT, except the core regions of RBD with minor differences, which was supposed as the different glycosylated level of two glycan sites. Interestingly, the region (residues 495-512) enclosing two key loops commanded receptor binding which was inspected with considerably lower deuterium uptake for the Delta variant, compared to WT and Kappa. Delta without any mutation at this region, therefore, the differences were supposed to be created by the mutation at residue T478K. T478K was responsible for the increment of positive charges, interestingly, it showed the long-distance effects on the interfaces of ACE2. Our study was consistent with previous crystal structures obtention from X-ray and Cryo-EM structure, supported an allosteric effects[166] of Delta on the binding interactions.

It was indicated that the conformational differences for the region (fragments 442-455) for the Kappa and Delta variants were mainly attributed to the profiles of hydrogen bonds within the main chain, via MD study. In the region, our HDX study adopted a consistent

result, which was observed in a more rigid structure of Delta. The inflexible structure might be explained by the more regular arrangement of β sheet, which resulted in the different hydrogen bond patterns.[156, 230]

The mutations of RBD created more stable patterns of Delta, which might provide a structural basis for the higher transmission and increased viral replication, certified by clinical recordings. It was demonstrated that L452R might serve for a better viral expression, which was closely related to the higher viral replication circulation.[231, 232] We firstly pointed out the allosteric effects on the binding interfaces, which were caused by the mutations of Delta. We believed that the rigid conformation could display an extraordinary viral fitness and emphasize the exceptional structural influences of mutations with charge reversal.

6.4 Multiple mutations within Omicron displaying the structural effects on RBD

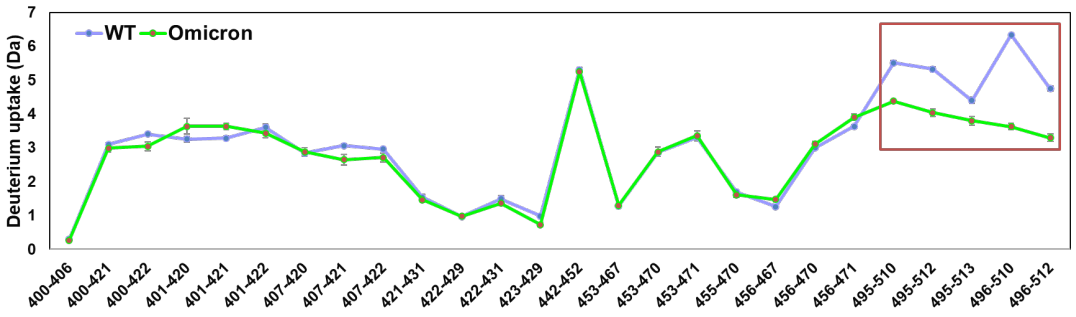

Figure 6.10 Deuterium uptake for WT and the Omicron RBD at unbound state, for 1 min.

Recently, a predominant variant with the most mutated residues within RBD was named Omicron, it was particularly of concern due to the higher population susceptibility.[162] In the study, we revealed the detailed conformational features of the Omicron RBD. As a consequence of the highest mutation number of Omicron, regrettably, we only determined several common peptides patterns between WT and the Omicron RBD. The significant difference of concern was the deuterium exchange for the vital binding region containing residues 495-512. Omicron comprised five mutations in this region, which completely changed its conformation. Several studies described a comparable binding affinity for the Omicron and WT RBD with ACE2,[233] while the others showed a slightly higher binding kinetics of the Omicron variant, as references.[182, 234] In this study, our results showed that the Omicron variant represented a more rigid and tightly arranged structure inside RBD, which might be beneficial for receptor binding.

6.5 Conformational dynamics of the binding interactions between WT RBD and ACE2

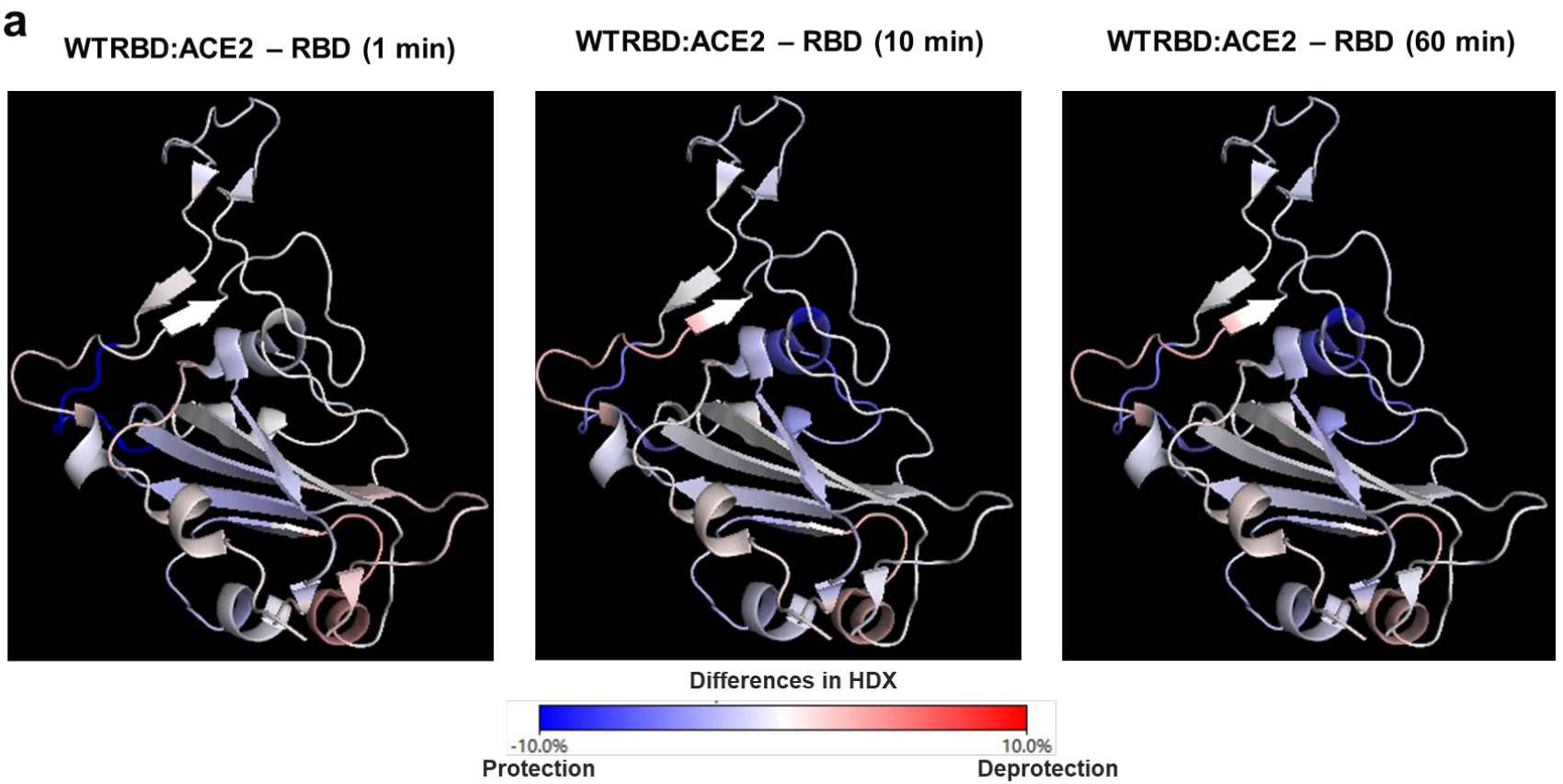

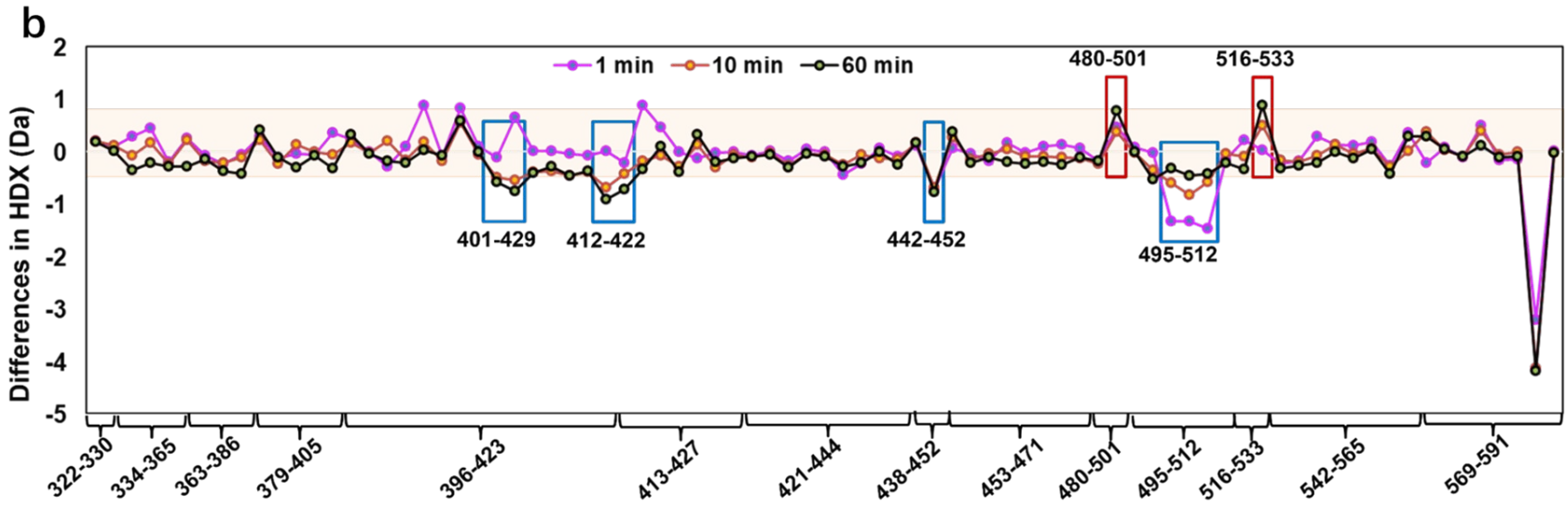

Figure 6.11 The effect of ACE2 binding on WT RBD.

(a) The differences in HDX uptake (ΔHDX) profiling at 1 min, 10 min, and 60 min HDX time, were mapped onto the structure of WTRBD at the opening state, respectively. (PDB ID: 6M0J). (b) Differences in HDX were plotted for all the identified peptides with peptides group clusters.

As Figure 6.11 shown, the region covering residues 495-512 presented a significant reduction in uptake, especially for 1 min deuterium exchange. The results suggested a vital binding function of this region with ACE2, which was consisted with the previously reported X-ray structure of RBD-ACE2 complex. The region involved a β-sheet covering P507-Vl512, an α helix, and a loop, which directly contacted the key binding region of ACE2. The deuterium differences of these fragments presented that, the helix containing G496-G503 was under protected from deuteriation. The protected properties were mainly contributed by the existed hydrogen bonds with ACE2. Our results supported previous high-resolution X-ray structure, which indicated three hydrophilic interactions as T500/N501 of SARS-CoV-2 and Y41 of ACE2, G502 of SARS-CoV-2 and K353 of ACE2, Y505 of SARS-CoV-2 and R393 of ACE2, were formed, in the region.[228]

The identified fragments covering residues 442-452 was another loop with notable decrement in deuteriation after ACE2 binding. The region was observed with considerable flexibility at free state, especially for the variant with single mutation at residue L452R. The region was far from the core of RBD, it might play the functions in facilitating receptor binding. The results also supported the two hydrogen bonds of Y449 of RBD with D38 of ACE2 and G446 of RBD with Q42 of ACE2, which were described in the high-resolution X-ray structure.[228] In addition, as a key position for receptor recognition, L455 was located in a neighboring loop.[170] The two loops of concern were visualized with uptake reduction, which might be closely related to the stabilized functions of the hydrogen bonds between RBD and ACE2.

To further study the potential binding sites, the levels of deuterium exchange for fragments 401 to 421, 401 to 422, 412 to 420, 412 to 421, and 412 to 422, were compared. The results presented a similar exchange degree for fragments 401 to 421 and 401 to 422, upon binding to ACE2. On the contrary, the region with residues 412-422 covering an important residue at K417 presented a visible reduction of deuterium exchange for 10 and 60 min. Therefore, the region (residues 412-422) provided an important contribution in exchange, while residues 401-412 were not involved and exhibited tiny fluctuations. The position of residue K417 was near but not directly in contact with the receptor, which was mentioned to form a salt bridge (co-existing of hydrogen bond and ion pair) with D31 of ACE2.[235] The formation of hydrogen bond led to a conformational change with protective functions and resulted in a less flexible structure for this region after binding.

A detectable increased HDX of peptides (residues 516-533) was involved within a loop at the boundary of RBD for 60 min exchange. The loop performed as a rather rigid region of WT RBD in unbound state, which increased its flexibility with receptor interaction. The lagging in response of the region was possibly attributed to the indirective effects of binding. Relatively more distinct decreased exchanges were indicative of a highly stable formation for RBD-ACE2-complex, after ACE2 intervention.

6.6 Comparison of Conformational Changes among the mutants of RBD

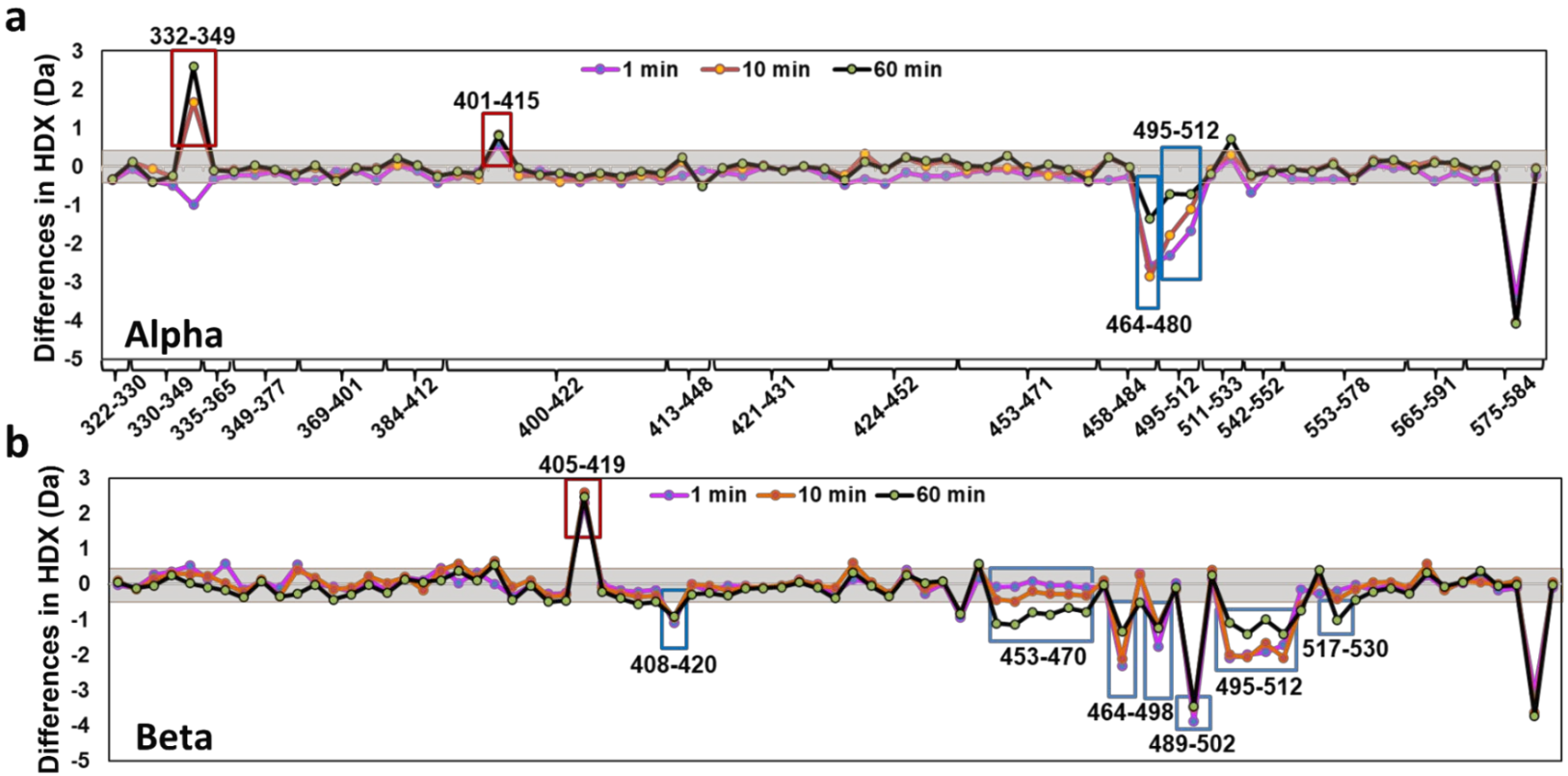

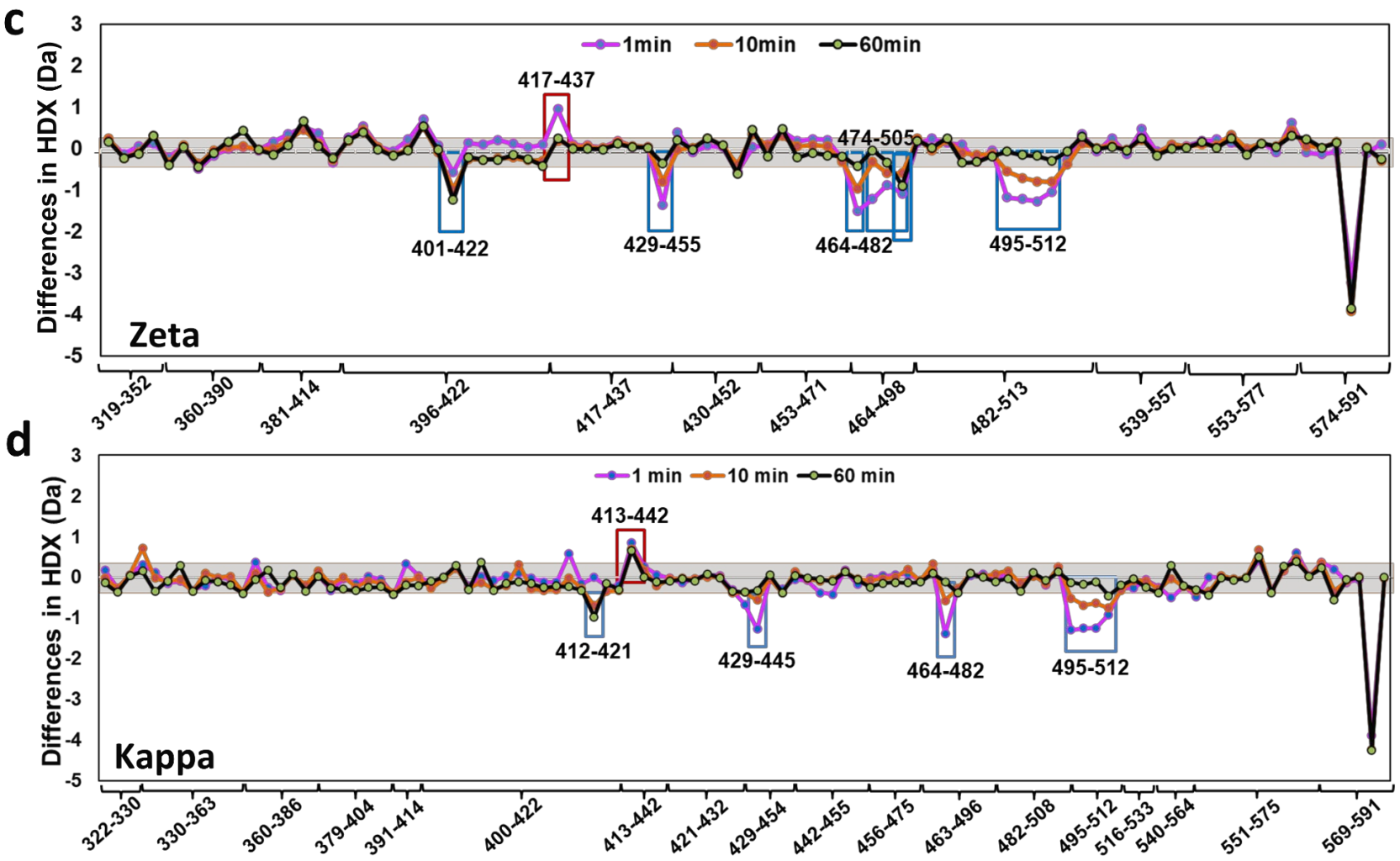
c
Differences in HDX (Da)
1min
10min
60min
417-437
474-505
401-422
429-455
464-482
495-512
Zeta
319-352
360-390
381-414
396-422
417-437
430-452
453-471
464-498
482-513
539-557
553-577
574-591
d
Differences in HDX (Da)
1 min
10 min
60 min
413-442
412-421
429-445
464-482
495-512
Kappa
322-330
330-363
360-386
379-404
391-414
400-422
413-442
421-432
429-454
442-455
456-475
463-496
482-508
495-512
516-533
540-564
551-575
569-591

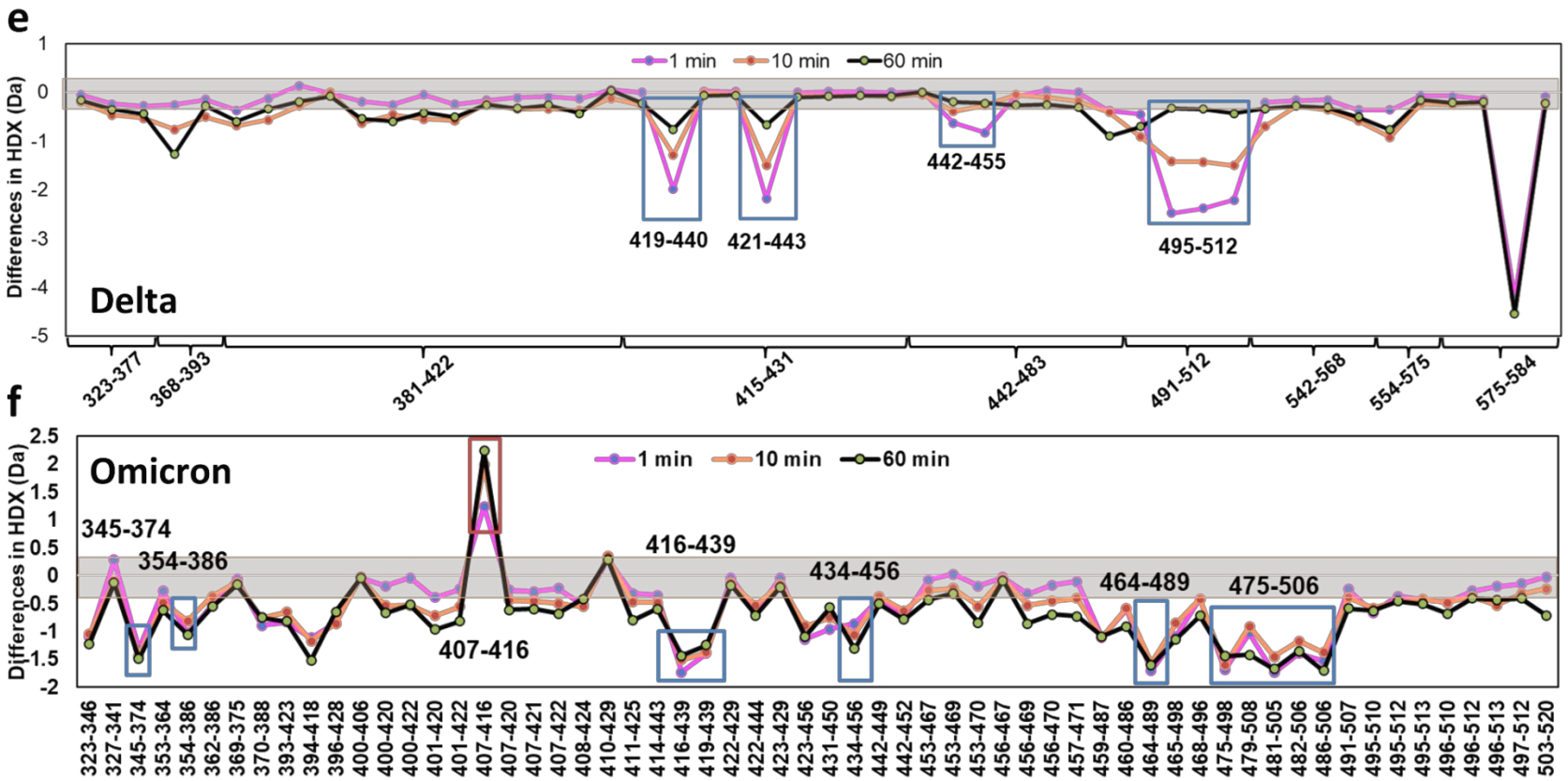

Figure 6.12 Differences in HDX of RBDs.

H/DX-MS presenting the interactions between RBDs and ACE2. Differences in H/DX of (a) the Alpha RBD with significant ΔHDX > 0.29 Da (b) the Beta RBD with significant ΔHDX > 0.27 Da; (c) the Zeta RBD with significant ΔHDX > 0.27 Da; (d) the Kappa RBD with significant ΔHDX > 0.24 Da; (e) the Delta RBD with significant ΔHDX > 0.22 Da; and (f) the Omicron RBD with significant ΔHDX > 0.25 Da, were plotted for all the identified peptides with peptides group clusters.

Studies experimentally determined the binding affinity of RBD-ACE2 formation by surface plasmon resonance (SPR) and biolayer interferometry (BLI) Assay, which presented K_D in the range of 0.566-31.4 nM among RBDs.[124, 181, 182, 228] Despite the discrepancy of K_D value, we obtained a more than 90% binding efficiency by calculating, for all sampled RBDs, which was fit to conduct HDX experiments.

States transformation was an essential step for RBDs converting into up conformation, which fully exposed RBM for receptor binding.[236] In this study, we compared the details of conformational dynamics among different RBDs and ACE2 and summarized as Figure 6.12 a-f. Similar to WT RBD, all RBDs presented a dramatic reduction in the region covering residues 495-512. However, among the six variants, higher level deuterium uptake reduction was observed in the Alpha, Beta and Omicron variants containing N501Y mutation. Interestingly, the mutation at N501Y created a more stable RBM for RBDs at unbound state, resulted in the enhanced binding potential. Our findings supported the higher binding affinity between N501Y mutation and ACE2 of previous studies.[173, 237]

6.6.1 Alpha

The widespread variant with N501Y mutation was indicated the vital function for enhancing the binding affinity between SARS-CoV-2 and ACE2.[238, 239] The region containing N501Y mutation showed a significant uptake reduction, which might affect the viral transmission. It was worth to mention that all the variants showed the reduction in exchange at the region covering F464-C480 adjacent to a β-sheet directly connected with ACE2, while invisible exchange was detected in wild type RBD. Interestingly, the three variants (Alpha, Beta and Omicron) containing the mutation at N501Y performed the most dramatic exchange in the region. The high-level exchange implied the mutation was able to create a more inaccessible and tightened structure of this region. The results also indicated that N501Y might strengthen the viral activities and resulted in a variant with higher binding affinity. In addition, a region (fragments 332-349) containing two glycosylation sites displayed a strong increased HDX within the Alpha variant at 10 and 60 mins. As major epitopes, glycosylation sites served as a discernible targeting for antibodies.[240] The changes of the peptides containing glycosylation sites in the Alpha variant were observed, which also supported the promoted functions of glycosylates for binding to ACE2.

6.6.2 Beta

The Beta variant containing three mutation sites would lead to a higher degree of conformational dynamics. Compared to WT RBD, the region with increased HDX covering E516-T530 became to an HDX reduction region. Based on the crystal structure of RBD-ACE2 complex, the region mainly contains a loop, which is close to the loop with

N417. A dramatically increased HDX was detected for the region (fragments 405-419) at 1 min, 10 min, and 60 min, for the Beta variant. The mutation at position N417K broke an existed salt bridge which was formed with D30 of ACE2. The dismiss of the salt bridge would lead to an easier solvent accessible conformation for the region. In addition, N417K of the Beta variant might form a more stable loop and further protect the spatially adjacent loop with fragments 516-530, resulted in a rather compact structure. Of the significantly reduced HDX, residues Y453-T470 was another attractive region, which was in an active loop for ACE2 interactions. It was observed that the region containing several fragments (453-467, 453-470, 453-471, 456-467, 456-470, and 456-471) presented a more strongly protective properties from HDX in 60 min, upon binding to ACE2. Due to the combined mutations of N501Y and E484K, they might create allosteric effects for stabling the loop with fragments 453-471. The vital interface region with a more stable structure might enhance the viral fitness, resulted in a more favorable receptor response.

6.6.3 Zeta and Kappa

Both the Zeta and Kappa variants shared the mutation at position E484, respectively to K484 and Q484. Due to the possible loss of neutralization, the mutation at 484 has attracted researchers' great attention.[222] For the mutation E484K, it was mainly reflected in charge conversion and reduced antibody neutralization, however, a slight impact was observed for the structure. Interestingly, the region containing residues 429-445 of the Zeta and Kappa variants performed a significant reduced deuterium exchange at 1 min. E484 locating within a sheet might prefer to form sheet-sheet interaction[241] with another sheet (covering residues 429-438). This interaction was likely to create the more compact sheets

of the core inside RBD, although the region was distal from the residue 484. To maintain the stability within RBD, the space neighbored helix within the RBD core (fragments 417-420) released its structure, therefore displayed as the promoted HDX. The findings indicated that the mutation at E484 might increase the structural dynamics for the core of RBD, but not affect the binding affinity between RBD and ACE2. A subsequently emerged variant (Kappa) with mutation at L452R was reported with higher binding affinity with ACE2 and stronger pathogenicity.[143, 144] The mutation of L452R also changed the charge of the loop, which might result in a stronger charge complementarity between RBD and ACE2.[242]

6.6.4 Kappa and Delta

The Kappa and Delta variants both contained the mutation at residue L452R, the structural impacts causing by the combined mutations of L452R/T478K in the Delta variant would be comprehensively explored. Due to the indirect receptor contacting location of L452R/T478K, for Delta RBD-ACE2-complex, none of additional regions with decreased HDX was observed, however, the region covering residues 495-512 performed a more dramatic reduction. These findings were consistent with the formation of new inner hydrogen bonds and induced conformational alterations of the loop caused by the mutation T478K, from the crystal structure. Subsequently, the loop created two new H-bonds with ACE2.[157] In addition, few regions presented increased uptake upon binding to ACE2, suggested a more rigid and inflexible structure of complex. The appropriate structure of Delta RBD-ACE2-complex could maximize the viral fitness and therefore be beneficial for leading pandemic.

6.6.5 Omicron

The Omicron RBD with 15 mutations displayed the highest level of conformational changes among all the selected strains. X-ray structure approved eight mutations responsible for ACE2 recognition locating at the interfaces, in which the mutations at T478K, Q493R, and Q498R increased the positive charge scale, in particular. HDX presented a significant difference for the region covering residues 475-506, which supported the newly formed H-bonds (N477 of Omicron RBD and S19 of ACE2) and salt bridge (R498 of RBD and Q42 of ACE2), obtained from Cryo-EM structure. Besides, the positive sites of Q493R and Q498R created a more attractable environment for a better connection with E35 and D38 with negative charge within ACE2, resulted in a more compact structure of the vital interfaces.[166] Interestingly, after binding to ACE2, several mutations positioning on the core of RBD presented a reduced HDX upon binding to ACE2, suggested a tightening up arrangement. Meanwhile, it displayed conformational deprotected functions on the spatially adjacent positions such as fragments 407-416 from HDX, allowing a more flexible region. Different structural effects of the mutations were observed, the new bonds' connection causing by the mutations would be beneficial for ACE2 recognition. Moreover, the mutation at H505 showed a weaker Van der Waals' with ACE2. Overall, although the heavily mutated RBD resulted in several strengthened and newly formed bonds, weakened and dismissed connections also occurred, which finally attained a stable Omicron RBD-ACE2-complex. Our HDX study also highlighted the conformational dynamics caused by the mutations with charge alterations, which would be not only related to ACE2 integration but also create a broader range of hosts.[166]

6.7 Conformational dynamics of ACE2 upon binding to RBDs

Figure 6.13 Coverage map for identified peptides of ACE2.

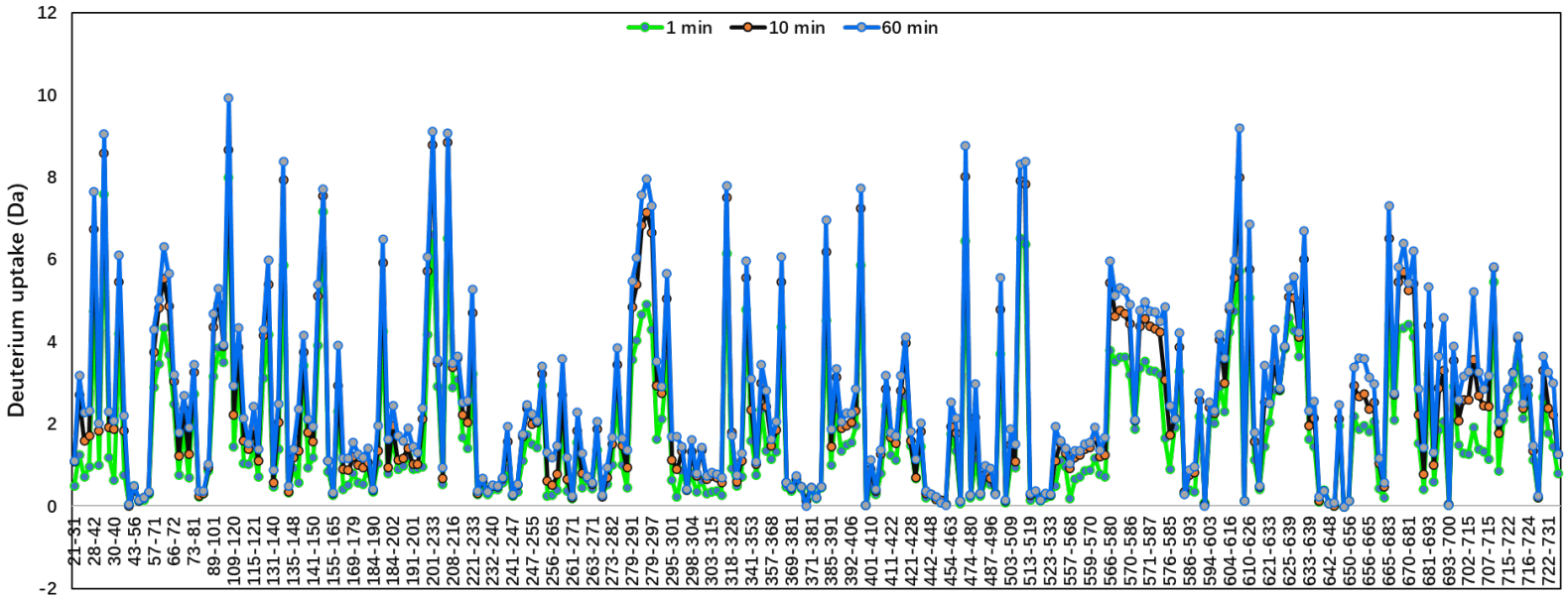

Figure 6.14 Deuterium uptake level of ACE2 for 1 min, 10 min, and 60 min exposure, at free state.

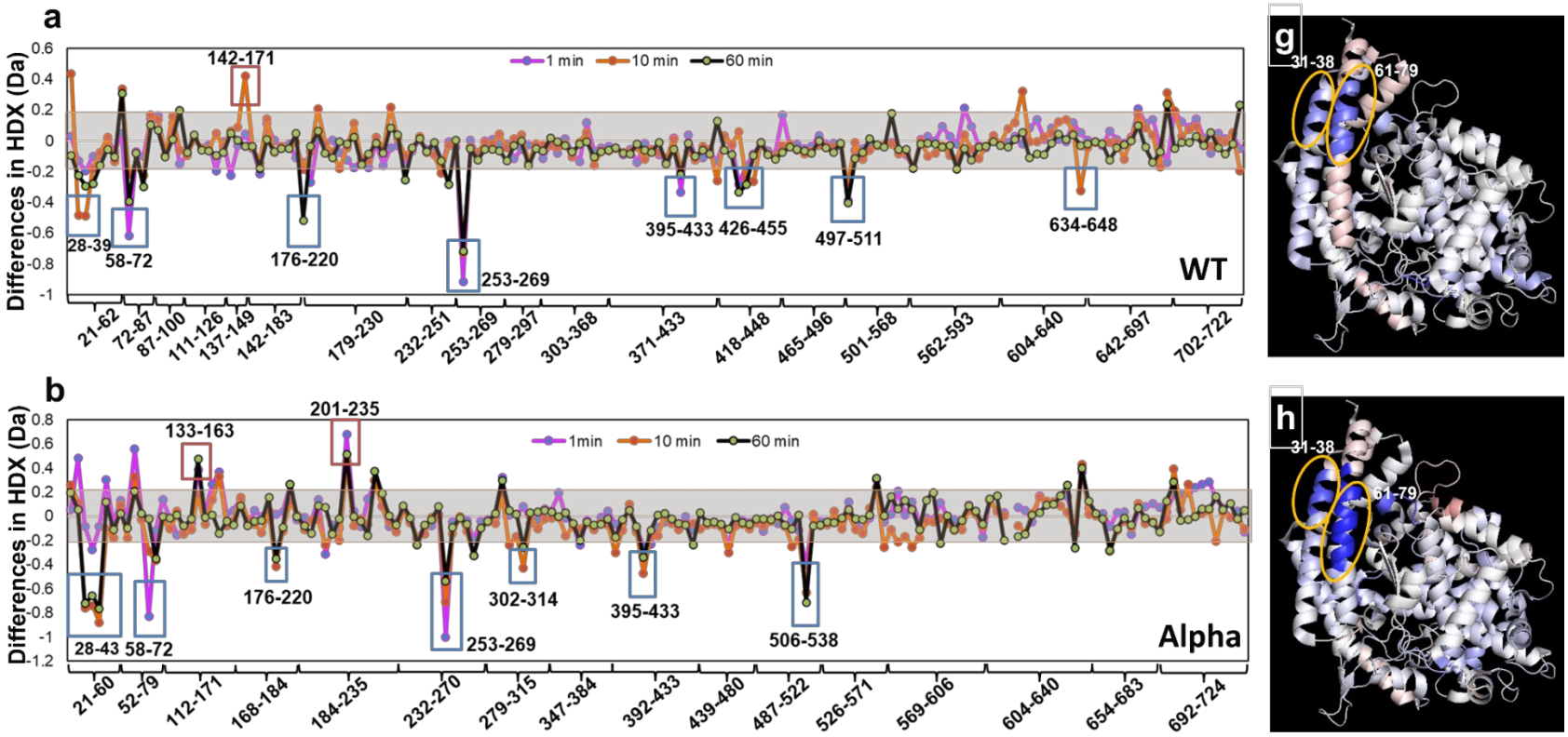
a
Differences in HDX (Da)
1 min
10 min
60 min
142-171
28-39
58-72
176-220
253-269
395-433
426-455
497-511
634-648
WT
21-62
72-87
87-100
111-126
137-149
142-183
179-230
232-251
253-269
279-297
303-368
371-433
418-448
465-496
501-568
562-593
604-640
642-697
702-722
b
Differences in HDX (Da)
1min
10 min
60 min
201-235
133-163
176-220
302-314
395-433
253-269
506-538
28-43
58-72
Alpha
21-60
52-79
112-171
168-184
184-235
232-270
279-315
347-384
392-433
439-480
487-522
526-571
569-606
604-640
654-683
692-724
g
31-38
61-79
h
31-38
61-79

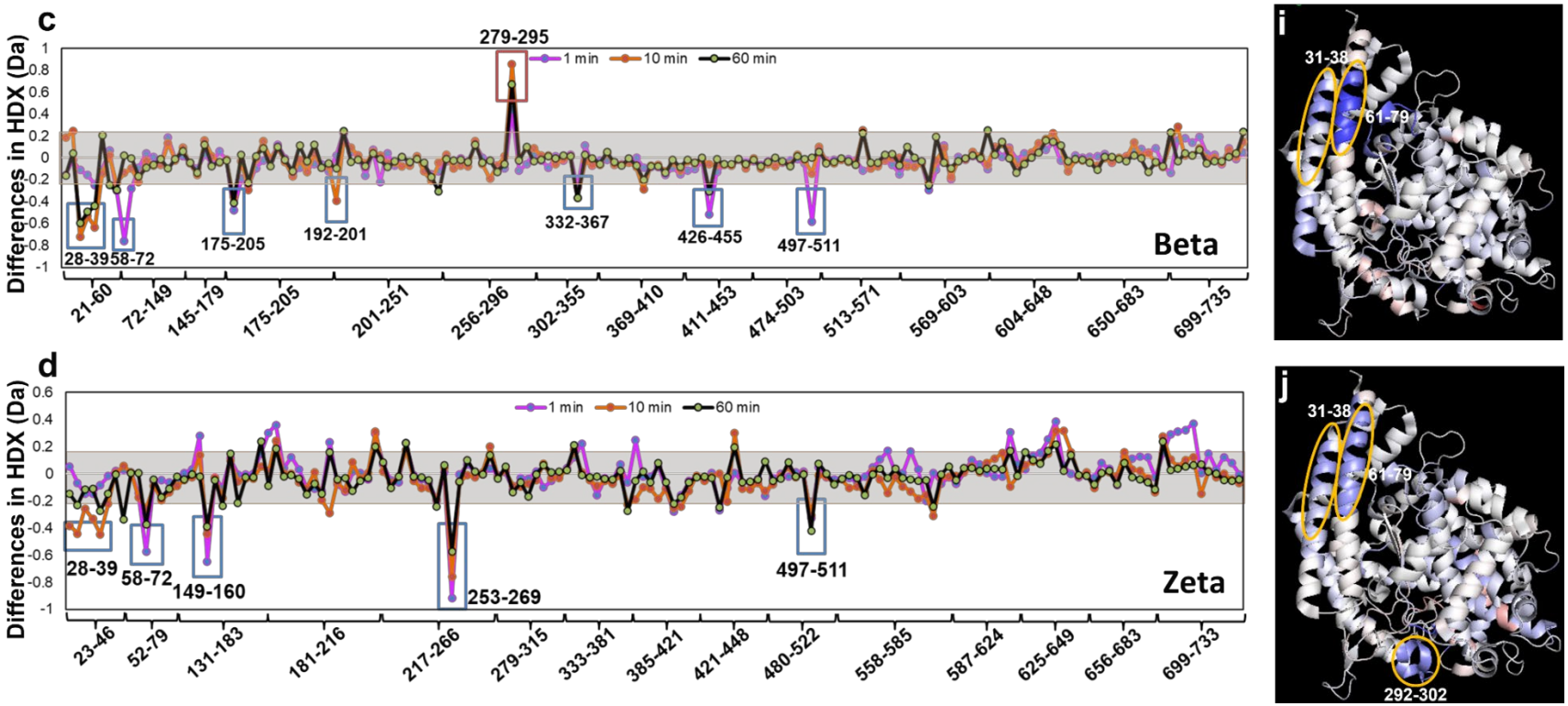
c
Differences in HDX (Da)
1 min
10 min
60 min
279-295
28-39
58-72
175-205
192-201
332-367
426-455
497-511
Beta
21-60
72-149
145-179
175-205
201-251
256-296
302-355
369-410
411-453
474-503
513-571
569-603
604-648
650-683
699-735
d
Differences in HDX (Da)
1 min
10 min
60 min
28-39
58-72
149-160
253-269
497-511
Zeta
23-46
52-79
131-183
181-216
217-266
279-315
333-381
385-421
421-448
480-522
558-585
587-624
625-649
656-683
699-733
i
31-38
61-79
j
31-38
61-79
292-302

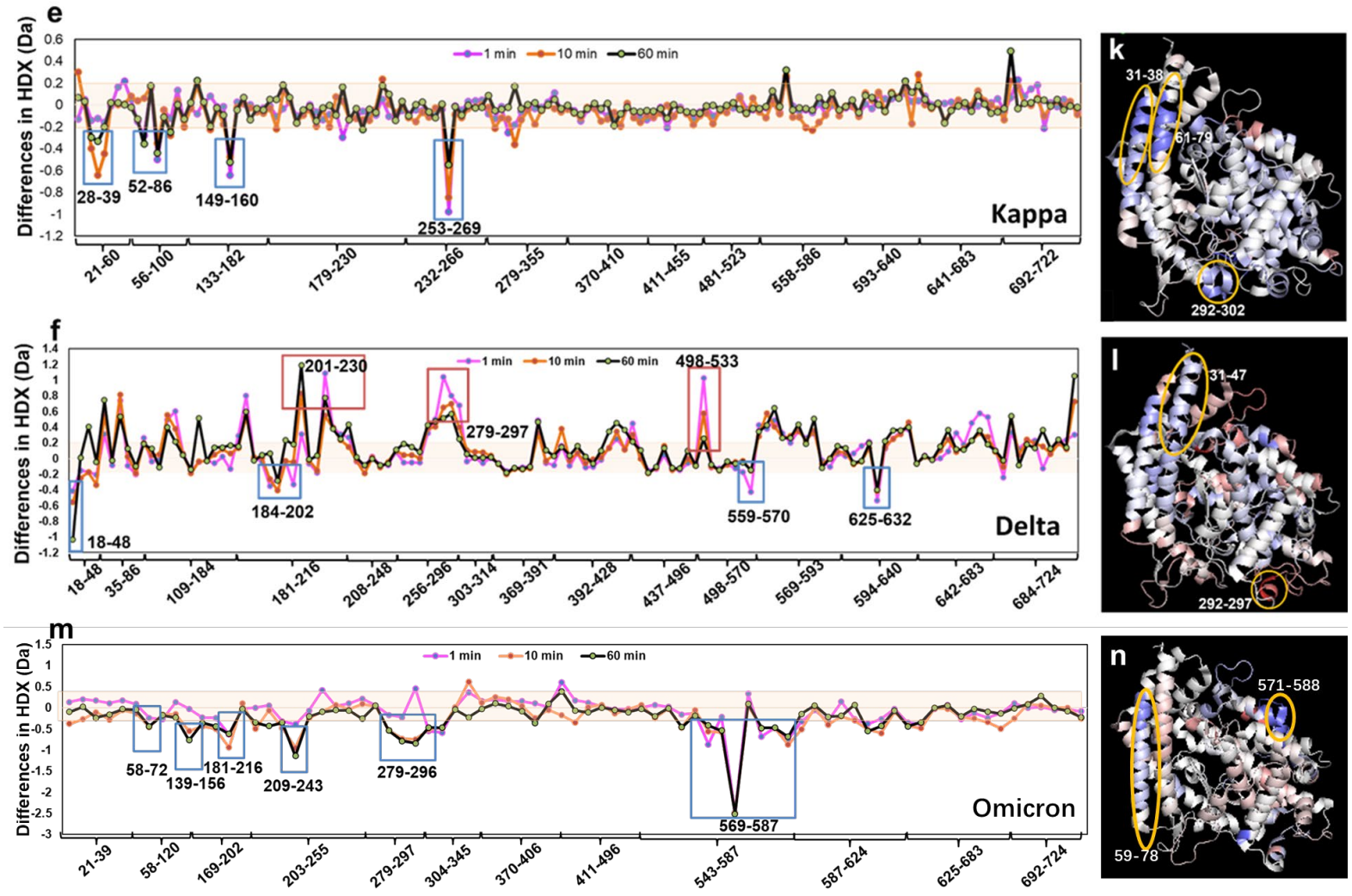

Figure 6.15 Differences in HDX of ACE2 binding with RBDs.

Differences in HDX of ACE2 interaction with (a) WT RBD, significant ΔHDX > 0.23 Da; (b) Alpha RBD, significant ΔHDX > 0.21 Da; (c) Beta RBD, significant ΔHDX > 0.19 Da; (d) Zeta RBD, significant ΔHDX > 0.2 Da; (e) Kappa RBD, significant ΔHDX > 0.18 Da; and (f) Delta RBD, significant ΔHDX > 0.15 Da were plotted for all the identified peptides with peptides group clusters. The differences in HDX of ACE2 which were displayed as Figure 6.15 g-k profiling 1 min were mapped onto the structure of ACE2 (PDB ID: 6M0J), and (l) was mapped onto the structure of ACE2 (PDB ID: 7W9I). Figure 6.15 m-n presented the differences in HDX with Omicron RBD interaction (significant ΔHDX > 0.32 Da) and the mapped structure.

As a type I membrane protein and entry receptor, ACE2 supported the entry of SARS-CoV-2 to the target host cells.[106] Recently, the structure of full length ACE2 has been described by using Cryo-EM.[105] In the study, we selected HDX-MS to investigate the conformational dynamics of ACE2 upon binding to RBDs and further revealed the viral entry mechanism. To evaluate how RBDs recognizing, and binding affect the structural plasticity of ACE2, we selected the monomeric ACE2 (Q18-S740) and compared the conformational dynamics of ACE2 before and after binding to various RBDs. The CHO human cell line expressed ACE2 was certified with over 95% purity by using SDS-PAGE, and the binding potential with RBDs was confirmed via ELISA (Figure 5.2). Revealing binding interactions and structural changes of ACE2 upon binding to different RBDs would be helpful to provide conformational support for detecting novel targeting hotpots of vaccines towards various variants.

ACE2 itself performed highly structural plasticity, which fulfilled the recognition and binding requirements of evolutionary RBDs. For ACE2 in free state, our results presented peptides with sequence coverage reaching 99.2% (Table 5.3). After interaction with RBDs, the deuterium exchange was displayed as Figure 6.15, which provided details for revealing the correlation between the mutations of the various RBD variants affecting HDX and those contributing to the allosteric changes. Most peptides within RBDs underwent HDX in short periods, which was also observed with significant changes for ACE2. Therefore, we chose 1 min exchanged profiling for mapping the crystal structure of ACE2 and presented as Figure 6.15 g-l.

6.7.1 Common effects

Two key binding domains containing fragments 28-39 and 58-72 were detected with significantly reduced HDX among all the selected variants except the Delta and Omicron variants, which indicated the possible binding hotpots at K31, D35, and E38 of ACE2, consistent with the previous study.[170] Common combination of the two regions inside ACE2 might demonstrate the vital roles of these hotpots for screening special targeting antibodies. The impact of the Alpha RBD with Y501 substitution on ACE2, was observed with the most dramatic decreased uptake in the region covering residues F28-S43 among all the RBDs. It might be associated with a newly formed hydrogen bond between Y501 substitution and Y41 of ACE2, which was performed by Cryo-EM structure.[129] Besides, compared to the Alpha and Beta RBDs, RBDs without mutation at N501 exhibited a lower level of HDX.

6.7.2 Allosteric changes

Intriguingly, our results showed the notable reduced HDX in the region with residues P253-D269, except for ACE2 interplaying with the Beta and Omicron RBDs. The presence of the dynamics indicated a stabilized function among WT, the Alpha, Zeta, and Kappa RBDs for the allosteric region. According to the crystal structure of full length ACE2 (PDB ID: 6M18) and RBD-ACE2-complex (PDB ID: 6M0J), the allosteric region was mainly located in a loop (loop 1 with fragments 250-261) and its connected helix at the edge of ACE2. In contrast, the Beta variant that has been widely supported with immune evasion,[140] performed destabilization for the region containing residues Y279-D295 of ACE2. ACE2 conferring the Beta variant binding induced loop 2 (covering S280-T294) activation and further led to the structural release to this region. Our findings firstly demonstrated the allosteric changes of two loops locating at the edge of ACE2, which were permitted by viral binding. The flexibility of loops at the edge of ACE2 might be regarded as a determining factor for viral binding.

A region (fragments 497-511) locating in the core of ACE2 was detected with significantly reduced HDX upon the binding of three RBDs including WT, the Beta and Zeta variants. The deeply inside helix was under highly structural protection of ACE2 in the unbound state, which was also influenced by the interactions with RBDs. The three RBDs were observed for allosteric stabilized a core helix inside ACE2, resulting in a more stable RBD-ACE2 complex. Notably, compared to WT and the Zeta variant, visible HDX of the Beta variant with three combined mutations was exclusively observed at 1 min. The findings

suggested that the mutations with possible higher infectivity such as N501Y and L452R would reduce or disrupt the stabilized functions.

Another allosteric protected region covering fragments 149-160 was detected among the Zeta and Kappa RBDs. The two variants both included the mutation at E484 and presented a similar structure as WT RBD. The region was in a highly structured position, which contained a basic formation of “helix-loop-helix”. The mutation at E484 led to the local changes in the electrostatic environment and played a minor role for conformational differences, as described. Surprisingly, because of the existence of electrostatic functions, the attractive mutation affected the allosteric sites of ACE2. The charge reversal might facilitate receptor recognition and create a preferable conformation for the acceptance of ACE2. However, due to the high class of structural changes caused by the combined mutation of the Beta variant, the allosteric effects might be offset. Besides neutralization properties, our results firstly suggested an allosteric change in conformational dynamics induced by the single mutation at E484.

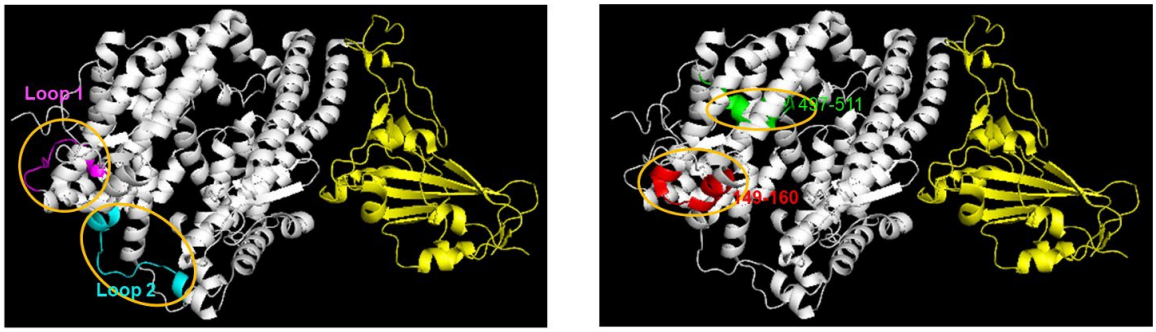

Figure 6.16 Allosteric regions in the structure of RBD-ACE2 complex.

The yellow color presented as RBD. (PDB ID: 6M0J)

Interestingly, upon binding to the Delta RBD, it displayed absolute various effects on ACE2. For other variants, except binding regions, several allosteric changes performed as decreased HDX, indicated more constricted regions for RBD-ACE2-complex. However, the Delta RBD caused noticeable structural release for ACE2. The region covering residues W203-F230 was visualized for a more compact conformation, which led to the reduced HDX upon binding to the Delta RBD and created a more flexible structure for the spatially adjacent "helix-loop-helix". Interactions with the Delta RBD, another loop (residues from 557-565) other than the binding interfaces at the edge of ACE2 was also observed with weaken HDX. In the study, we found the Delta RBD displayed the significant effects on the conformation of ACE2. The flexibility of loops positioning on the edge of ACE2 was visualized with several changes. In general, the loops locating on the edge of ACE2 became much looser, were performed higher flexibility. The conformational changes might be closely related to charge reversal effects causing by mutation T478K or the combined functions with L452R.

Delta was generally regarded as a variant with higher clinical pathogenicity and more serious disease presentations, especially for the pathological changes of lung. However, a slight difference could be observed for the binding affinity of the Delta RBD and ACE2, compared to that of WT RBD. In the study, we revealed multiple allosteric responds of ACE2, which might explain the significant effects caused by the Delta RBD. The dramatic conformational changes of ACE2 might assume responsibility for the Delta impact on lung, where was detected with a high-level expression of ACE2 on its surface.

The profile of exchange from the Omicron RBD-ACE2 was different from that of the other RBDs-ACE2-bound forms. The interaction of the Omicron RBD stabilized the vital interfaces, however, it showed the comparative lower reduced HDX than that of the other variants. Interestingly, the regions at the edge of ACE2 were under protected from exchange and became more rigid, while the inner domain of ACE2 became more flexible. These changes were different from that of the Delta RBD-ACE2 complex, which was observed with the more flexible conformation for the edge of ACE2. The various conformational effects of the Delta and Omicron variants on ACE2 might provide evidence to explain the different clinical symptoms for the patients infected with the Delta and Omicron variants. Interestingly, the ACE2 binding complexes with the two variants (Beta and Omicron) which have been supported with significant immune escape properties, showed the most significant reduced HDX. Several allosteric regions at the edge of ACE2 might be useful for developing the special targeted antibodies against the Beta and Omicron variants.

In the study, we determined the effects of various variants on the receptor binding, which further revealed the allosteric changes and favorable binding of ACE2. All the findings rendered the extensive spread mutations of the variants more prone to receptor binding, which might increase their ACE2-binding affinity and ultimately resulted in the upgrading viral fitness and transmissibility. The single mutation leading to a local charge difference might be a critical determinant and could affect the backbone dynamics and HDX exchange.

6.8 Summary

S protein of SARS-CoV-2 displayed a relatively higher mutation rate, resulting in the variants with spread advantages, neutralizing reduction, and better environmental fitness. In the study, we focused on investigating the characteristics and conformational dynamics of RBD, which presented the most vital functions for the interfaces of ACE2, via HDX-MS.

Our study firstly compared the conformational differences of WT and the variants RBD in unbound state. Interestingly, for the Alpha, Beta, and Omicron variants, the region with mutation N501Y displayed a lower deuterium uptake level. The region (residues 495-512) covering two vital loops for the interactions with ACE2 performed a more compact structure, which might be beneficial for the recognition and binding of ACE2. Interestingly, the natural emerged mutations were more easily to be detected in the loops, direct or indirect contact with the receptor. In addition to the more compact structure of the variants RBDs containing the vital mutation such as N501Y, the core of RBD became more rigid, as viral development. It was worth to mention that although the single mutation at E484K (charge reversal) exhibited slight conformational effects on RBDs, it showed more allosteric effects on the conformation of ACE2. The conformational differences for the vital binding regions among the variants may explain the increased inner stability and environmental tolerance for natural emerged variants, which can provide evidence for the virus infection in the population.

In this study, the conformational alterations of the RBDs for different deuterium exchange time upon binding to ACE2 was revealed. After binding to ACE2, two regions covering residues 495-512 and 464-480 were visualized with reduced deuterium uptake. The HDX changes further supported the previous reported interfaces from the crystal structure. WT RBD showed the existed covalent bonds for the region covering residues 405-419, with ACE2, while our results observed a more flexible region of the Beta variant, caused by the diminishing of one salt bridge. There was an attractive finding that the Delta variant was visualized with a much dramatic reduced HDX for the vital binding regions. However, as the other variant sharing the commonly emerged mutation at L452R, the Kappa variant showed the slight conformational dynamics for the region, suggested an enhancement for ACE2 recognition of the single mutation at T478K or the dual mutations at L452R/T478K.

It was worth to mention that the Omicron variant led to the highest class of conformational changes among the selected strains. Due to the heavily mutated RBD of the Omicron variant, more regions could be detected with notable HDX. Compared to WT RBD, the initial vital interfaces remained unchanged, however, several regions presented increased flexibility, upon binding to ACE2. The significant structural differences exactly maintained the binding capability of the Omicron variant, consistent with the similar binding affinity supported by bioassay.

The structural changes of ACE2 might provide the conformational details for indicating the special regions which would be beneficial to develop antibodies blocking RBDs binding. After binding to the Delta RBD, ACE2 exhibited fewer regions with a more

compact structure, compared to the structure at unbound state. Fewer regions with a slight reduction of HDX might describe a structure with fewer chemical bonds and therefore represented as reduced binding affinity. On the contrary, ACE2 displayed the significant reduction in HDX of several allosteric regions after binding to the Omicron RBD, which led to the more stable structure of the Omicron RBD-ACE2 complex. In addition, Beta was another variant of concern, it caused significant allosteric changes of ACE2, which indicated several regions with potential for blocking the viral interactions. This finding also emphasized the functions of point mutation (E484K in the Zeta variant) with charge reversal at the interfaces, for the possible correlation with the greatly reduced immune activities. Overall, our study indicated the more rigid structure of ACE2, upon binding to the variants supported with immune escape potential, such as the Beta and Omicron variants. The findings firstly revealed the special allosteric regions of ACE2, which might provide the vital information for presenting the edge regions of ACE2 with functions of allosteric blocking the binding of variants.

The study was the first one to systematically investigate the effects of SARS-CoV-2 variants-associated mutations on the conformational dynamics of RBD and its interaction with ACE2. The findings allowed us to obtain insights into the relation of the conformational dynamics with the evolutionary properties of SARS-CoV-2 variants and provide valuable information for improving the design of drugs and vaccines against SARS-CoV-2 variants.

Chapter 7. Conclusions

The thesis involved two parts, which described the delivery of zein-based NPs for targeting permeation via BBB for the treatment of glioma and the conformational dynamics of SARS-CoV-2 variants RBDs upon binding to its receptor-ACE2, were deeply investigated via HDX-MS, respectively.

The first part introduced the current development of nanomaterials for achieving targeting glioma therapy. A novel brain-targeting drug delivery system, zein-RVG-Dac_NP, was formed by the conjugation of RVG29 on the surface of the self-assembled zein NPs with the encapsulation of Dac. The results of FTIR and NMR confirmed the successful conjugation of zein and RVG29 as well as the encapsulation of Dac in the zein-RVG-Dac_NPs. The in vitro cytotoxicity study revealed that zein-RVG-Dac_NPs had similar cytotoxicity to the U87 cells as pure Dac in the Dac equivalent concentration range of 10-50 nM. Both zein and RVG29 enhanced the cellular uptake of the NPs to U87 cells with the latter being more efficient than the former.

We also focused on evaluating the in vivo efficacy of this novel nano-system with functional peptide decoration. Animal models were utilized for studying the biodistribution and brain targeting abilities of the NPs, both zein and RVG29 facilitated the BBTB penetration and GBM targeting, although RVG29 was more efficient than zein in this effect. As a result, a significantly higher amount (2.4-fold) of the zein-RVG-Dac_NPs penetrated through the BBTB than that of the zein-Dac_NPs, enabling zein-

RVG-Dac_NPs to present a better therapeutic effect than pure Dac on the orthotopic GBM mice models. In addition, no histopathological changes and side effects were detected in the major organs of the mice after the administration of the zein-RVG-Dac_NP. In summary, the RVG29-conjugated zein NPs are highly potential for drug delivery to the brain to treat brain-related diseases.

The second part was a conformational study for further indicating the entry mechanisms of SARS-CoV-2 into host cells, via RBD of its spike protein to the receptor, ACE2, at molecular level. In the study, the conformational dynamics of highly flexible proteins were identified by using HDX-MS, in solution. Besides evaluating the conformation dynamics of RBDs of SARS-CoV-2 wild type and the Alpha, Beta, Zeta and Kappa, Delta, and Omicron variants, as well as their bindings with ACE2. It appeared to be important to identify the conformational dynamics of ACE2 upon viral acceptance that were closely associated with blocking the viral interactions. It was a comprehensive study for indicating the structural effects of single/combined mutations inside RBDs and further revealed the inner connection between viral conformations and spread properties.

In the study, on the basis of previously reported X-ray structures, we conducted comprehensive comparisons and then referred to the possible effects of mutations inside RBDs among WT RBD and its variants. Interestingly, the mutations positioning at the interfaces led to a more inflexible structure of RBD, at free state, such as N501Y. With viral evolution, the core of RBD presented the decreased flexibility, resulted in a more favorable environmental stability, and subsequently promoted the survival period of

viruses. Besides the significant immune escape detected towards the Beta variant, it showed the significant allosteric effects associated with the combined mutations within the Beta RBD on the conformation of ACE2. As a consequence of another mutation with charge changes (T478K), binding to ACE2 resulted in a notable significant conformational diversification for the Delta variant. The findings firstly explained the possible structural effects that might be built by the mutations with charge changes on the ACE2 receptor. ACE2 was observed with the more rigid edge upon binding to the Omicron RBD. The study indicated several edge regions for the developing of ACE2-targeted antibodies against the possible immune escape of the emerged variants.

In summary, our study supported the hotspots responsible for ACE2 binding, which were consistent with the previous X-ray structure studies, by using another powerful strategy, HDX-MS. This study provided a novel view on the structural effects of the ACE2 receptor, which introduced several regions with great potential for allosteric blocking the viral interactions. These findings selected several variants firstly revealed the conformational dynamics with viral evolution and therefore deserved great attention for possible viral mutations in the future.

References

1. Bondy, M. L.; Scheurer, M. E.; Malmer, B.; Barnholtz-Sloan, J. S.; Davis, F. G.; Il'Yasova, D.; Kruchko, C.; McCarthy, B. J.; Rajaraman, P.; Schwartzbaum, J. A., Brain tumor epidemiology: consensus from the Brain Tumor Epidemiology Consortium. *Cancer* **2008,** *113* (S7), 1953-1968.

2. Ostrom, Q. T.; Barnholtz-Sloan, J. S., Current state of our knowledge on brain tumor epidemiology. *Current neurology and neuroscience reports* **2011,** *11* (3), 329-335.

3. Preusser, M.; De Ribaupierre, S.; Wöhrer, A.; Erridge, S. C.; Hegi, M.; Weller, M.; Stupp, R., Current concepts and management of glioblastoma. *Annals of neurology* **2011,** *70* (1), 9-21.

4. Koo, Y.-E. L.; Reddy, G. R.; Bhojani, M.; Schneider, R.; Philbert, M. A.; Rehemtulla, A.; Ross, B. D.; Kopelman, R., Brain cancer diagnosis and therapy with nanoplatforms. *Advanced drug delivery reviews* **2006,** *58* (14), 1556-1577.

5. Stummer, W.; Pichlmeier, U.; Meinel, T.; Wiestler, O. D.; Zanella, F.; Reulen, H.-J.; Group, A.-G. S., Fluorescence-guided surgery with 5-aminolevulinic acid for resection of malignant glioma: a randomised controlled multicentre phase III trial. *The lancet oncology* **2006,** *7* (5), 392-401.

6. Beez, T.; Sarikaya-Seiwert, S.; Steiger, H.-J.; Hänggi, D., Fluorescence-guided surgery with 5-aminolevulinic acid for resection of brain tumors in children—a technical report. *Acta neurochirurgica* **2014,** *156* (3), 597-604.

7. Mehta, S.; Shah, A.; Jung, H., Diagnosis and treatment options for sequelae following radiation treatment of brain tumors. *Clinical Neurology and Neurosurgery* **2017,** *163*, 1-8.

8. DeAngelis, L. M., Chemotherapy for brain tumors—a new beginning. Mass Medical Soc: 2005; Vol. 352, pp 1036-1038.

9. Rutkowski, S.; Gerber, N. U.; von Hoff, K.; Gnekow, A.; Bode, U.; Graf, N.; Berthold, F.; Henze, G. n.; Wolff, J. E.; Warmuth-Metz, M., Treatment of early childhood medulloblastoma by postoperative chemotherapy and deferred radiotherapy. *Neuro-oncology* **2009,** *11* (2), 201-210.

10. Castro, M. G.; Cowen, R.; Williamson, I. K.; David, A.; Jimenez-Dalmaroni, M. J.; Yuan, X.; Bigliari, A.; Williams, J. C.; Hu, J.; Lowenstein, P. R., Current and future strategies for the treatment of malignant brain tumors. *Pharmacology & therapeutics* **2003,** *98* (1), 71-108.

11. Betz, A. L.; Goldstein, G. W., Polarity of the blood-brain barrier: neutral amino acid transport into isolated brain capillaries. *Science* **1978,** *202* (4364), 225-227.

12. Armulik, A.; Genové, G.; Betsholtz, C., Pericytes: developmental, physiological, and pathological perspectives, problems, and promises. *Developmental cell* **2011,** *21* (2), 193-215.

13. Daneman, R.; Prat, A., The blood–brain barrier. *Cold Spring Harbor perspectives in biology* **2015,** *7* (1), a020412.

14. Van Itallie, C. M.; Holmes, J.; Bridges, A.; Gookin, J. L.; Coccaro, M. R.; Proctor, W.; Colegio, O. R.; Anderson, J. M., The density of small tight junction pores varies among cell types and is increased by expression of claudin-2. *Journal of cell science* **2008,** *121* (3), 298-305.

15. Abbott, N. J.; Patabendige, A. A.; Dolman, D. E.; Yusof, S. R.; Begley, D. J., Structure and function of the blood–brain barrier. *Neurobiology of disease* **2010,** *37* (1), 13-25.

16. Zhang, E. Y.; Knipp, G. T.; Ekins, S.; Swaan, P. W., Structural biology and function of solute transporters: implications for identifying and designing substrates. *Drug metabolism reviews* **2002,** *34* (4), 709-750.

17. Sauer, I.; Dunay, I. R.; Weisgraber, K.; Bienert, M.; Dathe, M., An apolipoprotein E-derived peptide mediates uptake of sterically stabilized liposomes into brain capillary endothelial cells. *Biochemistry* **2005,** *44* (6), 2021-2029.

18. Watkins, S.; Robel, S.; Kimbrough, I. F.; Robert, S. M.; Ellis-Davies, G.; Sontheimer, H., Disruption of astrocyte–vascular coupling and the blood–brain barrier by invading glioma cells. *Nature communications* **2014,** *5* (1), 1-15.

19. Korfel, A.; Thiel, E., Targeted therapy and blood-brain barrier. *Targeted Therapies in Cancer* **2007**, 123-133.

20. Van Tellingen, O.; Yetkin-Arik, B.; De Gooijer, M.; Wesseling, P.; Wurdinger, T.; De Vries, H., Overcoming the blood–brain tumor barrier for effective glioblastoma treatment. *Drug Resistance Updates* **2015,** *19*, 1-12.

21. Prinz, M.; Priller, J., The role of peripheral immune cells in the CNS in steady state and disease. *Nature neuroscience* **2017,** *20* (2), 136-144.

22. Armulik, A.; Genové, G.; Mäe, M.; Nisancioglu, M. H.; Wallgard, E.; Niaudet, C.; He, L.; Norlin, J.; Lindblom, P.; Strittmatter, K., Pericytes regulate the blood–brain barrier. *Nature* **2010,** *468* (7323), 557-561.

23. Banks, W. A., From blood–brain barrier to blood–brain interface: new opportunities for CNS drug delivery. *Nature reviews Drug discovery* **2016,** *15* (4), 275.

24. Park, T.-E.; Mustafaoglu, N.; Herland, A.; Hasselkus, R.; Mannix, R.; FitzGerald, E. A.; Prantil-Baun, R.; Watters, A.; Henry, O.; Benz, M., Hypoxia-enhanced Blood-Brain Barrier Chip recapitulates human barrier function and shuttling of drugs and antibodies. *Nature communications* **2019,** *10* (1), 1-12.

25. Tominaga, N.; Kosaka, N.; Ono, M.; Katsuda, T.; Yoshioka, Y.; Tamura, K.; Lötvall, J.; Nakagama, H.; Ochiya, T., Brain metastatic cancer cells release microRNA-181c-containing extracellular vesicles capable of destructing blood–brain barrier. *Nature communications* **2015,** *6* (1), 1-12.

26. Furtado, D.; Björnmalm, M.; Ayton, S.; Bush, A. I.; Kempe, K.; Caruso, F., Overcoming the blood–brain barrier: the role of nanomaterials in treating neurological diseases. *Advanced Materials* **2018,** *30* (46), 1801362.

27. Park, T.-E.; Singh, B.; Li, H.; Lee, J.-Y.; Kang, S.-K.; Choi, Y.-J.; Cho, C.-S., Enhanced BBB permeability of osmotically active poly (mannitol-co-PEI) modified with rabies virus glycoprotein via selective stimulation of caveolar endocytosis for RNAi therapeutics in Alzheimer's disease. *Biomaterials* **2015,** *38*, 61-71.

28. Ke, W.; Shao, K.; Huang, R.; Han, L.; Liu, Y.; Li, J.; Kuang, Y.; Ye, L.; Lou, J.; Jiang, C., Gene delivery targeted to the brain using an Angiopep-conjugated polyethyleneglycol-modified polyamidoamine dendrimer. *Biomaterials* **2009,** *30* (36), 6976-6985.

29. Sweeney, M. D.; Ayyadurai, S.; Zlokovic, B. V., Pericytes of the neurovascular unit: key functions and signaling pathways. *Nature neuroscience* **2016,** *19* (6), 771-783.

30. Hillaireau, H.; Couvreur, P., Nanocarriers' entry into the cell: relevance to drug delivery. *Cellular and molecular life sciences* **2009,** *66* (17), 2873-2896.

31. Hu, C.-M. J.; Zhang, L., Nanoparticle-based combination therapy toward overcoming drug resistance in cancer. *Biochemical pharmacology* **2012,** *83* (8), 1104-1111.

32. Singh, M., Transferrin as a targeting ligand for liposomes and anticancer drugs. *Current pharmaceutical design* **1999,** *5* (6), 443-452.

33. Kondapi, A. K., Targeting cancer with lactoferrin nanoparticles: recent advances. *Nanomedicine* **2020,** *15* (21), 2071-2083.

34. Sriramoju, B.; Kanwar, R. K.; Kanwar, J. R., Lactoferrin induced neuronal differentiation: A boon for brain tumours. *International Journal of Developmental Neuroscience* **2015,** *41*, 28-36.

35. Xie, H.; Zhu, Y.; Jiang, W.; Zhou, Q.; Yang, H.; Gu, N.; Zhang, Y.; Xu, H.; Xu, H.; Yang, X., Lactoferrin-conjugated superparamagnetic iron oxide nanoparticles as a specific MRI contrast agent for detection of brain glioma in vivo. *Biomaterials* **2011,** *32* (2), 495-502.

36. Marti, U.; Burwen, S. J.; Jones, A. L., Biological effects of epidermal growth factor, with emphasis on the gastrointestinal tract and liver: an update. *Hepatology (Baltimore, Md.)* **1989,** *9* (1), 126-138.

37. Zhang, Y.; Jeong Lee, H.; Boado, R. J.; Pardridge, W. M., Receptor-mediated delivery of an antisense gene to human brain cancer cells. *The Journal of Gene Medicine: A cross-disciplinary journal for research on the science of gene transfer and its clinical applications* **2002,** *4* (2), 183-194.

38. Wells, A., EGF receptor. *The international journal of biochemistry & cell biology* **1999,** *31* (6), 637-643.

39. Bradley, S. V.; Holland, E. C.; Liu, G. Y.; Thomas, D.; Hyun, T. S.; Ross, T. S., Huntingtin interacting protein 1 is a novel brain tumor marker that associates with epidermal growth factor receptor. *Cancer research* **2007,** *67* (8), 3609-3615.

40. Zalcman, N.; Canello, T.; Ovadia, H.; Charbit, H.; Zelikovitch, B.; Mordechai, A.; Fellig, Y.; Rabani, S.; Shahar, T.; Lossos, A., Androgen receptor: a potential therapeutic target for glioblastoma. *Oncotarget* **2018,** *9* (28), 19980.

41. Maletínská, L.; Blakely, E. A.; Bjornstad, K. A.; Deen, D. F.; Knoff, L. J.; Forte, T. M., Human glioblastoma cell lines: levels of low-density lipoprotein receptor and low-density lipoprotein receptor-related protein. *Cancer research* **2000,** *60* (8), 2300-2303.

42. Song, H.; Li, Y.; Lee, J.; Schwartz, A. L.; Bu, G., Low-density lipoprotein receptor-related protein 1 promotes cancer cell migration and invasion by inducing the expression of matrix metalloproteinases 2 and 9. *Cancer research* **2009,** *69* (3), 879-886.

43. Anderson, R. G.; Kamen, B. A.; Rothberg, K. G.; Lacey, S. W., Potocytosis: sequestration and transport of small molecules by caveolae. *Science* **1992,** *255* (5043), 410-411.

44. Sudimack, J.; Lee, R. J., Targeted drug delivery via the folate receptor. *Advanced drug delivery reviews* **2000,** *41* (2), 147-162.

45. Scaranti, M.; Cojocaru, E.; Banerjee, S.; Banerji, U., Exploiting the folate receptor α in oncology. *Nature Reviews Clinical Oncology* **2020,** *17* (6), 349-359.

46. Siu, M. K.; Kong, D. S.; Chan, H. Y.; Wong, E. S.; Ip, P. P.; Jiang, L.; Ngan, H. Y.; Le, X.-F.; Cheung, A. N., Paradoxical impact of two folate receptors, FRα and RFC, in ovarian cancer: effect on cell proliferation, invasion and clinical outcome. *PloS one* **2012,** *7* (11), e47201.

47. Mardilovich, K.; Pankratz, S. L.; Shaw, L. M., Expression and function of the insulin receptor substrate proteins in cancer. *Cell Communication and Signaling* **2009,** *7* (1), 1-15.

48. Egleton, R. D.; Brown, K. C.; Dasgupta, P., Nicotinic acetylcholine receptors in cancer: multiple roles in proliferation and inhibition of apoptosis. *Trends in pharmacological sciences* **2008,** *29* (3), 151-158.

49. Reubi, J. C., In vitro identification of vasoactive intestinal peptide receptors in human tumors: implications for tumor imaging. *Journal of Nuclear Medicine* **1995,** *36* (10), 1846-1853.

50. Dogrukol-Ak, D.; Banks, W. A.; Tuncel, N.; Tuncel, M., Passage of vasoactive intestinal peptide across the blood–brain barrier. *Peptides* **2003,** *24* (3), 437-444.

51. Gozes, I.; Bachar, M.; Bardea, A.; Davidson, A.; Rubinraut, S.; Fridkin, M.; Giladi, E., Protection against developmental retardation in apolipoprotein E-deficient mice by a fatty neuropeptide: Implications for early treatment of Alzheimer's disease. *Journal of neurobiology* **1997,** *33* (3), 329-342.

52. Wei, X.; Zhan, C.; Chen, X.; Hou, J.; Xie, C.; Lu, W., Retro-inverso isomer of Angiopep-2: a stable d-peptide ligand inspires brain-targeted drug delivery. *Molecular pharmaceutics* **2014,** *11* (10), 3261-3268.

53. Kurzrock, R.; Gabrail, N.; Chandhasin, C.; Moulder, S.; Smith, C.; Brenner, A.; Sankhala, K.; Mita, A.; Elian, K.; Bouchard, D., Safety, pharmacokinetics, and activity of GRN1005, a novel conjugate of angiopep-2, a peptide facilitating brain penetration, and paclitaxel, in patients with advanced solid tumors. *Molecular cancer therapeutics* **2012,** *11* (2), 308-316.

54. Hsu, S. P.; Dhawan, U.; Tseng, Y.-Y.; Lin, C.-P.; Kuo, C.-Y.; Wang, L.-F.; Chung, R.-J., Glioma-sensitive delivery of Angiopep-2 conjugated iron gold alloy nanoparticles ensuring simultaneous tumor imaging and hyperthermia mediated cancer theranostics. *Applied Materials Today* **2020,** *18*, 100510.

55. Miller, W. H.; Keenan, R. M.; Willette, R. N.; Lark, M. W., Identification and in vivo efficacy of small-molecule antagonists of integrin αvβ3 (the vitronectin receptor). *Drug discovery today* **2000,** *5* (9), 397-408.

56. Liu, S., Radiolabeled multimeric cyclic RGD peptides as integrin αvβ3 targeted radiotracers for tumor imaging. *Molecular pharmaceutics* **2006,** *3* (5), 472-487.

57. Zako, T.; Nagata, H.; Terada, N.; Utsumi, A.; Sakono, M.; Yohda, M.; Ueda, H.; Soga, K.; Maeda, M., Cyclic RGD peptide-labeled upconversion nanophosphors for tumor cell-targeted imaging. *Biochemical and biophysical research communications* **2009,** *381* (1), 54-58.

58. Chen, C.; Duan, Z.; Yuan, Y.; Li, R.; Pang, L.; Liang, J.; Xu, X.; Wang, J., Peptide-22 and cyclic RGD functionalized liposomes for glioma targeting drug delivery overcoming BBB and BBTB. *ACS applied materials & interfaces* **2017,** *9* (7), 5864-5873.

59. Miura, Y.; Takenaka, T.; Toh, K.; Wu, S.; Nishihara, H.; Kano, M. R.; Ino, Y.; Nomoto, T.; Matsumoto, Y.; Koyama, H., Cyclic RGD-linked polymeric micelles for targeted delivery of platinum anticancer drugs to glioblastoma through the blood–brain tumor barrier. *ACS nano* **2013,** *7* (10), 8583-8592.

60. Arap, W.; Pasqualini, R.; Ruoslahti, E., Cancer treatment by targeted drug delivery to tumor vasculature in a mouse model. *Science* **1998,** *279* (5349), 377-380.

61. Zhao, B.-J.; Ke, X.-Y.; Huang, Y.; Chen, X.-M.; Zhao, X.; Zhao, B.-X.; Lu, W.-l.; Lou, J.-N.; Zhang, X.; Zhang, Q., The antiangiogenic efficacy of NGR-modified PEG–DSPE micelles containing paclitaxel (NGR-M-PTX) for the treatment of glioma in rats. *Journal of Drug Targeting* **2011,** *19* (5), 382-390.

62. Fròsina, G.; Profumo, A.; Marubbi, D.; Marcello, D.; Ravetti, J. L.; Daga, A. J. R. O., ATR kinase inhibitors NVP-BEZ235 and AZD6738 effectively penetrate the brain after systemic administration. *Radiation Oncology* **2018,** *13* (1), 1-7.

63. Brooks, H.; Lebleu, B.; Vivès, E., Tat peptide-mediated cellular delivery: back to basics. *Advanced drug delivery reviews* **2005,** *57* (4), 559-577.

64. Lewin, M.; Carlesso, N.; Tung, C.-H.; Tang, X.-W.; Cory, D.; Scadden, D. T.; Weissleder, R., Tat peptide-derivatized magnetic nanoparticles allow in vivo tracking and recovery of progenitor cells. *Nature biotechnology* **2000,** *18* (4), 410-414.

65. Torchilin, V. P.; Rammohan, R.; Weissig, V.; Levchenko, T. S., TAT peptide on the surface of liposomes affords their efficient intracellular delivery even at low temperature and in the presence of metabolic inhibitors. *Proceedings of the National Academy of Sciences* **2001,** *98* (15), 8786-8791.

66. De la Fuente, J. M.; Berry, C. C., Tat peptide as an efficient molecule to translocate gold nanoparticles into the cell nucleus. *Bioconjugate chemistry* **2005,** *16* (5), 1176-1180.

67. Askarizadeh, A.; Barreto, G. E.; Henney, N. C.; Majeed, M.; Sahebkar, A., Neuroprotection by curcumin: A review on brain delivery strategies. *International journal of pharmaceutics* **2020,** *585*, 119476.

68. Qiao, L.; Yang, H.; Shao, X.-x.; Yin, Q.; Fu, X.-J.; Wei, Q., Research progress on nanoplatforms and nanotherapeutic strategies in treating glioma. *Molecular Pharmaceutics* **2022,** *19* (7), 1927-1951.

69. Kuang, Y.; An, S.; Guo, Y.; Huang, S.; Shao, K.; Liu, Y.; Li, J.; Ma, H.; Jiang, C., T7 peptide-functionalized nanoparticles utilizing RNA interference for glioma dual targeting. *International journal of pharmaceutics* **2013,** *454* (1), 11-20.

70. Wei, L.; Guo, X.-Y.; Yang, T.; Yu, M.-Z.; Chen, D.-W.; Wang, J.-C., Brain tumor-targeted therapy by systemic delivery of siRNA with Transferrin receptor-mediated core-shell nanoparticles. *International journal of pharmaceutics* **2016,** *510* (1), 394-405.

71. Yu, M.; Su, D.; Yang, Y.; Qin, L.; Hu, C.; Liu, R.; Zhou, Y.; Yang, C.; Yang, X.; Wang, G., D-T7 peptide-modified PEGylated bilirubin nanoparticles loaded with cediranib and paclitaxel for antiangiogenesis and chemotherapy of glioma. *ACS applied materials & interfaces* **2018,** *11* (1), 176-186.

72. Lentz, T. L.; Burrage, T. G.; Smith, A. L.; Crick, J.; Tignor, G. H., Is the acetylcholine receptor a rabies virus receptor? *Science* **1982,** *215* (4529), 182-184.

73. You, L.; Wang, J.; Liu, T.; Zhang, Y.; Han, X.; Wang, T.; Guo, S.; Dong, T.; Xu, J.; Anderson, G. J., Targeted brain delivery of rabies virus glycoprotein 29-modified deferoxamine-loaded nanoparticles reverses functional deficits in parkinsonian mice. *Acs Nano* **2018,** *12* (5), 4123-4139.

74. Kumar, P.; Wu, H.; McBride, J. L.; Jung, K.-E.; Hee Kim, M.; Davidson, B. L.; Kyung Lee, S.; Shankar, P.; Manjunath, N., Transvascular delivery of small interfering RNA to the central nervous system. *Nature* **2007,** *448* (7149), 39-43.

75. Mickler, F. M.; Möckl, L.; Ruthardt, N.; Ogris, M.; Wagner, E.; Bräuchle, C., Tuning nanoparticle uptake: live-cell imaging reveals two distinct endocytosis mechanisms mediated by natural and artificial EGFR targeting ligand. *Nano letters* **2012,** *12* (7), 3417-3423.

76. Biscaglia, F.; Rajendran, S.; Conflitti, P.; Benna, C.; Sommaggio, R.; Litti, L.; Mocellin, S.; Bocchinfuso, G.; Rosato, A.; Palleschi, A., Enhanced EGFR targeting activity of plasmonic nanostructures with engineered GE11 peptide. *Advanced healthcare materials* **2017,** *6* (23), 1700596.

77. Jia, Y.; Wang, X.; Hu, D.; Wang, P.; Liu, Q.; Zhang, X.; Jiang, J.; Liu, X.; Sheng, Z.; Liu, B., Phototheranostics: active targeting of orthotopic glioma using biomimetic proteolipid nanoparticles. *ACS nano* **2018,** *13* (1), 386-398.

78. Wang, H.; Wu, Y.; Zhao, R.; Nie, G., Engineering the assemblies of biomaterial nanocarriers for delivery of multiple theranostic agents with enhanced antitumor efficacy. *Advanced materials* **2013,** *25* (11), 1616-1622.

79. Shen, J.; Shao, K.; Zhang, W.; He, Y., Hypoxia-Triggered In Situ Self-Assembly of a Charge Switchable Azo Polymer with AIEgens for Tumor Imaging. *ACS Macro Letters* **2021,** *10* (6), 702-707.

80. Hou, H.; Zhang, D.; Zeng, J.; Zhou, L.; Wang, Z.; Yao, M.; Ren, J.; Hu, N.; Wang, Y., Bilayer Nanocarriers with Protein–Acid Conjugation for Prolonged Release and Enhanced Anticancer Effects. *Langmuir* **2019,** *35* (10), 3710-3716.

81. Hou, H.; Zhang, D.; Lin, J.; Zhang, Y.; Li, C.; Wang, Z.; Ren, J.; Yao, M.; Wong, K.-h.; Wang, Y., Zein-paclitaxel prodrug nanoparticles for redox-triggered drug delivery and enhanced therapeutic efficiency. *Journal of agricultural and food chemistry* **2018,** *66* (44), 11812-11822.

82. Gref, R.; Lück, M.; Quellec, P.; Marchand, M.; Dellacherie, E.; Harnisch, S.; Blunk, T.; Müller, R. H., 'Stealth'corona-core nanoparticles surface modified by polyethylene glycol (PEG): influences of the corona (PEG chain length and surface density) and of the core composition on phagocytic uptake and plasma protein adsorption. *Colloids and Surfaces B: Biointerfaces* **2000,** *18* (3-4), 301-313.

83. van Vlerken, L. E.; Vyas, T. K.; Amiji, M. M., Poly (ethylene glycol)-modified nanocarriers for tumor-targeted and intracellular delivery. *Pharmaceutical research* **2007,** *24* (8), 1405-1414.

84. Zhan, C.; Gu, B.; Xie, C.; Li, J.; Liu, Y.; Lu, W., Cyclic RGD conjugated poly (ethylene glycol)-co-poly (lactic acid) micelle enhances paclitaxel anti-glioblastoma effect. *Journal of Controlled Release* **2010,** *143* (1), 136-142.

85. Xin, H.; Sha, X.; Jiang, X.; Chen, L.; Law, K.; Gu, J.; Chen, Y.; Wang, X.; Fang, X., The brain targeting mechanism of Angiopep-conjugated poly (ethylene glycol)-co-poly (ε-caprolactone) nanoparticles. *Biomaterials* **2012,** *33* (5), 1673-1681.

86. Yang, Z.; Du, Y.; Sun, Q.; Peng, Y.; Wang, R.; Zhou, Y.; Wang, Y.; Zhang, C.; Qi, X., Albumin-based nanotheranostic probe with hypoxia alleviating potentiates synchronous multimodal imaging and phototherapy for glioma. *ACS nano* **2020,** *14* (5), 6191-6212.

87. Cohen, Z. R.; Ramishetti, S.; Peshes-Yaloz, N.; Goldsmith, M.; Wohl, A.; Zibly, Z.; Peer, D., Localized RNAi therapeutics of chemoresistant grade IV glioma using hyaluronan-grafted lipid-based nanoparticles. *ACS nano* **2015,** *9* (2), 1581-1591.

88. Fan, K.; Gao, L.; Yan, X., Human ferritin for tumor detection and therapy. *Wiley Interdisciplinary Reviews: Nanomedicine and Nanobiotechnology* **2013,** *5* (4), 287-298.

89. Fan, K.; Jia, X.; Zhou, M.; Wang, K.; Conde, J. o.; He, J.; Tian, J.; Yan, X., Ferritin nanocarrier traverses the blood brain barrier and kills glioma. *Acs Nano* **2018,** *12* (5), 4105-4115.

90. Li, D.; Gordon, S.; Schwendeman, A.; Remaley, A. T., Apolipoprotein mimetic peptides for stimulating cholesterol efflux. In *Apolipoprotein Mimetics in the Management of Human Disease*, Springer: 2015; pp 29-42.

91. Kuai, R.; Li, D.; Chen, Y. E.; Moon, J. J.; Schwendeman, A., High-density lipoproteins: nature's multifunctional nanoparticles. *ACS nano* **2016,** *10* (3), 3015-3041.

92. Kadiyala, P.; Li, D.; Nuñez, F. M.; Altshuler, D.; Doherty, R.; Kuai, R.; Yu, M.; Kamran, N.; Edwards, M.; Moon, J. J., High-density lipoprotein-mimicking nanodiscs for chemo-immunotherapy against glioblastoma multiforme. *ACS nano* **2019,** *13* (2), 1365-1384.

93. Maeda, H.; Wu, J.; Sawa, T.; Matsumura, Y.; Hori, K., Tumor vascular permeability and the EPR effect in macromolecular therapeutics: a review. *Journal of controlled release* **2000,** *65* (1-2), 271-284.

94. La'Verne, S. J.; Srivastava, S.; Srivastava, S.; Gupta, V. D., Vibrational dynamics of poly (L-glutamine). *Journal of applied polymer science* **2009,** *113* (3), 1406-1414.

95. Miao, Y.; Yang, R.; Deng, D. Y.; Zhang, L.-M., Poly (L-lysine) modified zein nanofibrous membranes as efficient scaffold for adhesion, proliferation, and differentiation of neural stem cells. *Rsc Advances* **2017,** *7* (29), 17711-17719.

96. Melis, M.; Aragoni, M. C.; Arca, M.; Cabras, T.; Caltagirone, C.; Castagnola, M.; Crnjar, R.; Messana, I.; Tepper, B. J.; Barbarossa, I. T., Marked increase in PROP taste responsiveness following oral supplementation with selected salivary proteins or their related free amino acids. *PloS one* **2013,** *8* (3), e59810.

97. Kim, J.-Y.; Choi, W. I.; Kim, Y. H.; Tae, G. J. B., Brain-targeted delivery of protein using chitosan-and RVG peptide-conjugated, pluronic-based nano-carrier. *Biomaterials* **2013,** *34* (4), 1170-1178.

98. Li, Y.; Cai, T.; Zhang, W.; Zhu, W.; Lv, S., Effects of Saikosaponin D on apoptosis in human U87 glioblastoma cells. *Molecular Medicine Reports* **2017,** *16* (2), 1459-1464.

99. Aniento, F.; Emans, N.; Griffiths, G.; Gruenberg, J., Cytoplasmic dynein-dependent vesicular transport from early to late endosomes. *The Journal of cell biology* **1993,** *123* (6), 1373-1387.

100. Lin, F.; de Gooijer, M. C.; Hanekamp, D.; Chandrasekaran, G.; Buil, L. C.; Thota, N.; Sparidans, R. W.; Beijnen, J. H.; Würdinger, T.; van Tellingen, O. J. C. C. R., PI3K–mTOR

pathway inhibition exhibits efficacy against high-grade glioma in clinically relevant mouse models. *Clinical Cancer Research* **2017,** *23* (5), 1286-1298.

101. Zhao, B.; Chen, Y.; Liu, J.; Zhang, L.; Wang, J.; Yang, Y.; Lv, Q.; Xie, M., Blood-brain barrier disruption induced by diagnostic ultrasound combined with microbubbles in mice. *Oncotarget* **2018,** *9* (4), 4897.

102. Dunn, G. P.; Rinne, M. L.; Wykosky, J.; Genovese, G.; Quayle, S. N.; Dunn, I. F.; Agarwalla, P. K.; Chheda, M. G.; Campos, B.; Wang, A. J. G.; development, Emerging insights into the molecular and cellular basis of glioblastoma. *Genes & development* **2012,** *26* (8), 756-784.

103. Lu, R.; Zhao, X.; Li, J.; Niu, P.; Yang, B.; Wu, H.; Wang, W.; Song, H.; Huang, B.; Zhu, N.; Bi, Y.; Ma, X.; Zhan, F.; Wang, L.; Hu, T.; Zhou, H.; Hu, Z.; Zhou, W.; Zhao, L.; Chen, J.; Meng, Y.; Wang, J.; Lin, Y.; Yuan, J.; Xie, Z.; Ma, J.; Liu, W. J.; Wang, D.; Xu, W.; Holmes, E. C.; Gao, G. F.; Wu, G.; Chen, W.; Shi, W.; Tan, W., Genomic characterisation and epidemiology of 2019 novel coronavirus: implications for virus origins and receptor binding. *The Lancet* **2020,** *395* (10224), 565-574.

104. Peiris, J. S. M.; Guan, Y.; Yuen, K. Y., Severe acute respiratory syndrome. *Nature Medicine* **2004,** *10* (12), S88-S97.

105. Yan, R.; Zhang, Y.; Li, Y.; Xia, L.; Guo, Y.; Zhou, Q., Structural basis for the recognition of SARS-CoV-2 by full-length human ACE2. *Science* **2020,** *367* (6485), 1444-1448.

106. Shang, J.; Wan, Y.; Luo, C.; Ye, G.; Geng, Q.; Auerbach, A.; Li, F., Cell entry mechanisms of SARS-CoV-2. *Proceedings of the National Academy of Sciences* **2020,** *117* (21), 11727-11734.

107. Mehdipour, A. R.; Hummer, G., Dual nature of human ACE2 glycosylation in binding to SARS-CoV-2 spike. *Proceedings of the National Academy of Sciences* **2021,** *118* (19).

108. Xiao, T.; Lu, J.; Zhang, J.; Johnson, R. I.; McKay, L. G. A.; Storm, N.; Lavine, C. L.; Peng, H.; Cai, Y.; Rits-Volloch, S., A trimeric human angiotensin-converting enzyme 2 as an anti-SARS-CoV-2 agent. *Nature Structural & Molecular Biology* **2021,** *28* (2), 202-209.

109. Hamming, I.; Timens, W.; Bulthuis, M. L. C.; Lely, A. T.; Navis, G. J. v.; van Goor, H., Tissue distribution of ACE2 protein, the functional receptor for SARS coronavirus. A first step in understanding SARS pathogenesis. *The Journal of Pathology: A Journal of the Pathological Society of Great Britain and Ireland* **2004,** *203* (2), 631-637.

110. Kuba, K.; Imai, Y.; Rao, S.; Gao, H.; Guo, F.; Guan, B.; Huan, Y.; Yang, P.; Zhang, Y.; Deng, W., A crucial role of angiotensin converting enzyme 2 (ACE2) in SARS coronavirus–induced lung injury. *Nature medicine* **2005,** *11* (8), 875-879.

111. Imai, Y.; Kuba, K.; Rao, S.; Huan, Y.; Guo, F.; Guan, B.; Yang, P.; Sarao, R.; Wada, T.; Leong-Poi, H., Angiotensin-converting enzyme 2 protects from severe acute lung failure. *Nature* **2005,** *436* (7047), 112-116.

112. Cao, Y.; Li, L.; Feng, Z.; Wan, S.; Huang, P.; Sun, X.; Wen, F.; Huang, X.; Ning, G.; Wang, W., Comparative genetic analysis of the novel coronavirus (2019-nCoV/SARS-CoV-2) receptor ACE2 in different populations. *Cell discovery* **2020,** *6* (1), 1-4.

113. Letko, M.; Marzi, A.; Munster, V., Functional assessment of cell entry and receptor usage for SARS-CoV-2 and other lineage B betacoronaviruses. *Nature microbiology* **2020,** *5* (4), 562-569.

114. Tai, W.; He, L.; Zhang, X.; Pu, J.; Voronin, D.; Jiang, S.; Zhou, Y.; Du, L., Characterization of the receptor-binding domain (RBD) of 2019 novel coronavirus: implication for development of RBD protein as a viral attachment inhibitor and vaccine. *Cellular & molecular immunology* **2020,** *17* (6), 613-620.

115. Wrapp, D.; Wang, N.; Corbett, K. S.; Goldsmith, J. A.; Hsieh, C.-L.; Abiona, O.; Graham, B. S.; McLellan, J. S., Cryo-EM structure of the 2019-nCoV spike in the prefusion conformation. *Science* **2020,** *367* (6483), 1260-1263.

116. Xiong, X.; Qu, K.; Ciazynska, K. A.; Hosmillo, M.; Carter, A. P.; Ebrahimi, S.; Ke, Z.; Scheres, S. H. W.; Bergamaschi, L.; Grice, G. L., A thermostable, closed SARS-CoV-2 spike protein trimer. *Nature structural & molecular biology* **2020,** *27* (10), 934-941.

117. Cai, Y.; Zhang, J.; Xiao, T.; Peng, H.; Sterling, S. M.; Walsh Jr, R. M.; Rawson, S.; Rits-Volloch, S.; Chen, B., Distinct conformational states of SARS-CoV-2 spike protein. *Science* **2020,** *369* (6511), 1586-1592.

118. Cai, Y.; Zhang, J.; Xiao, T.; Peng, H.; Sterling, S. M.; Walsh, R. M.; Rawson, S.; Rits-Volloch, S.; Chen, B., Distinct conformational states of SARS-CoV-2 spike protein. *Science* **2020,** *369* (6511), 1586-1592.

119. Hoffmann, M.; Kleine-Weber, H.; Schroeder, S.; Krüger, N.; Herrler, T.; Erichsen, S.; Schiergens, T. S.; Herrler, G.; Wu, N.-H.; Nitsche, A., SARS-CoV-2 cell entry depends on ACE2 and TMPRSS2 and is blocked by a clinically proven protease inhibitor. *cell* **2020,** *181* (2), 271-280.

120. Garcia-Beltran, W. F.; Lam, E. C.; Denis, K. S.; Nitido, A. D.; Garcia, Z. H.; Hauser, B. M.; Feldman, J.; Pavlovic, M. N.; Gregory, D. J.; Poznansky, M. C., Multiple SARS-CoV-2 variants escape neutralization by vaccine-induced humoral immunity. *Cell* **2021,** *184* (9), 2372-2383.

121. Fontanet, A.; Autran, B.; Lina, B.; Kieny, M. P.; Karim, S. S. A.; Sridhar, D., SARS-CoV-2 variants and ending the COVID-19 pandemic. *The Lancet* **2021,** *397* (10278), 952-954.

122. Cele, S.; Jackson, L.; Khoury, D. S.; Khan, K.; Moyo-Gwete, T.; Tegally, H.; San, J. E.; Cromer, D.; Scheepers, C.; Amoako, D., SARS-CoV-2 Omicron has extensive but

incomplete escape of Pfizer BNT162b2 elicited neutralization and requires ACE2 for infection. *MedRxiv* **2021**.

123. Abdool Karim, S. S.; de Oliveira, T., New SARS-CoV-2 variants—clinical, public health, and vaccine implications. *New England Journal of Medicine* **2021,** *384* (19), 1866-1868.

124. Liu, H.; Zhang, Q.; Wei, P.; Chen, Z.; Aviszus, K.; Yang, J.; Downing, W.; Jiang, C.; Liang, B.; Reynoso, L., The basis of a more contagious 501Y. V1 variant of SARS-CoV-2. *Cell Research* **2021,** *31* (6), 720-722.

125. Washington, N. L.; Gangavarapu, K.; Zeller, M.; Bolze, A.; Cirulli, E. T.; Barrett, K. M. S.; Larsen, B. B.; Anderson, C.; White, S.; Cassens, T., Emergence and rapid transmission of SARS-CoV-2 B. 1.1. 7 in the United States. *Cell* **2021,** *184* (10), 2587-2594.

126. Collier, D. A.; De Marco, A.; Ferreira, I. A. T. M.; Meng, B.; Datir, R. P.; Walls, A. C.; Kemp, S. A.; Bassi, J.; Pinto, D.; Silacci-Fregni, C., Sensitivity of SARS-CoV-2 B. 1.1. 7 to mRNA vaccine-elicited antibodies. *Nature* **2021,** *593* (7857), 136-141.

127. Socher, E.; Conrad, M.; Heger, L.; Paulsen, F.; Sticht, H.; Zunke, F.; Arnold, P., Computational decomposition reveals reshaping of the SARS-CoV-2–ACE2 interface among viral variants expressing the N501Y mutation. *Journal of cellular biochemistry* **2021,** *122* (12), 1863-1872.

128. Yang, T.-J.; Yu, P.-Y.; Chang, Y.-C.; Liang, K.-H.; Tso, H.-C.; Ho, M.-R.; Chen, W.-Y.; Lin, H.-T.; Wu, H.-C.; Hsu, S.-T. D., Effect of SARS-CoV-2 B. 1.1. 7 mutations on spike protein structure and function. *Nature Structural & Molecular Biology* **2021**, 1-9.

129. Zhu, X.; Mannar, D.; Srivastava, S. S.; Berezuk, A. M.; Demers, J.-P.; Saville, J. W.; Leopold, K.; Li, W.; Dimitrov, D. S.; Tuttle, K. S., Cryo-electron microscopy structures of the N501Y SARS-CoV-2 spike protein in complex with ACE2 and 2 potent neutralizing antibodies. *PLoS biology* **2021,** *19* (4), e3001237.

130. Tegally, H.; Wilkinson, E.; Giovanetti, M.; Iranzadeh, A.; Fonseca, V.; Giandhari, J.; Doolabh, D.; Pillay, S.; San, E. J.; Msomi, N., Detection of a SARS-CoV-2 variant of concern in South Africa. *Nature* **2021,** *592* (7854), 438-443.

131. Wang, P.; Nair, M. S.; Liu, L.; Iketani, S.; Luo, Y.; Guo, Y.; Wang, M.; Yu, J.; Zhang, B.; Kwong, P. D., Antibody resistance of SARS-CoV-2 variants B. 1.351 and B. 1.1. 7. *Nature* **2021,** *593* (7857), 130-135.

132. Wibmer, C. K.; Ayres, F.; Hermanus, T.; Madzivhandila, M.; Kgagudi, P.; Oosthuysen, B.; Lambson, B. E.; De Oliveira, T.; Vermeulen, M.; Van der Berg, K., SARS-CoV-2 501Y. V2 escapes neutralization by South African COVID-19 donor plasma. *Nature medicine* **2021,** *27* (4), 622-625.

133. Bhattarai, N.; Baral, P.; Gerstman, B. S.; Chapagain, P. P., Structural and Dynamical Differences in the Spike Protein RBD in the SARS-CoV-2 Variants B. 1.1. 7 and B. 1.351. *The Journal of Physical Chemistry B* **2021**.

134. Khan, A.; Zia, T.; Suleman, M.; Khan, T.; Ali, S. S.; Abbasi, A. A.; Mohammad, A.; Wei, D. Q., Higher infectivity of the SARS-CoV-2 new variants is associated with K417N/T, E484K, and N501Y mutants: An insight from structural data. *Journal of cellular physiology* **2021**.

135. Nelson, G.; Buzko, O.; Spilman, P. R.; Niazi, K.; Rabizadeh, S.; Soon-Shiong, P. R., Molecular dynamic simulation reveals E484K mutation enhances spike RBD-ACE2 affinity and the combination of E484K, K417N and N501Y mutations (501Y. V2 variant) induces conformational change greater than N501Y mutant alone, potentially resulting in an escape mutant. *BioRxiv* **2021**.

136. Bhattarai, N.; Baral, P.; Gerstman, B. S.; Chapagain, P. P., Structural and dynamical differences in the spike protein RBD in the SARS-CoV-2 variants B. 1.1. 7 and B. 1.351. *The Journal of Physical Chemistry B* **2021,** *125* (26), 7101-7107.

137. Yuan, M.; Huang, D.; Lee, C.-C. D.; Wu, N. C.; Jackson, A. M.; Zhu, X.; Liu, H.; Peng, L.; van Gils, M. J.; Sanders, R. W., Structural and functional ramifications of antigenic drift in recent SARS-CoV-2 variants. *Science* **2021**.

138. Wang, W. B.; Liang, Y.; Jin, Y. Q.; Zhang, J.; Su, J. G.; Li, Q. M., E484K mutation in SARS-CoV-2 RBD enhances binding affinity with hACE2 but reduces interactions with neutralizing antibodies and nanobodies: Binding free energy calculation studies. *Journal of Molecular Graphics and Modelling* **2021,** *109*, 108035.

139. Jangra, S.; Ye, C.; Rathnasinghe, R.; Stadlbauer, D.; Alshammary, H.; Amoako, A. A.; Awawda, M. H.; Beach, K. F.; Bermúdez-González, M. C.; Chernet, R. L., SARS-CoV-2 spike E484K mutation reduces antibody neutralisation. *The Lancet Microbe* **2021,** *2* (7), e283-e284.

140. Chen, R. E.; Zhang, X.; Case, J. B.; Winkler, E. S.; Liu, Y.; VanBlargan, L. A.; Liu, J.; Errico, J. M.; Xie, X.; Suryadevara, N., Resistance of SARS-CoV-2 variants to neutralization by monoclonal and serum-derived polyclonal antibodies. *Nature medicine* **2021,** *27* (4), 717-726.

141. Liu, Z.; VanBlargan, L. A.; Bloyet, L.-M.; Rothlauf, P. W.; Chen, R. E.; Stumpf, S.; Zhao, H.; Errico, J. M.; Theel, E. S.; Liebeskind, M. J., Identification of SARS-CoV-2 spike mutations that attenuate monoclonal and serum antibody neutralization. *Cell host & microbe* **2021,** *29* (3), 477-488.

142. Singh, J.; Rahman, S. A.; Ehtesham, N. Z.; Hira, S.; Hasnain, S. E., SARS-CoV-2 variants of concern are emerging in India. *Nature medicine* **2021**, 1-3.

143. Deng, X.; Garcia-Knight, M. A.; Khalid, M. M.; Servellita, V.; Wang, C.; Morris, M. K.; Sotomayor-González, A.; Glasner, D. R.; Reyes, K. R.; Gliwa, A. S., Transmission, infectivity, and neutralization of a spike L452R SARS-CoV-2 variant. *Cell* **2021**.

144. Motozono, C.; Toyoda, M.; Zahradnik, J.; Saito, A.; Nasser, H.; Tan, T. S.; Ngare, I.; Kimura, I.; Uriu, K.; Kosugi, Y., SARS-CoV-2 spike L452R variant evades cellular immunity and increases infectivity. *Cell host & microbe* **2021,** *29* (7), 1124-1136.

145. Starr, T. N.; Greaney, A. J.; Dingens, A. S.; Bloom, J. D., Complete map of SARS-CoV-2 RBD mutations that escape the monoclonal antibody LY-CoV555 and its cocktail with LY-CoV016. *Cell Reports Medicine* **2021,** *2* (4), 100255.

146. Khan, A.; Wei, D. Q.; Kousar, K.; Abubaker, J.; Ahmad, S.; Ali, J.; Al-Mulla, F.; Ali, S. S.; Nizam-Uddin, N.; Sayaf, A. M., Preliminary Structural Data Revealed That the SARS-CoV-2 B. 1.617 Variant's RBD Binds to ACE2 Receptor Stronger Than the Wild Type to Enhance the Infectivity. *ChemBioChem* **2021,** *22* (16), 2641.

147. Antony, P.; Vijayan, R., Molecular Dynamics Simulation Study of the Interaction between Human Angiotensin Converting Enzyme 2 and Spike Protein Receptor Binding Domain of the SARS-CoV-2 B. 1.617 Variant. *Biomolecules* **2021,** *11* (8), 1244.

148. Ferreira, I. A. T. M.; Kemp, S. A.; Datir, R.; Saito, A.; Meng, B.; Rakshit, P.; Takaori-Kondo, A.; Kosugi, Y.; Uriu, K.; Kimura, I., SARS-CoV-2 B. 1.617 mutations L452R and E484Q are not synergistic for antibody evasion. *The Journal of infectious diseases* **2021,** *224* (6), 989-994.

149. Liu, Y.; Rocklöv, J., The reproductive number of the Delta variant of SARS-CoV-2 is far higher compared to the ancestral SARS-CoV-2 virus. *Journal of travel medicine* **2021**.

150. Mlcochova, P.; Kemp, S. A.; Dhar, M. S.; Papa, G.; Meng, B.; Ferreira, I. A. T. M.; Datir, R.; Collier, D. A.; Albecka, A.; Singh, S., SARS-CoV-2 B. 1.617. 2 Delta variant replication and immune evasion. *Nature* **2021,** *599* (7883), 114-119.

151. Li, B.; Deng, A.; Li, K.; Hu, Y.; Li, Z.; Shi, Y.; Xiong, Q.; Liu, Z.; Guo, Q.; Zou, L., Viral infection and transmission in a large, well-traced outbreak caused by the SARS-CoV-2 Delta variant. *Nature Communications* **2022,** *13* (1), 1-9.

152. Zhang, J.; Xiao, T.; Cai, Y.; Lavine, C. L.; Peng, H.; Zhu, H.; Anand, K.; Tong, P.; Gautam, A.; Mayer, M. L., Membrane fusion and immune evasion by the spike protein of SARS-CoV-2 Delta variant. *Science* **2021,** *374* (6573), 1353-1360.

153. Dhar, M. S.; Marwal, R.; Vs, R.; Ponnusamy, K.; Jolly, B.; Bhoyar, R. C.; Sardana, V.; Naushin, S.; Rophina, M.; Mellan, T. A., Genomic characterization and epidemiology of an emerging SARS-CoV-2 variant in Delhi, India. *Science* **2021,** *374* (6570), 995-999.

154. Collier, A.-R. Y.; Brown, C. M.; McMahan, K. A.; Yu, J.; Liu, J.; Jacob-Dolan, C.; Chandrashekar, A.; Tierney, D.; Ansel, J. L.; Rowe, M., Characterization of immune responses in fully vaccinated individuals after breakthrough infection with the SARS-CoV-2 delta variant. *Science translational medicine* **2022,** *14* (641), eabn6150.

155. Farinholt, T.; Doddapaneni, H.; Qin, X.; Menon, V.; Meng, Q.; Metcalf, G.; Chao, H.; Gingras, M.-C.; Avadhanula, V.; Farinholt, P., Transmission event of SARS-CoV-2 Delta variant reveals multiple vaccine breakthrough infections. *BMC medicine* **2021,** *19* (1), 1-6.

156. Baral, P.; Bhattarai, N.; Hossen, M. L.; Stebliankin, V.; Gerstman, B. S.; Narasimhan, G.; Chapagain, P. P., Mutation-induced changes in the receptor-binding interface of the SARS-CoV-2 Delta variant B. 1.617. 2 and implications for immune evasion. *Biochemical and biophysical research communications* **2021,** *574*, 14-19.

157. Wang, Y.; Liu, C.; Zhang, C.; Wang, Y.; Hong, Q.; Xu, S.; Li, Z.; Yang, Y.; Huang, Z.; Cong, Y., Structural basis for SARS-CoV-2 Delta variant recognition of ACE2 receptor and broadly neutralizing antibodies. *Nature communications* **2022,** *13* (1), 1-12.

158. Karim, S. S. A.; Karim, Q. A., Omicron SARS-CoV-2 variant: a new chapter in the COVID-19 pandemic. *The Lancet* **2021,** *398* (10317), 2126-2128.

159. Shu, Y.; McCauley, J., GISAID: Global initiative on sharing all influenza data–from vision to reality. *Eurosurveillance* **2017,** *22* (13), 30494.

160. Wang, L.; Cheng, G., Sequence analysis of the emerging SARS-CoV-2 variant Omicron in South Africa. *Journal of medical virology* **2022,** *94* (4), 1728-1733.

161. Kumar, S.; Thambiraja, T. S.; Karuppanan, K.; Subramaniam, G., Omicron and Delta variant of SARS-CoV-2: a comparative computational study of spike protein. *Journal of medical virology* **2022,** *94* (4), 1641-1649.

162. Cui, Z.; Liu, P.; Wang, N.; Wang, L.; Fan, K.; Zhu, Q.; Wang, K.; Chen, R.; Feng, R.; Jia, Z., Structural and functional characterizations of infectivity and immune evasion of SARS-CoV-2 Omicron. *Cell* **2022,** *185* (5), 860-871.

163. Zhang, X.; Wu, S.; Wu, B.; Yang, Q.; Chen, A.; Li, Y.; Zhang, Y.; Pan, T.; Zhang, H.; He, X., SARS-CoV-2 Omicron strain exhibits potent capabilities for immune evasion and viral entrance. *Signal transduction and targeted therapy* **2021,** *6* (1), 1-3.

164. Hu, J.; Peng, P.; Cao, X.; Wu, K.; Chen, J.; Wang, K.; Tang, N.; Huang, A.-l., Increased immune escape of the new SARS-CoV-2 variant of concern Omicron. *Cellular & molecular immunology* **2022**, 1-3.

165. Liu, J.; Chandrashekar, A.; Sellers, D.; Barrett, J.; Jacob-Dolan, C.; Lifton, M.; McMahan, K.; Sciacca, M.; VanWyk, H.; Wu, C., Vaccines elicit highly conserved cellular immunity to SARS-CoV-2 Omicron. *Nature* **2022,** *603* (7901), 493-496.

166. Han, P.; Li, L.; Liu, S.; Wang, Q.; Zhang, D.; Xu, Z.; Han, P.; Li, X.; Peng, Q.; Su, C., Receptor binding and complex structures of human ACE2 to spike RBD from omicron and delta SARS-CoV-2. *Cell* **2022,** *185* (4), 630-640.

167. Lan, J.; He, X.; Ren, Y.; Wang, Z.; Zhou, H.; Fan, S.; Zhu, C.; Liu, D.; Shao, B.; Liu, T.-Y., Structural insights into the SARS-CoV-2 Omicron RBD-ACE2 interaction. *Cell research* **2022,** *32* (6), 593-595.

168. Yin, W.; Xu, Y.; Xu, P.; Cao, X.; Wu, C.; Gu, C.; He, X.; Wang, X.; Huang, S.; Yuan, Q., Structures of the Omicron Spike trimer with ACE2 and an anti-Omicron antibody. *Science* **2022,** *375* (6584), 1048-1053.

169. Smyth, M. S.; Martin, J. H. J., x Ray crystallography. *Molecular Pathology* **2000,** *53* (1), 8.

170. Shang, J.; Ye, G.; Shi, K.; Wan, Y.; Luo, C.; Aihara, H.; Geng, Q.; Auerbach, A.; Li, F., Structural basis of receptor recognition by SARS-CoV-2. *Nature* **2020,** *581* (7807), 221-224.

171. Kühlbrandt, W., Microscopy: cryo-EM enters a new era. *elife* **2014,** *3*, e03678.

172. Yuan, Y.; Cao, D.; Zhang, Y.; Ma, J.; Qi, J.; Wang, Q.; Lu, G.; Wu, Y.; Yan, J.; Shi, Y., Cryo-EM structures of MERS-CoV and SARS-CoV spike glycoproteins reveal the dynamic receptor binding domains. *Nature communications* **2017,** *8* (1), 1-9.

173. Xu, C.; Wang, Y.; Liu, C.; Zhang, C.; Han, W.; Hong, X.; Wang, Y.; Hong, Q.; Wang, S.; Zhao, Q., Conformational dynamics of SARS-CoV-2 trimeric spike glycoprotein in complex with receptor ACE2 revealed by cryo-EM. *Science advances* **2021,** *7* (1), eabe5575.

174. Song, W.; Gui, M.; Wang, X.; Xiang, Y., Cryo-EM structure of the SARS coronavirus spike glycoprotein in complex with its host cell receptor ACE2. *PLoS pathogens* **2018,** *14* (8), e1007236.

175. Fan, X.; Cao, D.; Kong, L.; Zhang, X., Cryo-EM analysis of the post-fusion structure of the SARS-CoV spike glycoprotein. *Nature communications* **2020,** *11* (1), 1-10.

176. Yan, L.; Ge, J.; Zheng, L.; Zhang, Y.; Gao, Y.; Wang, T.; Huang, Y.; Yang, Y.; Gao, S.; Li, M., Cryo-EM structure of an extended SARS-CoV-2 replication and transcription complex reveals an intermediate state in cap synthesis. *Cell* **2021,** *184* (1), 184-193.

177. Wang, P.; Casner, R. G.; Nair, M. S.; Wang, M.; Yu, J.; Cerutti, G.; Liu, L.; Kwong, P. D.; Huang, Y.; Shapiro, L., Increased resistance of SARS-CoV-2 variant P. 1 to antibody neutralization. *Cell host & microbe* **2021,** *29* (5), 747-751.

178. Mannar, D.; Saville, J. W.; Zhu, X.; Srivastava, S. S.; Berezuk, A. M.; Tuttle, K. S.; Marquez, A. C.; Sekirov, I.; Subramaniam, S., SARS-CoV-2 Omicron variant: Antibody evasion and cryo-EM structure of spike protein–ACE2 complex. *Science* **2022,** *375* (6582), 760-764.

179. Smoluchowski, M. v., Versuch einer mathematischen Theorie der Koagulationskinetik kolloider Lösungen. *Zeitschrift für physikalische Chemie* **1918,** *92* (1), 129-168.

180. Barton, M. I.; MacGowan, S. A.; Kutuzov, M. A.; Dushek, O.; Barton, G. J.; Van Der Merwe, P. A., Effects of common mutations in the SARS-CoV-2 Spike RBD and its ligand, the human ACE2 receptor on binding affinity and kinetics. *Elife* **2021,** *10*, e70658.

181. Yuan, M.; Huang, D.; Lee, C.-C. D.; Wu, N. C.; Jackson, A. M.; Zhu, X.; Liu, H.; Peng, L.; Van Gils, M. J.; Sanders, R. W., Structural and functional ramifications of antigenic drift in recent SARS-CoV-2 variants. *Science* **2021,** *373* (6556), 818-823.

182. Wu, L.; Zhou, L.; Mo, M.; Liu, T.; Wu, C.; Gong, C.; Lu, K.; Gong, L.; Zhu, W.; Xu, Z., SARS-CoV-2 Omicron RBD shows weaker binding affinity than the currently dominant Delta variant to human ACE2. *Signal transduction and targeted therapy* **2022,** *7* (1), 1-3.

183. Luan, B.; Wang, H.; Huynh, T., Enhanced binding of the N501Y-mutated SARS-CoV-2 spike protein to the human ACE2 receptor: insights from molecular dynamics simulations. *FEBS letters* **2021,** *595* (10), 1454-1461.

184. Williams, J. K.; Wang, B.; Sam, A.; Hoop, C. L.; Case, D. A.; Baum, J., Molecular dynamics analysis of a flexible loop at the binding interface of the SARS-CoV-2 spike protein receptor-binding domain. *Proteins: Structure, Function, and Bioinformatics* **2022,** *90* (5), 1044-1053.

185. Socher, E.; Heger, L.; Paulsen, F.; Zunke, F.; Arnold, P., Molecular dynamics simulations of the delta and omicron SARS-CoV-2 spike–ACE2 complexes reveal distinct changes between both variants. *Computational and structural biotechnology journal* **2022,** *20*, 1168-1176.

186. Nelson, G.; Buzko, O.; Spilman, P.; Niazi, K.; Rabizadeh, S.; Soon-Shiong, P., Molecular dynamic simulation reveals E484K mutation enhances spike RBD-ACE2 affinity and the combination of E484K, K417N and N501Y mutations (501Y. V2 variant) induces conformational change greater than N501Y mutant alone, potentially resulting in an escape mutant. *BioRxiv* **2021**.

187. Hvidt, A.; Linderstrøm-Lang, K., Exchange of hydrogen atoms in insulin with deuterium atoms in aqueous solutions. *Biochimica et biophysica acta* **1954,** *14* (4), 574-575.

188. Hvidt, A.; Linderstrom-Lang, K., The kinetics of the deuterium exchange of insulin with D2O; an amendment. *Biochimica et biophysica acta* **1955,** *16* (1), 168-169.

189. Benson, E. E.; Linderstrøm-Lang, K., Deuterium exchange between myoglobin and water. *Biochimica et biophysica acta* **1959,** *32*, 579-581.

190. Molday, R. S.; Englander, S. W.; Kallen, R. G., Primary structure effects on peptide group hydrogen exchange. *Biochemistry* **1972,** *11* (2), 150-158.

191. Tanaka, K.; Waki, H.; Ido, Y.; Akita, S.; Yoshida, Y.; Yoshida, T.; Matsuo, T., Protein and polymer analyses up to m/z 100 000 by laser ionization time-of-flight mass spectrometry. *Rapid communications in mass spectrometry* **1988,** *2* (8), 151-153.

192. Fenn, J. B.; Mann, M.; Meng, C. K.; Wong, S. F.; Whitehouse, C. M., Electrospray ionization for mass spectrometry of large biomolecules. *Science* **1989,** *246* (4926), 64-71.

193. Engen, J. R.; Smith, D. L., Peer Reviewed: Investigating Protein Structure and Dynamics by Hydrogen Exchange MS. *Anal. Chem* **2008,** *73*, 256.

194. Smith, D. L.; Deng, Y.; Zhang, Z., Probing the non-covalent structure of proteins by amide hydrogen exchange and mass spectrometry. *Journal of mass spectrometry* **1997,** *32* (2), 135-146.

195. Oganesyan, I.; Lento, C.; Wilson, D. J., Contemporary hydrogen deuterium exchange mass spectrometry. *Methods* **2018,** *144*, 27-42.

196. Englander, S. W.; Mayne, L.; Krishna, M. M. G., Protein folding and misfolding: mechanism and principles. *Quarterly reviews of biophysics* **2007,** *40* (4), 1-41.

197. Weis, D. D.; Wales, T. E.; Engen, J. R.; Hotchko, M.; Ten Eyck, L. F., Identification and characterization of EX1 kinetics in H/D exchange mass spectrometry by peak width analysis. *Journal of the American Society for Mass Spectrometry* **2006,** *17* (11), 1498-1509.

198. Lanucara, F.; Holman, S. W.; Gray, C. J.; Eyers, C. E., The power of ion mobility-mass spectrometry for structural characterization and the study of conformational dynamics. *Nature chemistry* **2014,** *6* (4), 281-294.

199. Cryar, A.; Groves, K.; Quaglia, M., Online hydrogen-deuterium exchange traveling wave ion mobility mass spectrometry (HDX-IM-MS): a systematic evaluation. *Journal of the American Society for Mass Spectrometry* **2017,** *28* (6), 1192-1202.

200. Black, W. A.; Stocks, B. B.; Mellors, J. S.; Engen, J. R.; Ramsey, J. M., Utilizing microchip capillary electrophoresis electrospray ionization for hydrogen exchange mass spectrometry. *Analytical chemistry* **2015,** *87* (12), 6280-6287.

201. Masson, G. R.; Jenkins, M. L.; Burke, J. E., An overview of hydrogen deuterium exchange mass spectrometry (HDX-MS) in drug discovery. *Expert opinion on drug discovery* **2017,** *12* (10), 981-994.

202. Wei, H.; Mo, J.; Tao, L.; Russell, R. J.; Tymiak, A. A.; Chen, G.; Iacob, R. E.; Engen, J. R., Hydrogen/deuterium exchange mass spectrometry for probing higher order structure of protein therapeutics: methodology and applications. *Drug discovery today* **2014,** *19* (1), 95-102.

203. Deng, Y.; Zhang, Z.; Smith, D. L., Comparison of continuous and pulsed labeling amide hydrogen exchange/mass spectrometry for studies of protein dynamics. *Journal of the American Society for Mass Spectrometry* **1999,** *10* (8), 675-684.

204. Englander, S. W.; Mayne, L., The nature of protein folding pathways. *Proceedings of the National Academy of Sciences* **2014,** *111* (45), 15873-15880.

205. Cravello, L.; Lascoux, D.; Forest, E., Use of different proteases working in acidic conditions to improve sequence coverage and resolution in hydrogen/deuterium exchange of large proteins. *Rapid communications in mass spectrometry* **2003,** *17* (21), 2387-2393.

206. Zhang, H.-M.; Kazazic, S.; Schaub, T. M.; Tipton, J. D.; Emmett, M. R.; Marshall, A. G., Enhanced digestion efficiency, peptide ionization efficiency, and sequence resolution for protein hydrogen/deuterium exchange monitored by Fourier transform ion cyclotron resonance mass spectrometry. *Analytical chemistry* **2008,** *80* (23), 9034-9041.

207. Marcoux, J.; Thierry, E.; Vivès, C.; Signor, L.; Fieschi, F.; Forest, E., Investigating alternative acidic proteases for H/D exchange coupled to mass spectrometry: plasmepsin 2 but not plasmepsin 4 is active under quenching conditions. *Journal of the American Society for Mass Spectrometry* **2010,** *21* (1), 76-79.

208. Kazazic, S.; Zhang, H.-M.; Schaub, T. M.; Emmett, M. R.; Hendrickson, C. L.; Blakney, G. T.; Marshall, A. G., Automated data reduction for hydrogen/deuterium exchange experiments, enabled by high-resolution Fourier transform ion cyclotron resonance mass spectrometry. *Journal of the American Society for Mass Spectrometry* **2011,** *21* (4), 550-558.

209. Zhang, Z.; Zhang, A.; Xiao, G., Improved protein hydrogen/deuterium exchange mass spectrometry platform with fully automated data processing. *Analytical chemistry* **2012,** *84* (11), 4942-4949.

210. Gattiker, A.; Bienvenut, W. V.; Bairoch, A.; Gasteiger, E., FindPept, a tool to identify unmatched masses in peptide mass fingerprinting protein identification. *Proteomics* **2002,** *2* (10), 1435-1444.

211. Prieto, G.; Aloria, K.; Osinalde, N.; Fullaondo, A.; Arizmendi, J. M.; Matthiesen, R., PAnalyzer: a software tool for protein inference in shotgun proteomics. *BMC bioinformatics* **2012,** *13* (1), 1-8.

212. Claesen, J.; Burzykowski, T., Computational methods and challenges in hydrogen/deuterium exchange mass spectrometry. *Mass spectrometry reviews* **2017,** *36* (5), 649-667.

213. Konermann, L.; Pan, J.; Liu, Y.-H., Hydrogen exchange mass spectrometry for studying protein structure and dynamics. *Chemical Society Reviews* **2011,** *40* (3), 1224-1234.

214. Walters, B. T.; Ricciuti, A.; Mayne, L.; Englander, S. W., Minimizing back exchange in the hydrogen exchange-mass spectrometry experiment. *Journal of the American Society for Mass Spectrometry* **2012,** *23* (12), 2132-2139.

215. Zhang, H.-M.; McLoughlin, S. M.; Frausto, S. D.; Tang, H.; Emmett, M. R.; Marshall, A. G., Simultaneous reduction and digestion of proteins with disulfide bonds for hydrogen/deuterium exchange monitored by mass spectrometry. *Analytical chemistry* **2010,** *82* (4), 1450-1454.

216. Vadas, O.; Jenkins, M. L.; Dornan, G. L.; Burke, J. E., Using hydrogen–deuterium exchange mass spectrometry to examine protein–membrane interactions. *Methods in enzymology* **2017,** *583*, 143-172.

217. Huang, L.; So, P.-K.; Chen, Y. W.; Leung, Y.-C.; Yao, Z.-P., Conformational dynamics of the helix 10 region as an allosteric site in class A β-lactamase inhibitory binding. *Journal of the American Chemical Society* **2020,** *142* (32), 13756-13767.

218. Wong, S. K.; Li, W.; Moore, M. J.; Choe, H.; Farzan, M., A 193-amino acid fragment of the SARS coronavirus S protein efficiently binds angiotensin-converting enzyme 2. *Journal of Biological Chemistry* **2004,** *279* (5), 3197-3201.

219. Suryamohan, K.; Diwanji, D.; Stawiski, E. W.; Gupta, R.; Miersch, S.; Liu, J.; Chen, C.; Jiang, Y.-P.; Fellouse, F. A.; Sathirapongsasuti, J. F., Human ACE2 receptor polymorphisms and altered susceptibility to SARS-CoV-2. *Communications biology* **2021,** *4* (1), 1-11.

220. Raghuvamsi, P. V.; Tulsian, N. K.; Samsudin, F.; Qian, X.; Purushotorman, K.; Yue, G.; Kozma, M. M.; Hwa, W. Y.; Lescar, J.; Bond, P. J., SARS-CoV-2 S protein: ACE2 interaction reveals novel allosteric targets. *Elife* **2021,** *10*, e63646.

221. Cerutti, G.; Guo, Y.; Liu, L.; Liu, L.; Zhang, Z.; Luo, Y.; Huang, Y.; Wang, H. H.; Ho, D. D.; Sheng, Z., Cryo-EM structure of the SARS-CoV-2 Omicron spike. *Cell reports* **2022,** *38* (9), 110428.

222. Liu, C.; Ginn, H. M.; Dejnirattisai, W.; Supasa, P.; Wang, B.; Tuekprakhon, A.; Nutalai, R.; Zhou, D.; Mentzer, A. J.; Zhao, Y., Reduced neutralization of SARS-CoV-2 B. 1.617 by vaccine and convalescent serum. *Cell* **2021,** *184* (16), 4220-4236.

223. Sztain, T.; Ahn, S.-H.; Bogetti, A. T.; Casalino, L.; Goldsmith, J. A.; Seitz, E.; McCool, R. S.; Kearns, F. L.; Acosta-Reyes, F.; Maji, S., A glycan gate controls opening of the SARS-CoV-2 spike protein. *Nature Chemistry* **2021,** *13* (10), 963-968.

224. Huang, H.-Y.; Liao, H.-Y.; Chen, X.; Wang, S.-W.; Cheng, C.-W.; Shahed-Al-Mahmud, M.; Liu, Y.-M.; Mohapatra, A.; Chen, T.-H.; Lo, J. M., Vaccination with SARS-CoV-2 spike protein lacking glycan shields elicits enhanced protective responses in animal models. *Science Translational Medicine* **2022**, eabm0899.

225. Alaofi, A. L.; Shahid, M., Mutations of SARS-CoV-2 RBD may alter its molecular structure to improve its infection efficiency. *Biomolecules* **2021,** *11* (9), 1273.

226. Li, Q.; Nie, J.; Wu, J.; Zhang, L.; Ding, R.; Wang, H.; Zhang, Y.; Li, T.; Liu, S.; Zhang, M., SARS-CoV-2 501Y. V2 variants lack higher infectivity but do have immune escape. *Cell* **2021,** *184* (9), 2362-2371.

227. Dejnirattisai, W.; Zhou, D.; Supasa, P.; Liu, C.; Mentzer, A. J.; Ginn, H. M.; Zhao, Y.; Duyvesteyn, H. M. E.; Tuekprakhon, A.; Nutalai, R., Antibody evasion by the P. 1 strain of SARS-CoV-2. *Cell* **2021,** *184* (11), 2939-2954.

228. Lan, J.; Ge, J.; Yu, J.; Shan, S.; Zhou, H.; Fan, S.; Zhang, Q.; Shi, X.; Wang, Q.; Zhang, L., Structure of the SARS-CoV-2 spike receptor-binding domain bound to the ACE2 receptor. *Nature* **2020,** *581* (7807), 215-220.

229. Ahamad, S.; Hema, K.; Ahmad, S.; Kumar, V.; Gupta, D., Insights into the structure and dynamics of SARS-CoV-2 spike glycoprotein double mutant L452R-E484Q. *3 Biotech* **2022,** *12* (4), 1-11.

230. Kumar, V.; Singh, J.; Hasnain, S. E.; Sundar, D., Possible link between higher transmissibility of alpha, kappa and delta variants of SARS-CoV-2 and increased structural stability of its spike protein and hACE2 affinity. *International journal of molecular sciences* **2021,** *22* (17), 9131.

231. Starr, T. N.; Greaney, A. J.; Hilton, S. K.; Ellis, D.; Crawford, K. H. D.; Dingens, A. S.; Navarro, M. J.; Bowen, J. E.; Tortorici, M. A.; Walls, A. C., Deep mutational scanning of SARS-CoV-2 receptor binding domain reveals constraints on folding and ACE2 binding. *cell* **2020,** *182* (5), 1295-1310.

232. McCallum, M.; Walls, A. C.; Sprouse, K. R.; Bowen, J. E.; Rosen, L. E.; Dang, H. V.; De Marco, A.; Franko, N.; Tilles, S. W.; Logue, J., Molecular basis of immune evasion by the Delta and Kappa SARS-CoV-2 variants. *Science* **2021,** *374* (6575), 1621-1626.

233. Zhang, J.; Cai, Y.; Lavine, C. L.; Peng, H.; Zhu, H.; Anand, K.; Tong, P.; Gautam, A.; Mayer, M. L.; Rits-Volloch, S., Structural and functional impact by SARS-CoV-2 Omicron spike mutations. *Cell Reports* **2022,** *39* (4), 110729.

234. Lupala, C. S.; Ye, Y.; Chen, H.; Su, X.-D.; Liu, H., Mutations on RBD of SARS-CoV-2 Omicron variant result in stronger binding to human ACE2 receptor. *Biochemical and biophysical research communications* **2022,** *590*, 34-41.

235. Laffeber, C.; de Koning, K.; Kanaar, R.; Lebbink, J. H. G., Experimental evidence for enhanced receptor binding by rapidly spreading SARS-CoV-2 variants. *Journal of molecular biology* **2021,** *433* (15), 167058.

236. Jackson, C. B.; Farzan, M.; Chen, B.; Choe, H., Mechanisms of SARS-CoV-2 entry into cells. *Nature Reviews Molecular Cell Biology* **2022,** *23* (1), 3-20.

237. Liu, Y.; Liu, J.; Plante, K. S.; Plante, J. A.; Xie, X.; Zhang, X.; Ku, Z.; An, Z.; Scharton, D.; Schindewolf, C., The N501Y spike substitution enhances SARS-CoV-2 infection and transmission. *Nature* **2021**, 1-9.

238. Huang, H.; Zhu, Y.; Niu, Z.; Zhou, L.; Sun, Q., SARS-CoV-2 N501Y variants of concern and their potential transmission by mouse. *Cell Death & Differentiation* **2021,** *28* (10), 2840-2842.

239. Ali, F.; Kasry, A.; Amin, M., The new SARS-CoV-2 strain shows a stronger binding affinity to ACE2 due to N501Y mutant. *Medicine in drug discovery* **2021,** *10*, 100086.

240. Ye, F.; Zhao, J.; Xu, P.; Liu, X.; Yu, J.; Shangguan, W.; Liu, J.; Luo, X.; Li, C.; Ying, T., Synthetic Homogeneous Glycoforms of the SARS-CoV-2 Spike Receptor-Binding Domain Reveals Different Binding Profiles of Monoclonal Antibodies. *Angewandte Chemie International Edition* **2021,** *60* (23), 12904-12910.

241. Nath Jha, A.; Vishveshwara, S.; Banavar, J. R., Amino acid interaction preferences in proteins. *Protein Science* **2010,** *19* (3), 603-616.

242. Mannar, D.; Saville, J. W.; Zhu, X.; Srivastava, S. S.; Berezuk, A. M.; Zhou, S.; Tuttle, K. S.; Kim, A.; Li, W.; Dimitrov, D. S., Structural analysis of receptor binding domain

mutations in SARS-CoV-2 variants of concern that modulate ACE2 and antibody binding. *Cell reports* **2021,** *37* (12), 110156.